INFLUENCE OF LOCAL CAPILLARY TRAPPING ON CONTAINMENT SYSTEM EFFECTIVENESS

FINAL SCIENTIFIC REPORT

1 OCTOBER 2010
31 MARCH 2014

STEVEN BRYANT

JUNE 2014

DE-FE0004956

CENTER FOR PETROLEUM AND GEOSYSTEMS ENGINEERING
THE UNIVERSITY OF TEXAS AT AUSTIN
AUSTIN, TX 78712-0228

DISCLAIMER

ABSTRACT

Immobilization of CO_2 injected into deep subsurface storage reservoirs is a critical component of risk assessment for geologic CO_2 storage (GCS). Local capillary trapping (LCT) is a recently established mode of immobilization that arises when CO_2 migrates due to buoyancy through heterogeneous storage reservoirs. This project sought to assess the amount and extent of LCT expected in storage formations under a range of injection conditions, and to confirm the persistence of LCT if the seal overlying the reservoir were to lose its integrity. Numerical simulation using commercial reservoir simulation software was conducted to assess the influence of injection. Laboratory experiments, modeling and numerical simulation were conducted to assess the effect of compromised seal integrity.

Bench-scale (0.6 m by 0.6 m by 0.03 m) experiments with surrogate fluids provided the first empirical confirmation of the key concepts underlying LCT: accumulation of buoyant nonwetting phase at above residual saturations beneath capillary barriers in a variety of structures, which remains immobile under normal capillary pressure gradients. Immobilization of above-residual saturations is a critical distinction between LCT and the more familiar "residual saturation trapping."

To estimate the possible extent of LCT in a storage reservoir an algorithm was developed to identify all potential local traps, given the spatial distribution of capillary entry pressure in the reservoir. The algorithm assumes that the driving force for CO_2 migration can be represented as a single value of "critical capillary entry pressure" $P_{c,entry}^{crit}$, such that cells with capillary entry pressure greater/less than $P_{c,entry}^{crit}$ act as barriers/potential traps during CO_2 migration. At intermediate values of $P_{c,entry}^{crit}$, the barrier regions become more laterally extensive in the reservoir, approaching a percolation threshold while non-barrier regions remain numerous. The maximum possible extent of LCT thus occurs at $P_{c,entry}^{crit}$ near this threshold.

Testing predictions of this simple algorithm against full-physics simulations of buoyancy-driven CO_2 migration support the concept of critical capillary entry pressure. However, further research is needed to determine whether a single value of critical capillary entry pressure always applies and how that value can be determined *a priori.*

Simulations of injection into high-resolution (cells 0.3 m on a side) 2D and 3D heterogeneous domains show two characteristic behaviors. At small gravity numbers (vertical flow velocity much less than horizontal flow velocity) the CO_2 fills local traps as well as regions that would act as local barriers if CO_2 were moving only due to buoyancy. When injection ceases, the CO_2 migrates vertically to establish large saturations within local traps and residual saturation elsewhere. At large gravity numbers, the CO_2 invades a smaller portion of the perforated interval. Within this smaller swept zone the local barriers are not invaded, but local traps are filled to large saturation during injection and remain during post-injection gravity-driven migration. The small gravity number behavior is expected in the region within 100 m of a vertical injection well at anticipated rates of injection for commercial GCS.

Simulations of leakage scenarios (through-going region of large permeability imposed in overlying seal) indicate that LCT persists (i.e. CO_2 remains held in a large fraction of the local

traps) and the persistence is independent of injection rate during storage. Simulations of leakage for the limiting case of CO_2 migrating vertically from an areally extensive emplacement in the lower portion of a reservoir showed similar strong persistence of LCT.

This research has two broad implications for GCS. The first is that LCT can retain a significant fraction of the CO_2 stored in a reservoir – above and beyond the residual saturation -- if the overlying seal were to fail. Thus frameworks for risk assessment should be extended to account for LCT. The second implication is that compared to pressure driven flow in reservoirs, CO_2 migration and trapping behave in a qualitatively different manner in heterogeneous reservoirs when buoyancy is the dominant driving force for flow. Thus simulations of GCS that neglect capillary heterogeneity will fail to capture important features of the CO_2 plume.

While commercial reservoir simulation software can account for fine scale capillary heterogeneity, it has not been designed to work efficiently with such domains, and no simulators can handle fine-scale resolution throughout the reservoir. A possible way to upscale the migration and trapping is to apply an “effective residual saturation” to coarse-scale grids. While the extent of overall immobilization can be correlated in this way, all coarser grids failed to capture the distance traveled by the migrating CO_2 for large gravity number. Thus it remains unclear how best to account for LCT in the routine simulation work-flow that will be needed for large-scale GCS. Alternatives meriting investigation include streamline methods, reduced-physics proxies (e.g. particle tracking), and biased invasion percolation algorithms, which are based on precisely the capillary heterogeneity essential for LCT.

TABLE OF CONTENTS

DISCLAIMER iii
ABSTRACT iv
EXECUTIVE SUMMARY 1
1 OBJECTIVES 3
1.1 Motivation and Overall Objective 3
1.2 Task Objectives and Research Goals 3
2 TASKS 4
2.1 Reservoir Simulation Software Used in this Project 5
2.2 Fluid Properties 5
2.2.1 BIC: Effect of CO_2 Solubility 6
2.2.2 VSP: Effect of Phase Density 6
2.2.3 Viscosity 7
2.2.4 Phase Identity 9
3 RESULTS 10
3.1 Determining the Potential for Local Capillary Trapping in Storage Reservoirs 10
3.1.1 Preparation of Model Storage Formations 11
3.1.2 Estimation of Local Capillary Trapping Capacity from Geologic Models 25
3.1.3 Geologic Controls on Potential Trapping Structures 74
3.1.4 Summary of Influence of Geologic Parameters on Volume of Local Traps 98
3.2 Experimental Assessment of Local Capillary Trapping 98
3.2.1 Experimental Apparatus 100
3.2.2 Experimental Design Considerations 103
3.2.3 Fluids 105
3.2.4 Wettability and Contact Angle 108
3.2.5 Beads 110
3.2.6 Experiment Procedures 114
3.2.7 Types of Experimental Domains 117
3.2.8 Experimental Observations 119
3.2.9 Summary of Experimental Observations 176
3.3 Effect of Injection Rate on Extent and Persistence of Local Capillary Trapping 176
3.3.1 Effect of Injection Rate on Extent and Persistence of Local Capillary Trapping 176
3.3.2 Upscaling Local Capillary Trapping 217
4 CONCLUSIONS 237
REFERENCES 240
LIST OF ACRONYMS AND ABBREVIATIONS 242

EXECUTIVE SUMMARY

Immobilization of CO_2 injected into deep subsurface storage reservoirs is a critical component of risk assessment for geologic CO_2 storage (GCS). This project sought to assess the amount and extent of *local capillary trapping* (LCT) that could be expected in storage formations.

LCT refers to the phenomenon in which CO_2 migrating under buoyancy within the storage reservoir accumulates beneath local capillary barriers, establishing large saturations before continuing its migration beyond the spill points of the local barriers. The essential physical conditions for LCT are i) the storage reservoir is spatially heterogeneous, particularly regarding capillary entry pressure and ii) the driving force for CO_2 migration is comparable to the capillary forces in the reservoir. The first condition is readily satisfied; all geologic formations are heterogeneous. The second condition is commonly satisfied for buoyancy-driven CO_2 flow.

The research in this project focused on two aspects of LCT: the influence of injection and injection rate on the degree to which local traps get filled, and the amount of CO_2 that remains in local traps if the seal overlying the reservoir were to lose its integrity. Numerical simulation using commercial reservoir simulation software was conducted to assess the influence of injection, and laboratory experiments, modeling and numerical simulation were conducted to assess the effect of compromised seal integrity.

Bench-scale (0.6 m by 0.6 m by 0.03 m) experiments examined the migration of a buoyant nonwetting phase accompanied by displacement of a denser nonwetting phase using surrogate fluids (brine/glycerol mixture and a decane/mineral oil mixture served as analogs to reservoir brine and supercritical CO_2, respectively). These experiments provided the first empirical confirmation of two key concepts underlying LCT: (i) nonwetting phase migrating due to gravity can accumulate beneath capillary barriers in a variety of structures, and (ii) buoyant nonwetting phase accumulated in this fashion remains immobile as long as the capillary pressure gradient does not exceed the value prevailing when the accumulation was established. In this manner the research confirmed that capillarity is the essential physical mechanism that governs this mode of immobilization and that LCT does establish above-residual saturations.

Predicting the possible extent of LCT in a storage reservoir is therefore an important consideration in designing the injection phase and the monitoring/verification/accounting phase of a storage project. An algorithm was developed to find all potential local traps assuming some knowledge of the geology of the reservoir. Starting from a geostatistical realization of the permeability in the reservoir, the capillary entry pressure was computed for each cell in the model using a Leverett *J*-function. The algorithm assumes that the driving force for CO_2 migration can be represented as a single value of "critical capillary entry pressure" $P_{c,entry}^{crit}$, such that cells with capillary entry pressure exceeding $P_{c,entry}^{crit}$ act as barriers to CO_2 migration. The concept of a critical entry pressure introduces a percolation threshold which has significant influence on the extent of LCT. At an intermediate value of $P_{c,entry}^{crit}$, the barrier regions within the reservoir become more laterally extensive and approach a percolation threshold, yet non-barrier regions remain numerous. The maximum possible extent of LCT thus occurs at some value of $P_{c,entry}^{crit}$ near this threshold.

Testing predictions of this simple algorithm against full-physics simulations of buoyancy-driven CO_2 migration show that the concept of critical capillary entry pressure is a reasonable approximation of the physical process by which traps are filled. But the simulations also indicate that a single value of critical capillary entry pressure may not be sufficient to determine which traps actually get filled in some storage scenarios, nor is it clear how to determine that value from the physical and geologic conditions of the storage process.

Simulations of injection wells and the near wellbore reservoir (ca. 100 m extent) using high-resolution (cells 0.3 m on a side) 2D and 3D heterogeneous domains show two characteristic behaviors. At large-scale commercial injection rates the CO_2 invades the entire thickness of perforated interval in the storage reservoir, and thus fills local traps as well as local barriers. When injection ceases, the CO_2 migrates vertically to establish large saturations within local traps and residual saturation elsewhere. At small injection rates, the CO_2 flow regime is "capillary channeling," invading a smaller portion of the perforated interval. Within this smaller swept zone the local barriers are not invaded at all, but local traps are filled to large saturation. The capillary channeling behavior is of interest because buoyancy becomes dominant at greater distances from the injection well. Regardless of injection rate the filling of local traps in the portion of reservoir invaded by CO_2 was essentially complete.

In simulations intended to examine the persistence of LCT, a column of large permeability grid blocks was created after buoyancy-driven CO_2 migration reached a steady state. Because the steady state distribution of CO_2 saturation in local traps was practically independent of the rate at which CO_2 was injected, the persistence of LCT was also independent of injection rate and was very similar to previous results for the limiting case of CO_2 migrating vertically from an areally extensive emplacement in the lower portion of a reservoir.

This research has two broad implications for GCS. The first is that neglecting heterogeneity of capillary entry pressures in storage reservoirs gives a worst-case estimate of long-term storage security. That is, LCT can retain a significant fraction of the CO_2 stored in a reservoir – above and beyond the residual saturation -- if the overlying seal were to fail. Thus frameworks for risk assessment should be extended to account for LCT. The second implication is that CO_2 migration and trapping are qualitatively different in heterogeneous reservoirs when buoyancy is the dominant driving force for flow. This is often the case: in most of the storage reservoir far from vertical injection wells, in almost all the reservoir when horizontal injection wells are used, and in the entire reservoir after injection ends. Thus simulations of GCS that neglect capillary heterogeneity will fail to capture important features of the CO_2 plume.

While commercial reservoir simulation software can account for fine scale capillary heterogeneity, it has not been designed to work efficiently with such domains, and no simulators can handle fine-scale resolution throughout the reservoir. To address this problem, the possibility of representing LCT in fine-scale grids as an "effective residual saturation" in coarse-scale grids was investigated. While the extent of overall immobilization can be correlated in this way, all coarser grids failed to capture the distance traveled by the migrating CO_2 in the capillary channeling flow regime (buoyancy dominated, large gravity number). Thus it remains unclear how best to account for LCT in the routine simulation work-flow that will be needed for large-scale GCS. Alternatives such as streamline methods, reduced-physics proxies (e.g. particle tracking), and biased invasion percolation algorithms, which are based on precisely the capillary heterogeneity essential for LCT, are suggested.

1 OBJECTIVES

1.1 Motivation and Overall Objective

Immobilization of CO_2 injected into deep subsurface storage reservoirs is a critical component of risk assessment for geologic CO_2 storage (GCS). This project sought to assess the amount and extent of *local capillary trapping* (LCT) that could be expected in storage formations.

LCT refers to the phenomenon in which CO_2 migrating under buoyancy within the storage reservoir encounters locally continuous regions of larger-than-average capillary entry pressure. The CO_2 accumulates beneath these local capillary barriers, establishing large saturations before continuing its migration beyond the spill points of the local barriers. The essential physical conditions for LCT are i) spatial heterogeneity of the petrophysical properties of the storage reservoir, particularly capillary entry pressure and ii) driving force for CO_2 migration that is comparable to the capillary forces in the reservoir. The first condition is readily satisfied; all geologic formations are heterogeneous. Theory and previous simulations suggest that the second condition is commonly satisfied when CO_2 is migrating because of buoyancy only.

The overall objective of this project is to determine the extent of local capillary trapping, i.e., CO_2 immobilization beneath small-scale capillary barriers, which can be expected in typical heterogeneous storage formations.

1.2 Task Objectives and Research Goals

The research in this project focused on two aspects of LCT: the influence of injection and injection rate on the degree to which local traps get filled, and the amount of CO_2 that remains in local traps if the seal overlying the reservoir were to lose its integrity. Numerical simulation using commercial reservoir simulation software was conducted to assess the influence of injection, and laboratory experiments, modeling and numerical simulation were conducted to assess the effect of compromised seal integrity.

To accomplish the overall objective, task objectives include: i) characterize the petrophysical and geologic controls upon the number and volume of potential local capillary traps; ii) determine the degree to which potential local capillary traps are filled in anticipated storage schemes; iii) quantify the extent of immobilization persisting after loss of integrity of the overlying seal of the storage formation; iv) incorporate the results into a functional form which can be readily integrated into existing reservoir simulation packages; and v) conduct lab-scale experiments to validate simulations.

2 TASKS

The project undertook a set of modeling tasks (2, 3 and 8), experimental tasks (4 and 5) and simulation tasks (6 and 7) in a two phases. For reference the tasks and subtasks are included below.

- TASK 2.0: Characterize Structure of Potential Local Traps
  - Task 2.1: Gather Correlations Between Key Formation Properties
  - Task 2.2: Gather Suite of Geostatistical Models
  - Task 2.3: Construct Suite of Model Storage Formations
  - Task 2.4: Find Potential Local Capillary Traps in Model Storage Formations
- TASK 3.0: Determine Influence of Geologic Setting on Potential Trapping Structures
- TASK 4.0: Establish Protocol for Laboratory Assessment of Local Capillary Trapping
- TASK 5.0: Evaluate Security of Local Capillary Trapping in Heterogeneous 2D Models
- TASK 6.0: Determine Influence of Operating Conditions on Local Trap Filling
  - Task 6.1: Effect of Buoyancy-dominated Displacement
  - Task 6.2: Effect of Viscous Forces
  - Task 6.3: Effect of CO_2 Volume
- TASK 7.0: Quantify Extent of Local Capillary Trapping Realized After Seal Rupture
- TASK 8.0: Determine Coarse-scale Representation of Local Capillary Trapping

The deliverables for these tasks are tabulated below for reference. Sections of this report contain material that constitutes these deliverables. These sections are footnoted to indicate the corresponding deliverable.

Deliverable	Description
2.1.1	Set of correlations between permeability and porosity, between porosity and $S_{w,irr}$, between porosity and S_{gr} representative of likely storage formations
2.1.2	Set of *J*-functions and $P_{c,entry}^{crit}$ representative of likely storage formations
2.2	Suite of realizations in which variograms and permeability variance are independently varied for ranges representative of likely storage formations
2.3	Set of model storage formations with petrophysical properties relevant to local capillary trapping (k, ϕ, $S_{w;irr}$, S_{gr}, P_c^{entry} and drainage/imbibition curves)
2.4.1	Relationship between the characteristic capillary barrier size $L^{avg}{}_{barrier,local}$ and the value of $P_{c,entry}^{crit}$ for that barrier.
2.4.2	Histograms of sizes of potential local capillary traps
2.4.3	Histograms of potential local capillary trap volumes, analysis of volume fraction held in such traps as function of primary geologic, petrophysical controls
3.1	Effect of dip angle on relationship between the characteristic capillary barrier size $L^{avg}{}_{barrier,local}$ and the value of $P_{c,entry}^{crit}$ for that barrier.
3.2	Histograms of dimensions of potential local capillary traps for several dip angles
3.3	Histograms of potential local capillary trap volumes, analysis of volume fraction held in such traps for different dip angles.

Deliverable	Description
4.1	Procedure for establishing saturation distribution resulting from buoyant displacement of wetting by nonwetting phase in heterogeneous porous medium
5.1	Experimental evaluation of extent of local capillary trapping that persists in heterogeneous porous media after top seal is ruptured
6.1	Trend of the fraction of potential local capillary traps filled as a function of primary controls for displacement driven by buoyancy.
6.2	Trend of fraction of potential local capillary traps filled as function of primary controls including effect of the injection period for a range of gravity numbers
6.3.1	Trend of fraction of potential local capillary traps filled under buoyancy as function of primary controls for different volumes of emplaced CO_2.
6.3.2	Trend of fraction of potential local capillary traps filled as a function of primary controls, including injection period, for range of gravity numbers and volumes of emplaced CO_2.
7.0	Trend of fraction of CO_2 above residual that remains trapped after seal rupture for range of operating conditions in a representative set of storage formations.
8.0	A function in a form readily incorporated in existing data structures in reservoir simulators that accounts for the amount of local capillary trapping in terms of geologic and petrophysical and operating parameters.

2.1 Reservoir Simulation Software Used in this Project

Our simulation studies will be based on simulations performed with Computer Modeling Group's (CMG) commercial simulator. GEM (General Equation of state Model) is CMG's general equation of state (EOS)-based compositional reservoir simulator for modeling the flow of three-phase, multicomponent fluids. GEM is a robust, fully compositional simulator used to model any type of reservoir where the importance of the fluid composition and their interactions are essential to the understanding of the process. So it is a proper tool in this project where our main discussion is about heterogeneity and its effect on capillary pressure. GEM has all the features required to implement our simplified model in a simulator. The main features used in this study are reviewed in the following sections.

2.2 Fluid Properties

In compositional simulators all hydrocarbon phase properties are calculated using an equation of state (EOS). GEM utilizes either the Peng-Robinson or the Soave-Redlich-Kwong equation of state to predict the phase equilibrium compositions and densities of the oil and gas phases, and supports various schemes for computing related properties such as oil and gas viscosities.

Two methods can be used in GEM to model the dissolution of CO_2 in brine:

1. Henry's method: Modeling brine as the "aqueous" phase and using Henry's law and an equation of state.
2. Tuned-EOS method: Modeling brine as the "oil" phase and tuning an equation of state to experimental data on solubility.

In this study, the second method is used which is described briefly here. In the Tuned-EOS method, S_w is assumed to be zero while brine is modeled as the "oil" phase and the EOS is used for flash calculations. The basic properties needed for EOS calculations are the critical properties of each component and the interaction coefficients of each component pair in the conditions of process. Kumar *et al.* (2005) tuned the Peng-Robinson equation of state (PREOS) using experimental data for density and solubility over a wide range of pressures, temperatures and salinities related to aquifer conditions. Solubility determines how much CO_2 goes into solution in brine and density determines how fast the buoyant forces sequester the injected gases.

2.2.1 BIC: Effect of CO_2 Solubility

The binary interaction coefficient (BIC) for H_2O-CO_2 pair was tuned by Kumar (2004) to match the experimental values of CO_2 solubility in brine. He developed the following correlation for BIC of H_2O-CO_2 pair in PR equation of state:

$$k_{H_2O-CO_2} = -0.093625 + 4.861\times10^{-4}\left(T-113\right) + 2.29\times10^{-7}\,S \qquad (1)$$

where:

$k_{H_2O-CO_2}$ = Binary interaction coefficient for H_2O-CO_2 pair

T = $1.8T_{fluid}$ +32 where T_{fluid} is temperature in °C

S = Salinity, ppm

So the effect of temperature and brine salinity on CO_2 solubility is considered implicitly in calculation of the BIC which is introduced to simulator.

In this study, we used the typical reservoir temperature of $T_{fluid} = 60$ °C and salinity of $S = 100,000$ ppm which gives $k_{H_2O-CO_2} = -0.0576003$. The corresponding keyword in GEM is *BIN.

2.2.2 VSP: Effect of Phase Density

The volume shift parameter (VSP) for brine was tuned by Kumar (2004) to match the brine density data. The following correlation was developed for VSP of brine on a wide range of temperature, pressure and salinity in PR equation of state:

$$v^s_{H_2O} = 0.179 + 2.2222\times10^{-4}\left(T-113\right) + 4.9867\times10^{-7}\,S \qquad (2)$$

where:

$v^s_{H_2O}$ = Volume shift parameter for H_2O

and *T* and *S* are as above.

According to Kumar, this correlation gives a good match for pure brine density values, but uncertain predictions for CO_2-saturated brine because of lack of sufficient experimental data points.

Using the typical reservoir temperature of $T_{fluid} = 60$ °C T =Œ and salinity of $S = 100,000$ ppm in this study leads to $v^s_{H_2O} = 0.2348669$. The constant value of 0.024668 is used as $v^s_{CO_2}$ which is the value for pure CO_2. The keyword for VSP in GEM is *VSHIFT.

2.2.3 Viscosity

There are five methods to calculate the oil and gas phase viscosities in GEM. We use the corresponding states correlation given in Pedersen *et al.* (1984). This option is set by keyword: *VISCOR *PEDERSEN.

Under this option the hydrocarbon phase viscosities are functions of fluid composition, pressure, and temperature. The viscosity of a mixture calculated using the Pedersen model depends strongly on the critical pressures, critical temperatures, and molecular weights of the components, as well as the coefficient values.

The viscosity of the mixture is computed according to the following formula:

$$\frac{\mu_{mix}(P,T)}{\mu_0(P_0,T_0)} = \left(\frac{T_{cmix}}{T_{c0}}\right)^{-\frac{1}{6}} \left(\frac{P_{cmix}}{P_{c0}}\right)^{\frac{2}{3}} \left(\frac{M_{mix}}{M_0}\right)^{\frac{1}{2}} \left(\frac{\alpha_{mix}}{\alpha_0}\right) \tag{3}$$

where:

μ = Viscosity

T_c = Critical temperature

P_c = Critical pressure

M = Molecular weight

α = Rotational coupling coefficient

The subscript “mix” refers to the mixture property, and the subscript “0” refers to the reference substance property. The reference substance for the Pedersen model is methane.

The mixture critical temperature and pressure are calculated using mixing rules that are a function of the component critical temperatures and pressures, and mole fractions. The molecular weight of the mixture is determined from:

$$M_{mix} = coef(1) \times \left(M_w^{coef(2)} - M_n^{coef(2)} \right) + M_n \tag{4}$$

where M_w is the weight fraction averaged molecular weight, and M_n is the mole fraction averaged molecular weight.

The rotational coupling coefficient is calculated as follows:

$$\alpha = 1 + coef(3) \times \rho_{r0}^{coef(4)} M^{coef(5)} \tag{5}$$

where ρ_{r0} is the reduced density of the reference substance.

The coefficients are introduced to GEM using the keyword *VISCOEFF in order from 1 to 5. Coefficients used for Pedersen correlation and other fluid properties used in this work are given in Table 1, Table 2 and Table 3.

Table 1: Coefficients Used for Pedersen Correlation

Coefficient No.	Value
1	0.291
2	1.4
3	0.0005747
4	4.265
5	1.0579

Table 2: Component Properties of the Model

Property	CO_2	H_2O
Critical pressure, atm	72.8090	217.7546
Critical temperature, K	304.1278	647.0944
Critical volume, m^3/k.mol	0.094	0.056
Molecular weight, g/g.mol	44.01	18.015
Acentric factor	0.22394	0.344
Parachor	78	52
Boiling point, °C	-78.4	100

Table 3: Tuning Parameters of the Model

Property	CO_2	H_2O
Volume shift parameter	0.024668	0.234867
Binary interaction coefficient with respect to H_2O	-0.0576003	0

2.2.4 Phase Identity

When the EOS calculation determines that the hydrocarbon fluid exists as a single phase, the simulator alone cannot determine whether a phase should be called “oil” or “gas” without tedious critical point calculations. Nevertheless, phase identity is important in reservoir simulation, as the oil and gas phases use different relative permeabilities and capillary pressure data. In GEM, the identity of a single phase appearing during the simulation can be determined by four approaches. In this study, phase is classified by whether its mass density is closer to a reference gas density or a reference oil density. If necessary, these reference densities are taken from the unstable phases found during stability testing. This method is invoked with the following keyword: *PHASEID *DEN.

3 RESULTS

The results of the research are grouped in three main sub-sections, as tabulated below, which arrange the Tasks described above.

Tasks	Subsection Title
2, 3	Determining the Potential for Local Capillary Trapping in Storage Reservoirs
4, 5	Experimental Assessment of Local Capillary Trapping
6, 7, 8	Effect of Injection Rate on Extent and Persistence of Local Capillary Trapping

3.1 Determining the Potential for Local Capillary Trapping in Storage Reservoirs

The goal of Tasks 2 and 3 is to examine a range of model reservoirs and evaluate the number and volume of the local capillary traps expected in those reservoirs. The heterogeneity of the capillary entry pressure is by far the most important petrophysical property that influences LCT. Other properties (porosity, permeability, relative permeability) affect the time scale for filling local traps and the total mass of CO_2 held in these traps, but these are second-order effects compared to difference between migration in a domain with homogeneous capillary entry pressure (a single capillary pressure curve) vs migration in a domain with heterogeneous capillary entry pressure (the capillary pressure curve starts at a different entry pressure in each grid block). Thus we focus on extracting a model of the capillary entry pressure distribution from the geologic description of a storage reservoir.

Capillary entry pressures are not routinely measured nor are they commonly available in the literature. This is not a serious disadvantage because Leverett showed that the permeability of a porous medium is strongly correlated with the capillary entry pressure of the medium. This correlation is embodied in the classical Leverett *J*-function. The *J*-function describes very well the behavior of samples with a wide range of permeability and porosity, as long as all the samples are from the same rock type. Thus we can obtain the spatial distribution of entry pressure in a reservoir if we have a spatial realization of the permeability in a reservoir and a reasonable idea of the *J*-function(s) for the rock types in the reservoir. Such realizations are routinely generated in modern geostatistical approaches. The variogram that defines the correlation structure of a permeability field can be related to the depositional environment and other features of the geologic description. Thus to meet the objectives of this part of the research it suffices to examine a range of geostatistical models, to invoke typical correlations between permeability and porosity (because the Leverett *J*-function also depends on porosity), and apply representative *J*-functions to compute the capillary entry pressure for each grid block. This is a straightforward extension of routine workflow in reservoir simulation, so this idea is readily implemented.

3.1.1 Preparation of Model Storage Formations[1]

The base case analysis is performed on a 30 m high, 120 m wide domain with grid blocks of 0.3 m by 0.3 m length, thus involving 40,000 grid blocks. The aquifer is assumed to be located 1615 m below the surface, with initial pressure of 15.6 MPa at constant temperature of 60°C and a salinity of 100,000 ppm which are typical of a deep saline aquifer.

Petrophysical Properties

Permeability[2]

The permeability field is generated for all grid blocks using a probabilistic approach that represents the permeability as an outcome of a spatial random function. This will lead to a heterogeneous permeability field, rather than using homogeneous or layered description. The random function is characterized by the mean permeability value; the variance, which is a quantitative measure of heterogeneity, and the semivariogram, which indicates the spatial arrangement and correlation structure of the permeability values. The permeability values are assumed to be lognormally distributed.

The correlation structure is modeled using the semivariogram. The semivariogram measures the mean-squared difference between pairs of data points separated by a given lag distance and direction. It is defined as

$$\gamma\left(\vec{h}\right)=\frac{1}{2}Var\left[k\left(\overrightarrow{x_i}\right)-k\left(\overrightarrow{x_i}+\vec{h}\right)\right]=\frac{1}{2n}\sum_{i=1}^{n}\left[k\left(\overrightarrow{x_i}\right)-k\left(\overrightarrow{x_i}+\vec{h}\right)\right]^2 \quad (6)$$

where γ is the estimated semivariance of the permeability data k for a separation distance and direction specified by the lag distance vector $\vec{h}$, n is the number of data pairs used for the calculation, and $\overrightarrow{x_i}$ indicates the data locations. More description and discussion of semivariograms and their usage can be found in several references (e.g., Deutsch, 2002; Caers, 2005).

Figure 1 shows the theoretical variogram model that we use in this work. It starts at c_n at no lag distance which is called the nugget. It shows the component of variability that is spatially uncorrelated. Then, the semivariance increases with increasing lag distance until a certain distance is reached at which it levels off and becomes constant at its maximum value. The lag distance at which the variogram levels off is defined as the correlation length or range. It indicates the separation distance beyond which pairs of data points are no longer correlated. The value of the variogram at this point is called the sill. It shows the variability (i.e., semivariance)

[1] The collection of results in this section constitutes Project Deliverable 2.3 Set of model storage formations with petrophysical properties relevant to local capillary trapping (k, ϕ, $S_{w;irr}$, S_{gr}, P_c^{entry} and drainage/imbibition curves)

[2] This section constitutes Project Deliverable 2.2: Suite of realizations in which variograms and permeability variance are independently varied for ranges representative of likely storage formations

of the entire data set. In cases where the semivariogram reaches the sill asymptotically, the range is the taken to be the lag at which 95% of the sill is reached. In geologic structures, the correlation length commonly shows anisotropy: the correlation lengths in the vertical direction are usually smaller than those in the lateral direction.

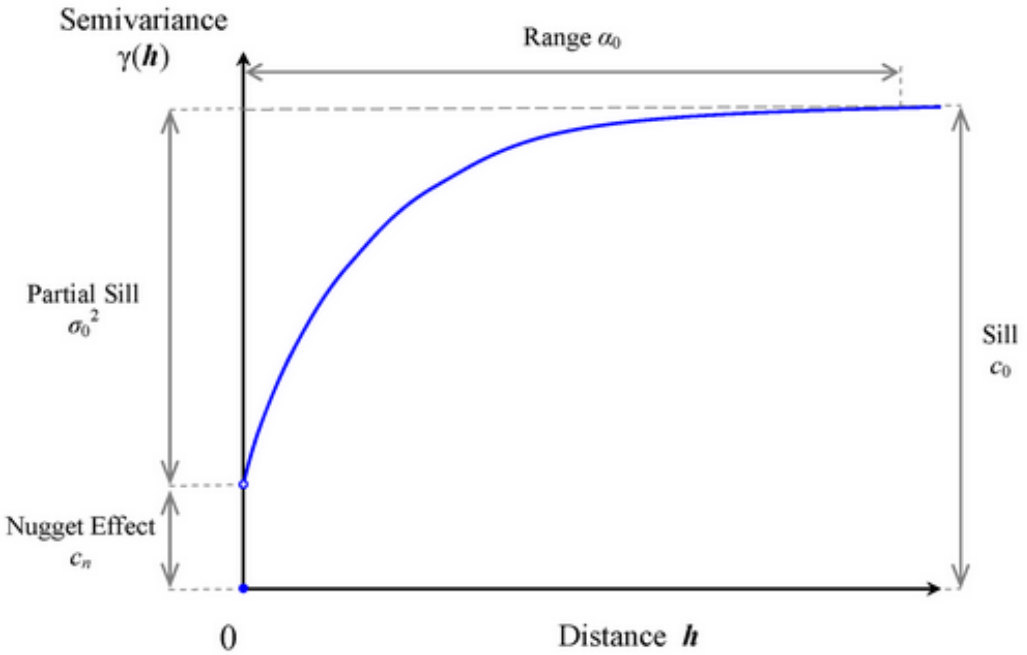

Figure 1: A theoretical semivariogram of spherical type and its characteristics.

A well behaved theoretical model for the variogram structure is given by the stable semivariogram

$$\gamma(h) = s\left[1 - exp\left(-\left(\frac{h}{a}\right)^p\right)\right] \tag{7}$$

where s is the variance or sill parameter, a is the range parameter, and p is the asymptotic power-law exponent. This model represents various popular variogram models. For $p = 0$, the model describes the nugget effect model (no correlation). $p = 1$ produces the more common exponential model. $p = 2$ leads to the Gaussian model. In this study, we will use $p = 1$ to generate permeability fields based on an exponential model for spatial distribution.

An alternative method of generating permeability fields is to identify and map the rock facies directly from reservoir measurements, e.g., seismic data. In this work, the use of synthetic models based on theoretical variogram model is preferred since it allows a more systematic study.

Implementation

A stochastic simulation technique based on spectral transforms is used to generate permeability field realizations (Jennings *et al.*, 2000). The input autocorrelation structure is converted into a covariance function, which is sampled on the grid used for the flow calculations. The Fast Fourier Transform (FFT) algorithm is used to produce the amplitude spectrum of the permeability covariance function. This is multiplied by the FFT of an uncorrelated Gaussian noise and inverted to produce a realization that has a standard normal distribution. This data is then transformed to a lognormal distribution of the desired mean and variance. All the points in the permeability realization thus produced are globally conditioned to the input parameters of the semivariogram. The method is fast even for large number of grid blocks.

For a typical model, permeability values were generated for all 40,000 grid blocks in aquifer model. Two realizations of permeability field were used in the simulations:

- 1.5 m correlation length in the horizontal direction
- 15 m correlation length in the horizontal direction

Both realizations are uncorrelated in the vertical direction. Stochastic parameters used to generate the permeability fields are given in Table 4. The probability distribution of the permeability fields is shown in Figure 2. Figure 3 shows the two different realizations of permeability field. The aquifer was considered to be isotropic. Therefore, the y-direction and z-direction permeability is set to be equal to the x-direction value.

Table 4: Stochastic Parameters Used for Generation of Permeability Field

Parameter	Value
Correlation length in x direction, m	1.5 or 15
Correlation length in y direction, m	0.3
Correlation length in z direction, m	0.3
Mean, m^2	194×10^{-15}
Standard deviation of Ln(k)	1.2
Dykstra-Parson's coefficient	0.7

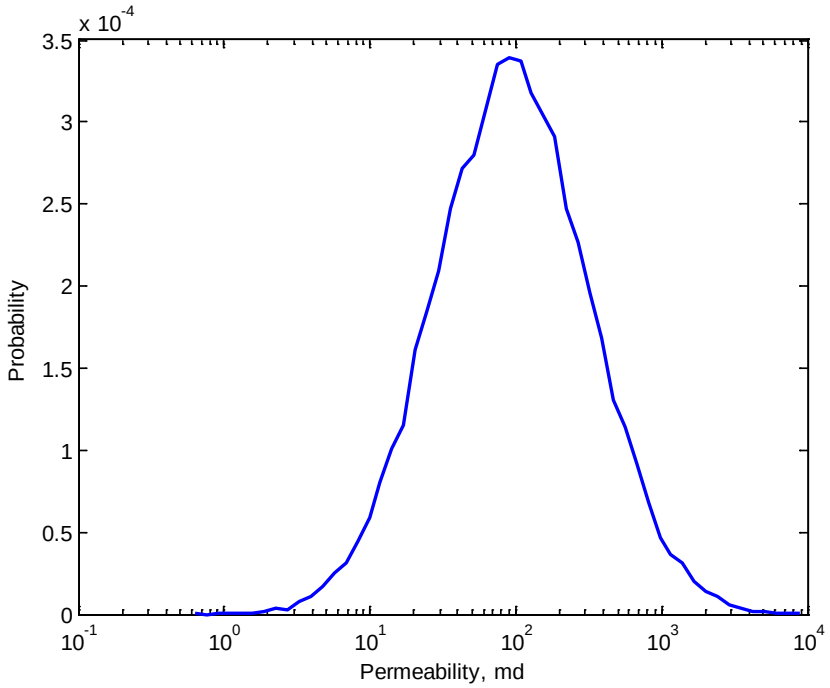

Figure 2: The probability distribution of the permeability field.

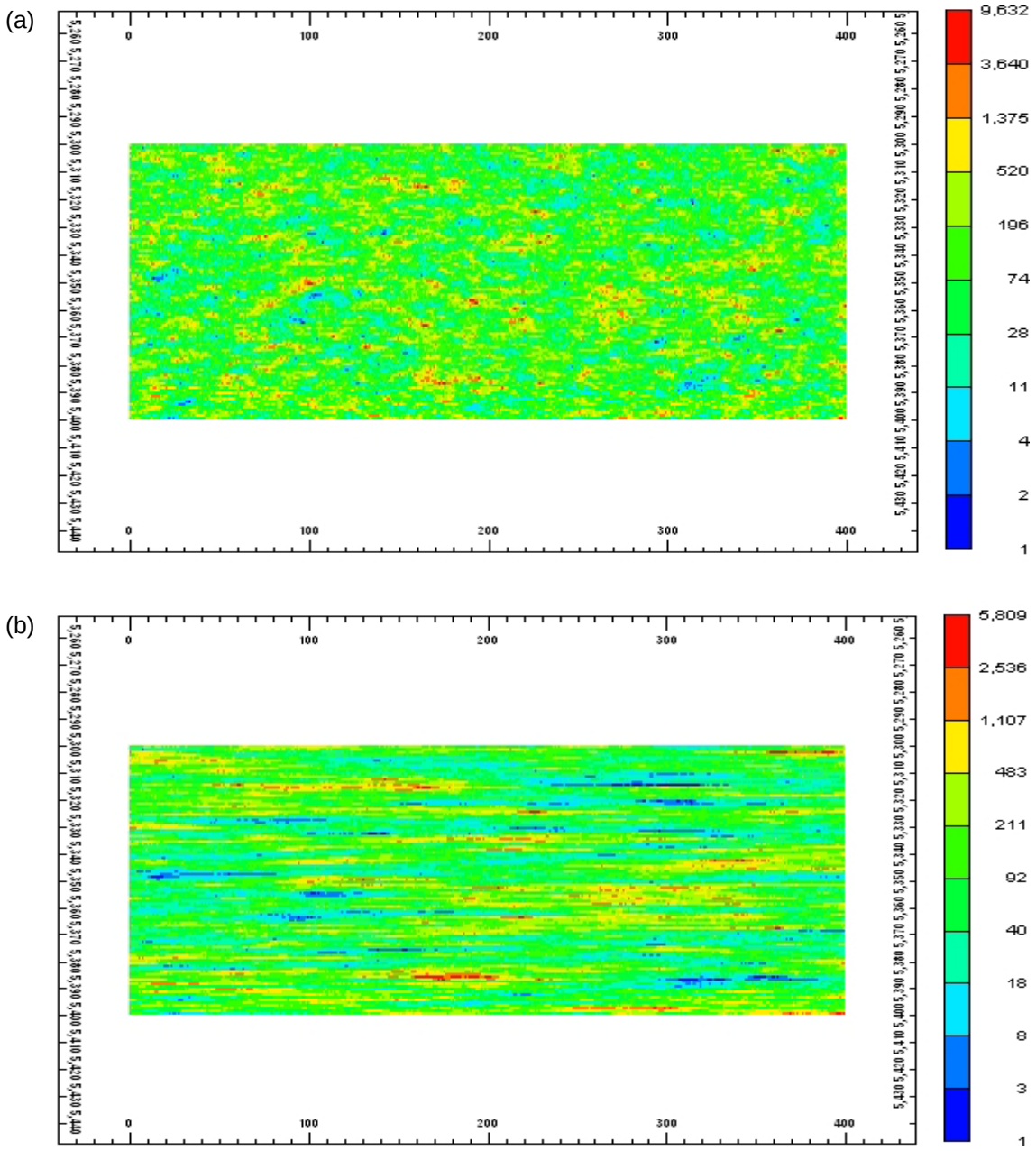

Figure 3: Geostatistical realizations of permeability (in mD or 10^{-15} m^2) at a 0.3 m ft by 0.3 m scale used in this work. The vertical scale is exaggerated by a factor of two. The fields have (a) 1.5 m correlation length in horizontal direction, (b) 15 m correlation length in horizontal direction. Both are uncorrelated in the vertical direction.

Other Petrophysical Properties[3]

It is a common practice in simulation studies to use correlations relating porosity, permeability, maximum residual gas saturation, and irreducible water saturation for sandstones to evaluate

[3] This section constitutes Project Deliverable 2.1.1: Set of correlations between permeability and porosity, between porosity and $S_{w,irr}$, between porosity and S_{gr} representative of likely storage formations

these properties from synthetically generated permeability field. We will review some commonly used cross-property correlations from the literature.

Timur (1968) conducted laboratory measurements on a total of 155 whole core samples obtained from the sand sections of four wells in three different oil fields: a Gulf Coast field, a Colorado field, and a California field. The Gulf Coast cores were obtained from the sand section of a well, between 9,000 and 12,000 ft. They were, in general, poorly consolidated, well-sorted sandstones with relatively high porosities. The same sand section was cored in two wells in a Colorado field, between 6,000 and 7,000 ft. Unlike those from the Gulf Coast field, these were well-consolidated, tight sandstones. Whole cores were also obtained between 9,000 and 10,000 ft in a well in the California field. These were moderately well-consolidated but poorly sorted micaceous sandstones.

He suggested the generalized relationship for estimating permeability from measurements of ϕ and S_{wr} as

$$k = 0.136\frac{\phi^{4.4}}{S_{wr}^{2}} \tag{8}$$

However, the regression coefficients b_1 and b_2 corresponding to the parameter $v = \frac{\phi^{4.4}}{S_{wr}^{2}}$ in generalized equation $k = b_2 v^{b_1}$, vary slightly from field to field. Timur finds that Eq. (8) predicts permeability of the core samples with considerably low standard error except in the Gulf Coast field.

Timur also concluded that the generalized equation

$$S_{wr} = 3.5\frac{\phi^{1.26}}{k^{0.35}} - 1 \tag{9}$$

might be used for estimating S_{wr} from the combination of measurements of ϕ and k with a standard error of 13% pore volume.

Keelan and Pugh (1975) presented the laboratory measurements of petrophysical properties and residual gas saturations after gas displacement by wetting-phase imbibition for selected carbonate reservoirs. They tabulated basic information for core samples including permeability and porosity. Figure 4 shows the plot relating permeability and porosity for the various reservoirs in their study. The variation in the permeability vs. porosity plot is indicative of varying rock matrix and pore-size distribution and considerable difference in pore geometry of different reservoirs, as evidenced by capillary pressure and pore entry histograms.

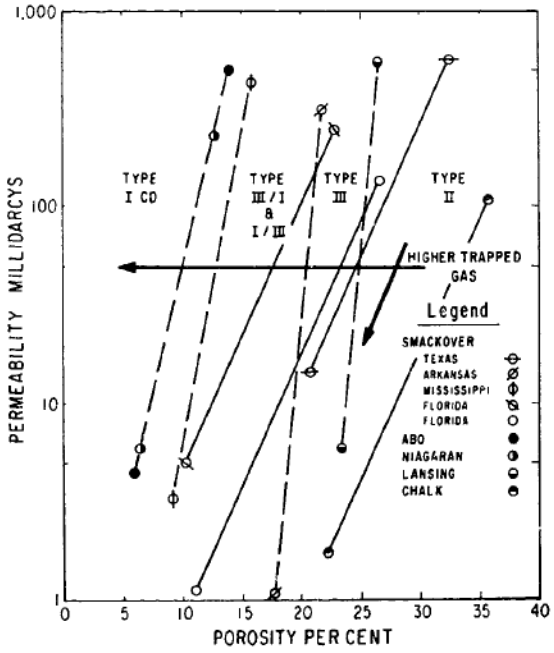

Figure 4: Permeability versus porosity for all reservoirs in Keelan and Pugh (1975).

Figure 5 illustrates porosity versus residual gas saturation data extracted by Kellan and Pugh for an initial gas saturation of 80 percent. The data are grouped by rock type, which indicates that the pore throat connections as reflected by matrix characteristics are more important than the total porosity.

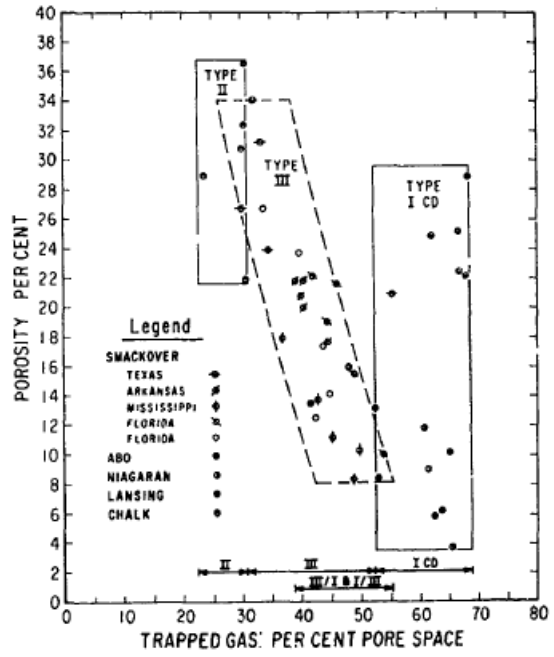

Figure 5: Residual gas saturation correlation with porosity and rock type.

Type III samples show a greater dependence on porosity. A trend of increasing trapped gas with decreasing porosity is noted on both an intra-reservoir and inter-reservoir basis. Each reservoir

exhibits its own trend, which is essentially parallel but different from the others, and reflects the differences noted on the permeability vs. porosity plot of Figure 4.

From the data of Miocene section, offshore Louisiana, shown in Figure 6, Holtz (2002) determined the relationship between porosity and permeability by generating a best-fit equation between the two properties with a good accuracy:

$$k = 7 \times 10^{7} \phi^{9.606} \tag{10}$$

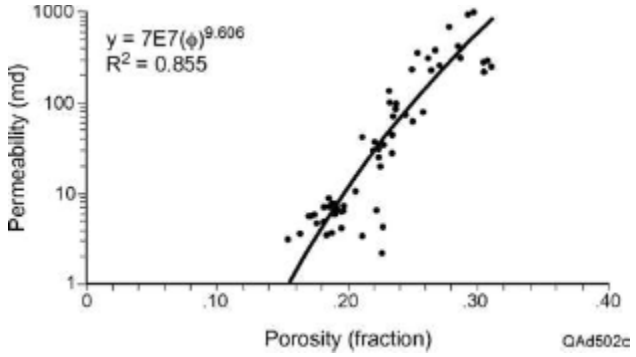

Figure 6: Permeability and porosity data from offshore Louisiana and correlation between them developed by Holtz (2002).

Holtz also determined an expression for initial water saturation by assuming that pore geometry controls petrophysical interrelationships. He concluded that the ratio of $\log k / \phi$ should give a measure of the pore geometry and use the fact that the capillary pressure curves that demonstrate low irreducible water saturations correspond to larger $\log k / \phi$ ratios to suggest the following relationship for calculating irreducible water saturation:

$$S_{wir} = 5.159 \left(\frac{\log k}{\phi} \right)^{-1.559} \tag{11}$$

A robust model of residual gas saturation was also developed by Holtz from field and published data. He documented a strong relationship between increasing porosity and decreasing residual gas saturation, as can be seen in Figure 7. The trend is linear, and the best fitting equation is given as

$$S_{grm} = -0.9696\phi + 0.5473 \tag{12}$$

Holtz validated the S_{grm} model by finding similar S_{grm} values and porosity-S_{grm} trends derived from wireline logs.

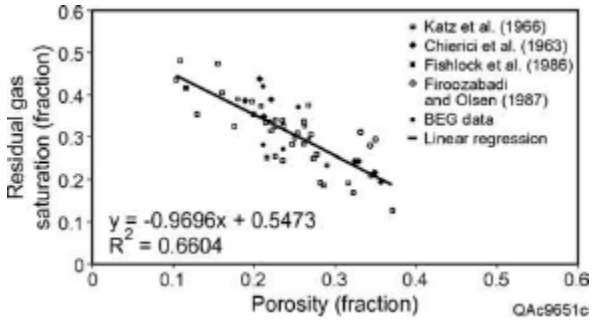

Figure 7: Residual gas saturation vs. porosity data and their correlation as an inverse linear relationship developed by Holtz (2002).

Since the data used in the study by Holtz (2002) are from a typical offshore sandstone formation, the developed correlations relating porosity, permeability, maximum residual gas saturation and residual water saturation are suitable for our study. So we will use Eq. (10) to calculate the porosity of each grid block from its stochastically generated permeability value. Also, Eq. (11) is used for calculating irreducible water saturation based on average porosity and permeability of the field. In these equations k is permeability in md (i.e. 10^{-15} m^2) and ϕ is porosity in fraction.

Capillary Pressure

Bennion and Bachu (2006) conducted brine-CO_2 interfacial tension (IFT) measurements for equilibrium brine and CO_2 at reservoir conditions. They also conducted the detailed 700 MPa mercury-injection capillary pressure tests on several rock samples to determine specific pore size distributions. Three sandstone and three carbonate potential sequestration zones in the Wabamun Lake area in Alberta, Canada were evaluated, together with a caprock shale. The results are published as graphs of capillary pressure curves for the ten rock sample sets.

Plug and Bruining (2007) developed and validated a capillary pressure set-up that can be used to measure the capillary pressure behavior for CO_2 sequestration applications. For the small injection rates applied, the viscous forces are negligible and the capillary pressure curves are considered as static. Their experimental results are presented for the unconsolidated sand–CO_2–water system at pressure of 85 bars in Figure 8. Both liquid and supercritical CO_2 are used. The drainage capillary pressure for liquid CO_2 and supercritical CO_2 is of the same range.

Pini *et al.* (2012) measured CO_2-water drainage capillary pressure curves at representative reservoir pressure and temperature conditions on two sandstone cores with different grain sorting, namely a Berea sandstone and a core from the Arqov formation in Israel. Figure 9 shows the results.

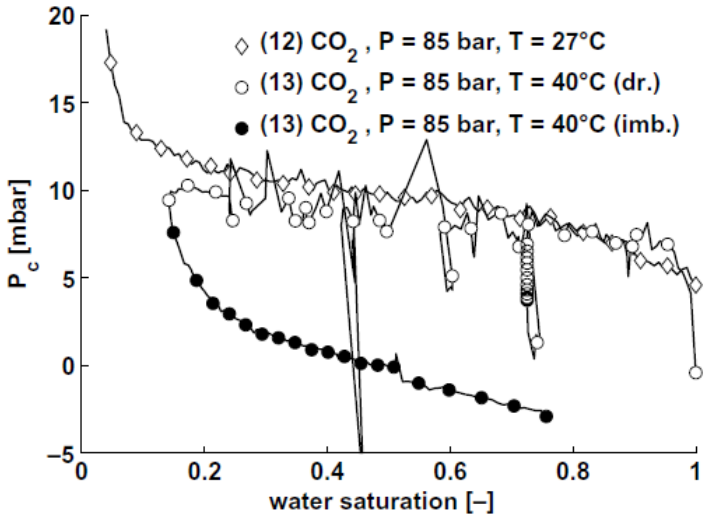

Figure 8: Experimental capillary pressure curves for liquid and supercritical CO_2 published by Plug and Bruining (2007).

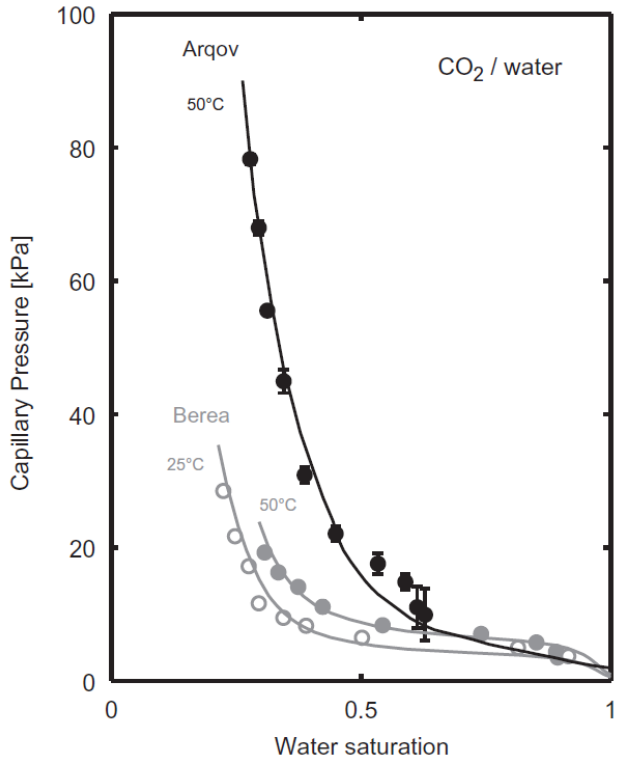

Figure 9: Experimental capillary pressure curves for the Berea and Arqov samples published by Pini et al. (2012).

In order to simplify reservoir simulations it is common to fit analytical models to capillary pressure curves. A popular empirical model for capillary pressure in petroleum engineering is Brooks-Corey model (Brooks and Corey, 1966). They proposed the drainage capillary pressure model of the form:

$$P_c = p_e \cdot \left(S_w^*\right)^{-\frac{1}{\lambda}} \tag{13}$$

where:

p_e = value of P_c at $S_w = 1$

λ = pore size distribution index

S_w^* = reduced wetting phase saturation defined as:

$$S_w^* = \frac{S_w - S_{wir}}{1 - S_{wir}} \tag{14}$$

The parameter λ controls the slope of the plot. A large value of λ gives a small slope, which corresponds to the capillary pressure curve with a narrow pore size distribution whereas a small value of λ gives a large slope, which corresponds to the capillary pressure curve for a wide pore size distribution. A porous medium with a uniform pore size corresponds to $\lambda = \infty$. λ is called the pore size distribution index in view of these observations.

The Brooks-Corey model cannot adequately fit an S-shaped capillary pressure curve with an inflection. It gives a good fit when the capillary pressure curve has a hyperbolic shape.

Table 5 shows the parameters of Brooks-Corey model for capillary pressure curve used in this study. Figure 10 shows the calculated capillary pressure curve with those parameters. The curve is typical of sedimentary rocks with an entry capillary pressure of 8.3 kPa and a maximum capillary pressure of 15.9 kPa at irreducible water saturation.

Table 5: Parameters of Brooks-Corey Model for Reference Capillary Pressure Curve

Parameter	Value
p_e	8.3 kPa
λ	8.49
Irreducible water saturation, S_{wir}	0.15

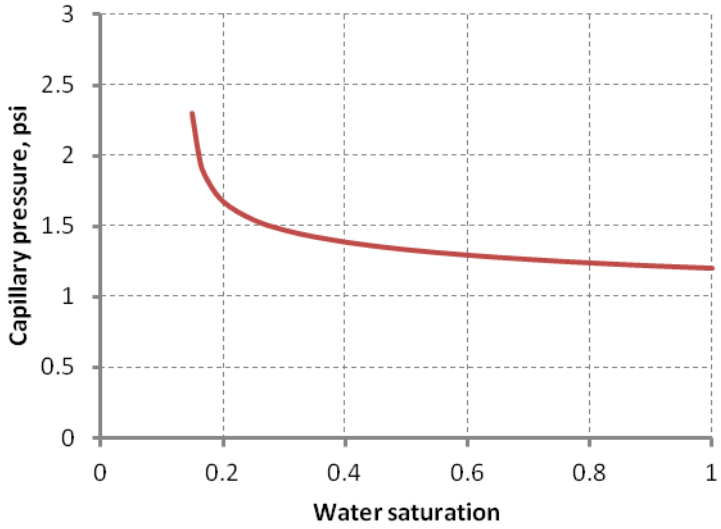

Figure 10: Reference capillary pressure curve generated by Brooks-Corey model.

Capillary pressure scaling[4]

The capillary entry pressure is inversely proportional to the radius of a typical pore throat, while absolute permeability varies with the square of the pore throat radius. Thus, heterogeneity of permeability, Figure 3, implies heterogeneity of capillary entry pressure. In the other words, the capillary pressure curves for rock samples from the same reservoir having different permeabilities will be different. The heterogeneity of capillary pressure can be taken into account using the Leverett *J*-function, which is a dimensionless capillary pressure function (Leverett, 1941):

$$J\left(S_w\right) = \frac{P_c}{\sigma \cos\theta}\sqrt{\frac{k}{\phi}} \tag{15}$$

where:

S_w = Water saturation

P_c = Capillary pressure

k = Permeability

ϕ = Porosity

σ = Surface tension

θ = Contact angle

[4] This section constitutes Project Deliverable 2.1.2: Set of *J*-functions and P_c^{entry} representative of likely storage formations

It suggests that porous media that have the same pore structure but different permeability and porosity will have the same Leverett *J*-function. Therefore, if the different capillary pressure curves of the porous media are rescaled as a Leverett *J*-function, they should plot as one curve. This curve provides the means to average capillary pressure data. Figure 11 shows the Leverett *J*-function for several unconsolidated sands with widely different permeabilities. All the data are plotted as one single curve.

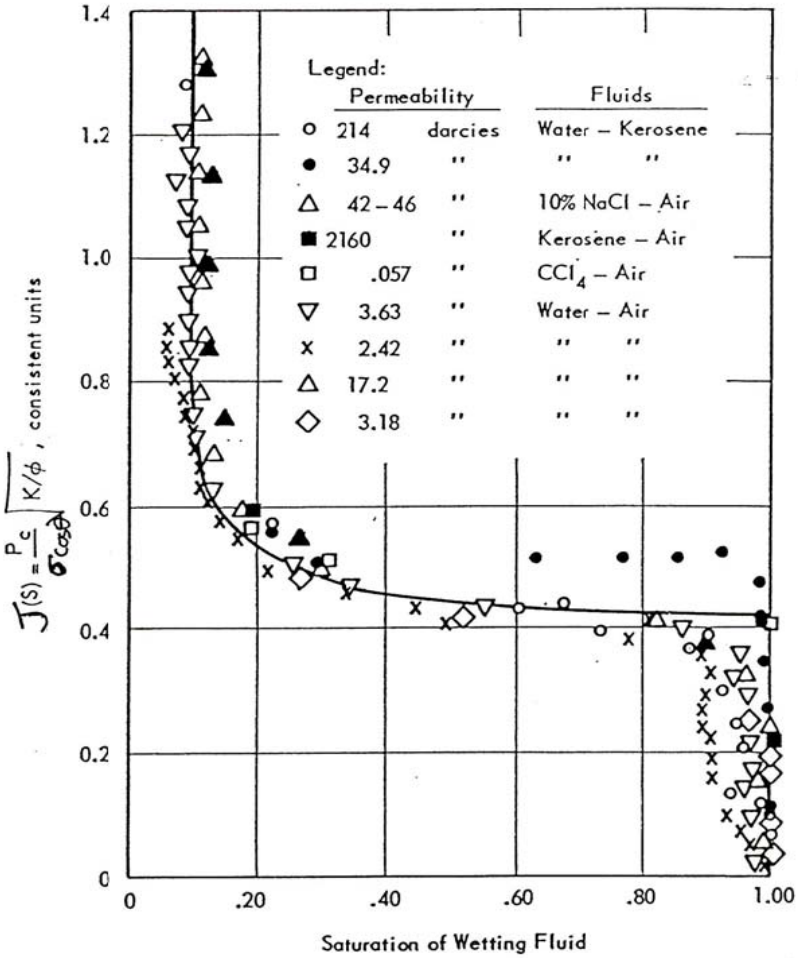

Figure 11: Leverett *J*-function for unconsolidated sands (from Leverett, 1941).

The Leverett *J*-function is an attempt to extrapolate capillary pressure data for a given rock to rocks that are similar but with differing permeability, porosity and wetting properties.

To scale the capillary pressure curve for each grid block in the aquifer, we assume that the wetting properties (interfacial tension and contact angle) do not vary spatially. Thus, for any arbitrary grid block with permeability k and porosity ϕ,

$$J\left(S_w\right) = \frac{P_c\left(S_w\right)}{\sigma \cos\theta}\sqrt{\frac{k}{\phi}} = \frac{P_{c0}\left(S_w\right)}{\sigma \cos\theta}\sqrt{\frac{k_0}{\phi_0}} \tag{16}$$

Hence,

$$P_c\left(S_w\right) = P_{c0}\left(S_w\right)\sqrt{\frac{k_0}{k}}\sqrt{\frac{\phi}{\phi_0}} \tag{17}$$

Subscript 0 denotes the properties of the rock for which we know the capillary pressure curve. This is called reference rock and k_0 and ϕ_0 are called reference permeability and porosity, respectively.

For example, if we assign a curve (P_{c0}) to capillary pressure of a rock (grid block) with permeability of 283.35 md (i.e. 283.35×10^{-15} m^2) and porosity of 0.30, then for another grid block which has $k = 127.904$ and $\phi = 0.15$, the capillary pressure curve would be:

$$P_c\left(S_w\right) = P_{c0}\left(S_w\right)\sqrt{\frac{283.35}{127.90}}\sqrt{\frac{0.15}{0.30}} = 1.0715 \times P_{c0}\left(S_w\right) \tag{18}$$

Hence, if we have already introduced the reference capillary pressure curve (P_{c0}) to simulator, then we just need to give the scale coefficient of 1.0715 to it so that it would be able to find capillary pressure function for second grid block with $k = 127.904$ md (i.e. 127.904×10^{-15} m^2) and $\phi = 0.15$.

In GEM, the keyword *PCGMAX is used to scale the gas-liquid capillary pressure table to a different end point value for each grid block. Therefore, we use it to introduce the scaling coefficient for each grid block to simulator.

In summary, to implement a particular scaling we must choose a reference value of permeability and associate this value with the reference capillary pressure curve. Based on the chosen reference permeability and porosity, for each grid block in the domain we calculate the new gas-liquid capillary pressure value at the connate liquid saturation. We provide these values in the input deck to the simulator. The result is that the vertical scale in reference curve is stretched or contracted by a factor of PCGMAX.

In practice, measurements of the petrophysical properties on a single core sample would be the natural way to set the reference values. In this study, we assign the reference capillary pressure developed in previous section to several values of permeability for a single realization of permeability field. This better illustrates the influence of capillary heterogeneity.

Figure 12 shows the reference capillary pressure curve with two scaled curves for two other grid blocks, one with higher, another one with lower permeability than reference permeability, assuming equal porosities. The grid block with higher permeability than reference value has smaller entry pressure than reference and vice versa.

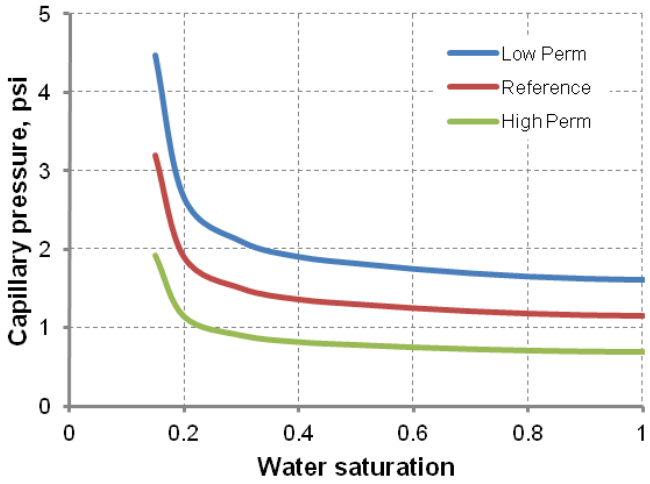

Figure 12: Reference capillary pressure curve (typical of 200x10^{-15} m^2 sedimentary rock) and two scaled capillary pressure curves for two other grid blocks, one with higher, another one with lower permeability than reference permeability. The reference capillary pressure curve is scaled via Leverett scaling group.

3.1.2 Estimation of Local Capillary Trapping Capacity from Geologic Models[5]

The effectiveness of a structure as local capillary barrier depends on the magnitude of the capillary entry pressure. In other words, if the capillary entry pressure of the structure is larger than a threshold value, it can act as an effective barrier and if it is smaller than that threshold value, then it will not be able to act as an effective barrier. This value is called critical capillary entry pressure. The magnitude of this critical entry pressure depends on several factors. It depends on range of capillary entry pressure values in the domain; if the average value of entry pressures is larger in a domain A than domain B, then the critical entry pressure is also larger for domain A. Also, the critical entry pressure depends on geometry of the domain. The value of critical entry pressure should be different for an anticline structure and a syncline structure with identical entry pressure values.

Finding this critical entry pressure is a key step in estimation of local capillary traps from geologic models. This critical pressure can be constant throughout the domain, or can change, for example as a function of height. Assuming that we know the distribution of critical entry pressure in the domain, we are going to describe an algorithm that can be used for detection of local capillary traps.

Algorithm

The following steps describe the algorithm used to find the local capillary trap in a 3D domain of capillary entry pressure.

[5] The "barrier maps" in this section constitute Project Deliverable 2.4.1 Relationship between the characteristic capillary barrier size $L^{avg}_{barrier,local}$ and the value of $P_{c,entry}^{crit}$ for that barrier

Step 1: Find Barriers and Non-Barriers

Find all the blocks in domain that have entry pressure exceeding the critical capillary entry pressure as barriers, and all the blocks that have entry pressure smaller than the critical capillary entry pressure as non-barriers.

Figure 13 shows the result of this step in a sample 2D domain which shows the blocks with entry pressure higher than critical value in orange. In Figure 13(a) the critical entry pressure is assumed to be constant and this leads to denser distribution of high entry pressure blocks. In Figure 13(b) the critical entry pressure is assumed to increase with height h from initial CO_2 accumulation level (bottom of domain) based on

$$P_{c,entry}^{crit}(h) = P_{c,entry}^{0} + \Delta\rho g h \tag{19}$$

where $\Delta\rho$ is density difference between fluids. This formula assumes that if CO_2 reaches the height h inside the domain it has maintained a contiguous column of CO_2 from the accumulation level up to that height, hence the critical entry pressure should increase in order for a structure to be effective in trapping CO_2. The distribution of potential traps is sparser in this case and they significantly decrease at higher elevations inside the formation.

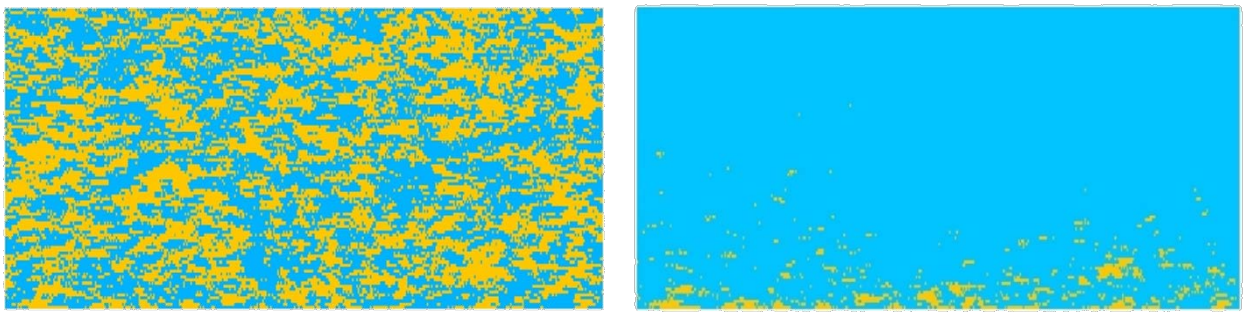

(a) (b)

Figure 13: The blocks that have entry pressure exceeding the critical capillary entry pressure are orange. The critical entry pressure (a) is constant, and (b) increases with height from initial CO_2 accumulation level.

Step 2: Find Non-Barrier Clusters

Find all the connected clusters of the non-barrier blocks from previous step. The blocks are considered connected if they share a face, not an edge. Each of these connected clusters is a potential capillary trapping structure that might be able to effectively trap CO_2 at some parts of its structure. We will find these parts in the next step.

Figure 14 shows a sample 2D domain that contains three different connected clusters of non-barrier blocks (cyan, green, and yellow). The orange blocks are barrier blocks.

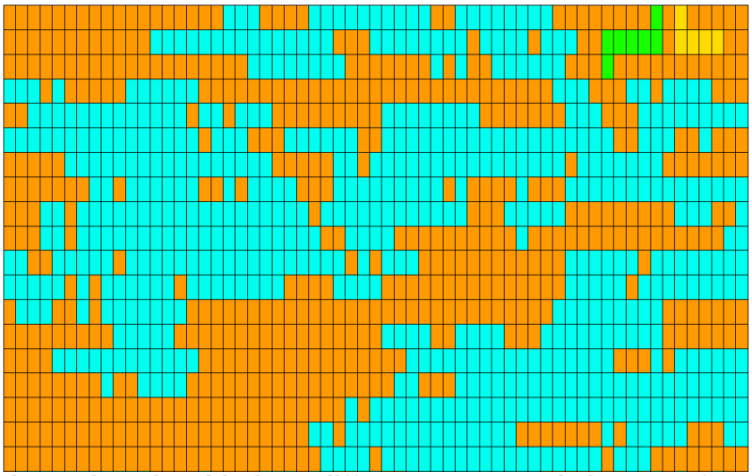

Figure 14: Sample 2D domain with three different connected clusters of non-barrier blocks (cyan, green, and yellow) as a result of step 2. The orange blocks are barrier blocks.

Step 3: Find Trapping Structures

For each non-barrier cluster, find all non-barrier blocks that are surrounded (from top and sides) by barrier blocks.

In fact, if a trapping structure is not connected to the top of the formation, it will be assumed to be a local capillary trap. If a trapping structure is connected to the top of the formation, then this step finds the local spill points in that trapping structure and determines the blocks above the spill point which could contribute in local capillary trapping. Each of these blocks is a potential local capillary trap that might be able to securely contain some CO_2 if CO_2 could find a way through these traps. The blocks below the spill point has a connected path toward the top surface of the domain. Therefore, they are not able to contribute in local capillary trapping.

Figure 15 shows the potential local capillary traps of Figure 14, i.e., the non-barrier blocks that are surrounded from top and sides by barrier blocks.

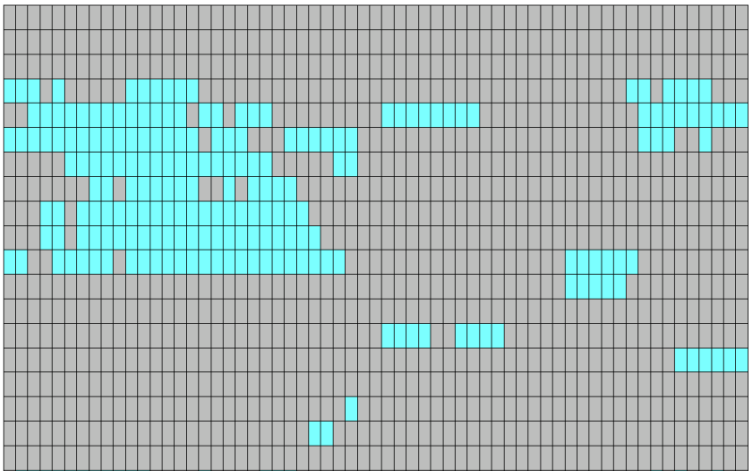

Figure 15: The potential local capillary traps as a result of step 3, corresponding to the sample 2D domain in Figure 14. These are non-barrier blocks that are surrounded (from top and sides) by barrier blocks and located above the local spill point of the trapping structure in which they are located.

Verification

In order to verify the validity of this method, we want to know how much the results agree with the results generated by flow simulator. We will apply our method to detect the local capillary traps in sample geological models for which we have the simulation results of buoyancy-driven CO_2 flow available. Then we compare the results of the two methods with each other. Two 2D models and two 3D models are considered for this purpose.

2D Domain – 1.5 m Correlation Length

The sample 2D geologic model is shown in Figure 16. The domain is 120 m wide and 30 m high and consists of 0.3×0.3 m grid blocks. The permeability field, Figure 16(a), is correlated in horizontal direction with 1.5 m correlation length, but uncorrelated in vertical direction. The reference capillary entry pressure curve is shown in Figure 17 with reference entry pressure of 8.3 kPa. The entry pressure field, Figure 16(b), is generated using the Leverett *J*-function:

$$J\left(S_w\right)=\frac{P_c}{\sigma\cos\theta}\sqrt{\frac{k}{\phi}} \tag{20}$$

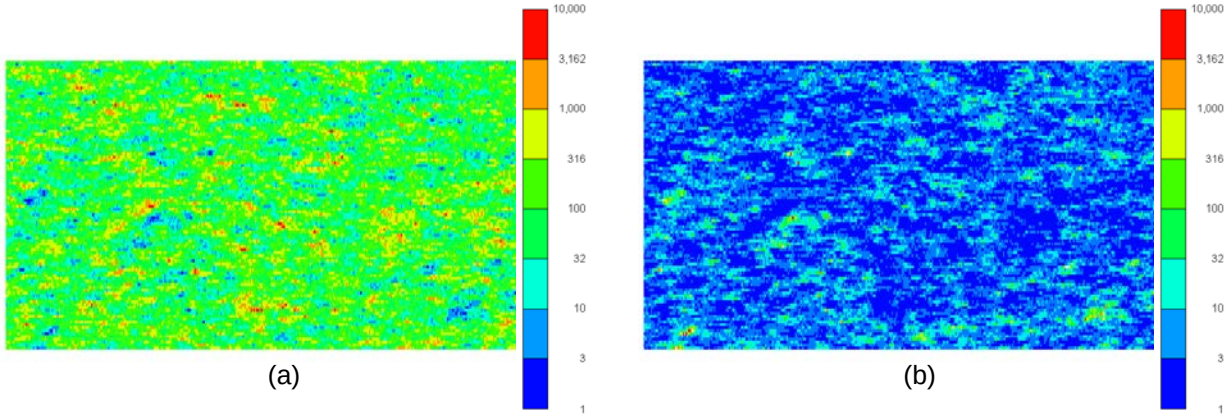

Figure 16: Sample 2D geologic model with 1.5 m correlation length in horizontal direction: (a) permeability field, and (b) the corresponding entry pressure field based on Leverett *J*-function.

Figure 18 shows the result of flow simulation for the sample model in Figure 16. It shows the gas saturation profile after five years of buoyancy-driven flow of CO_2 inside the formation, while CO_2 was initially emplaced at the bottom of the aquifer at saturation of $S_g = 1 - S_{wr}$. At this time, the CO_2 displacement stops and after that the long term trapping mechanisms, including dissolution trapping and mineral trapping, continue to store more CO_2 inside the formation.

The entry pressure field has mean value of 14.5 kPa and standard deviation of 9.7 kPa. We use a constant critical capillary entry pressure for the whole domain and choose several values in the range of 4.8 to 19.3 kPa for it. Of course a solid method is required to enable us select the correct value of critical entry pressure without trial and error.

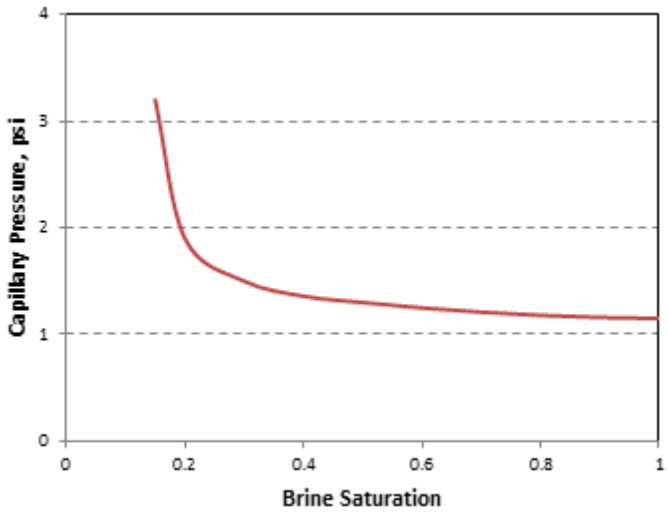

Figure 17: Reference capillary pressure curve used for the 2D case.

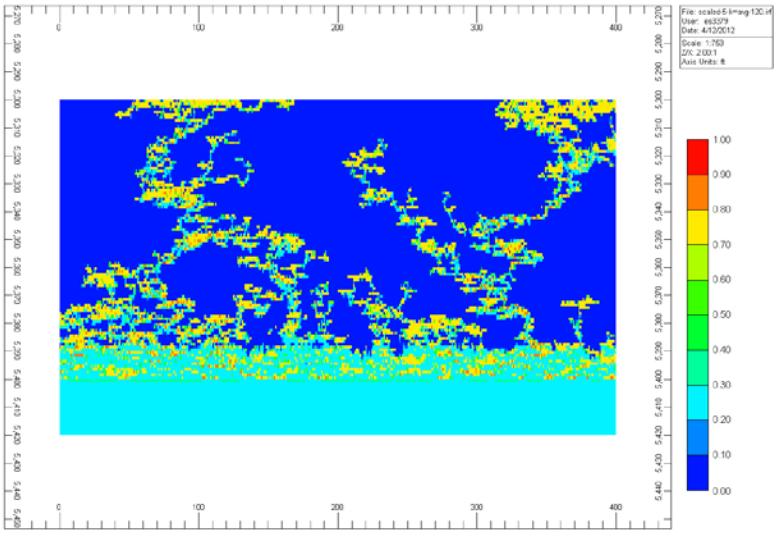

Figure 18: Result of flow simulation for the sample model in Figure 16 shows gas saturation profile after 5 years of buoyancy-driven flow of CO_2.

Figure 19 through Figure 24 show the results of applying step 1 on the entry pressure field using critical entry pressure of 4.8, 6.9, 8.3, 9.7, 12.4 and 13.8 kPa, respectively. The red blocks represent the barrier blocks and blue blocks are non-barrier blocks. This suggests that CO_2 should not be able to go through these red blocks and the path of CO_2 vertical flow should pass through the blue region. As the critical capillary entry pressure increases, there is more non-barrier blocks available for CO_2 to pass through them.

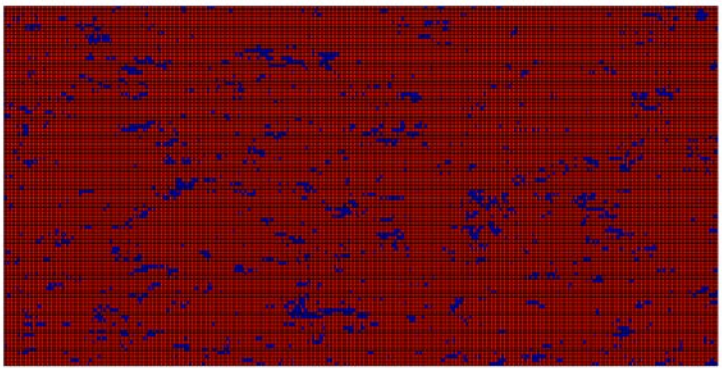

Figure 19: Barrier map resulting from step 1 of the algorithm applied on sample 2D domain in Figure 16 using critical entry pressure of 4.8 kPa.

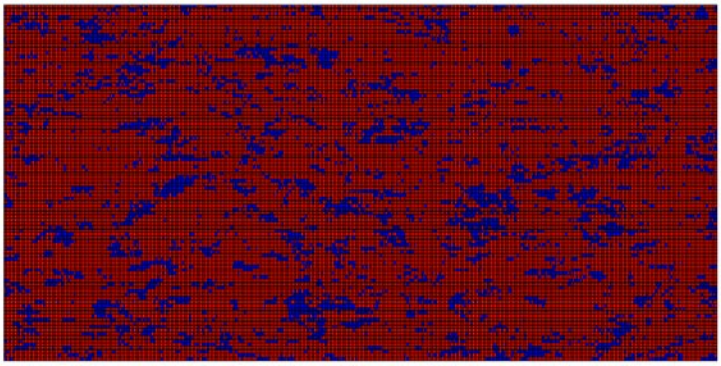

Figure 20: Barrier map resulting from step 1 of the algorithm applied on sample 2D domain in Figure 16 using critical entry pressure of 6.9 kPa.

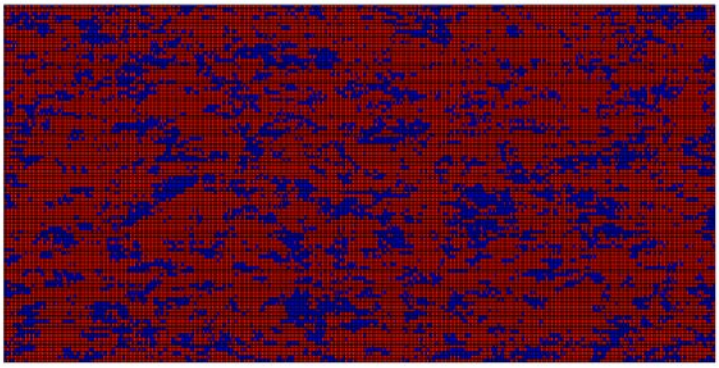

Figure 21: Barrier map resulting from step 1 of the algorithm applied on sample 2D domain in Figure 16 using critical entry pressure of 8.3 kPa.

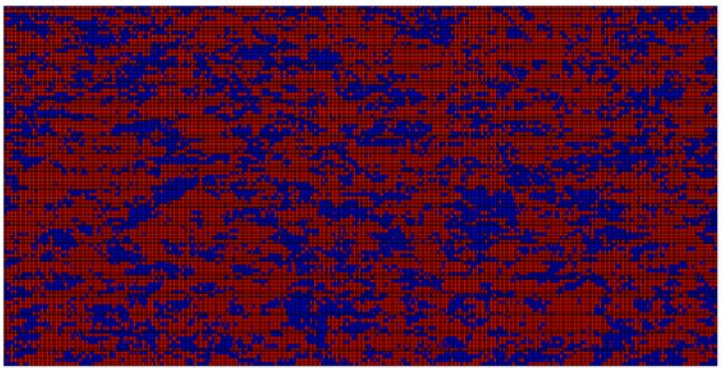

Figure 22: Barrier map resulting from step 1 of the algorithm applied on sample 2D domain in Figure 16 using critical entry pressure of 9.7 kPa.

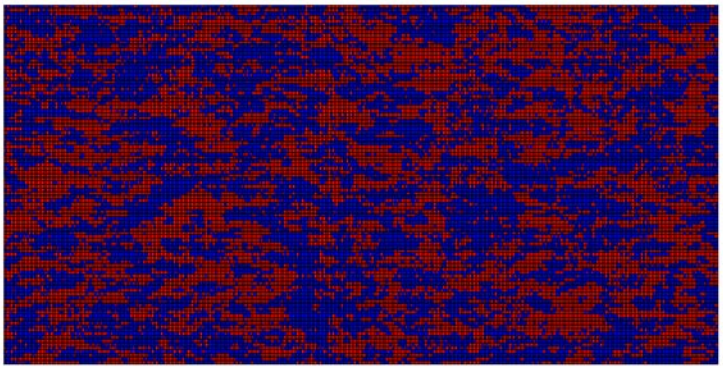

Figure 23: Barrier map resulting from step 1 of the algorithm applied on sample 2D domain in Figure 16 using critical entry pressure of 12.4 kPa.

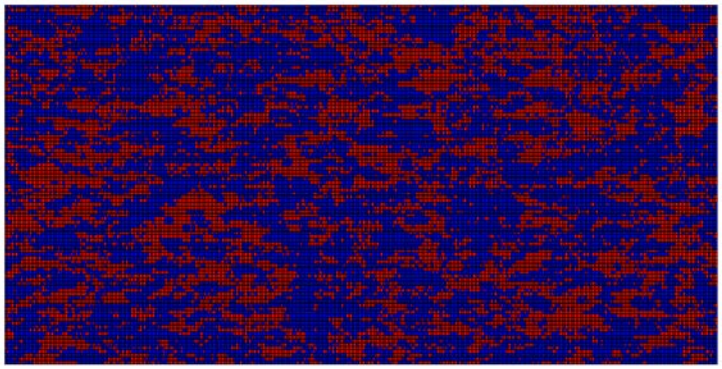

Figure 24: Barrier map resulting from step 1 of the algorithm applied on sample 2D domain in Figure 16 using critical entry pressure of 13.8 kPa.

Comparing the result of flow simulation of buoyancy-driven displacement, which is shown in Figure 18, with these figures suggests that CO_2 flow paths match best with the barrier map with critical entry pressure of 13.8 kPa. In Figure 25, the flow path is overlaid on this barrier map. The green blocks show the flow path which goes through the non-barrier blocks (which is expected to occur), and the red blocks show the flow path which goes through the barrier blocks (which is not expected to occur). There is an excellent agreement between the results and hence, prediction of barrier and non-barrier regions inside the geologic model is successful. Note that in

this case the critical entry pressure close to mean entry pressure of the field reveals the CO_2 flow path.

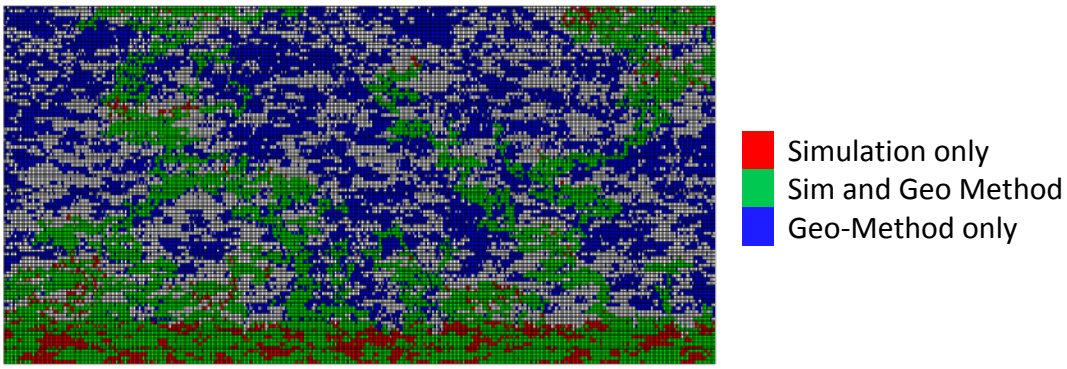

Figure 25: Overlaying the result of flow simulation on the barrier map of Figure 24 that uses critical entry pressure of 13.8 kPa.

In the next step, the algorithm finds the connected clusters of non-barrier blocks. This step uses the barrier map from step 1 as an input and finds the different clusters of non-barriers as output. In fact, each of these clusters is a potential structure that might be capable of holding CO_2 at some locations inside it if it is properly surrounded by capillary barriers. In Figure 26 through Figure 31, part (a) shows different clusters of connected non-barriers found in the sample 2D domain using critical capillary entry pressure of 4.8, 6.9, 8.3, 9.7, 12.4, and 13.8 kPa, respectively. In these figures the color shows the identification number of each cluster. Part (b) of Figure 26 through Figure 31 shows histogram of size of clusters in part (a). For small values of critical entry pressure, size of the non-barrier clusters is very small (in Figure 26 the largest cluster has fewer than 10^2 blocks), but for larger values of critical entry pressure (e.g., Figure 31) at least a large cluster (with the size in the order of 10^4 blocks) appears that connects from bottom to the top of the formation. So the possibility of local capillary trapping in the domain increases.

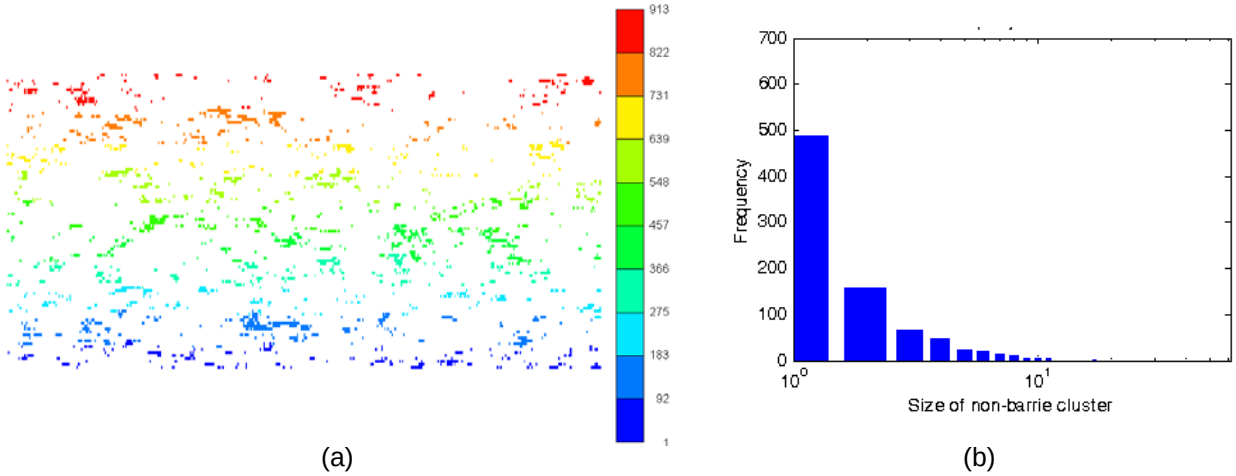

(a) (b)

Figure 26: (a) Clusters of connected non-barriers in the sample 2D domain in Figure 16 using $P_{c,entry}^{crit}$ = 4.8 kPa, (b) Histogram of size of clusters in (a).

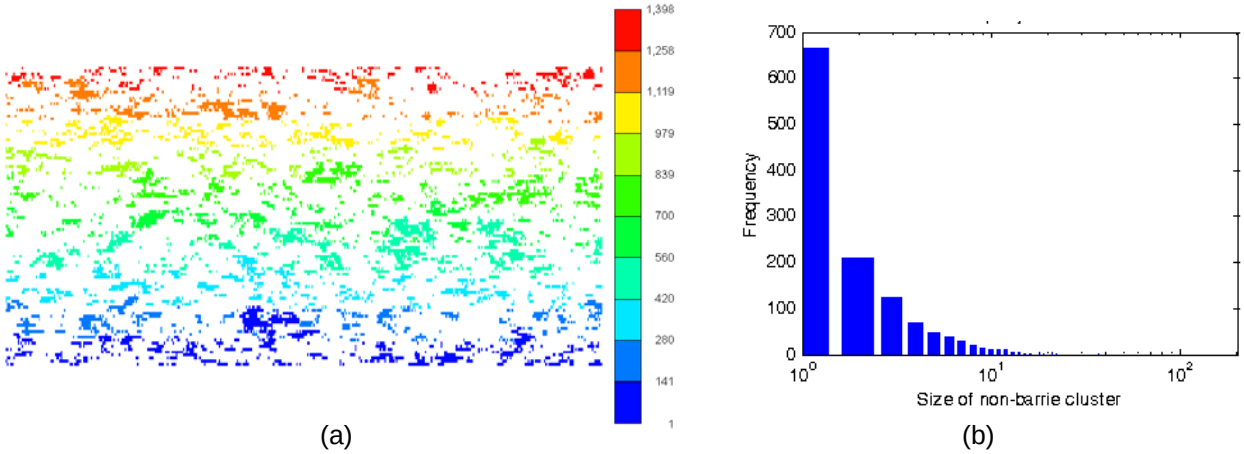

(a) (b)

Figure 27: (a) Clusters of connected non-barriers in the sample 2D domain in Figure 16 using $P_{c,entry}^{crit}$ = 6.9 kPa, (b) Histogram of size of clusters in (a).

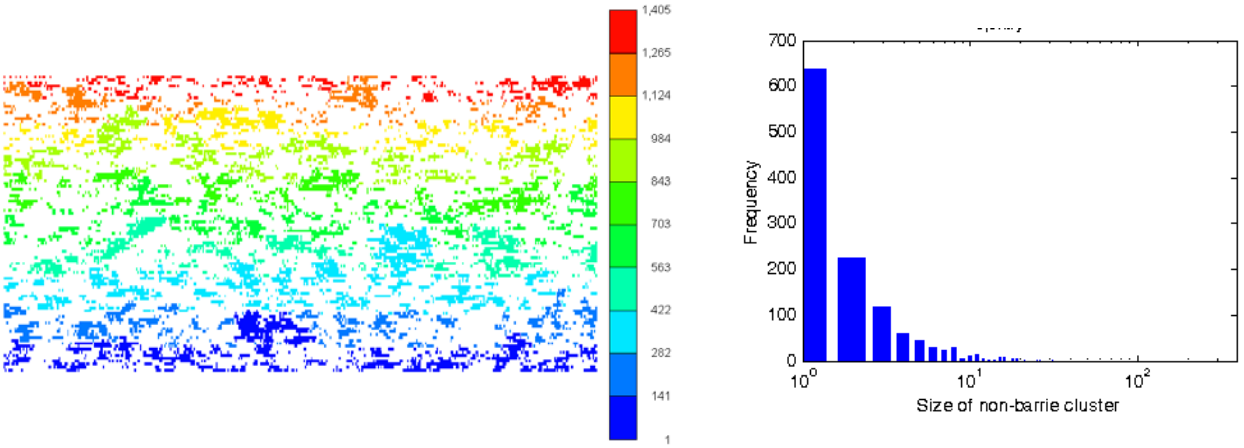

(a) (b)

Figure 28: (a) Clusters of connected non-barriers in the sample 2D domain in Figure 16 using $P_{c,entry}^{crit}$ = 8.3 kPa, (b) Histogram of size of clusters in (a).

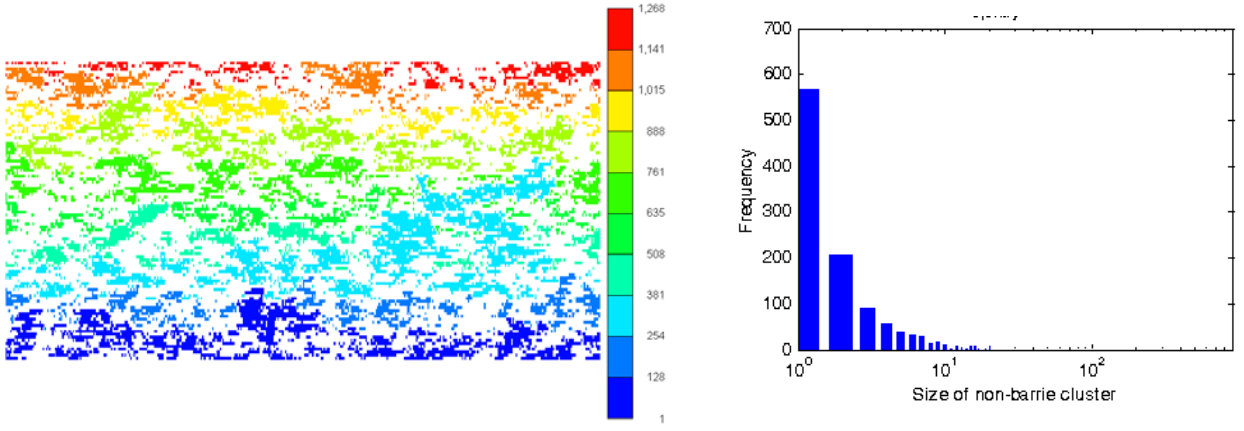

(a) (b)

Figure 29: (a) Clusters of connected non-barriers in the sample 2D domain in Figure 16 using $P_{c,entry}^{crit}$ = 9.7 kPa, (b) Histogram of size of clusters in (a).

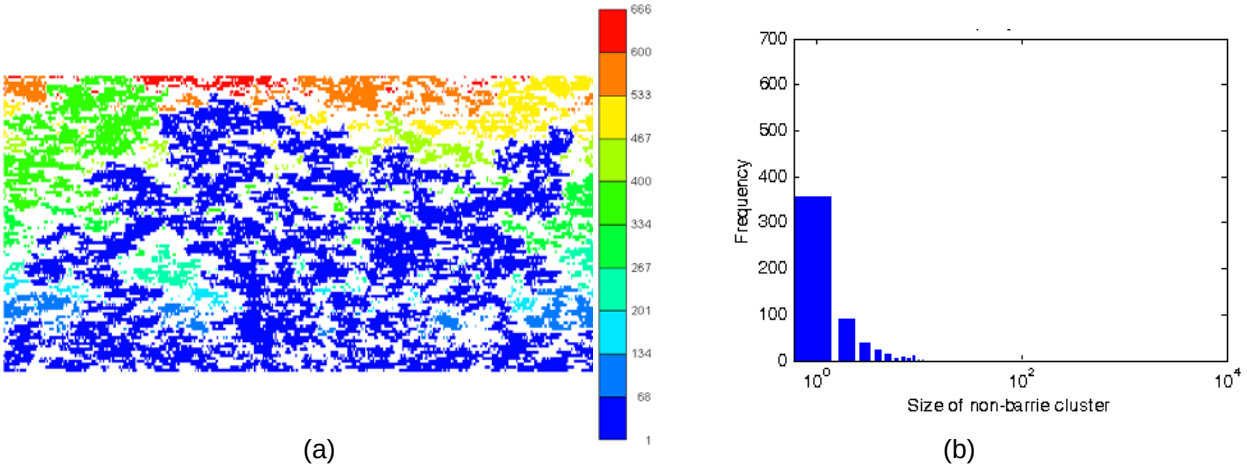

(a) (b)

Figure 30: (a) Clusters of connected non-barriers in the sample 2D domain in Figure 16 using $P_{c,entry}^{crit}$ = 12.4 kPa, (b) Histogram of size of clusters in (a).

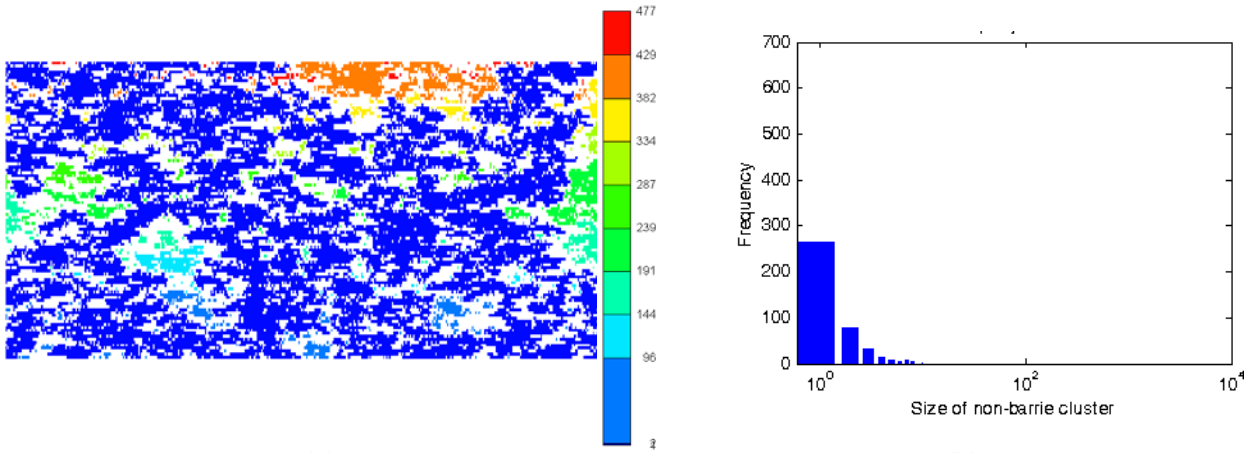

(a) (b)

Figure 31: (a) Clusters of connected non-barriers in the sample 2D domain in Figure 16 using $P_{c,entry}^{crit}$ = 13.8 kPa, (b) Histogram of size of clusters in (a).

Figure 31 shows the 477 different clusters of connected non-barriers for the case with $P_{c,entrr}^{crit}$ = 13.8 kPa. Most of these clusters only contain a few non-barrier blocks which would not be able to have a significant contribution in local capillary trapping of CO_2. This can be seen from the histogram of size of clusters which shows that 260 (i.e., more than half) of the clusters contain only a single block. However, still there is a single large cluster that predominates the formation with 20,412 blocks and contains more than 51% of the blocks in the domain. Therefore, there is a significant potential for local capillary trapping in this domain.

In the last step, we run the subroutine that finds the holes that are surrounded by capillary barriers. Figure 32 through Figure 37 show the clusters of traps that are surrounded from top and sides by barrier blocks in the sample 2D domain using critical capillary entry pressure of 4.8, 6.9, 8.3, 9.7, 12.4, and 13.8 kPa, respectively. For small values of critical entry pressure (e.g., Figure 32) the local capillary traps contain almost the entire non-barrier blocks, because the non-barrier clusters are very small (see Figure 26) and very few of them which are very close to the top of the formation are actually connected to the top. As the critical capillary entry pressure increases,

the size of non-barrier clusters increase while they remain isolated from the top. Therefore, number of local capillary traps initially increases. At some threshold value of critical entry pressure, the large non-barrier clusters become connected to the top of the formation. At this point most of the non-barrier blocks become ineffective in trapping CO_2 and hence, the capacity of local capillary traps starts to decrease (cf. Figure 37).

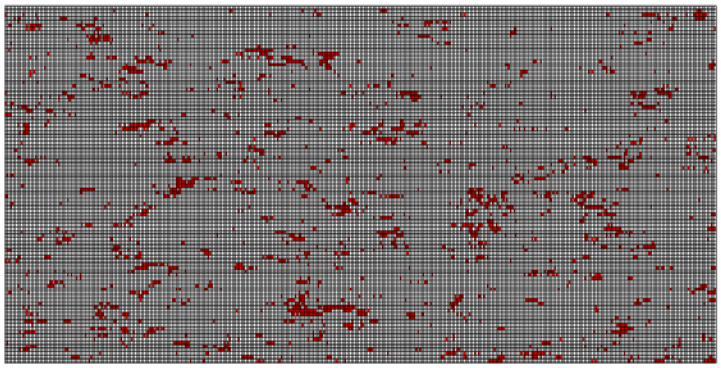

Figure 32: Local capillary trap map resulting from step 3 of the algorithm applied on sample 2D domain in Figure 16 using critical entry pressure of 4.8 kPa.

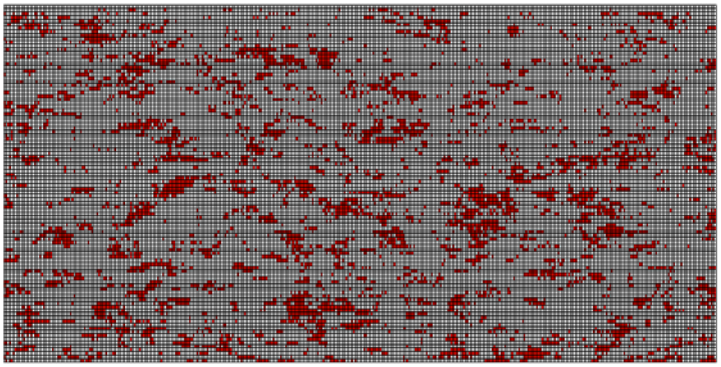

Figure 33: Local capillary trap map resulting from step 3 of the algorithm applied on sample 2D domain in Figure 16 using critical entry pressure of 6.9 kPa.

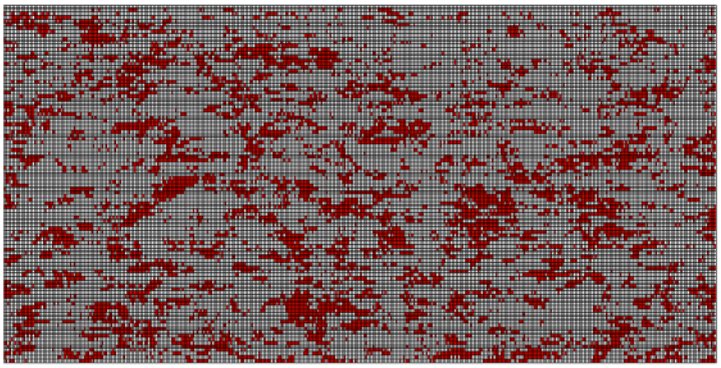

Figure 34: Local capillary trap map resulting from step 3 of the algorithm applied on sample 2D domain in Figure 16 using critical entry pressure of 8.3 kPa.

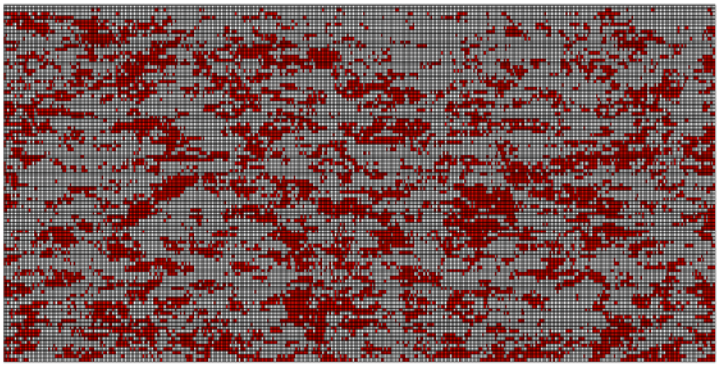

Figure 35: Local capillary trap map resulting from step 3 of the algorithm applied on sample 2D domain in Figure 16 using critical entry pressure of 9.7 kPa.

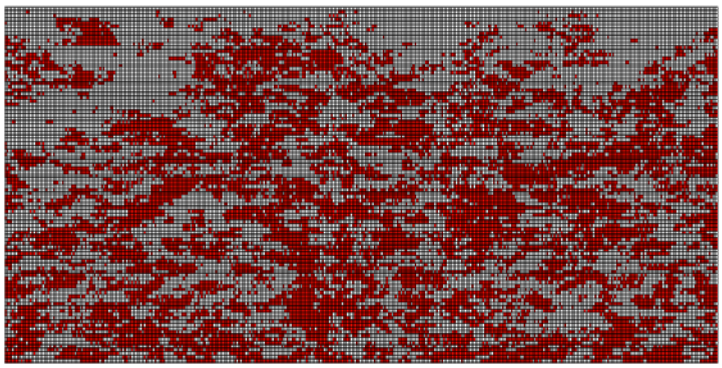

Figure 36: Local capillary trap map resulting from step 3 of the algorithm applied on sample 2D domain in Figure 16 using critical entry pressure of 12.4 kPa.

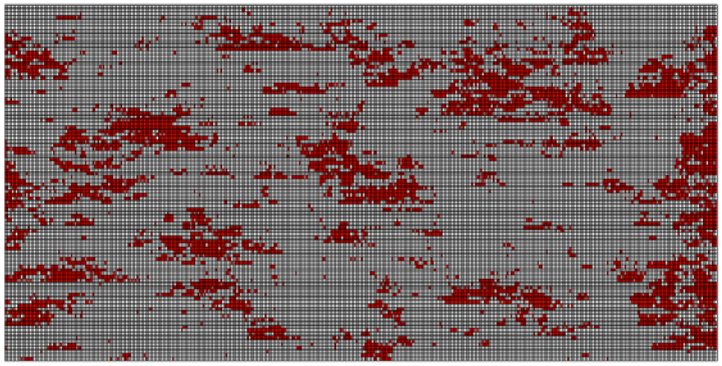

Figure 37: Local capillary trap map resulting from step 3 of the algorithm applied on sample 2D domain in Figure 16 using critical entry pressure of 13.8 kPa.

We extract the local capillary traps from the flow simulation result of Figure 18, as can be seen in Figure 38(a). Note that the blocks close to the top right and top left of the domain are accumulation of CO_2 below the top seal and should not actually be considered as local capillary traps. Then we compare it with the results of geological method in Figure 33, as regenerated here in Figure 38(b). We see that most of the local capillary traps, e.g. green circles on the simulation result, are predicted by our method using the geological model. On the other hand, there are some predicted traps, e.g. blue circles, which do not appear in the simulation result, since the CO_2 is not able to reach them. Therefore, there is not a one to one correspondence between the

results of this geological method and the simulation result, but the geological method is capable of predicting the local capillary traps with high accuracy.

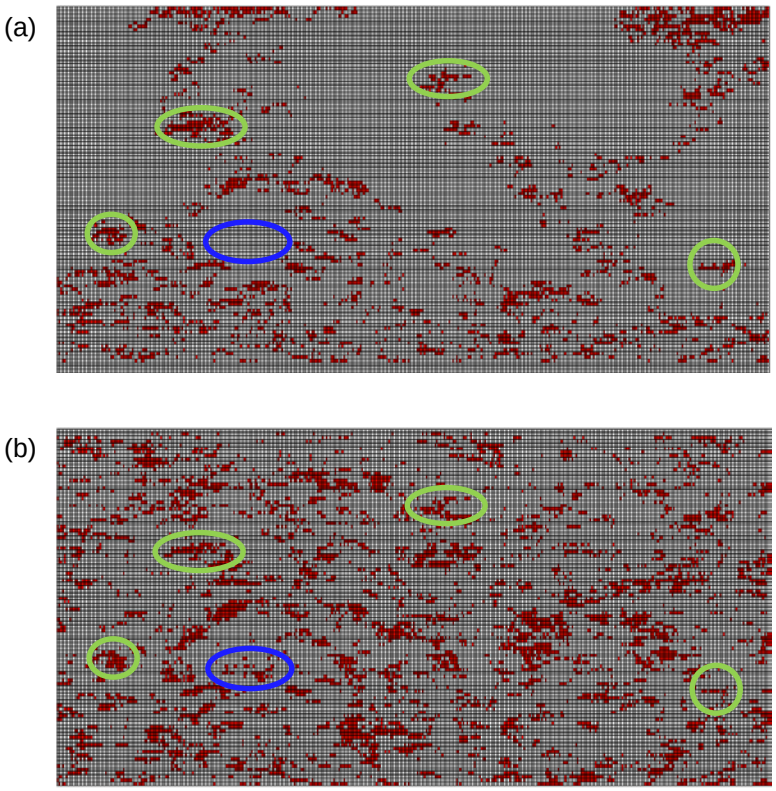

Figure 38: (a) Clusters of local capillary traps in the sample 2D domain in Figure 16 using the simulation result file of Figure 18. (b) Reproduction of Figure 33 ($P_{c,entry}^{crit}$ = 6.9 kPa) for comparison with part (a).

Precise block by block comparison of the results of geological method with the results of simulation is shown in Figure 39 through Figure 41 for critical entry pressures of 6.9, 8.3, and 9.7 kPa, respectively. In these figures, the green blocks show the local capillary traps that exist in both methods, the red blocks show the local capillary traps that exist in simulation results but not in the result of geological method, and the blue blocks show the local capillary traps that are predicted by geological method, but do not exist in simulation results. The higher the percentage of green blocks in the domain, the more agreement exists between the results of two methods. The results are also summarized in Table 6 which shows local capillary trapping capacity (percentage of total number of grid blocks) using simulation method and geological method, and the common capacity predicted by both methods using critical entry pressure values of 6.9, 8.3, and 9.7 kPa for geological method. While the $P_{c,entry}^{crit}$ = 9.7 kPa is capable of capturing almost the entire local capillary traps in the results of simulation, it is overestimating the local capillary trapping capacity of the model (34% compared to 9%). For $P_{c,entry}^{crit}$ = 6.9 kPa, the local capillary trapping capacity of the model is better predicted by geological method (18% compared to 9%), but it is only capable of capturing almost three forth of the local capillary traps in the results of simulation. However, we can see in Figure 39 that almost all of the larger clusters of local capillary traps are captured and it is the smaller clusters (with very few grid blocks) that are not being captured.

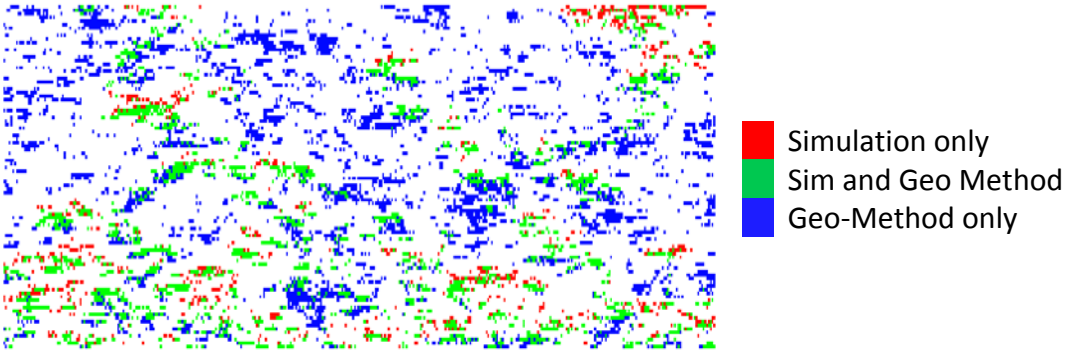

Figure 39: Comparison of the local capillary traps predicted by geological method (using $P_{c,entry}^{crit}$ = 6.9 kPa) and the simulation results.

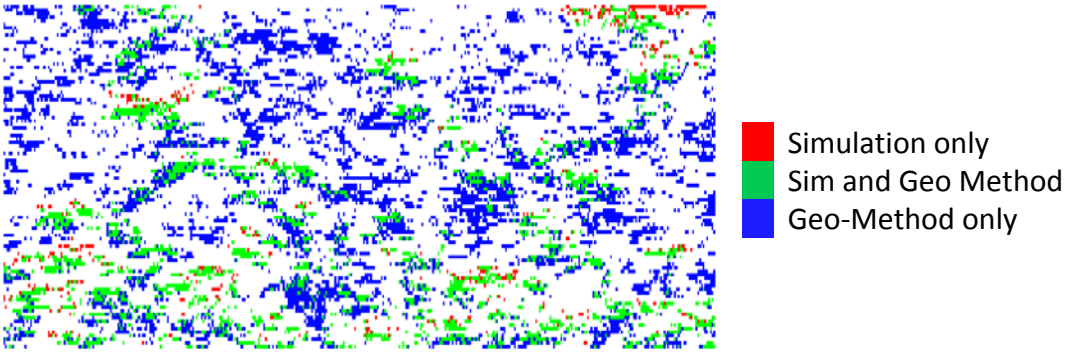

Figure 40: Comparison of the local capillary traps predicted by geological method (using $P_{c,entry}^{crit}$ = 8.3 kPa) and the simulation results.

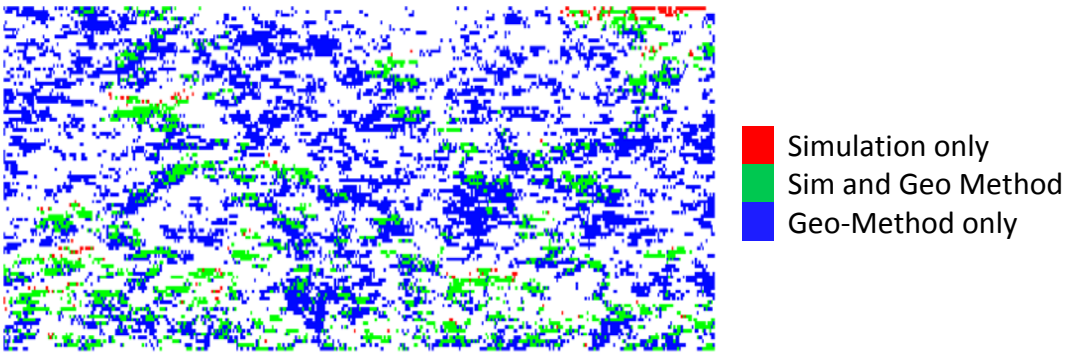

Figure 41: Comparison of the local capillary traps predicted by geological method (using $P_{c,entry}^{crit}$ = 9.7 kPa) and the simulation results.

Table 6: Local Capillary Trapping Capacity (Percentage of Total Number of Grid Blocks) for 2D Domain in Figure 16 Using Simulation Method and Geological Method, and the Common Capacity Predicted by both Methods Using Different Critical Entry Pressure Values for Geological Method

	$P_{c,entry}^{crit}$, kPa		
	6.9	8.3	9.7
Simulation Method	8.9 %	8.9 %	8.9 %
Geological Method	17.5 %	25.6 %	34.2 %
Common in Both Methods	6.6 %	7.7 %	8.3 %

The results of geological method shows that 6,989 blocks have the potential to contribute to local capillary trapping; that is close to 17.5% of the total blocks in the domain and determines an upper limit for local capillary trapping capacity.

2D Domain – 15 m Correlation Length

The second sample 2D geologic model is shown in Figure 42. The domain is 120 m wide and 30 m high and consists of 0.3×0.3 m grid blocks. The permeability field, Figure 42(a), is correlated in horizontal direction with 15 m correlation length, but uncorrelated in vertical direction. The reference capillary entry pressure curve is the same as previous sample, as shown in Figure 17, with reference entry pressure of 8.3 kPa. The entry pressure field, Figure 42(b), is generated using the Leverett *J*-function.

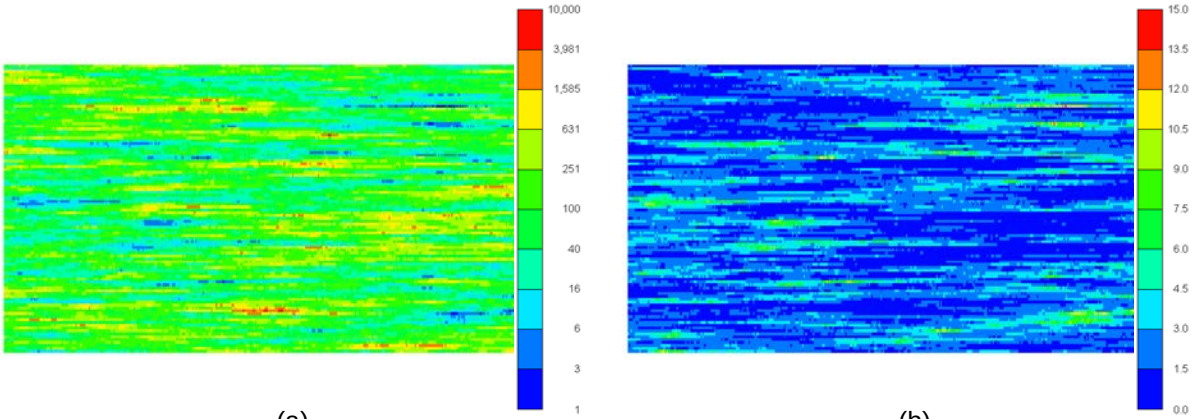

Figure 42: Sample 2D geologic model with 15 m correlation length in horizontal direction: (a) permeability field, and (b) the corresponding entry pressure field based on Leverett *J*-function.

Figure 43 shows the result of flow simulation for the sample model in Figure 42. It shows the gas saturation profile after 100 years of buoyancy-driven flow of CO_2 inside the formation, while CO_2 was initially emplaced at the bottom of the aquifer at saturation of $S_g = 1 - S_{wr}$. At this time, the CO_2 displacement stops and after that the long term trapping mechanisms, including dissolution trapping and mineral trapping, continue to store more CO_2 inside the formation.

The entry pressure field has mean value of 14.5 kPa and standard deviation of 9.7 kPa like the previous 2D model. We use a constant critical capillary entry pressure for the whole domain and choose its value to be 4.8. 9.7, 12.4, 13.8, 14.5, and 19.3 kPa.

Figure 44 through Figure 49 show the results of applying step 1 on the entry pressure field using critical entry pressure of 4.8. 9.7, 12.4, 13.8, 14.5, and 19.3 kPa, respectively. The red blocks represent the barrier blocks that CO_2 should not be able to go through them. The blue blocks are non-barrier blocks that the path of CO_2 buoyancy-driven flow should pass through them. Again, as the critical capillary entry pressure increases, there is more non-barrier blocks available for CO_2 to pass through them.

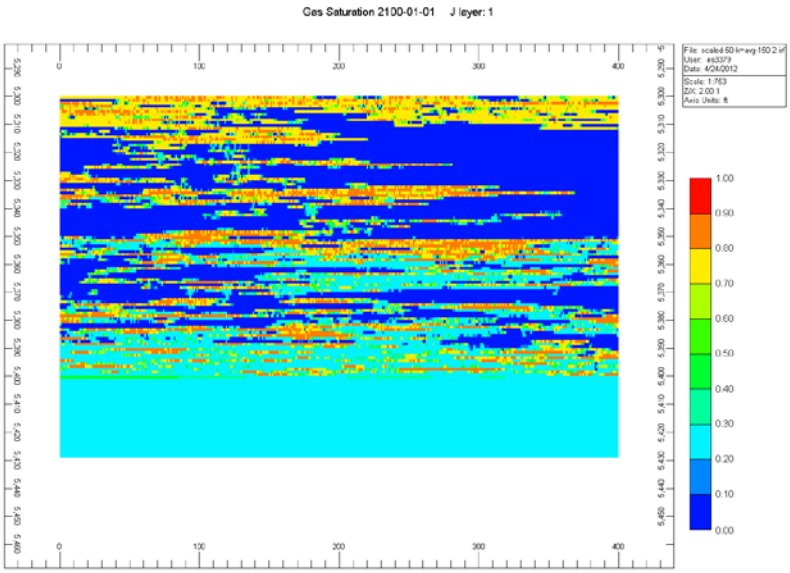

Figure 43: Result of flow simulation for the sample model in Figure 42 shows gas saturation profile after 100 years of buoyancy-driven flow of CO_2.

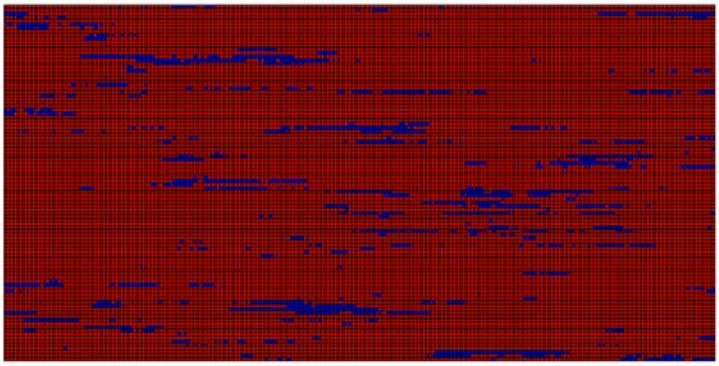

Figure 44: Barrier map resulting from step 1 of the algorithm applied on sample 2D domain in Figure 42 using critical entry pressure of 4.8 kPa.

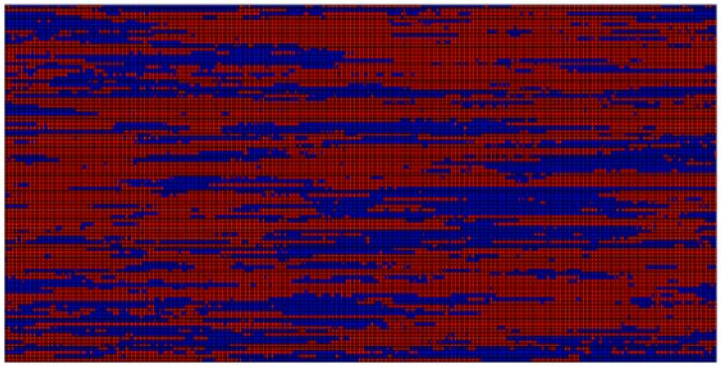

Figure 45: Barrier map resulting from step 1 of the algorithm applied on sample 2D domain in Figure 42 using critical entry pressure of 9.7 kPa.

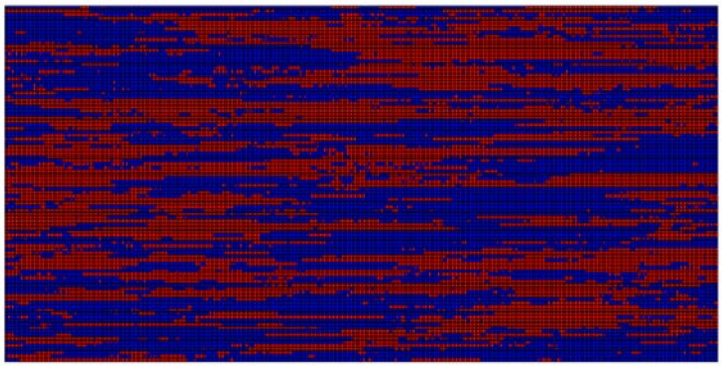

Figure 46: Barrier map resulting from step 1 of the algorithm applied on sample 2D domain in Figure 42 using critical entry pressure of 12.4 kPa.

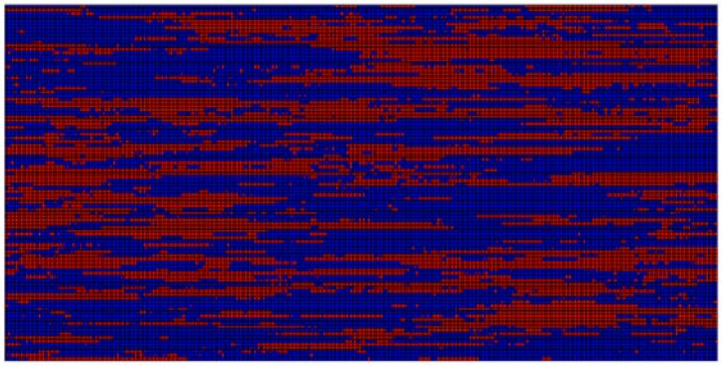

Figure 47: Barrier map resulting from step 1 of the algorithm applied on sample 2D domain in Figure 42 using critical entry pressure of 13.8 kPa.

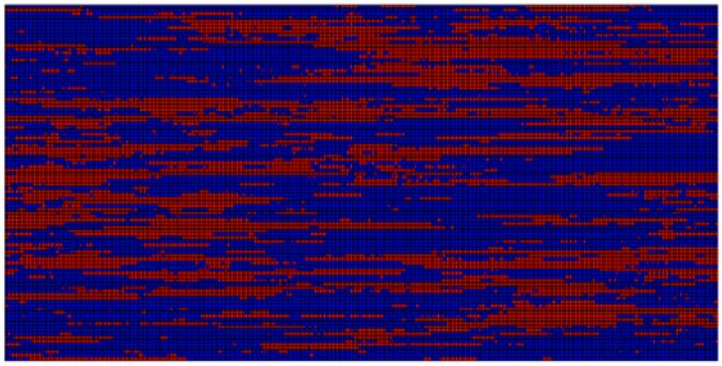

Figure 48: Barrier map resulting from step 1 of the algorithm applied on sample 2D domain in Figure 42 using critical entry pressure of 14.5 kPa.

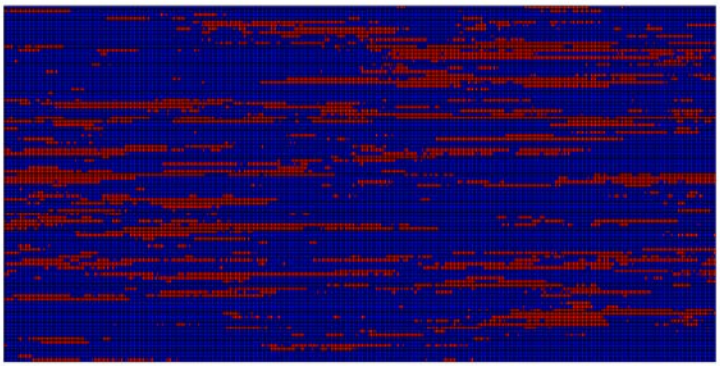

Figure 49: Barrier map resulting from step 1 of the algorithm applied on sample 2D domain in Figure 42 using critical entry pressure of 19.3 kPa.

Now we compare the result of flow simulation of buoyancy-driven displacement in Figure 43 with these figures and conclude that the CO_2 flow paths completely follow the blue region in the barrier map with critical entry pressure of 14.5 kPa. Figure 50 through Figure 54 show the simulation flow path which is overlaid on the barrier maps for critical entry pressure of 6.9, 9.7, 12.4, 13.8 and 14.5 kPa, respectively. The green blocks are the CO_2 flow path which is also a part of non-barrier blocks in barrier map. Table 7 compares the number of grid blocks that contribute to CO_2 flow path in the results of flow simulation and the results of geological method (for critical entry pressure of 6.9, 9.7, 12.4, 13.8 and 14.5 kPa). It shows that by increasing $P_{c,entry}^{crit}$ more of the local capillary traps from flow simulation are captured by geological method (for $P_{c,entry}^{crit}$ = 14.5 kPa almost 90% of the flow path lies inside the non-barrier region, as can be seen in Figure 54). However, using higher values of $P_{c,entry}^{crit}$ for geological method shows more grid blocks available to CO_2 flow (e.g., for $P_{c,entry}^{crit}$ = 14.5 kPa, 41% compared to 32% for flow simulation) and there is not a complete agreement between the results. Nevertheless, the results of geological method using $P_{c,entry}^{crit}$ = 12.4 kPa are acceptable in predicting barrier and non-barrier regions inside the geologic model. Note that in this case the critical entry pressure smaller than the mean entry pressure of the field is able to predict the CO_2 flow path.

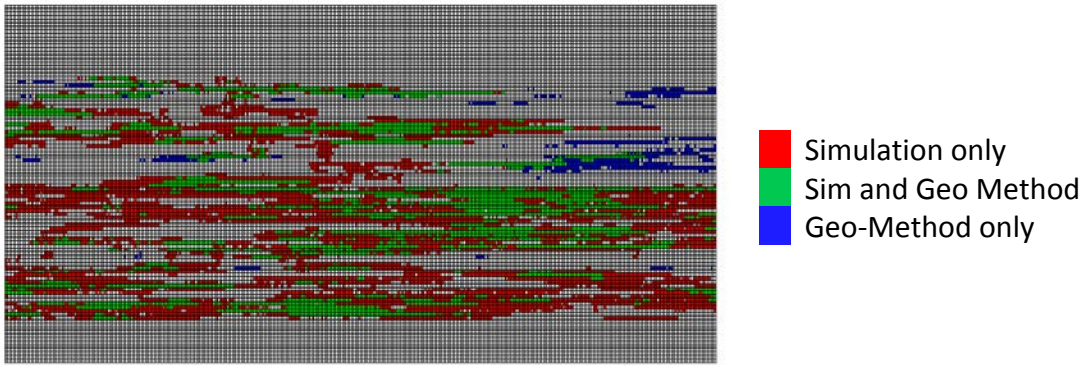

Figure 50: Comparison of the CO_2 flow path predicted by geological method (using $P_{c,entry}^{crit}$ = 6.9 kPa) and the simulation results.

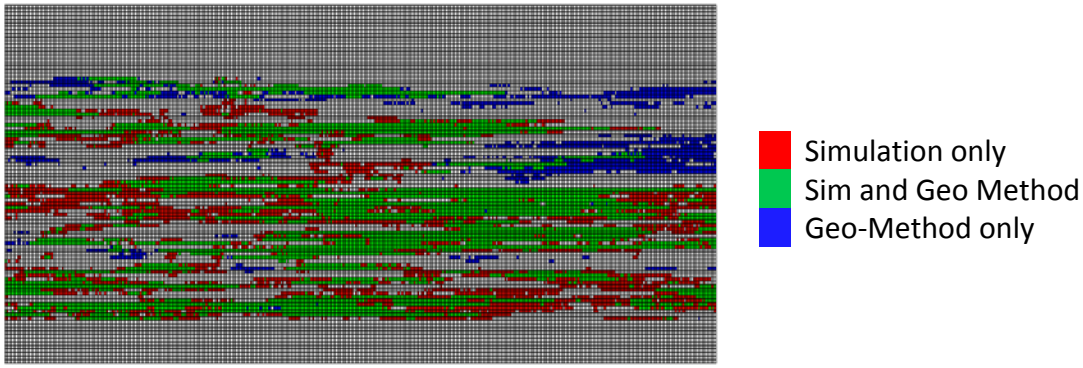

Figure 51: Comparison of the CO_2 flow path predicted by geological method (using $P_{c,entry}^{crit}$ = 9.7 kPa) and the simulation results.

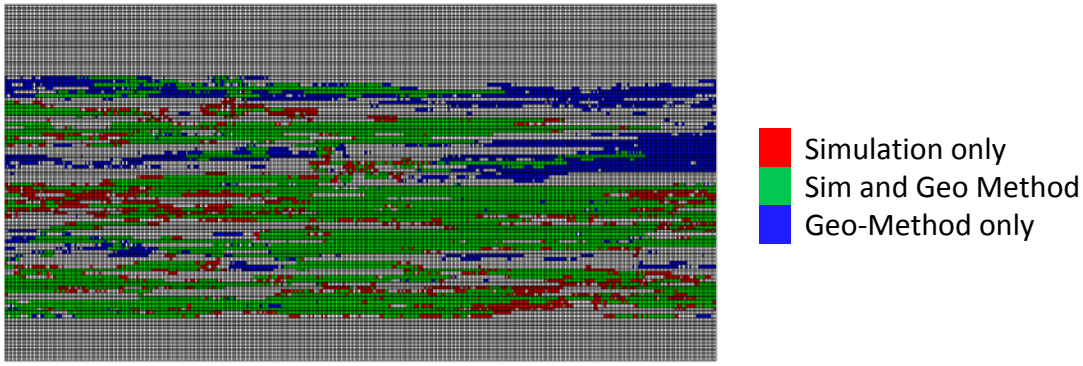

Figure 52: Comparison of the CO_2 flow path predicted by geological method (using $P_{c,entry}^{crit}$ = 12.4 kPa) and the simulation results.

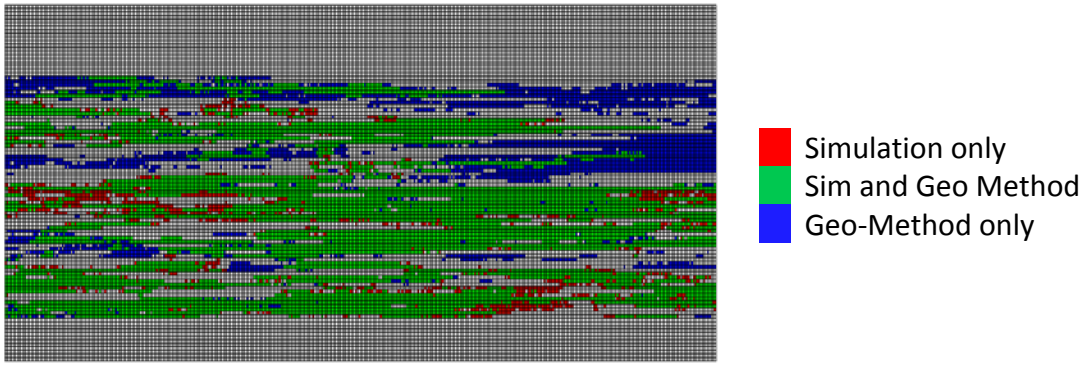

Figure 53: Comparison of the CO_2 flow path predicted by geological method (using $P_{c,entry}^{crit}$ = 13.8 kPa) and the simulation results.

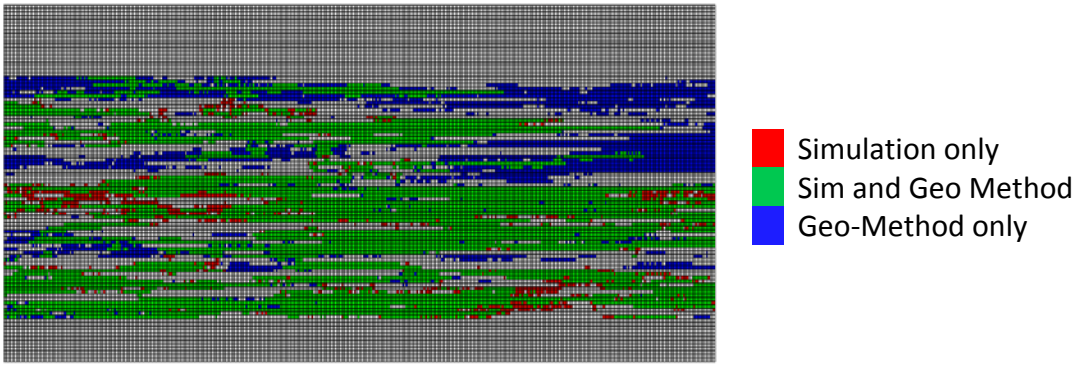

Figure 54: Comparison of the CO_2 flow path predicted by geological method (using $P_{c,entry}^{crit}$ = 14.5 kPa) and the simulation results.

Table 7: CO_2 Flow Path (Percentage of Total Number of Grid Blocks) for 2D Domain in Figure 42 Using Simulation Method and Geological Method, and the Common Path Predicted by Both Methods Using Different Critical Entry Pressure Values for Geological Method

	$P_{c,entry}^{crit}$, kPa				
	6.9	9.7	12.4	13.8	14.5
Simulation Method	32.2 %	32.2 %	32.2 %	32.2 %	32.2 %
Geological Method	13.2 %	24.2 %	34.4 %	38.6 %	40.6 %
Common in Both Methods	11.4 %	19.3 %	25.7 %	28 %	28.9 %

As a result of next two steps of the algorithm, we find the holes that are surrounded by capillary barriers. Figure 55 through Figure 60 show the clusters of traps that are surrounded from top and sides by barrier blocks in the sample 2D domain using critical capillary entry pressure of 4.8, 9.7, 12.4, 13.8, 14.5, and 19.3 kPa respectively. For small values of critical entry pressure the non-barrier clusters are very small and almost all of them are completely surrounded by capillary barriers, except very few of them which are very close to the top of the formation and are actually connected to the top. Therefore, the local capillary traps contain almost the entire non-barrier blocks. For example, Figure 55 which shows the local capillary traps using critical entry pressure of 4.8 kPa matches the non-barrier clusters of Figure 44. As the critical capillary entry pressure increases, the number of local capillary traps initially increases, because the size of non-barrier clusters increases but they are still not connected to the top of the formation. At some threshold value of critical entry pressure, the larger non-barrier clusters start to connect to each other and also become connected to the top of the formation. At this point most of the non-barrier blocks become ineffective in trapping CO_2 and hence, the capacity of local capillary traps starts to decrease.

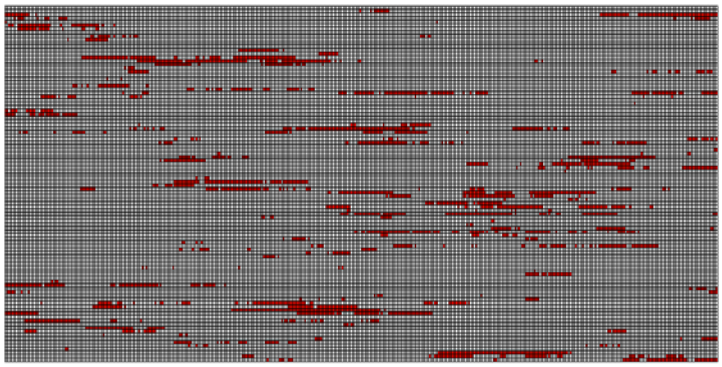

Figure 55: Local capillary trap map resulting from step 3 of the algorithm applied on sample 2D domain in Figure 42 using critical entry pressure of 4.8 kPa.

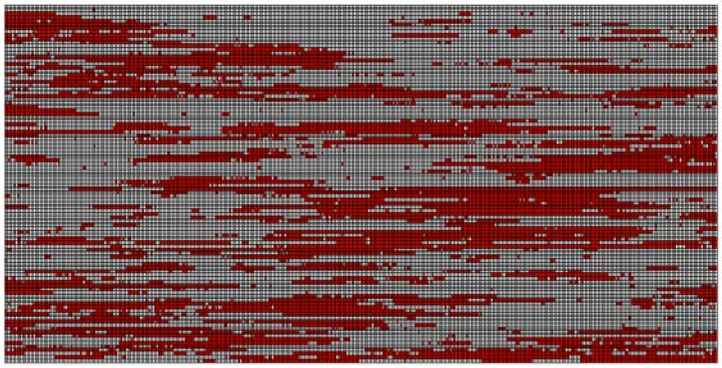

Figure 56: Local capillary trap map resulting from step 3 of the algorithm applied on sample 2D domain in Figure 42 using critical entry pressure of 9.7 kPa.

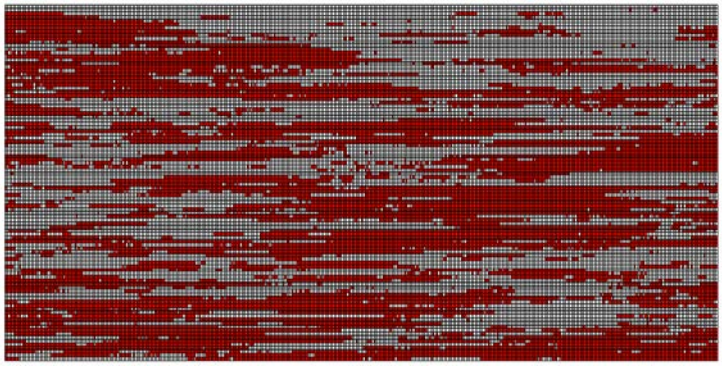

Figure 57: Local capillary trap map resulting from step 3 of the algorithm applied on sample 2D domain in Figure 42 using critical entry pressure of 12.4 kPa.

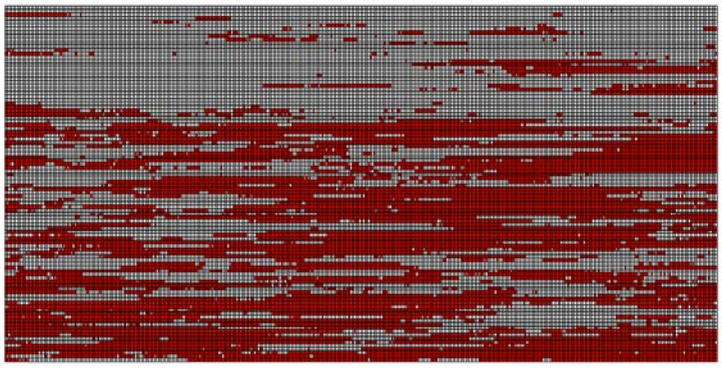

Figure 58: Local capillary trap map resulting from step 3 of the algorithm applied on sample 2D domain in Figure 42 using critical entry pressure of 13.8 kPa.

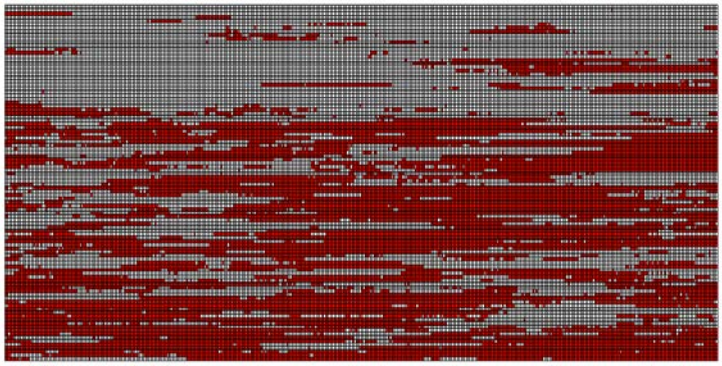

Figure 59: Local capillary trap map resulting from step 3 of the algorithm applied on sample 2D domain in Figure 42 using critical entry pressure of 14.5 kPa.

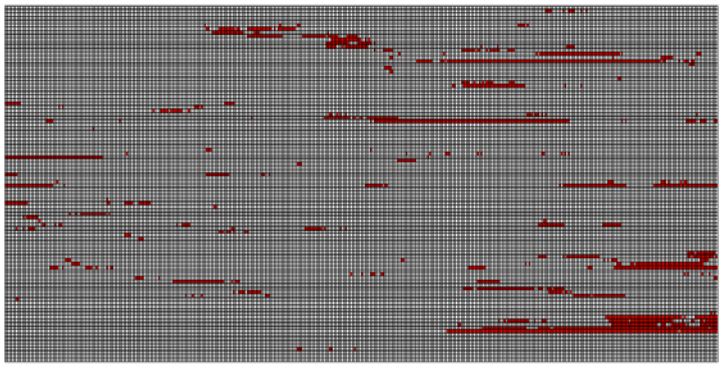

Figure 60: Local capillary trap map resulting from step 3 of the algorithm applied on sample 2D domain in Figure 42 using critical entry pressure of 19.3 kPa.

As we compare the local capillary traps from the flow simulation result of Figure 43 with the results of geological method in Figure 59, we can see that most of the local capillary traps are shown in the result of geological method. This comparison is shown in Figure 61 through Figure 65 for critical entry pressures of 6.9, 9.7, 12.4, 13.8, and 14.5 kPa, respectively. In these figures, the green blocks show the local capillary traps that exist in both methods, the red blocks show the local capillary traps that exist in simulation results but not in the result of geological method, and the blue blocks show the local capillary traps that are predicted by geological method, but do not exist in simulation results. The local capillary trapping capacity as percentage of total number of grid blocks is reported in Table 8 using critical entry pressure values of 6.9, 9.7, 12.4,

13.8, and 14.5 kPa for geological method. We can see that using the critical entry pressures above 9.7 kPa leads to a very good prediction of the local capillary traps (e.g., the $P_{c,entry}^{crit}$ = 12.4 kPa is capable of capturing the entire local capillary traps in the results of simulation). However, it is overestimating the local capillary trapping capacity of the model and the difference between the results increases with increase in critical entry pressure. For example using $P_{c,entry}^{crit}$ = 14.5 kPa, the geological method predicts local capillary trapping capacity of the model three times that of simulation result (i.e., 36% compared to 11%). This is better predicted by geological method when using $P_{c,entry}^{crit}$ = 6.9 kPa, but it is only capable of capturing almost 70% of the local capillary traps in the results of simulation. However, we can see in Figure 62 that using $P_{c,entry}^{crit}$ = 9.7 kPa almost all of the larger clusters of local capillary traps are captured and this is the approximate value of critical entry pressure for this model that can give an acceptable estimation of local capillary trapping.

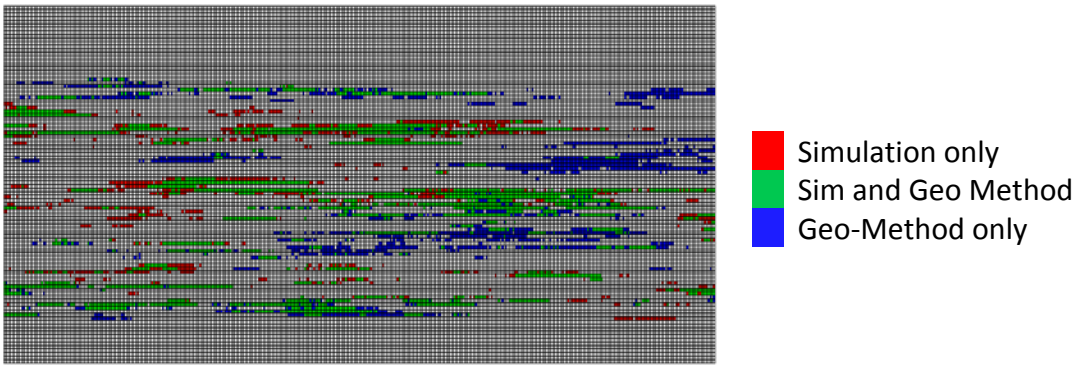

Figure 61: Comparison of the local capillary traps predicted by geological method (using $P_{c,entry}^{crit}$ = 6.9 kPa) and the simulation results.

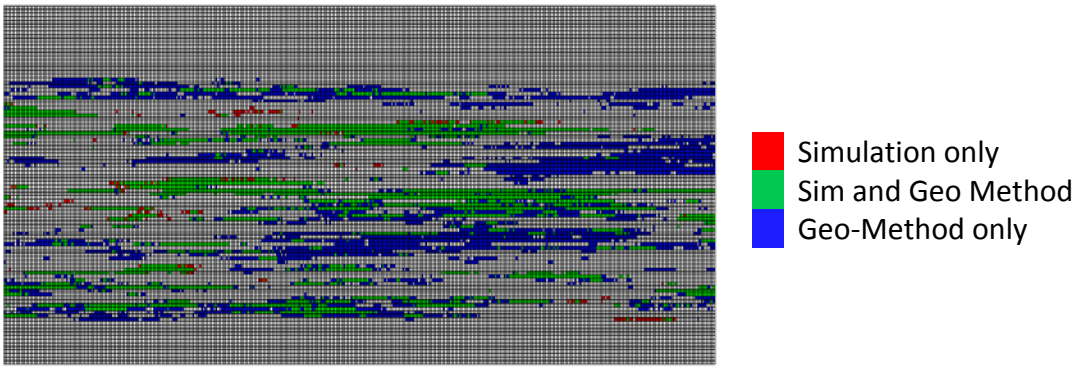

Figure 62: Comparison of the local capillary traps predicted by geological method (using $P_{c,entry}^{crit}$ = 9.7 kPa) and the simulation results.

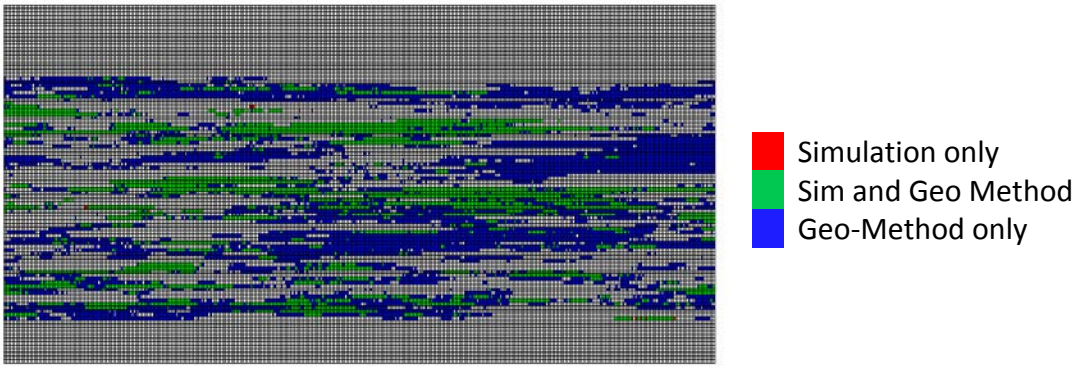

Figure 63: Comparison of the local capillary traps predicted by geological method (using $P_{c,entry}^{crit}$ = 12.4 kPa) and the simulation results.

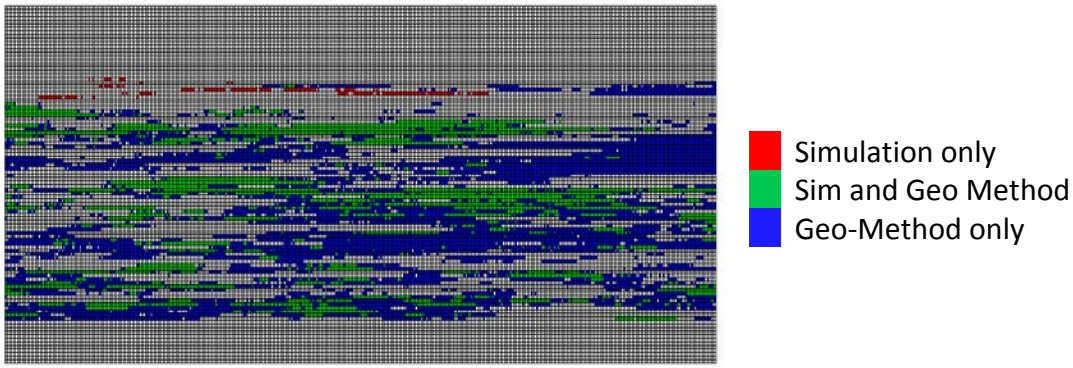

Figure 64: Comparison of the local capillary traps predicted by geological method (using $P_{c,entry}^{crit}$ = 13.8 kPa) and the simulation results.

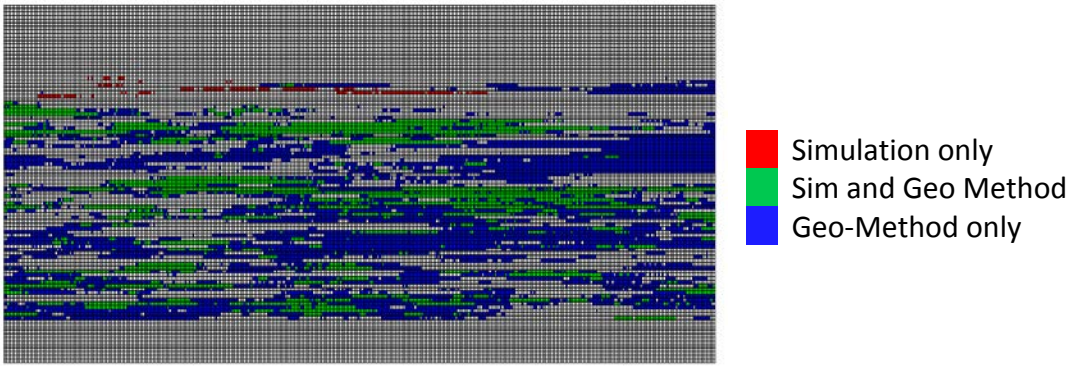

Figure 65: Comparison of the local capillary traps predicted by geological method (using $P_{c,entry}^{crit}$ = 14.5 kPa) and the simulation results.

Table 8: Local Capillary Trapping Capacity (Percentage of Total Number of Grid Blocks) for 2D Domain in Figure 42 Using Simulation Method and Geological Method, and the Common Capacity Predicted by Both Methods Using Different Critical Entry Pressure Values

	$P_{c,entry}^{crit}$, kPa				
	6.9	9.7	12.4	13.8	14.5
Simulation Method	11.2 %	11.2 %	11.2 %	11.2 %	11.2 %
Geological Method	13.2 %	24.3 %	34.3 %	34.2 %	35.9 %
Common in Both Methods	7.9 %	10.6 %	11.2 %	10.7 %	10.7 %

Therefore, for a domain with longer correlation length although there is not a one to one correspondence between the results of the geological method and the simulation result, the geological method is able to give a good prediction of the CO_2 flow path and local capillary traps using a critical entry pressure smaller than the mean entry pressure of the field. This critical entry pressure was located around half of the standard deviation below the mean of the entry pressure field in the case studied in this section.

3D Domain – 1.5 m Correlation Length

The first sample 3D geologic model is 19.5 m long, 9.8 m wide, and 9.8 m high. It consists of 0.3×0.3 m grid blocks, so it contains 65,536 grid blocks. The small size of the model is selected so that the 3D flow simulation with scaled capillary pressure field could be feasible in reasonable amount of time (still this small domain takes around 5 days to run). The permeability field is correlated in x and y horizontal directions with 1.5 m correlation length, but uncorrelated in vertical direction. Figure 66 and Figure 67 show 3D view and top areal view (I-J 2D view) of the permeability field in eight middle layers of the model, i.e., layers 13 through 20. The reference capillary entry pressure curve is the same as previous samples, as shown in Figure 17, with reference entry pressure of 8.3 kPa. The entry pressure field is generated using the Leverett *J*-function. Figure 68 shows top areal view (I-J 2D view) of the capillary entry pressure field in eight middle layers of the model, i.e., layers 13 through 20.

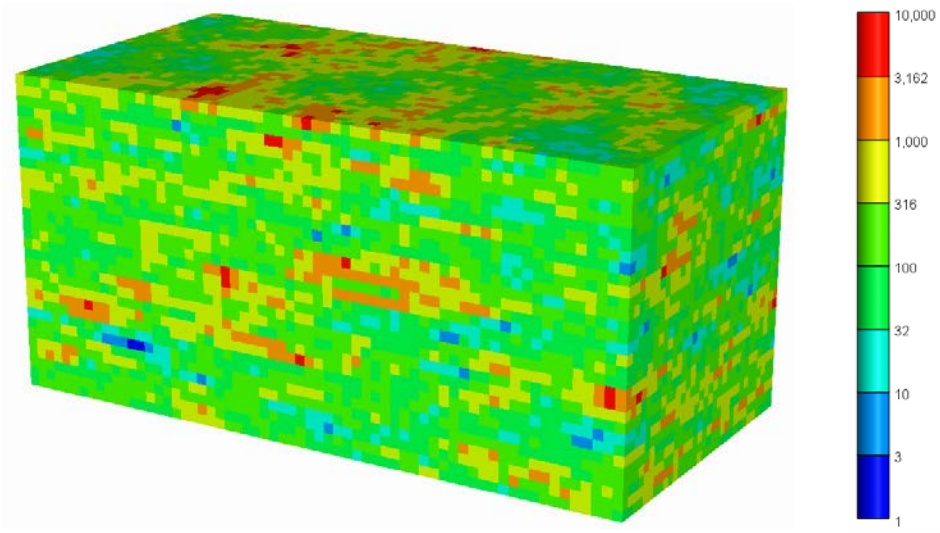

Figure 66: 3D view of permeability field of the sample 3D geologic model with 1.5 m correlation length in x and y horizontal directions and uncorrelated in vertical direction.

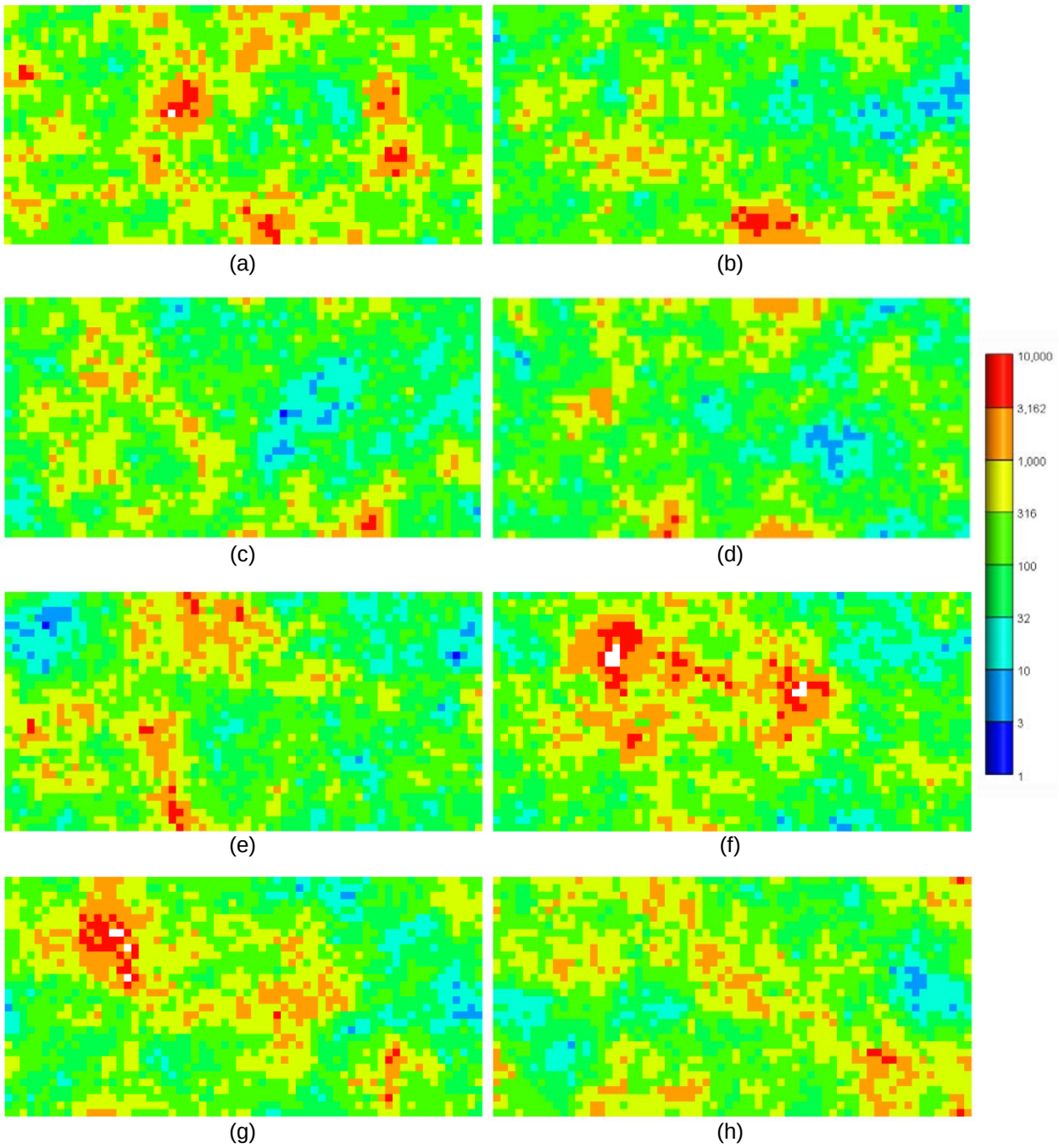

Figure 67: Top areal view of permeability field of the sample 3D geologic model in Figure 66. (a) through (h) show layers 13 through 20, respectively.

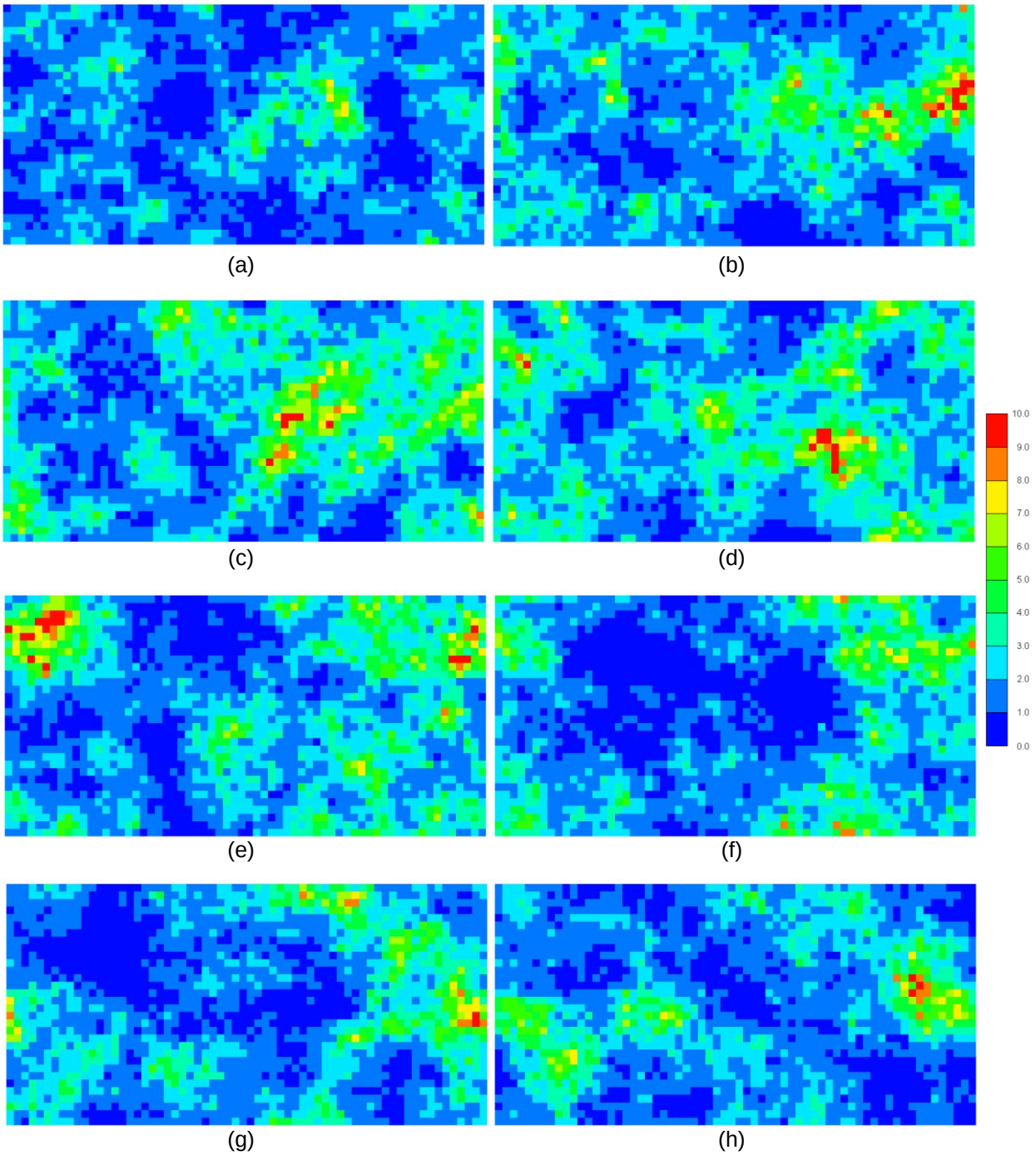

Figure 68: Top areal view of capillary entry pressure field of the sample 3D geologic model with 1.5 m correlation length in x and y horizontal directions. (a) through (h) show layers 13 through 20, respectively.

The entry pressure field has mean value of 8.3 kPa and standard deviation of 4.1 kPa. We use a constant critical capillary entry pressure for the whole domain and choose its value to be 4.1, 6.2, 6.9, 7.6, 8.3, 9.0, and 12.4 kPa.

Figure 69 shows the result of flow simulation for the sample model in Figure 66. It shows the gas saturation profile after 25 years of buoyancy-driven flow of CO_2 inside the formation. The CO_2 was initially emplaced at the bottom of the aquifer at saturation of $S_g = 1 - S_{wr}$ and the system is close to steady state at this time. The high saturation of CO_2 at the top of the formation is accumulation of gas below the top seal and is not considered local capillary trapping.

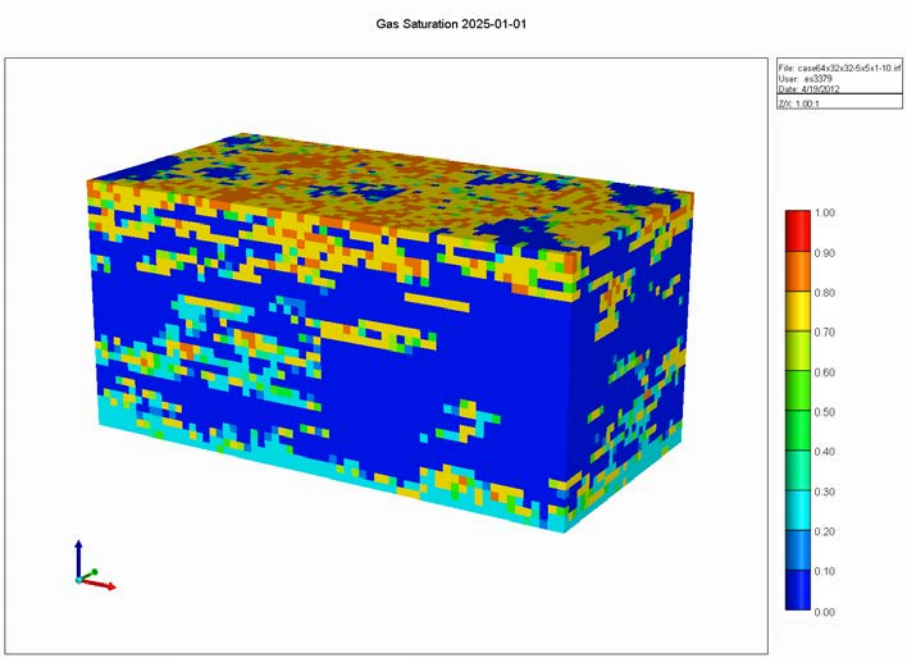

Figure 69: Result of flow simulation for the model in Figure 66 shows gas saturation profile after 25 years of buoyancy-driven flow of CO_2.

After running the algorithm on the model in Figure 66 with critical entry pressures of 4.1, 6.2, 6.9, 7.6, 8.3, 9.0, and 12.4 kPa we find the barrier maps and the local capillary trapping map of the model for these critical entry pressures. Then we compare these results with the corresponding results from flow simulation in Figure 69. For this block-by-block comparison, we neglect the top 5 layers of the formation because the simulation results contain CO_2 accumulation at these levels and it is not possible to extract local capillary trapping in these layers. We find that the critical entry pressure of 6.9 kPa gives the closest results to the results of flow simulation. Figure 70 through Figure 75 show the results of geological method for the model in Figure 66.

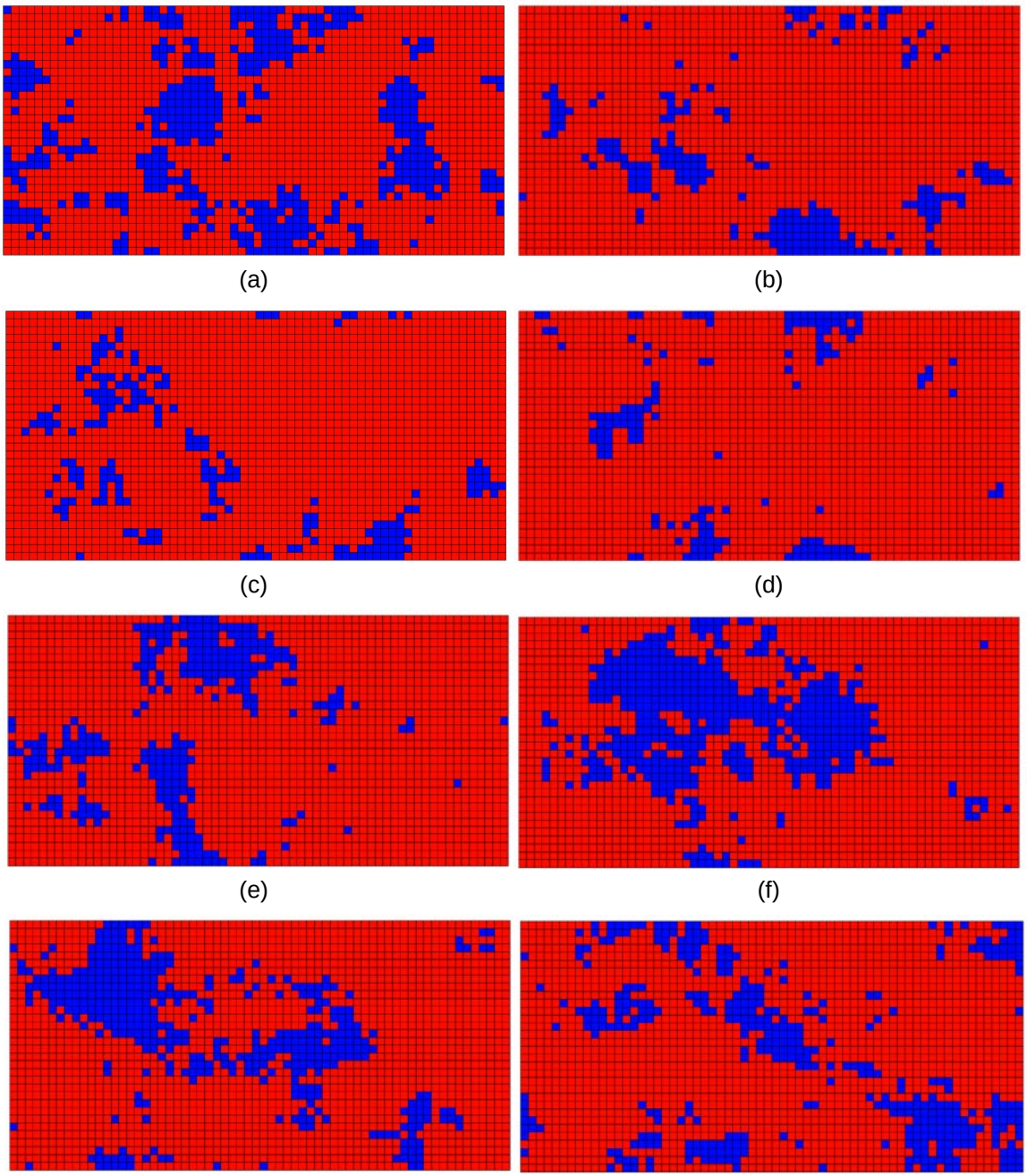

Figure 70: Top areal view of barrier map of the sample 3D geologic model in Figure 66 using $P_{c,entry}^{crit}$ = 6.9 kPa. (a) through (h) show layers 13 through 20, respectively.

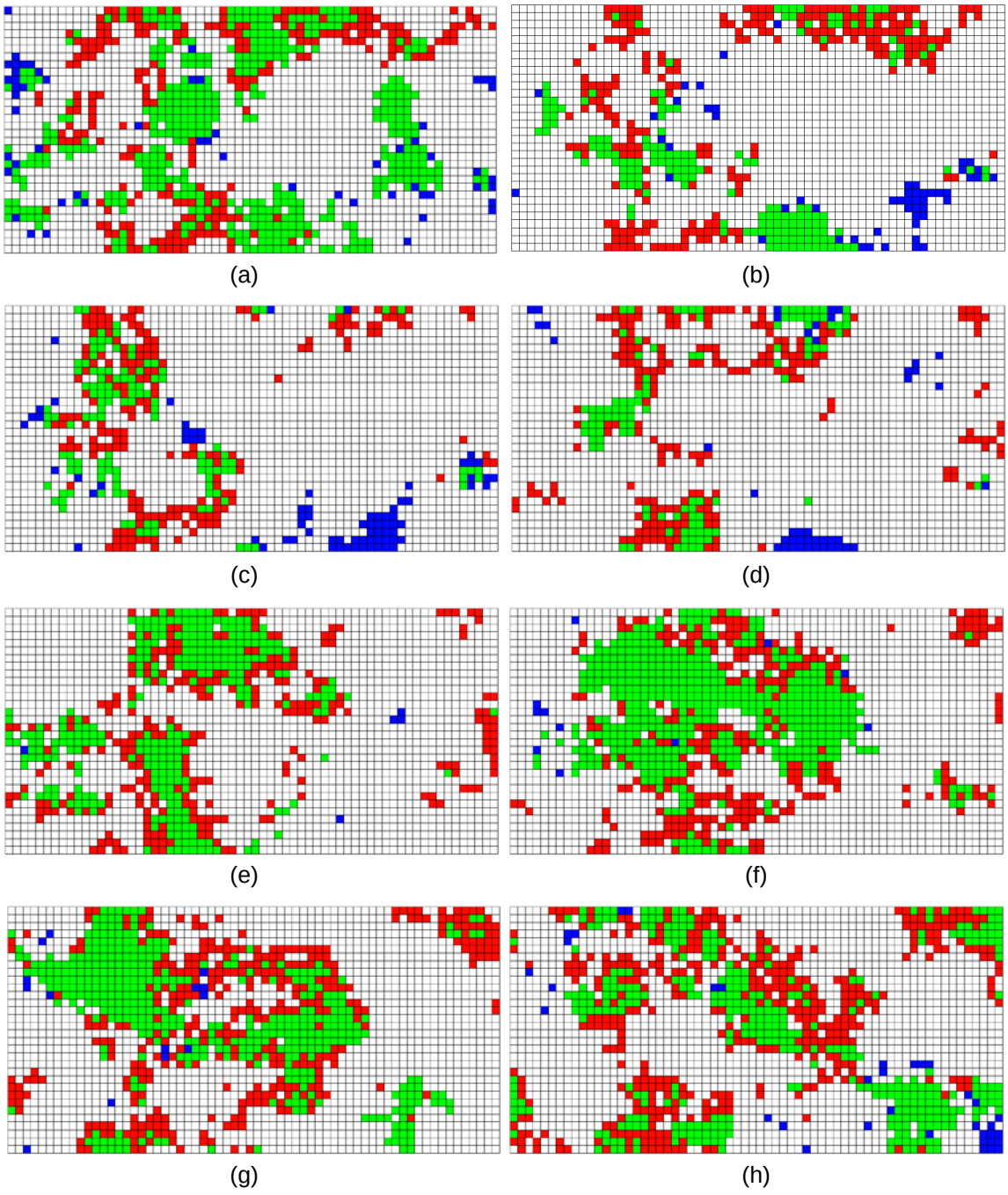

Figure 71: Top areal view of the CO_2 flow path for 3D geologic model of Figure 66 predicted by geological method (using $P_{c,entry}^{crit}$ = 6.9 kPa) and by the simulation results. (a) through (h) show layers 13 through 20, respectively. Red is simulation result only, blue is geological result only, and green is common in both methods.

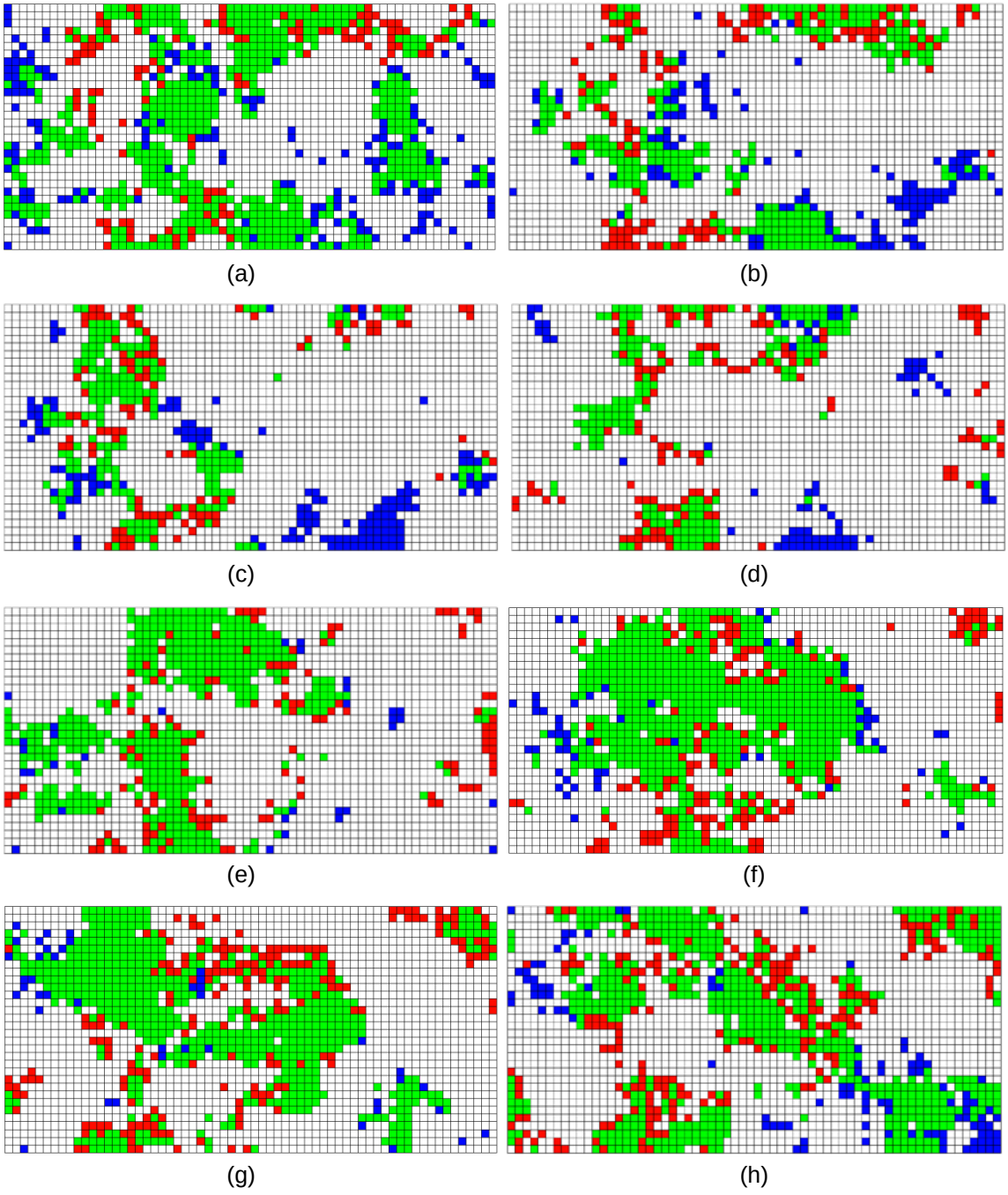

Figure 72: Top areal view of the CO_2 flow path for 3D geologic model of Figure 66 predicted by geological method (using $P_{c,entry}^{crit}$ = 8.3 kPa) and by the simulation results. (a) through (h) show layers 13 through 20, respectively. Red is simulation result only, blue is geological result only, and green is common in both methods.

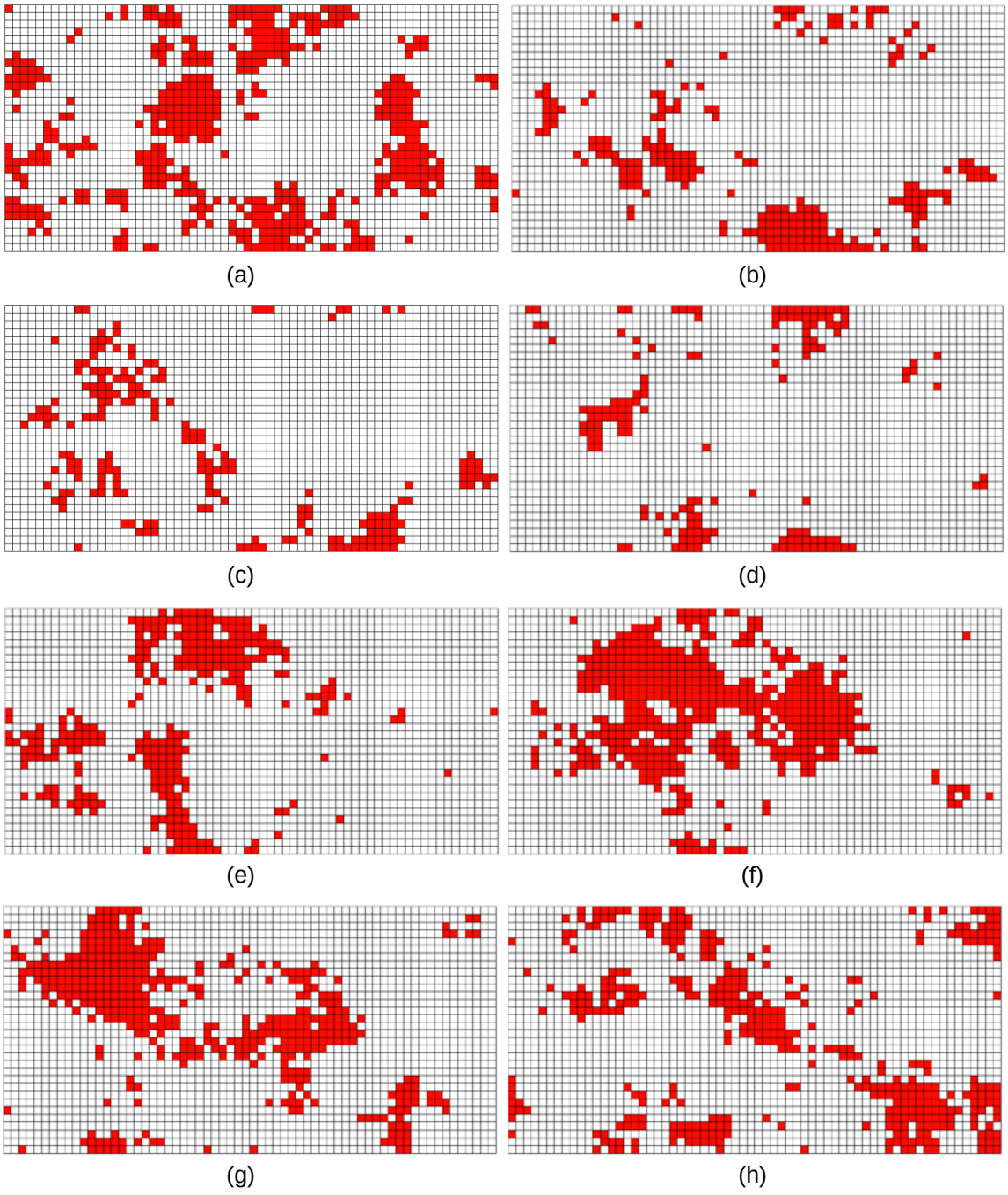

Figure 73: Top areal view of local capillary trap map of the sample 3D geologic model in Figure 66 using $P_{c,entry}^{crit}$ = 6.9 kPa. (a) through (h) show layers 13 through 20, respectively.

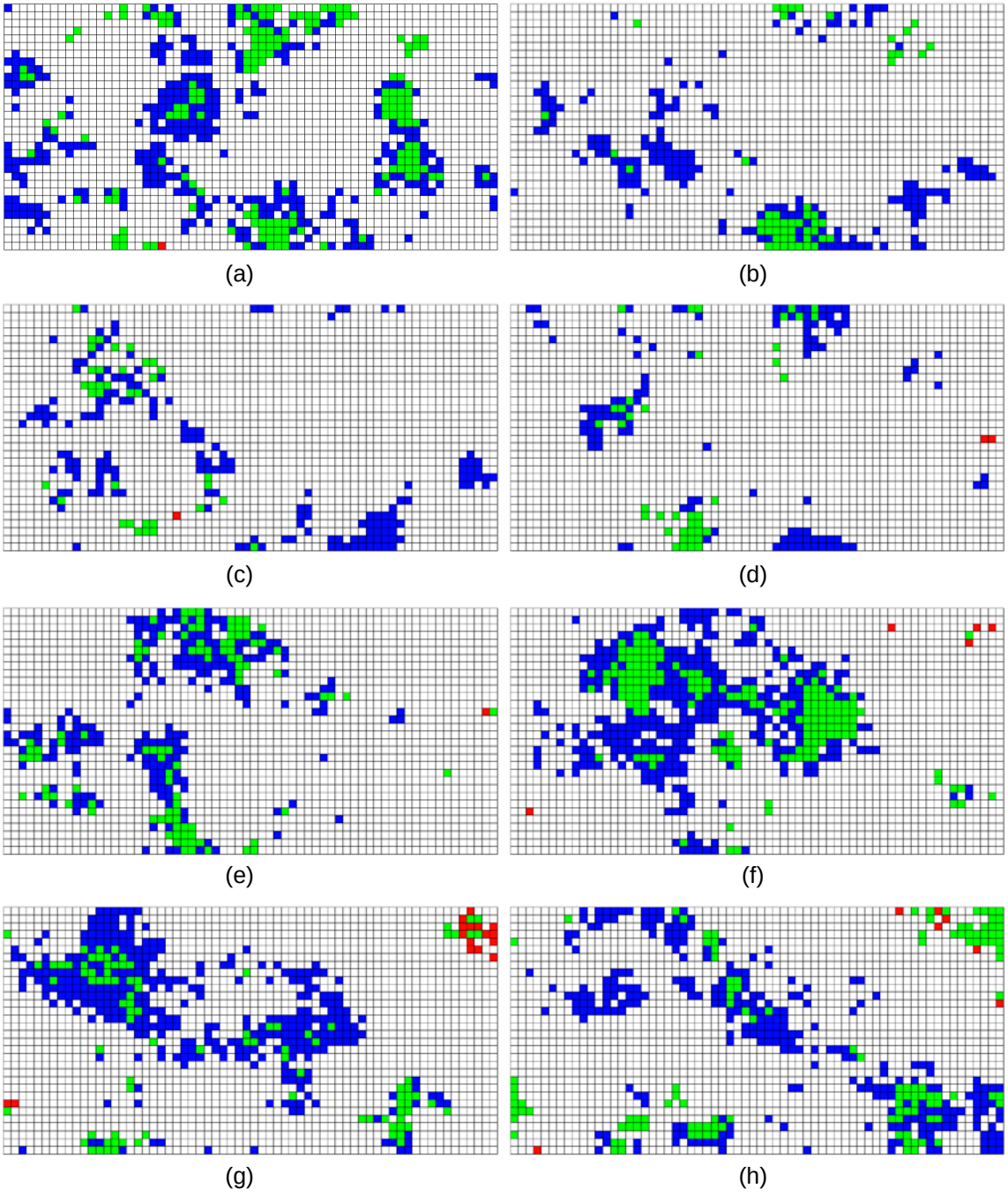

Figure 74: Top areal view of the local capillary trap for 3D geologic model of Figure 66 predicted by geological method (using $P_{c,entry}^{crit}$ =6.9 kPa) and by the simulation results. (a) through (h) show layers 13 through 20, respectively. Red is simulation result only, blue is geological result only, and green is common in both methods.

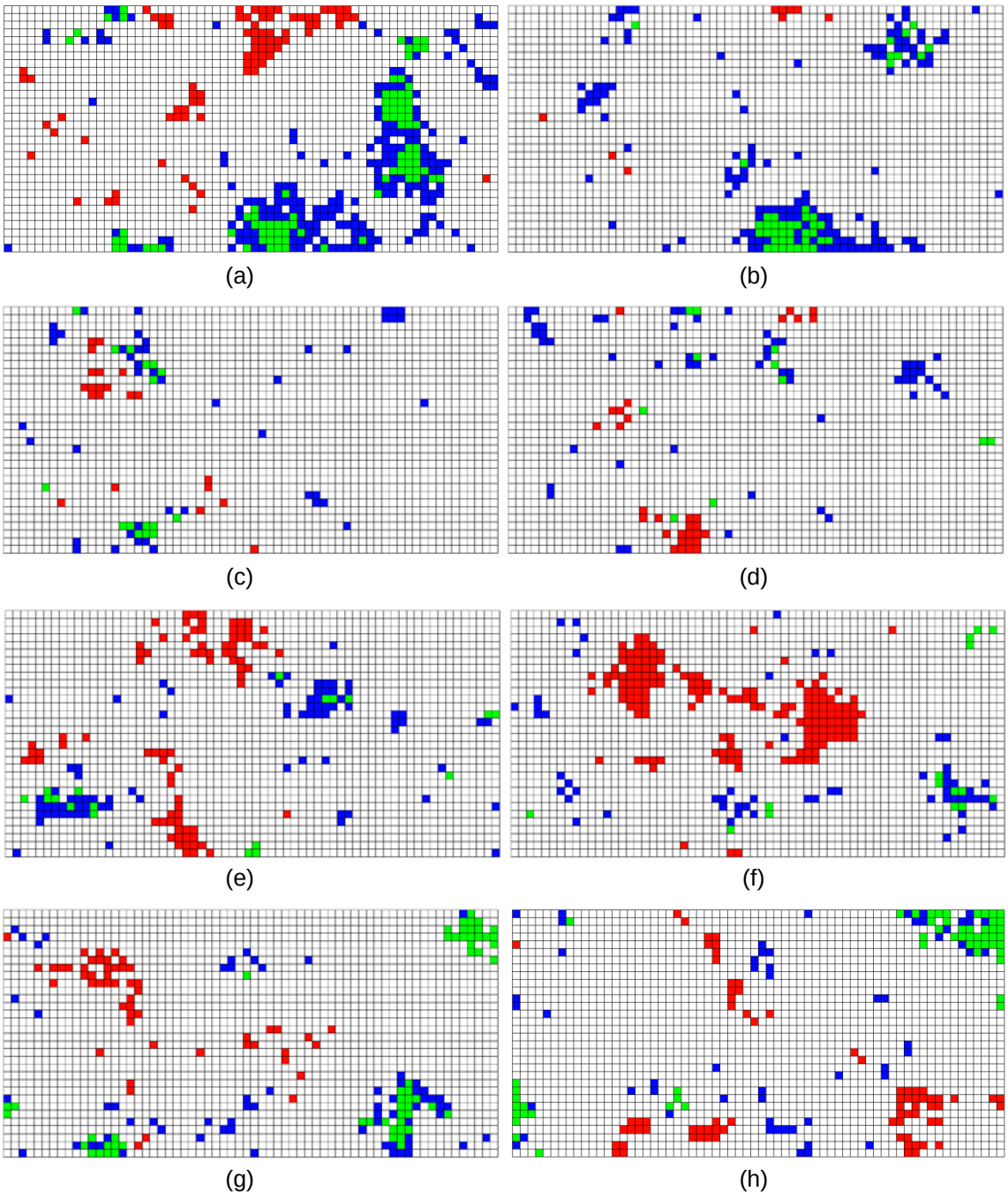

Figure 75: Top areal view of the local capillary trap for 3D geologic model of Figure 66 predicted by geological method (using $P_{c,entry}^{crit}$ =8.3 kPa) and by the simulation results. (a) through (h) show layers 13 through 20, respectively. Red is simulation result only, blue is geological result only, and green is common in both methods.

All of these results are presented as the top areal view (I-J 2D view) for eight middle layers of the model, i.e., layers 13 through 20. Figure 70 shows the barrier map of the model in Figure 66 as a result of applying step 1 of geological method on the entry pressure field. The red blocks represent the barrier blocks that CO_2 should not be able to go through them and the blue blocks

are non-barrier blocks. As it is expected, increasing the critical capillary entry pressure causes more non-barrier blocks to appear and provide the path for CO_2 to pass through.

Figure 71 shows the flow path which is overlaid on the barrier map in Figure 70 for $P_{c,entry}^{crit}$ = 6.9 kPa. Figure 72 shows the comparison of simulation flow path with barrier map for $P_{c,\,entry}^{crit}$ = 8.3 kPa. The green blocks are the part of CO_2 flow path that matches the non-barrier blocks in barrier map. It shows that the majority of flow path lies inside the non-barrier region and there is an excellent agreement between the results, especially in Figure 72. The geological method is able to predict barrier and non-barrier regions inside the geologic model with good enough accuracy. Note that also in this case the critical entry pressure is close to the mean entry pressure of the field.

Table 9 quantifies the grid blocks that have been CO_2 flow path (as percentage of total number of grid blocks) in simulation results and in the results of geological method. The number of grid blocks that are commonly predicted by both methods gives a representation of the degree of agreement between the results. Increasing the critical entry pressure increases the number of grid blocks open to flow and also, fits more of the simulation flow path. As can be seen in the table, using $P_{c,entry}^{crit}$ = 8.3 kPa can predict about 70% of CO_2 flow path compared to simulation results.

Table 9: CO_2 Flow Path (Percentage of Total Number of Grid Blocks) for 3D Domain in Figure 66 Using Simulation Method and Geological Method, and the Common Path Predicted by Both Methods Using Different Critical Entry Pressure Values for Geological Method

	$P_{c,entry}^{crit}$, kPa			
	6.2	6.9	7.6	8.3
Simulation Method	22.4 %	22.4 %	22.4 %	22.4 %
Geological Method	8.6 %	11.5 %	14.6 %	17.6 %
Common in Both Methods	8.3 %	10.8 %	13.4 %	15.6 %

Finally, we find the local capillary traps which are surrounded by capillary barriers in the domain. Figure 73 shows the clusters of traps that are surrounded from top and sides by barrier blocks in the sample 3D domain using critical capillary entry pressure of 6.9 kPa for layers 13 through 20. For small values of critical entry pressure almost all of the non-barrier clusters contribute to local capillary trapping because they are very small and completely surrounded by capillary barriers. Increasing the critical capillary entry pressure initially causes the number of local capillary traps to increase, but as larger non-barrier clusters start to connect to the top of the formation at some threshold value of critical entry pressure, then the local capillary traps start to decrease.

Figure 74 shows the comparison between the results of geological method (using critical entry pressures of 6.9 kPa) with the results of simulation for layers 13 through 20. Figure 75 shows this comparison using critical entry pressures of 8.3 kPa for geological method. In these figures, the green blocks show the local capillary traps that are predicted commonly by both methods, the red blocks show the local capillary traps in simulation results that do not exist in the result of geological method, and the blue blocks show the local capillary traps that are predicted by geological method, but do not exist in simulation results. The local capillary trapping capacity as percentage of total number of grid blocks is reported in Table 10 using critical entry pressure values of 6.2, 6.9, 7.6, and 8.3 kPa for geological method. While the $P_{c,entry}^{crit}$ = 6.9 kPa is

capable of capturing almost 80% of local capillary traps in the results of simulation, it is overestimating the local capillary trapping capacity of the model (11.4% compared to 5%). For $P_{c,entry}^{crit}$ = 8.3 kPa, the local capillary trapping capacity of the model is better predicted by geological method (4.1% compared to 5%), but it is only capable of capturing 1.6% of that 5% local capillary traps in the results of simulation. Therefore, although there is not a one to one correspondence between the results of the geological method and the simulation result, the geological method is able to give a good prediction of the local capillary traps when using $P_{c,entry}^{crit}$ = 6.9 kPa as critical capillary entry pressure. This critical entry pressure is located below the mean entry pressure of the field.

Table 10: Local Capillary Trapping Capacity (Percentage of Total Number of Grid Blocks) for 3D Domain in Figure 66 Using Simulation Method and Geological Method, and the Common Capacity Predicted by Both Methods Using Different Critical Entry Pressure Values for Geological Method

	$P_{c,entry}^{crit}$, kPa			
	6.2	6.9	7.6	8.3
Simulation Method	5 %	5 %	5 %	5 %
Geological Method	8.6 %	11.4 %	6.2 %	4.1 %
Common in Both Methods	3.6 %	4.1 %	2.6 %	1.6 %

3D Domain – 4.6 m Correlation Length

The second sample 3D geologic model is also 19.5 m long, 9.8 m wide, and 9.8 m high to make the 3D flow simulation with scaled capillary pressure field feasible in reasonable amount of time. It consists of 0.3×0.3 m grid blocks, so it contains 65,536 grid blocks. The permeability field is correlated in x and y horizontal directions with 4.6 m correlation length, but uncorrelated in vertical direction. Figure 76 and Figure 77 show 3D view and top areal view (I-J 2D view) of the permeability field in eight middle layers of the model, i.e., layers 13 through 20. The reference capillary entry pressure curve is the same as previous samples, as shown in Figure 17, with reference entry pressure of 8.3 kPa. The entry pressure field is generated using the Leverett *J*-function. Figure 78 shows top areal view (I-J 2D view) of the capillary entry pressure field in eight middle layers of the model, i.e., layers 13 through 20.

The entry pressure field has mean value of 8.3 kPa and standard deviation of 4.1 kPa. We use a constant critical capillary entry pressure for the whole domain and choose its value to be 4.1, 5.5, 6.2, 6.9, 7.6, 8.3, 9.0, and 12.4 kPa.

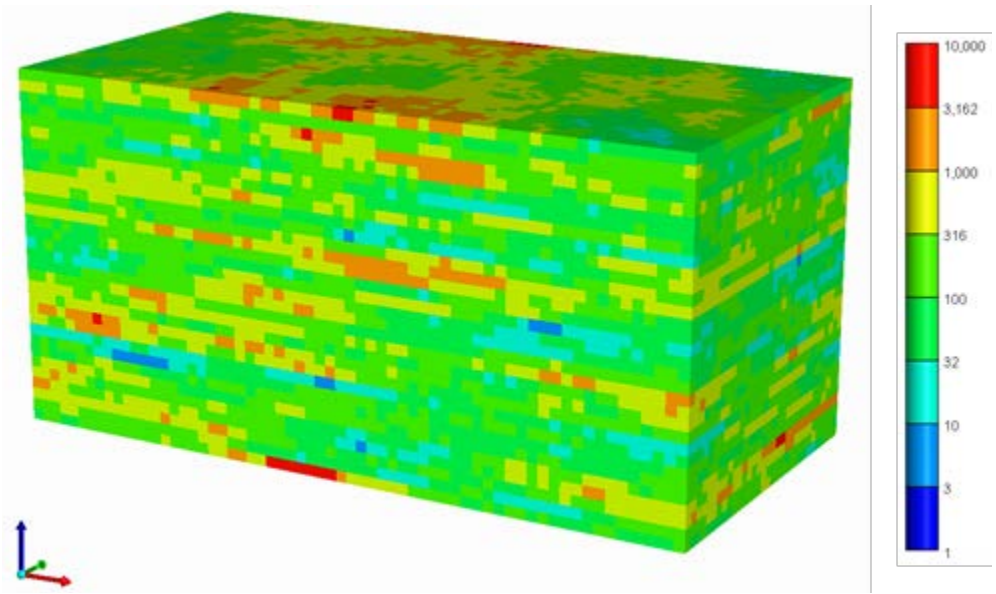

Figure 76: 3D view of permeability field of the sample 3D geologic model with 4.6 m correlation length in x and y horizontal directions and uncorrelated in vertical direction.

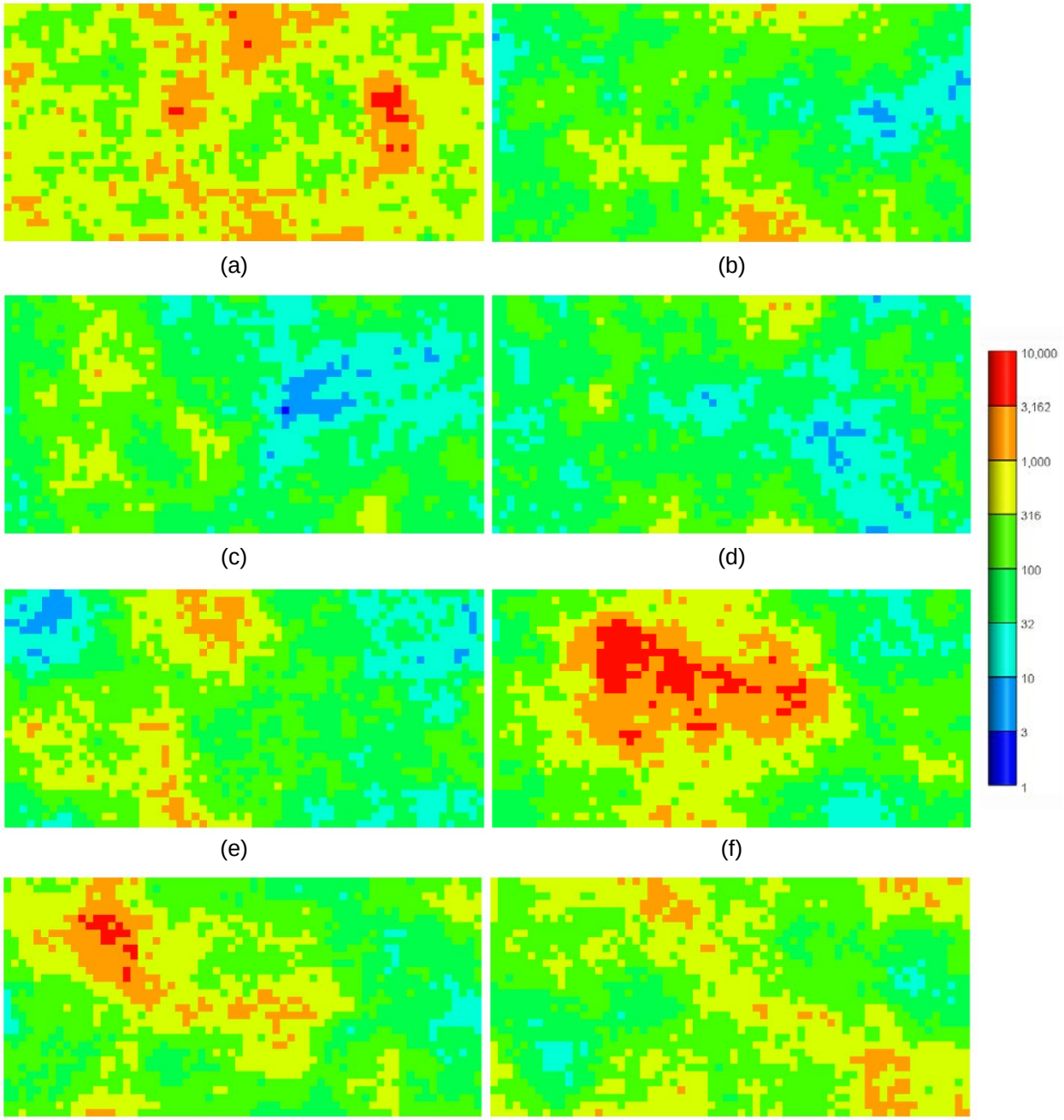

Figure 77: Top areal view of permeability field of the sample 3D geologic model in Figure 76. (a) through (h) show layers 13 through 20, respectively.

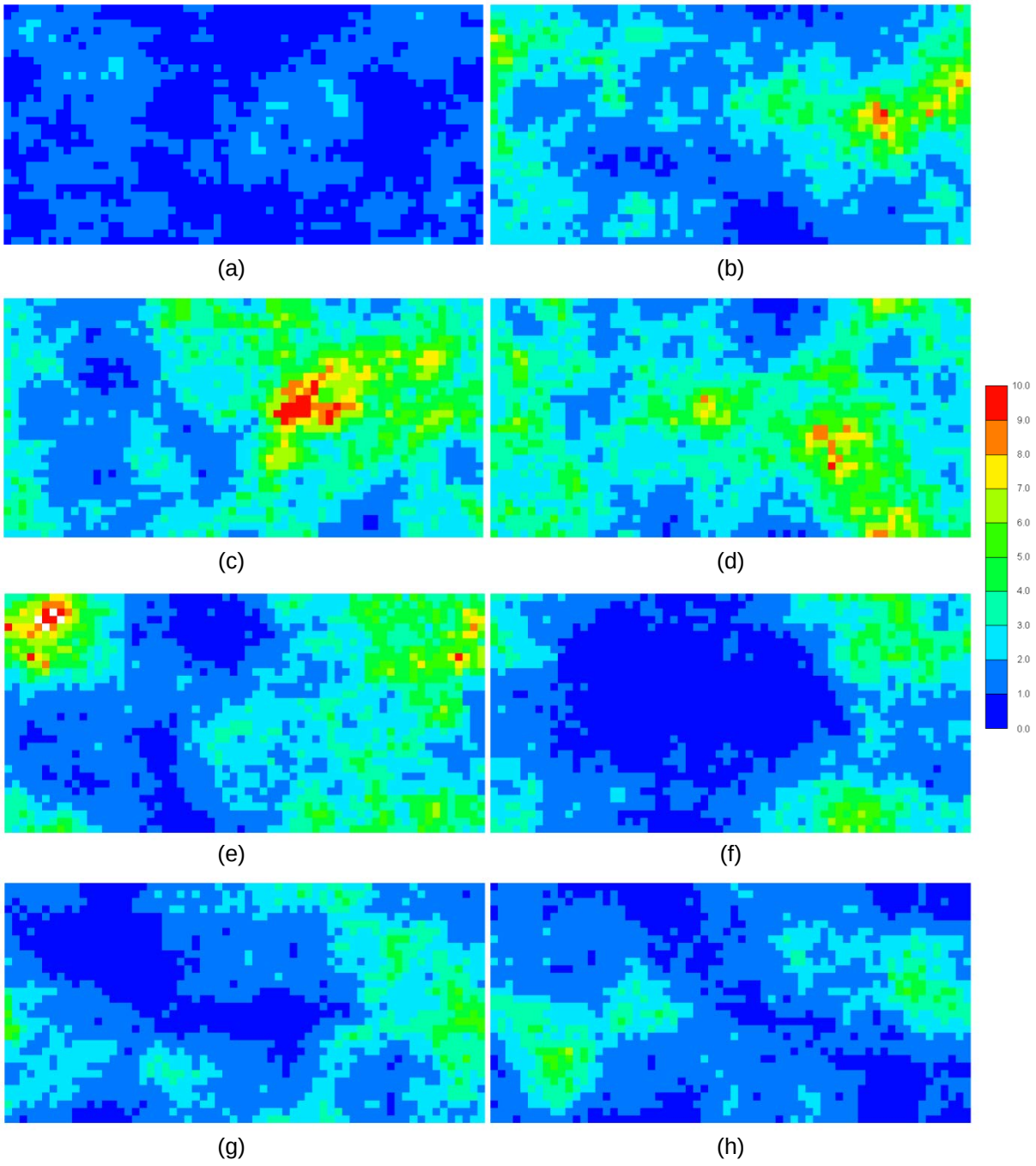

Figure 78: Top areal view of capillary entry pressure field of the sample 3D geologic model with 4.6 m correlation length in x and y horizontal directions. (a) through (h) show layers 13 through 20, respectively.

Figure 79 shows the result of flow simulation for the sample model in Figure 76. It shows the gas saturation profile after 25 years of buoyancy-driven flow of CO_2 inside the formation. The CO_2 was initially emplaced at the bottom of the aquifer at saturation of $S_g = 1 - S_{wr}$ and the gas displacement is stopped at this time. The high saturation of CO_2 at the top of the formation is accumulation of gas below the top seal and is not considered local capillary trapping.

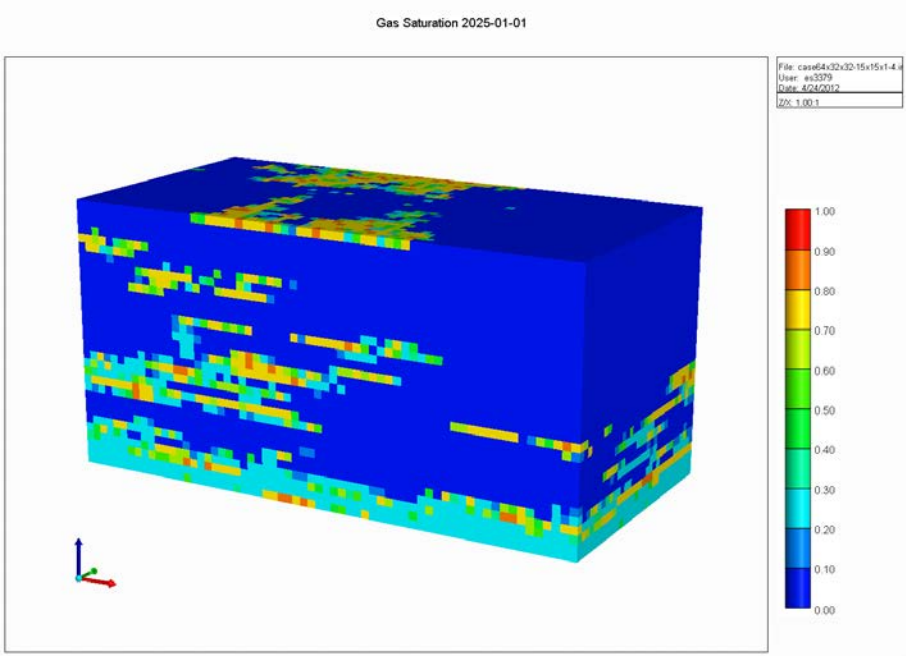

Figure 79: Result of flow simulation for the model in Figure 76 shows gas saturation profile after 25 years of buoyancy-driven flow of CO_2.

Now we use the geological method to find the barrier maps and the local capillary trapping map of the model in Figure 76 with critical entry pressures of 4.1, 6.2, 6.9, 7.6, 8.3, 9.0, and 12.4 kPa. The results are then compared with the flow simulation results in Figure 79. Since the simulation result contains CO_2 accumulation at the top 2 layers of the formation (which covers the local capillary traps) we neglect these levels in comparing the results. We find that the critical entry pressure of 5.5 kPa gives the closest results to the local capillary trapping results of flow simulation. Figure 80 through Figure 82 show the results of geological method for the model in Figure 76. All of these results are presented as the top areal view (I-J 2D view) for eight middle layers of the model, i.e., layers 13 through 20.

Figure 80 shows the barrier map of the model in Figure 76 as a result of applying step 1 of geological method on the entry pressure field. The red blocks represent the barrier blocks and the blue blocks are non-barrier blocks.

Figure 81 shows the flow path which is overlaid on the barrier map in Figure 80 for $P_{c,entry}^{crit}$ = 5.5 kPa. Figure 82 shows the comparison of simulation flow path with barrier map for $P_{c,entry}^{crit}$ = 8.3 kPa. The green blocks are the part of CO_2 flow path that matches the non-barrier blocks in barrier map. It shows that the majority of flow path lies inside the non-barrier region and there is an excellent agreement between the results, especially in Figure 82. Although Figure 81 shows that $P_{c,entry}^{crit}$ = 5.5 kPa is not able to accurately match the CO_2 flow path in the model, the geological method is able to successfully predict the core axis of the CO_2 flow path inside the domain.

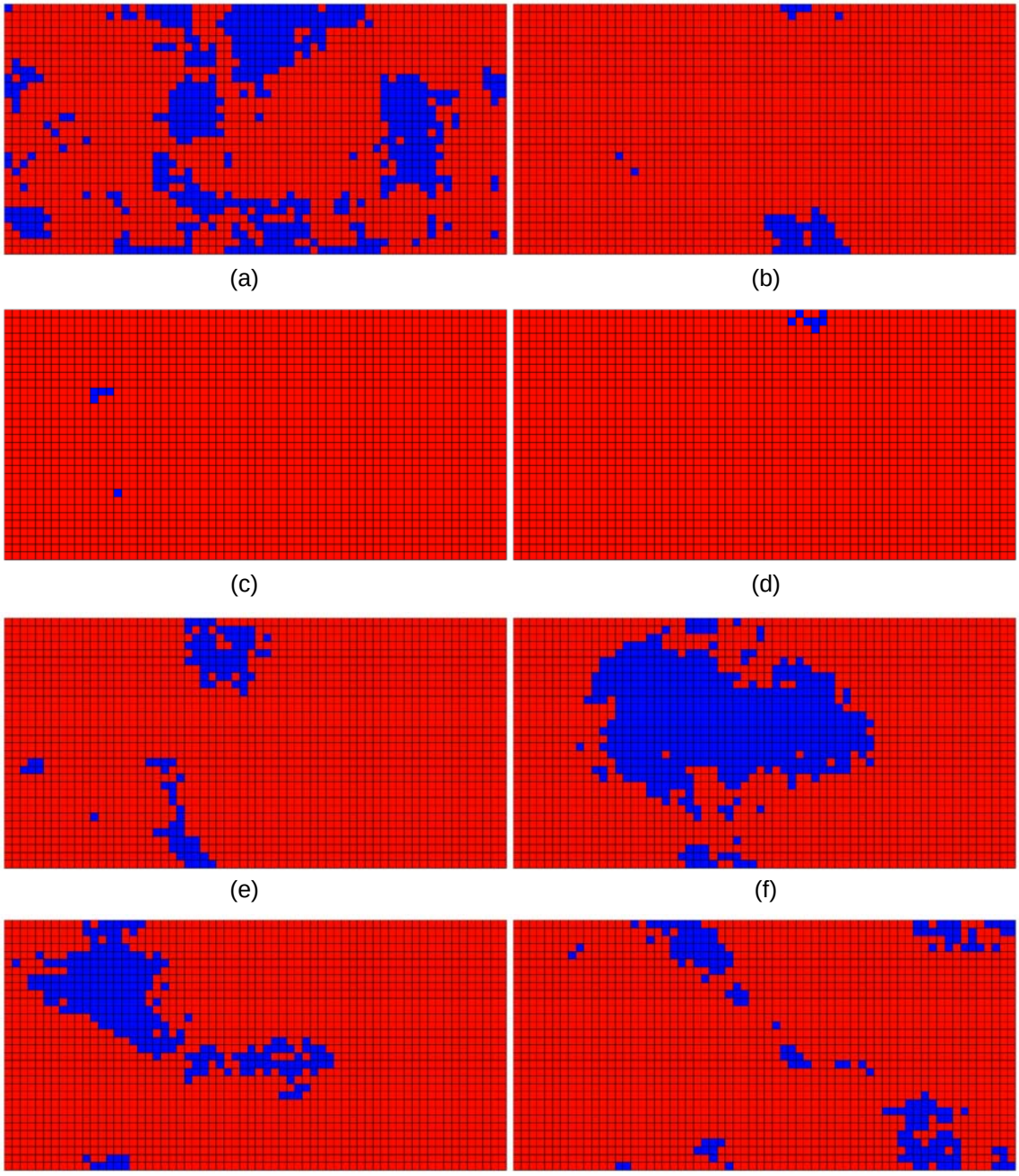

Figure 80: Top areal view of barrier map of the sample 3D geologic model in Figure 76 using $P_{c,entry}^{crit}$ = 5.5 kPa. (a) through (h) show layers 13 through 20, respectively.

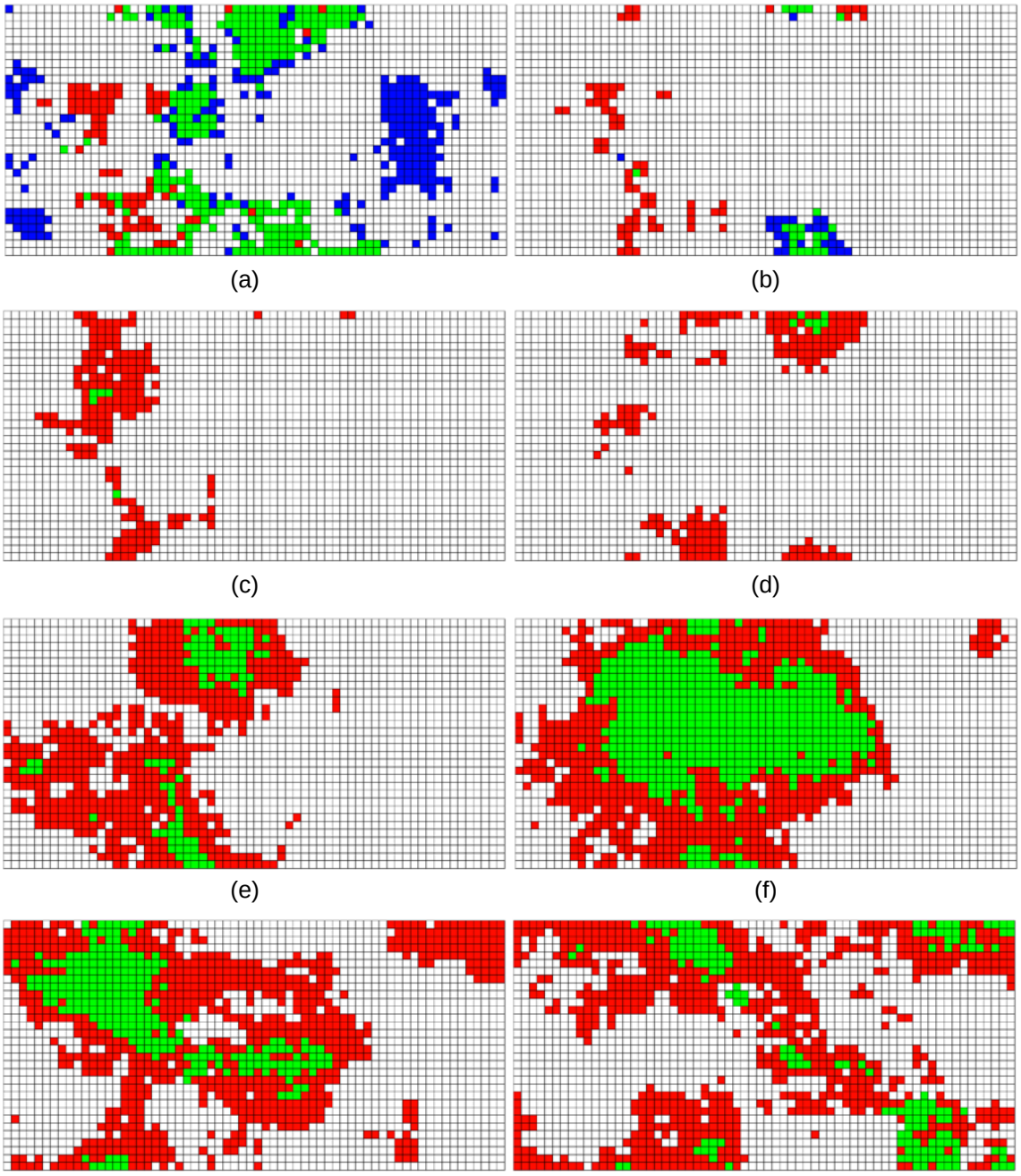

Figure 81: Top areal view of the CO2 flow path for 3D geologic model of Figure 76 predicted by geological method (using $P_{c,entry}^{crit}$ = 5.5 kPa) and by the simulation results. (a) through (h) show layers 13 through 20, respectively. Red is simulation result only, blue is geological result only, and green is common in both methods.

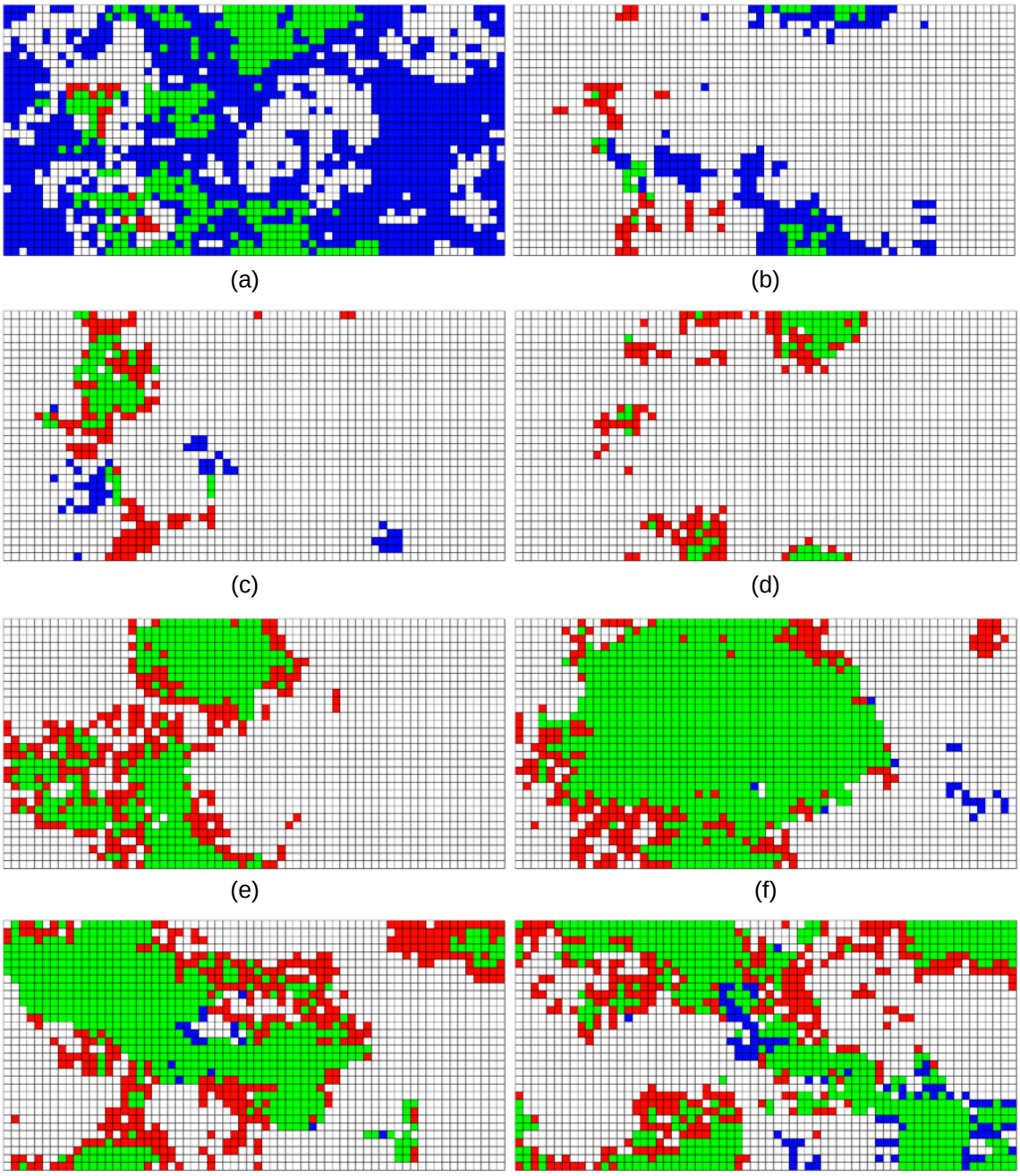

Figure 82: Top areal view of the CO_2 flow path for 3D geologic model of Figure 76 predicted by geological method (using $P_{c,entry}^{crit}$ = 8.3 kPa) and by the simulation results. (a) through (h) show layers 13 through 20, respectively. Red is simulation result only, blue is geological result only, and green is common in both methods.

Table 11 shows the number of grid blocks (as percentage of total number of grid blocks) that constitute CO_2 flow path in simulation results and in the results of geological method (using various critical entry pressure values). The number of grid blocks that are commonly predicted by both methods gives a representation of the degree of agreement between the results. Increasing the critical entry pressure increases the number of grid blocks open to flow and also,

fits more of the simulation flow path. As can be seen in the table, using $P_{c,entry}^{crit}$ = 8.3 kPa can predict more than 70% of CO_2 flow path compared to simulation results (14.4% out of 20.2%). This ratio is about 30% using $P_{c,entry}^{crit}$ = 5.5 kPa (6% out of 20.2%). However, as stated earlier, Figure 81 shows that it is still able to show the core axis of the CO_2 flow path in the domain.

Table 11: CO_2 Flow Path (Percentage of Total Number of Grid Blocks) for 3D Domain in Figure 76 Using Simulation Method and Geological Method, and the Common Path Predicted by Both Methods Using Different Critical Entry Pressure Values for Geological Method

	$P_{c,entry}^{crit}$, kPa				
	5.5	6.2	6.9	7.6	8.3
Simulation Method	20.2 %	20.2 %	20.2 %	20.2 %	20.2 %
Geological Method	7.5 %	10.9 %	14.6 %	18.7 %	23.1 %
Common in Both Methods	6 %	8.2 %	10.3 %	12.4 %	14.4 %

In the final step, we find the local capillary traps which are surrounded by capillary barriers in the domain. Figure 83 shows the clusters of traps that are surrounded from top and sides by barrier blocks in the 3D domain using critical capillary entry pressure of 5.5 kPa for layers 13 through 20. The small values of critical entry pressure causes the non-barrier blocks in layers not close to the top of the formation to be separated from the top and hence, almost all of the non-barrier clusters contribute to local capillary trapping. Because of the longer correlation length in this case, increasing the critical capillary entry pressure up to the mean entry pressure still causes the number of local capillary traps to increase, since the non-barrier clusters are not as sparse as cases with smaller correlation length and it is hard for them to connect to the top of the formation.

Figure 84 shows the comparison between the results of geological method (using critical entry pressures of 5.5 kPa) with the results of simulation for layers 13 through 20. Figure 85 shows this comparison using critical entry pressures of 8.3 kPa for geological method. In these figures, the green blocks show the local capillary traps that are predicted commonly by both methods, the red blocks show the local capillary traps in simulation results that are not predicted by geological method, and the blue blocks show the local capillary traps that are predicted by geological method, but do not exist in simulation results. The local capillary trapping capacity as percentage of total number of grid blocks is reported in Table 12 using critical entry pressure values of 5.5, 6.2, 6.9, 7.6, and 8.3 kPa for geological method. Using $P_{c,entry}^{crit}$ = 8.3 kPa the geological method is able to capture almost entire local capillary traps in the results of simulation, but it is drastically overestimating the local capillary trapping capacity of the model (17.1% compared to 3.2%). For $P_{c,entry}^{crit}$ = 5.5 kPa, the local capillary trapping capacity of the model is better predicted by geological method (5.5% compared to 3.2%) and it is able to capture 2.5% of those 3.2% local capillary traps in the results of simulation. Therefore, the geological method can make a satisfactory prediction of the local capillary traps when using $P_{c,entry}^{crit}$ = 5.5 kPa as critical capillary entry pressure. This critical entry pressure is located below the mean entry pressure of the field.

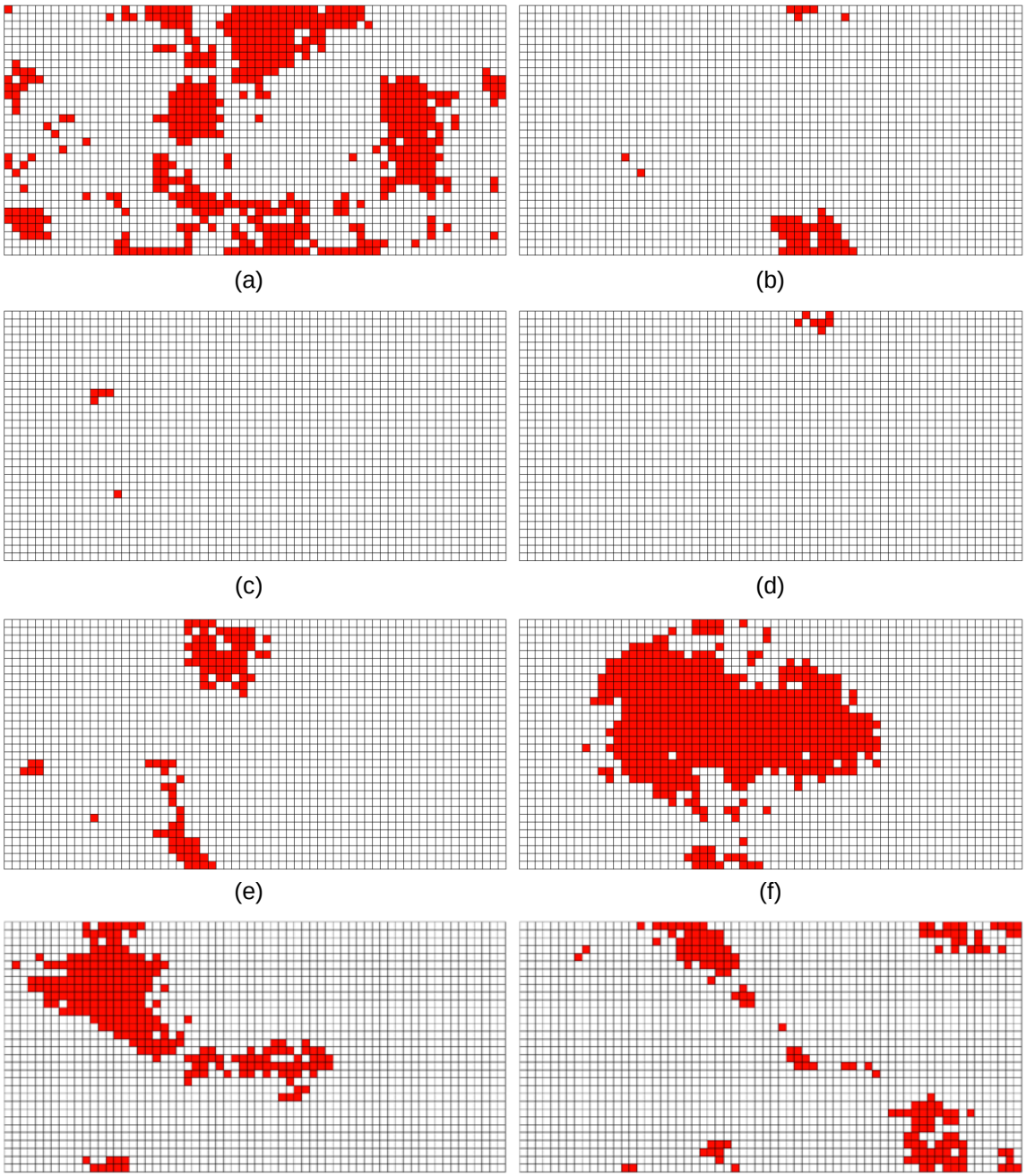

Figure 83: Top areal view of local capillary trap map of the sample 3D geologic model in Figure 76 using $P_{c,entry}^{crit}$ = 5.5 kPa. (a) through (h) show layers 13 through 20, respectively.

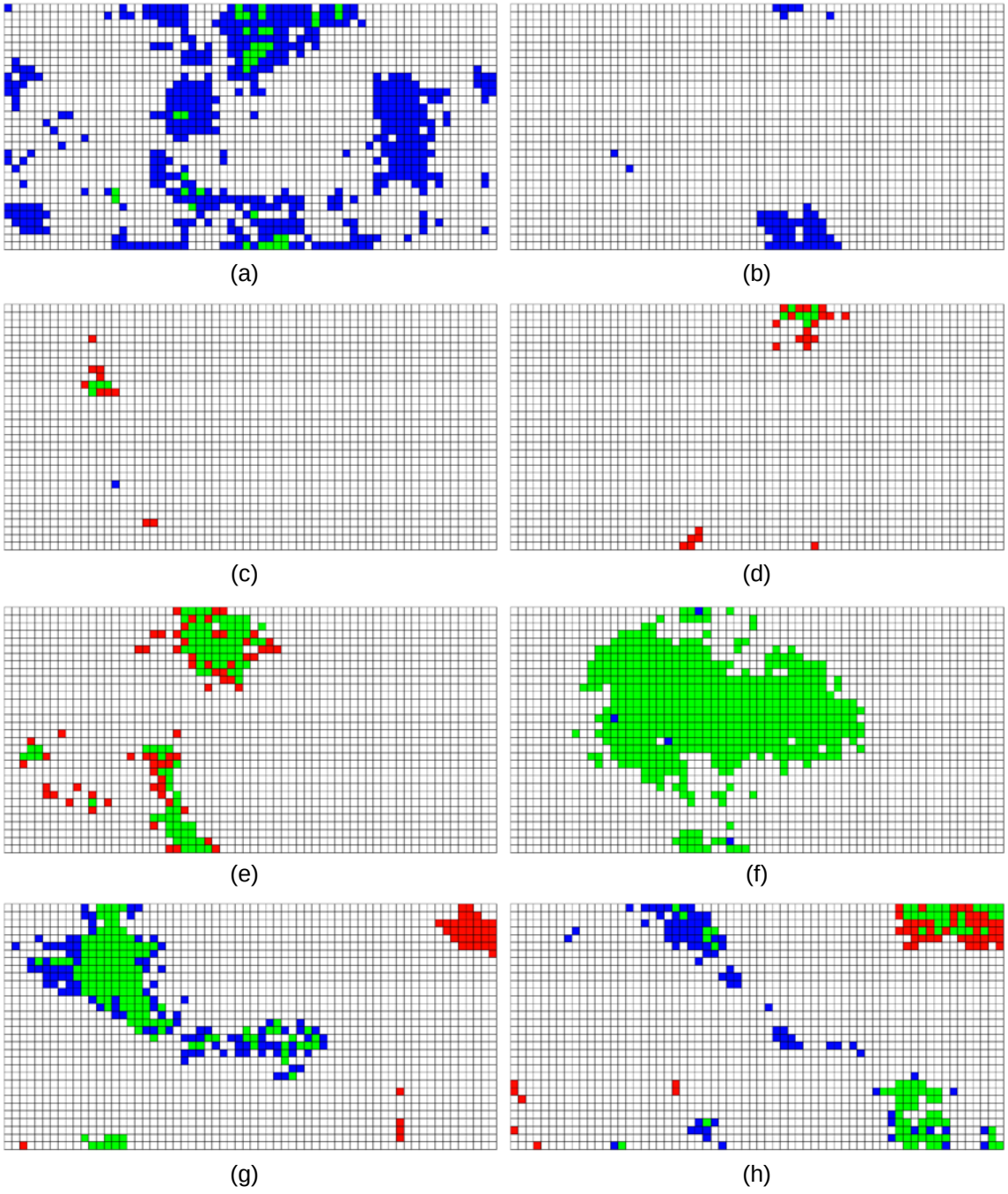

Figure 84: Top areal view of the local capillary trap for 3D geologic model of Figure 76 predicted by geological method (using $P_{c,entry}^{crit}$ = 5.5 kPa) and by the simulation results. (a) through (h) show layers 13 through 20, respectively. Red is simulation result only, blue is geological result only, and green is common in both methods.

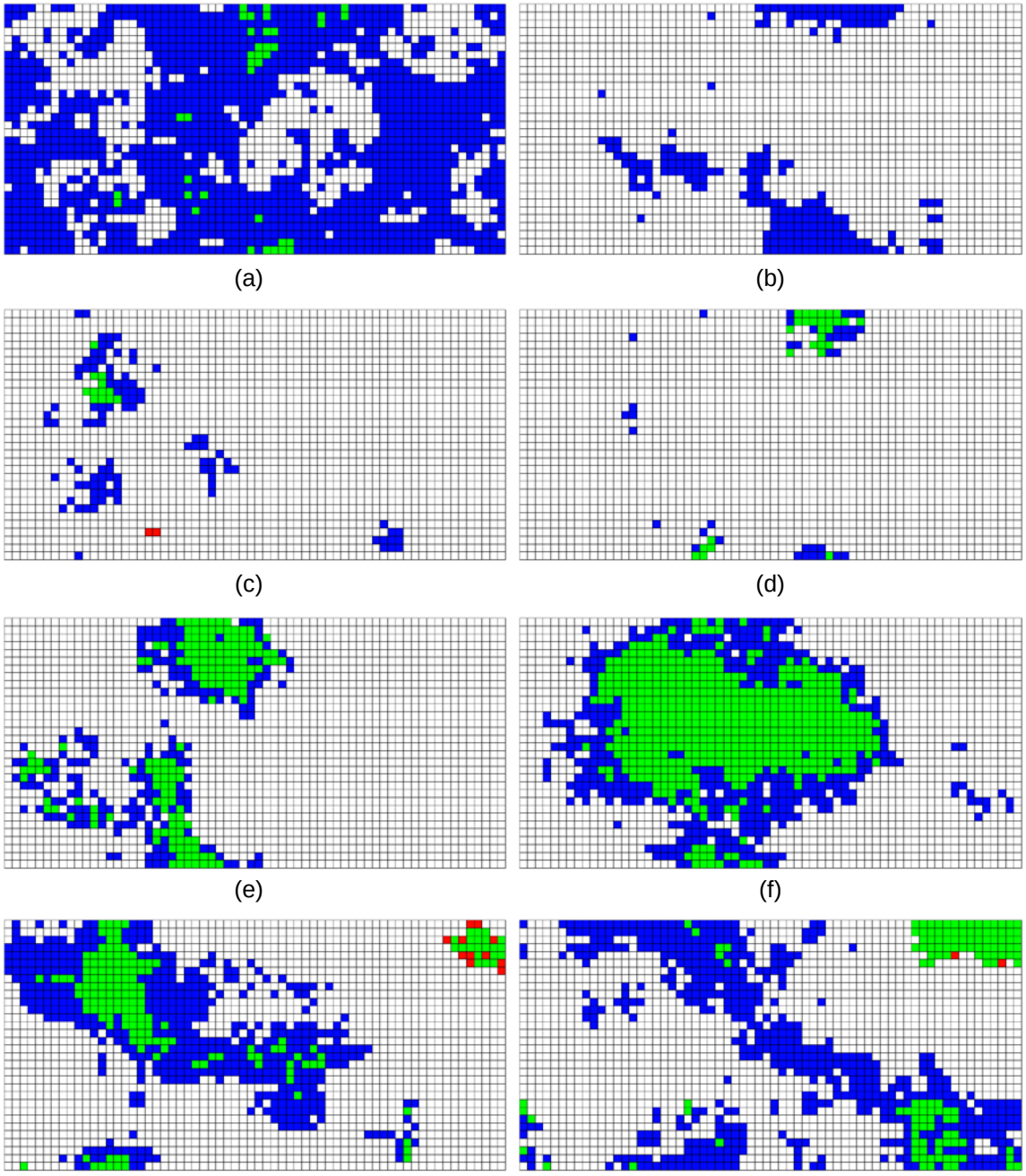

Figure 85: Top areal view of the local capillary trap for 3D geologic model of Figure 76 predicted by geological method (using $P_{c,entry}^{crit}$ = 8.3 kPa) and by the simulation results. (a) through (h) show layers 13 through 20, respectively. Red is simulation result only, blue is geological result only, and green is common in both methods.

Table 12: Local Capillary Trapping Capacity (Percentage of Total Number of Grid Blocks) for 3D Domain in Figure 76 Using Simulation Method and Geological Method, and the Common Capacity Predicted by Both Methods Using Different Critical Entry Pressure Values for Geological Method.

	$P_{c,entry}^{crit}$, kPa				
	5.5	6.2	6.9	7.6	8.3
Simulation Method	3.2 %	3.2 %	3.2 %	3.2 %	3.2 %
Geological Method	5.5 %	8.1 %	10.8 %	13.8 %	17.1 %
Common in Both Methods	2.5 %	2.8 %	3 %	3.1 %	3.1 %

Summary of Algorithm for Estimating Volume of Local Traps

The results of four cases considered in this section are summarized in following figures. Figure 86 and Figure 87 show the evolution of the local capillary trapping volume with critical entry pressure for 2D cases and 3D cases, respectively. The critical entry pressure is normalized by mean, μ, and standard deviation, σ, of the capillary entry pressure field to show the normalized distance to the mean as

$$P_{c,entry}^{Cr\ *} = \frac{P_{c,entry}^{\mathrm{Cr}} - \mu}{\sigma} \tag{21}$$

The figures show that there is a threshold value for critical entry pressure in which a step change occurs in volume of local capillary traps. This suggests a behavior similar to that seen in percolation theory. The arrows on the plots show the value of critical entry pressure that leads to detection of local capillary traps in the simulation results and the color of the arrows matches the color of the plots. In all cases, the value of critical entry pressure that leads to detection of local capillary traps is less than this threshold value.

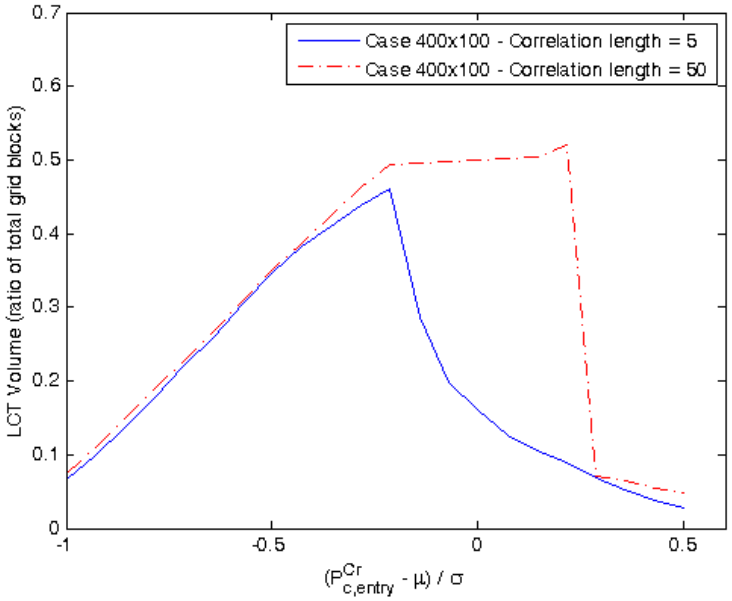

Figure 86: Evolution of the local capillary trapping volume with normalized critical capillary entry pressure for 2D cases in Figure 16 and Figure 42.

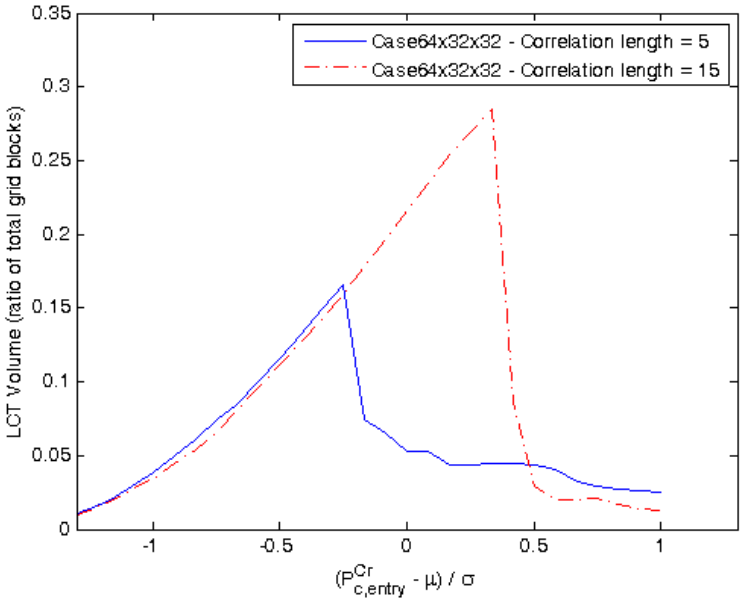

Figure 87: Evolution of the local capillary trapping volume with normalized critical capillary entry pressure for 3D cases in Figure 66 and Figure 76.

This type of graph can help us in determination of the limiting bounds for local capillary trapping. We use the geologic method (which is a very fast method compared to flow simulation) to generate a plot of the volume of local capillary traps versus critical entry pressure. The maximum value of the curve which is read at the threshold critical entry pressure is an upper bound for local capillary trapping in this domain. Values of critical entry pressure smaller than the threshold value should be selected based on the operational conditions to give a better estimate of the local capillary trapping volume in the domain.

Comparison of Run Times

As discussed in previous sections, using the geological method in predicting post-injection behavior of CO_2 in heterogeneous formations and finding the local capillary traps may not lead to precise results as developed by flow simulators. However, this method provides a fast technique for finding approximate behavior at initial stages of the CO_2 storage project. The speed of this method is several orders of magnitude faster than flow simulations. Table 13 shows the run time (CPU seconds used) for running the four cases considered in this section using a 3 GHz processor. The flow simulation run times are given for running the cases for 25 years of post-injection time. As can be seen in the results, the geological method is 3 to 5 order of magnitude faster than the flow simulation. Given the fairly accurate (but acceptable) results predicted by geologic method, its huge speed advantage makes it the better choice for an appropriate method of finding the estimated behavior of the CO_2 after the injection.

Table 13: CPU Seconds Used for Finding Local Capillary Trapping Capacity for Different Cases Studied in This Section Using Simulation Method and Geological Method

	2D		3D	
	1.5 m	15 m	1.5 m	4.6 m
Simulation Method	95,000	87,000	456,000	401,000
Geological Method	97	3	2	1

3.1.3 Geologic Controls on Potential Trapping Structures

Effect of Critical Capillary Entry Pressure

In this section, we perform simulations using geological method. We set up several cases by varying the critical capillary entry pressure. The base case dimensions are 78 m × 78 m × 9.8 m with grid block size of 0.3 m × 0.3 m × 0.3 m. This is populated with a correlated field which has 15 m correlation length in x-direction and y-direction, but uncorrelated (range 0.3 m) in vertical direction. Capillary entry pressure field is lognormally distributed and has mean value of 8.3 kPa with standard deviation of 4.1 kPa. We use critical entry pressures as low as one and a half standard deviation below the mean value up to the mean value, including 2.1, 2.8, 3.4, 4.1, 5.5, and 8.3 kPa.

We will show the results in two layers, which are layers 8 and 24 and located close to top and bottom of the domain, respectively. Figure 88 and Figure 89 show the effect of critical entry pressure on barrier map of the domain. As critical entry pressure increases, the number and size of barrier clusters decrease and more space becomes available for CO_2 vertical flow. This has two opposing effects on number of local capillary traps. On one hand, more non-barrier blocks become available as potential local capillary traps. This effect tends to increase the volume of local capillary traps. On the other hand, the number of barrier blocks decrease as potential structures that limit the upward movement of CO_2 (i.e., potential local capillary barriers.) This effect tends to decrease the volume of local capillary traps. At very low values of critical entry pressure, the majority of the grid blocks are acting as local capillary barriers and by a small increment in critical entry pressure value, the former effect becomes dominant, leading to an increase in the volume of local capillary traps. At higher values of critical entry pressure where the number of non-barrier blocks becomes comparable to barrier blocks, any increase in critical entry pressure causes the later effect to become dominant. In fact, more non-barrier blocks that already were trapped below barriers now become un-trapped than the previously barrier blocks that now turn into trapped non-barrier blocks. As a result, the volume of local capillary traps decrease. This behavior can be seen in Figure 90 and Figure 91. Table 14 and Figure 92 also quantify the volume of local capillary traps in the domain. As critical entry pressure increases from 2.1 to 4.1 kPa, the volume of local capillary trapping increases from 0.6% to 16.1% of the grid blocks. At $P_{c,entry}^{crit}$ = 4.1 kPa the volume of local capillary traps abruptly drops and as the critical entry pressure increases more, the volume of local capillary trapping decrease down to 0.5% at $P_{c,entry}^{crit}$ = 8.3 kPa.

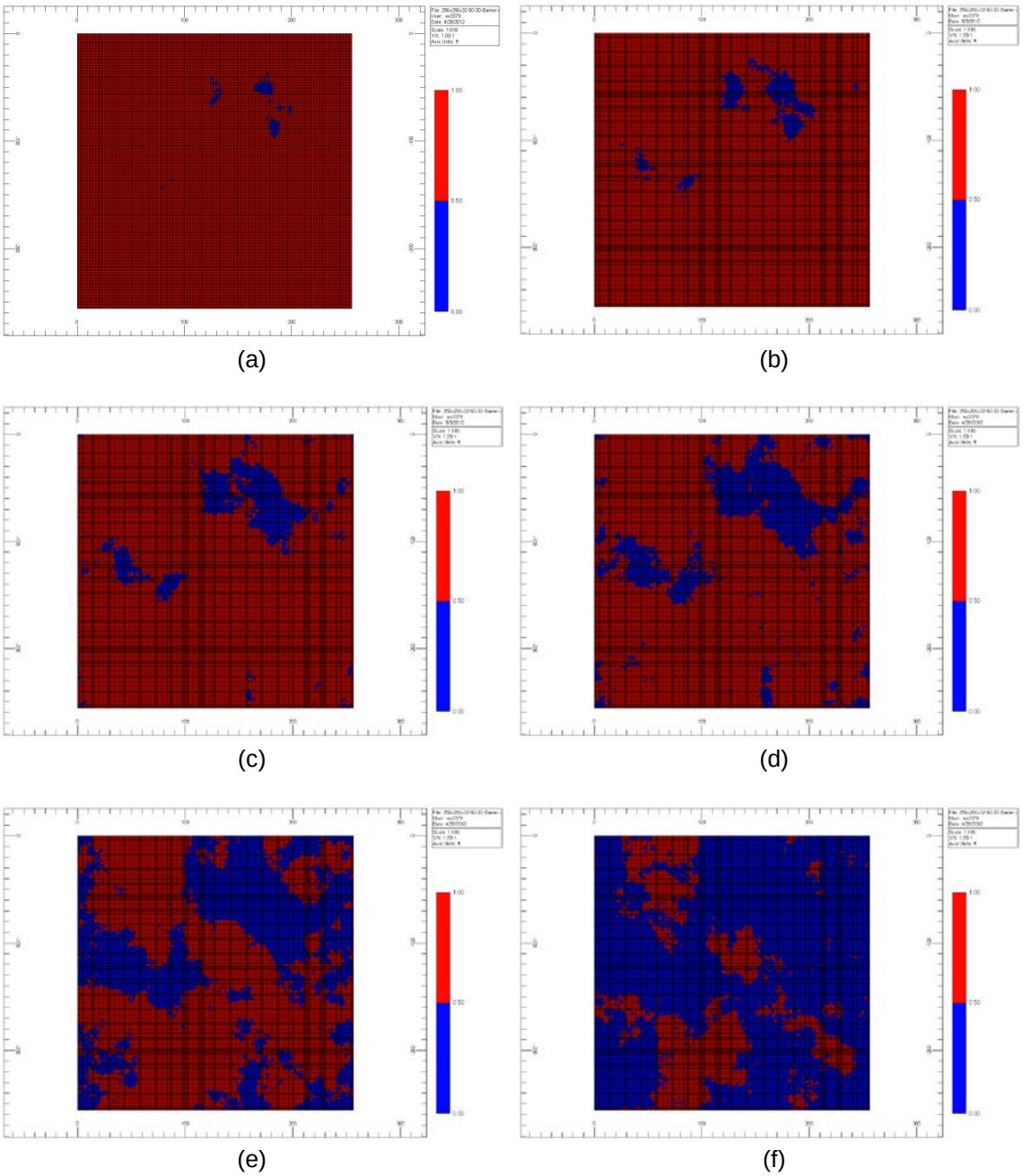

Figure 88: Top areal view of barrier map of the base case at layer 8 using critical entry pressure of (a) 2.1 kPa, (b) 2.8 kPa, (c) 3.4 kPa, (d) 4.1 kPa, (e) 5.5 kPa, and (f) 8.3 kPa.

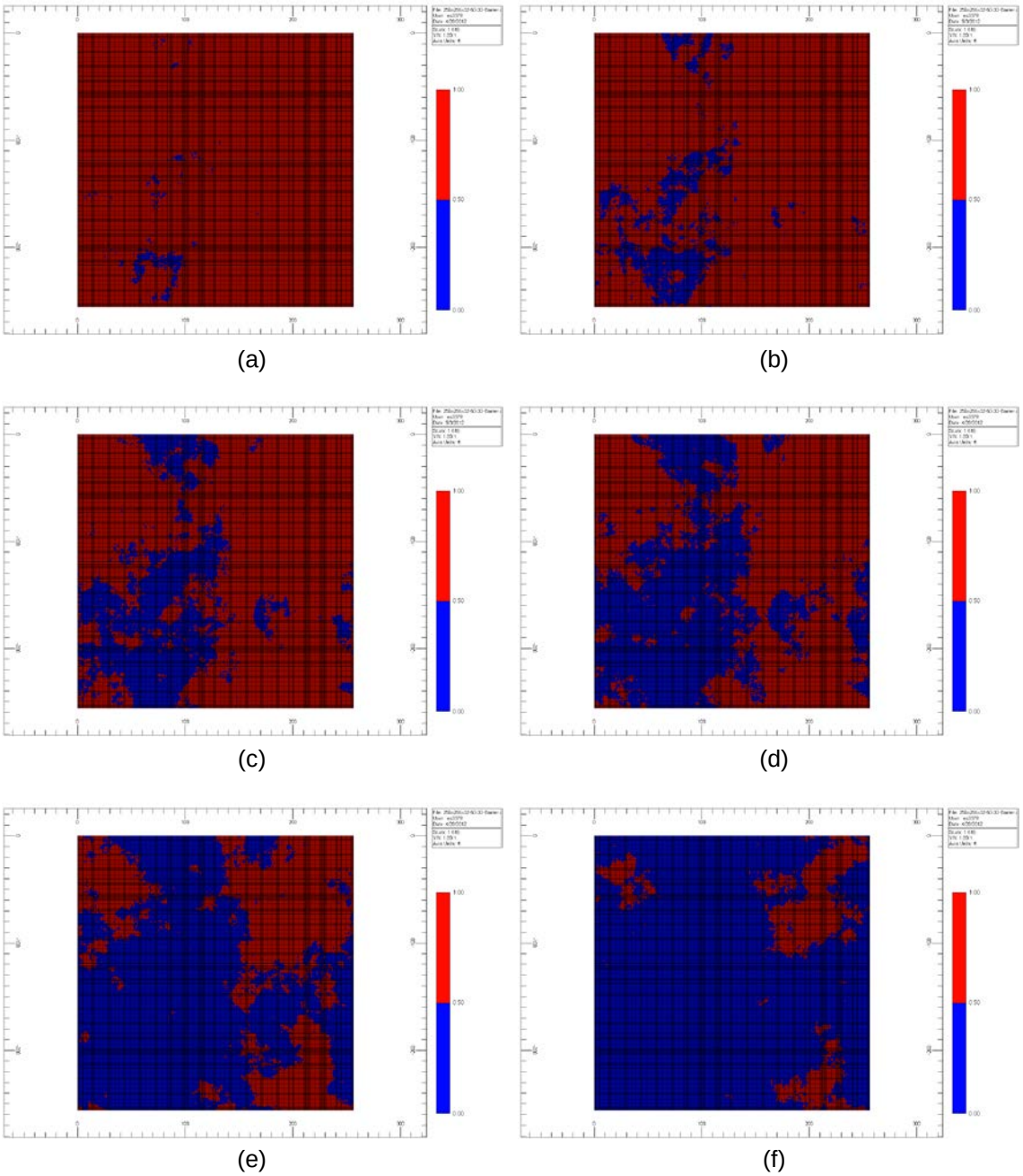

(a) (b) (c) (d) (e) (f)

Figure 89: Top areal view of barrier map of the base case at layer 24 using critical entry pressure of (a) 2.1 kPa, (b) 2.8 kPa, (c) 3.4 kPa, (d) 4.1 kPa, (e) 5.5 kPa, and (f) 8.3 kPa.

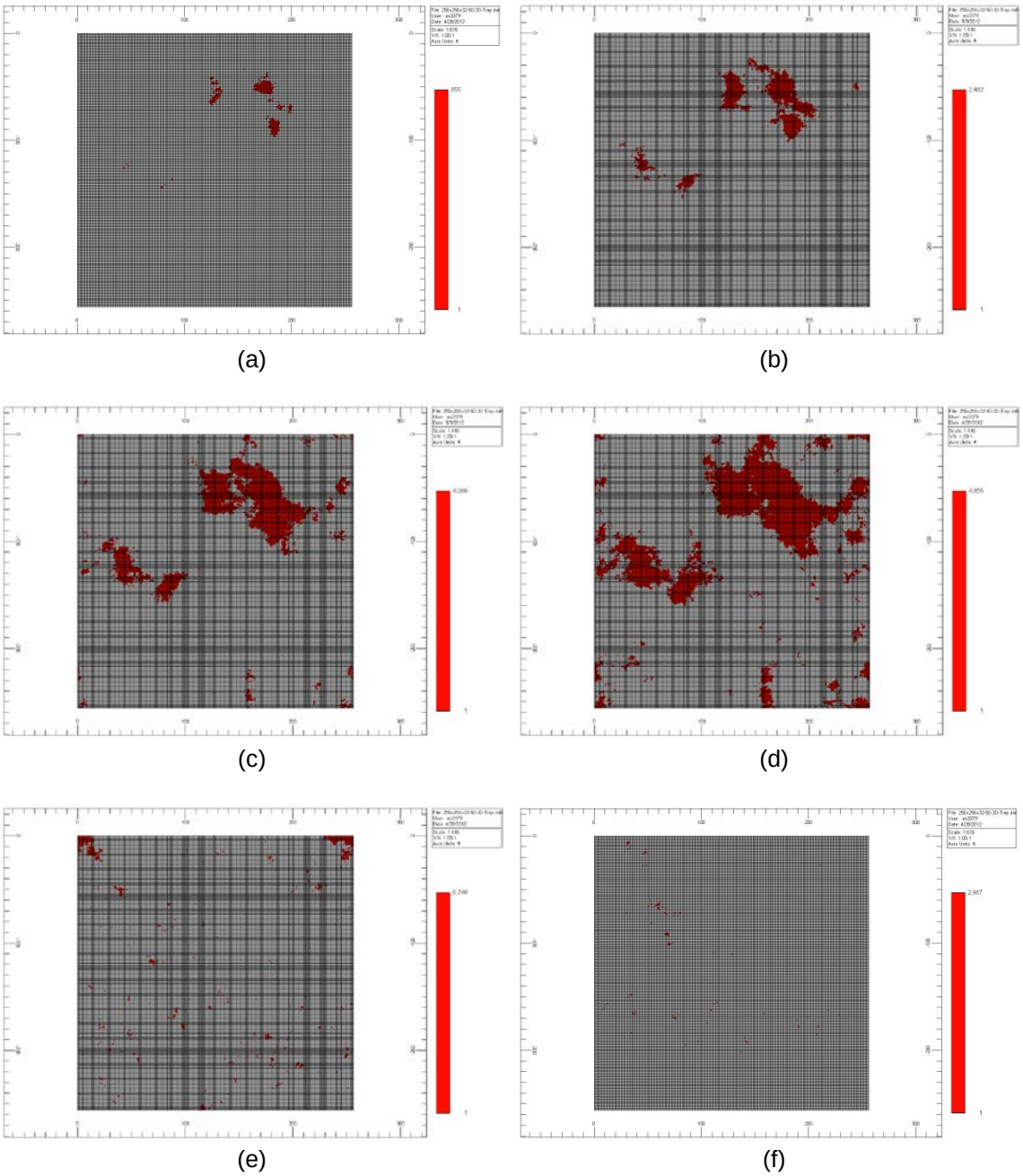

Figure 90: Top areal view of local capillary trap map of the base case at layer 8 using critical entry pressure of (a) 2.1 kPa, (b) 2.8 kPa, (c) 3.4 kPa, (d) 4.1 kPa, (e) 5.5 kPa, and (f) 8.3 kPa.

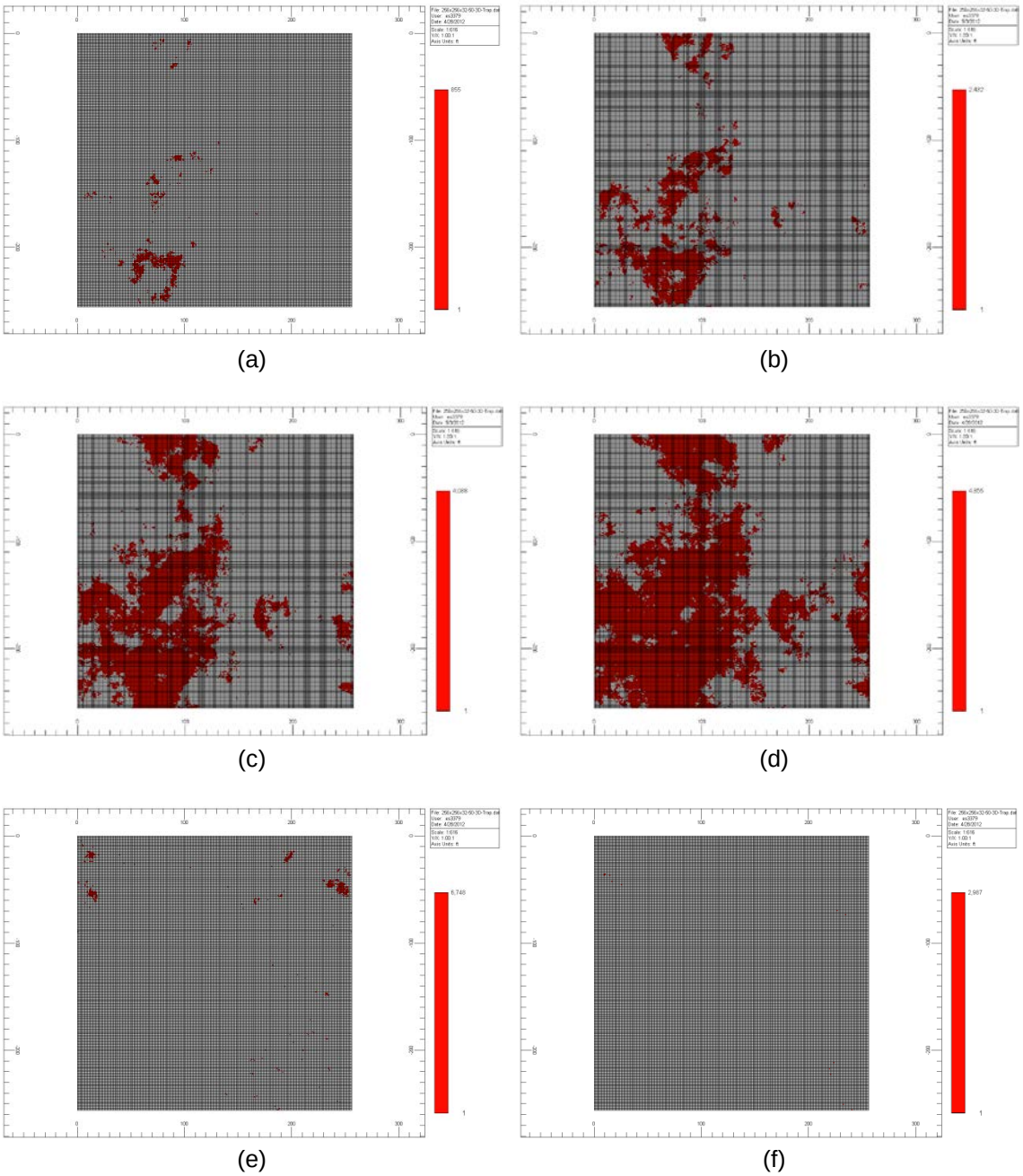

Figure 91: Top areal view of local capillary trap map of the base case at layer 24 using critical entry pressure of (a) 2.1 kPa, (b) 2.8 kPa, (c) 3.4 kPa, (d) 4.1 kPa, (e) 5.5 kPa, and (f) 8.3 kPa.

Table 14: Local Capillary Trapping Capacity (Percentage of Total Number of Grid Blocks) for Base Case Using Different Critical Entry Pressure Values for Geological Method

	$P_{c,entry}{}^{crit}$, kPa					
	2.1	2.8	3.4	4.1	5.5	8.3
Local capillary trapping capacity	0.6%	3%	8.3%	16.1%	2.8%	0.5%

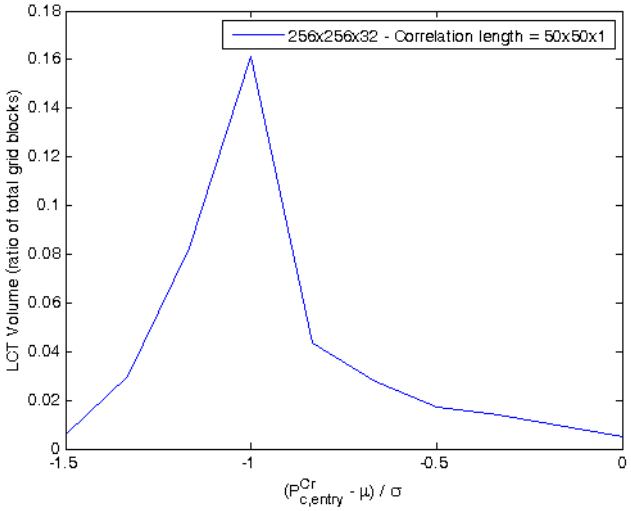

Figure 92: Evolution of the local capillary trapping volume with normalized critical capillary entry pressure for base case with 256×256×32 grid blocks.

Analogy to Percolation Theory

The behavior seen here is similar to behavior described by percolation theory, which is the formation of long-range connectivity in random systems. Percolation theory describes the behavior of connected clusters in a random graph where a cluster can be occupied with probability *p* or remain empty with probability 1-*p*. According to this theory, the probability of an open path from the top to the bottom of the graph increases sharply from very close to zero to very close to one in a short span of values of *p*. That sharp change occurs at a critical probability which is called percolation threshold. In our problem of local capillary trapping, non-barrier and barrier blocks represent the occupied and empty sites, respectively. The critical capillary entry pressure is in fact determining the occupation probability. If critical entry pressure is small (i.e., smaller than the percolation threshold) then a small portion of the sites are occupied (i.e., non-barrier blocks) and we see that occupied sites tend to group into many small clusters of various shapes and sizes. As critical entry pressure increases, many of the occupied sites are nested and increase in size. At some probability, many of the sites become joined into one giant cluster that spans the entire array vertically. The probability at which this happens is called percolation threshold.

The role of percolation theory in determining the amount of local capillary trapping is shown in Figure 93. The x-axis is the critical capillary entry pressure (the value used to define a barrier in the algorithm) in dimensionless form, where μ is the mean and σ is the variance in the distribution of capillary entry pressures in the domain. The y-axis is the fraction of grid blocks in the domain which correspond to local capillary traps. In each pair of inset images, the upper image shows the capillary barriers (red pixels) and the pore space open to flow (blue pixels); the lower image shows the traps (red pixels) beneath the barriers. The images are for illustration; the data for the blue curve are for a 3D domain of two million cells with a 50 cell correlation length in the lateral directions.

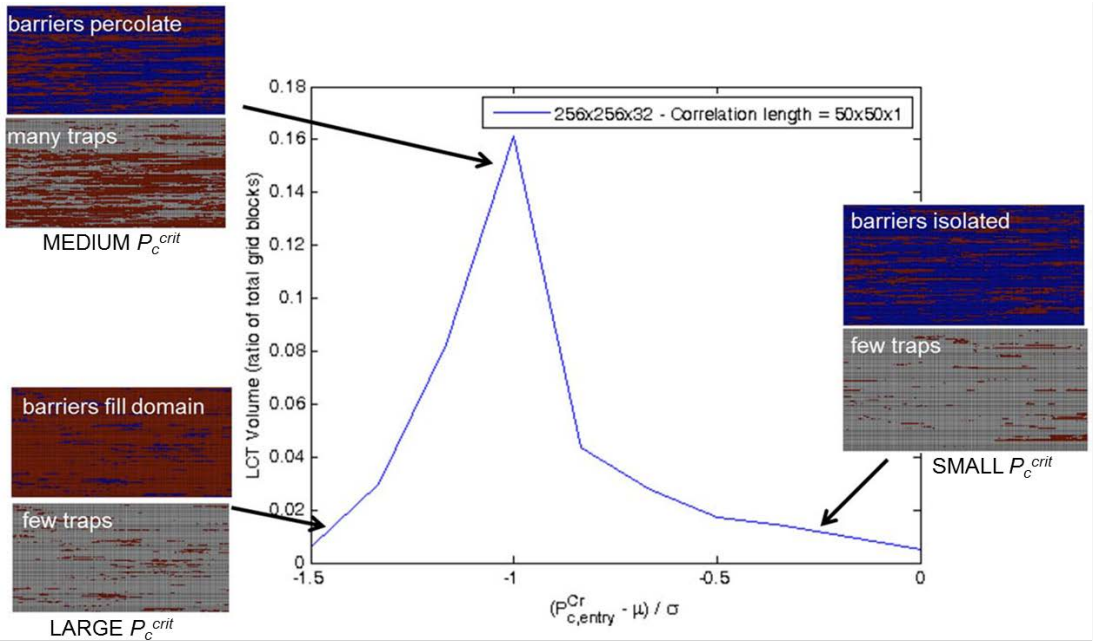

Figure 93: Critical capillary entry pressure strongly influences potential trapping volume due to percolation thresholds. At small values of $P_{c,entry}^{crit}$, almost all regions in the domain are barriers, and consequently few traps exist. At the other extreme of large $P_{c,entry}^{crit}$, almost none of the domain acts a barrier, and consequently few traps exist. At intermediate $P_{c,entry}^{crit}$, the barriers begin to percolate, creating the maximum volume of traps.

At small values of critical capillary entry pressure, most of the domain acts as a barrier to the rising CO_2. There are few traps simply because there are few non-barrier cells. As the critical capillary entry pressure increases, the number of cells through which CO_2 can rise increases, and the fraction of the domain acting as a barrier decreases. The number of potential traps correspondingly increases. At a threshold value of critical capillary entry pressure, the barriers percolate through the domain. Here "percolation" connotes the concept that at larger values of critical capillary entry pressure, the barrier clusters become less connected. At smaller values of critical capillary entry pressure, the barrier clusters are connected across much of the domain. In effect, crossing this threshold creates holes within barriers, and consequently the number of traps decreases rapidly. At large values of critical capillary entry pressure, only a small fraction of the cells in the domain act as barriers. These cells can form only small clusters, and consequently very little of domain can be a local capillary trap.

The occurrence of a clear maximum in the volume of local capillary traps is characteristic of all the domains examined with the algorithm. The qualitative connection to percolation theory described in preceding paragraph can be made quantitative. For a 2D domain with an uncorrelated capillary entry pressure field, the maximum fraction of local capillary traps occurs at a dimensionless critical capillary entry pressure of -0.1. At this value, the cumulative probability distribution function for the capillary entry pressure field is 0.58. This is quite close to the 2D square lattice site percolation threshold of 0.59. Similarly in an uncorrelated 3D domain, the cumulative probability function for the capillary entry pressure field was 0.29 at the value of critical capillary entry pressure that gave maximum fraction of traps. The corresponding 3D cubic lattice site percolation threshold is 0.31. We conclude that percolation theory is a good foundation for explaining two key factors: i) the existence of a maximum possible amount of

local capillary trapping in any domain and ii) the influence of measures of heterogeneity (correlation length, variance) on potential local capillary trapping.

To verify this analogy, we have set up a series of 2D and 3D simulations with different domain sizes and various correlation lengths. Capillary entry pressure field is lognormally distributed and has mean value of 14.5 kPa with standard deviation of 9.7 kPa. We use critical entry pressures as low as one standard deviation below the mean value (i.e., 4.8 kPa) up to one and a half (1.5) standard deviation above the mean (i.e., 29 kPa). All the models have aspect ratio of one.

For 2D simulations, the case dimensions are 4.9 m × 4.9 m, 9.8 m × 9.8 m, 19.5 m × 19.5 m, 39 m × 39 m, 78 m × 78 m, and 156 m × 156 m, all with grid block size of 0.3 m × 0.3 m. The largest domain is populated with various correlated fields which have 0.3 m (i.e., uncorrelated), 1.5 m, 3 m, 7.6 m, 15 m, and 30 m correlation length in x-direction, but uncorrelated in vertical direction. The smaller domains are populated with correlation lengths less than half of their lateral size (e.g., 9.8 m× 9.8 m domain with correlation lengths of 0.3, 1.5, and 3 m).

For 3D simulations, the case dimensions are 4.9 m × 4.9 m × 4.9 m, 9.8 m × 9.8 m × 9.8 m, 19.5 m × 19.5 m × 19.5 m, and 39 m × 39 m × 39 m, all with grid block size of 0.3 m × 0.3 m × 0.3 m. The largest domain (with size 128^3) is populated with various correlated fields which have 0.3 m (i.e., uncorrelated), 1.5 m, 3 m, 7.6 m, and 15 m correlation length in both x- and y-direction, but uncorrelated in vertical direction. As in 2D cases, the smaller domains are populated with correlation lengths less than half of their lateral size (e.g., 19.5 m × 19.5 m × 19.5 m domain with correlation lengths of 0.3 m, 1.5 m, 3 m, and 7.6 m).

Figure 94 through Figure 99 show the volume of local capillary traps for 2D cases as a function of critical entry pressure which is shown as a normalized distance from the mean entry pressure on the x-axis. Figure 100 through Figure 103 show the same for 3D cases. All the cases confirm the existence of a percolation threshold where the volume of traps suddenly drops from a maximum value. In 2D cases with uncorrelated entry pressure field, i.e., the blue curves with correlation length of 0.3 m, the percolation occurs near the normalized distance of around -0.1. Using the lognormal CDF, we can find that this point belongs to cumulative distribution of 0.575. This value is, in fact, very close to the site percolation threshold for a 2D square lattice which is approximately 0.593 (Newman and Ziff, 2000). In 3D cases with uncorrelated entry pressure field (i.e., the blue curves) the percolation occurs near the normalized distance of around -0.6. Again, the lognormal CDF gives a cumulative distribution of 0.286 for this point. This value is also close to the site percolation threshold for a 3D simple cubic lattice which is approximately 0.311 (Harter, 2005). As the correlation length of the entry pressure field increases, the percolation threshold also increases. This is probably due to the finite size of the domain. We will study the effect of correlation length in more details in a subsequent section. It can be seen that with increase in the size of the domain, the cases with smaller correlation lengths act more like the uncorrelated field and have a percolation threshold closer to that of uncorrelated field.

Since the maximum theoretical local capillary trapping volume occurs at critical entry pressure closely smaller than the percolation threshold, then from the practical point of view we are

interested to know the percolation threshold for a domain so that we know the upper bound for the local capillary trapping volume.

We should note that there are a few differences between the geologic method and percolation theory. A substantial difference is that in percolation theory, the emphasis is on the randomness of the medium, while in geologic method the assignment of entry pressures to grid blocks is not purely random and involves a covariance function (correlation length). In other words, the capillary entry pressure field is a correlated field.

One other difference is that while percolation theory is interested in occupied sites and the percolating cluster, we do not take into account any non-barrier block (i.e., occupied site) that is connected to the top of the domain (even if it not connected to the bottom) as it cannot trap the gas. Also above the percolation threshold, we are not interested in the occupied sites of the percolating cluster anymore because we are looking for local capillary traps and hence, we want to extract that part of the percolating cluster that is surrounded from top and sides by barrier blocks. Therefore, not all the theory, mathematical aspects, and analysis of the percolation theory is applicable to our problem.

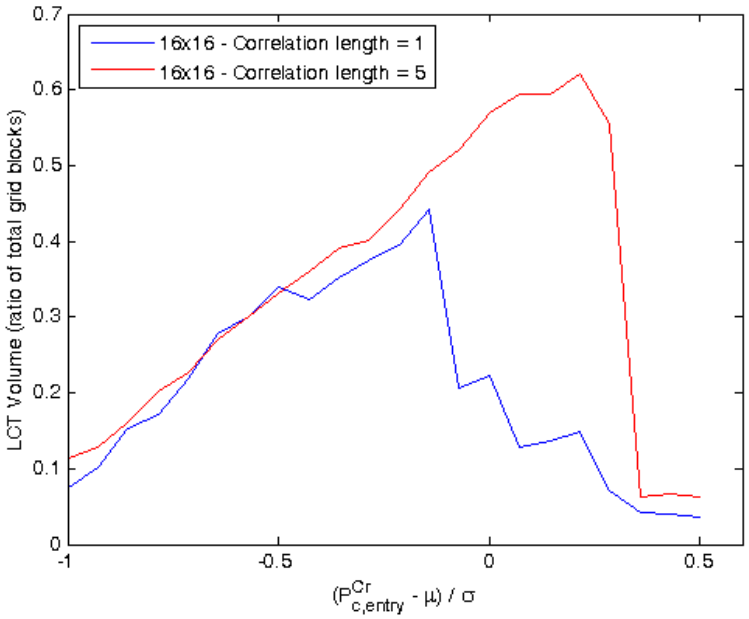

Figure 94: Evolution of the local capillary trapping volume with normalized critical capillary entry pressure for 2D case with 16×16 grid blocks.

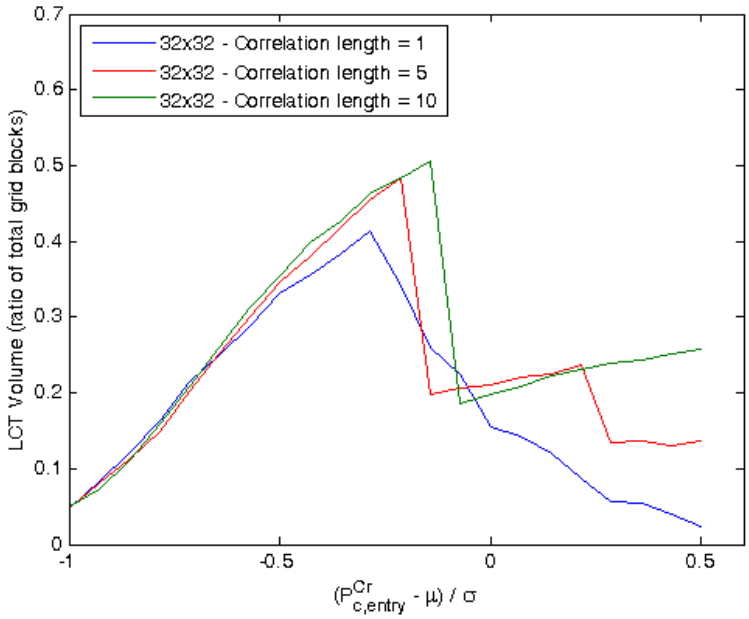

Figure 95: Evolution of the local capillary trapping volume with normalized critical capillary entry pressure for 2D case with 32×32 grid blocks.

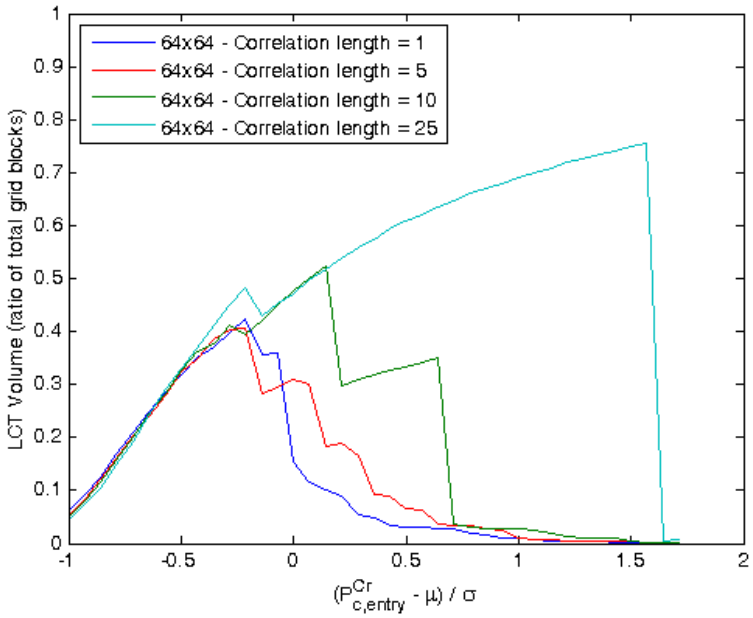

Figure 96: Evolution of the local capillary trapping volume with normalized critical capillary entry pressure for 2D case with 64×64 grid blocks.

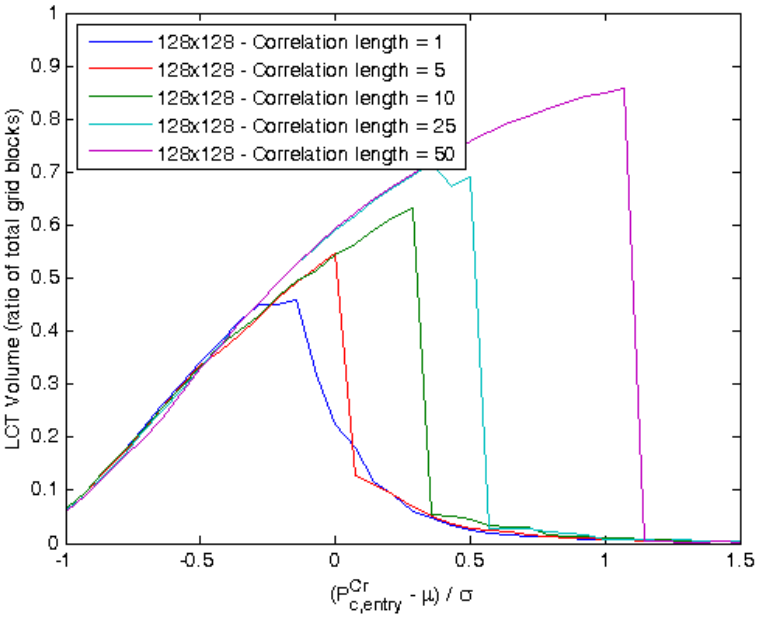

Figure 97: Evolution of the local capillary trapping volume with normalized critical capillary entry pressure for 2D case with 128×128 grid blocks.

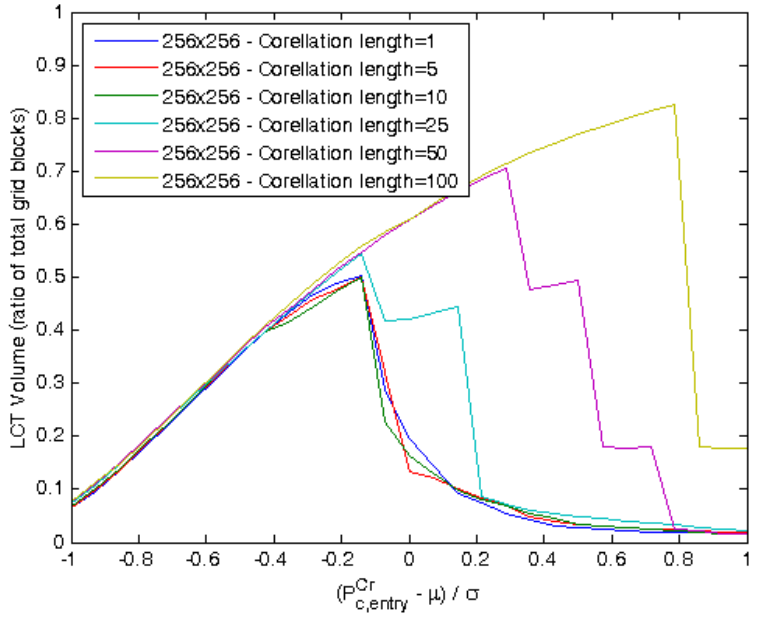

Figure 98:Evolution of the local capillary trapping volume with normalized critical capillary entry pressure for 2D case with 256×256 grid blocks.

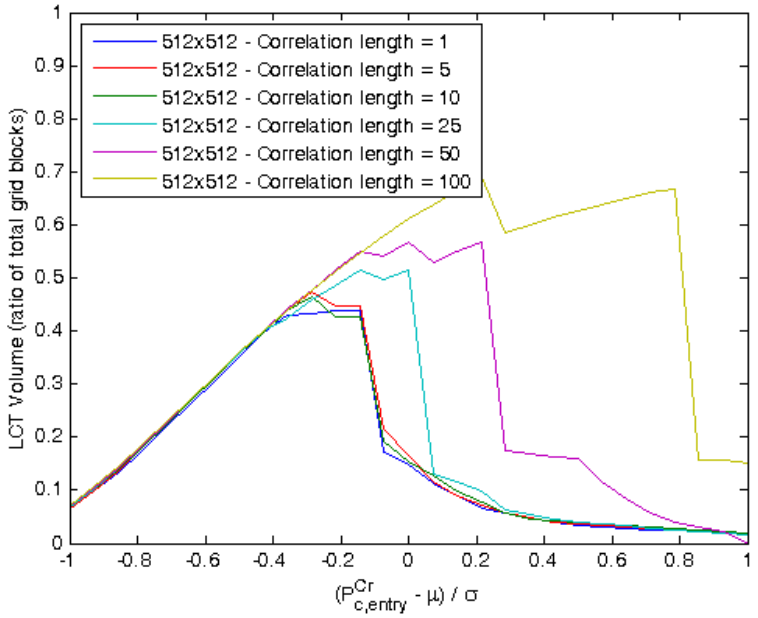

Figure 99:Evolution of the local capillary trapping volume with normalized critical capillary entry pressure for 2D case with 512×512 grid blocks.

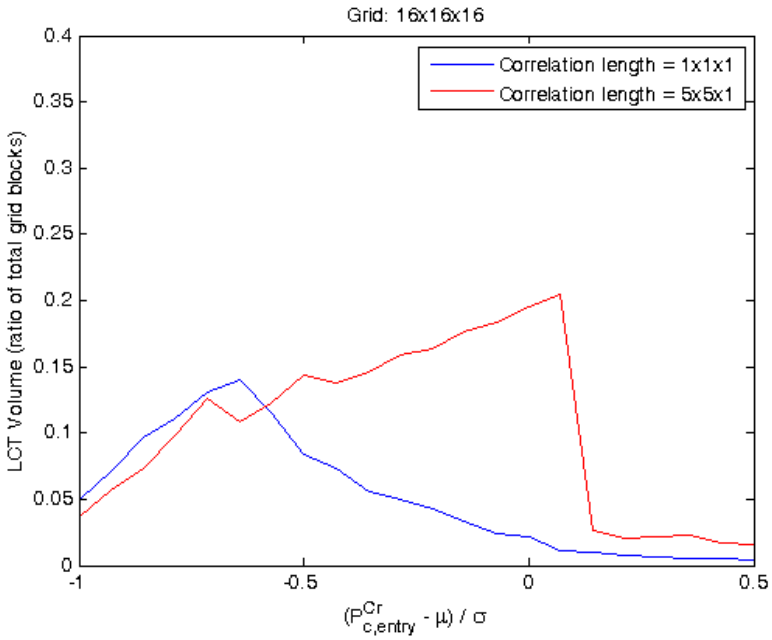

Figure 100: Evolution of the local capillary trapping volume with normalized critical capillary entry pressure for 3D case with 16×16×16 grid blocks.

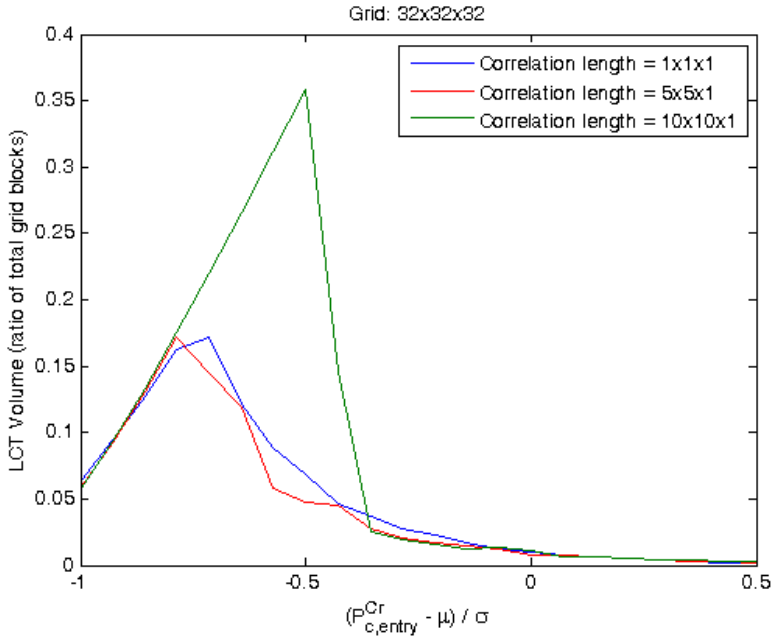

Figure 101: Evolution of the local capillary trapping volume with normalized critical capillary entry pressure for 3D case with 32×32×32 grid blocks.

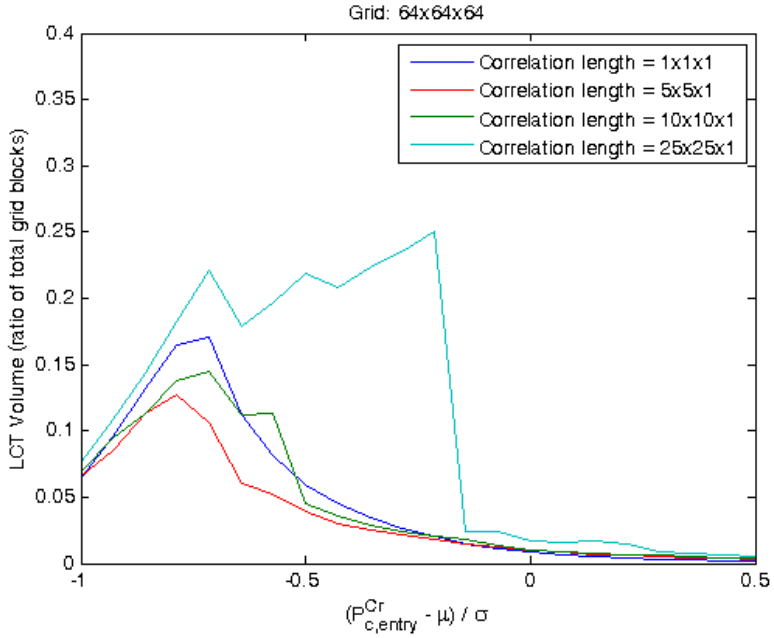

Figure 102: Evolution of the local capillary trapping volume with normalized critical capillary entry pressure for 3D case with 64×64×64 grid blocks.

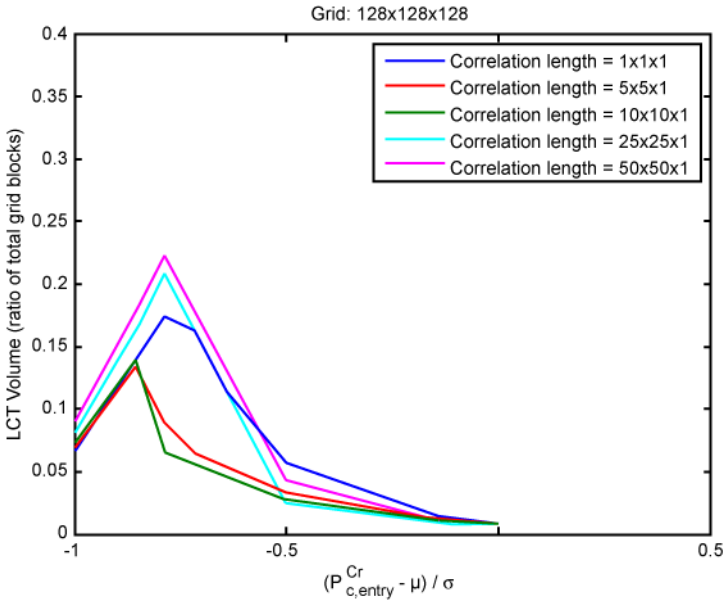

Figure 103: Evolution of the local capillary trapping volume with normalized critical capillary entry pressure for 3D case with 128×128×128 grid blocks.

Size Distribution of Traps[6]

Figure 104 shows the distribution of the size of traps for different values of critical entry pressure. We can see that using any value of critical entry pressure the size of the majority of the local capillary traps is very small (less than 10 blocks). This behavior (which is sometimes expressed more simply as the Pareto principle or the "80-20 rule") can be modeled by Generalized Pareto (GP) distribution. The GP is a right-skewed distribution, parameterized with a shape parameter, k, and a scale parameter, σ. The GP distribution is defined and discussed in more details in Appendix. We will fit the distribution to local capillary trap size data using maximum likelihood. To visually assess how good the fit is, we plot a cumulative distribution function of the data, overlaid with the distribution function of the GP that we have estimated, Figure 105. The plots show a very good fit between the results. To quantify the precision of the estimates, we use standard errors computed from the asymptotic covariance matrix of the maximum likelihood estimators. Table 15 shows the standard errors. These standard errors indicate high precision of the estimate for both parameters.

Figure 104 also gives the average size of the local capillary traps and their standard deviation. While using larger values of critical entry pressure (greater than 0.6) leads to average size of smaller than 10 blocks, a small value of critical entry pressure may lead to a larger average size for local capillary traps. The reason is that with a value of critical entry pressure smaller than the percolation threshold, the non-barrier blocks join each other without connecting to the top boundary (i.e., the whole non-barrier cluster is still surrounded from top and sides by barrier blocks) and hence, a few local capillary traps will appear that are very large (several thousand

[6] This section constitutes Project Deliverable 2.4.2 Histograms of sizes of potential local capillary traps and Project Deliverable 2.4.3 Histograms of potential local capillary trap volumes, analysis of volume fraction held in such traps as function of primary geologic, petrophysical controls

blocks). The large value of standard deviation in the case of $P_{c,entry}^{crit}$ = 4.1 kPa verifies this behavior. Note that the maximum value on the x-axis shows the size of the largest local capillary trapping cluster in the domain.

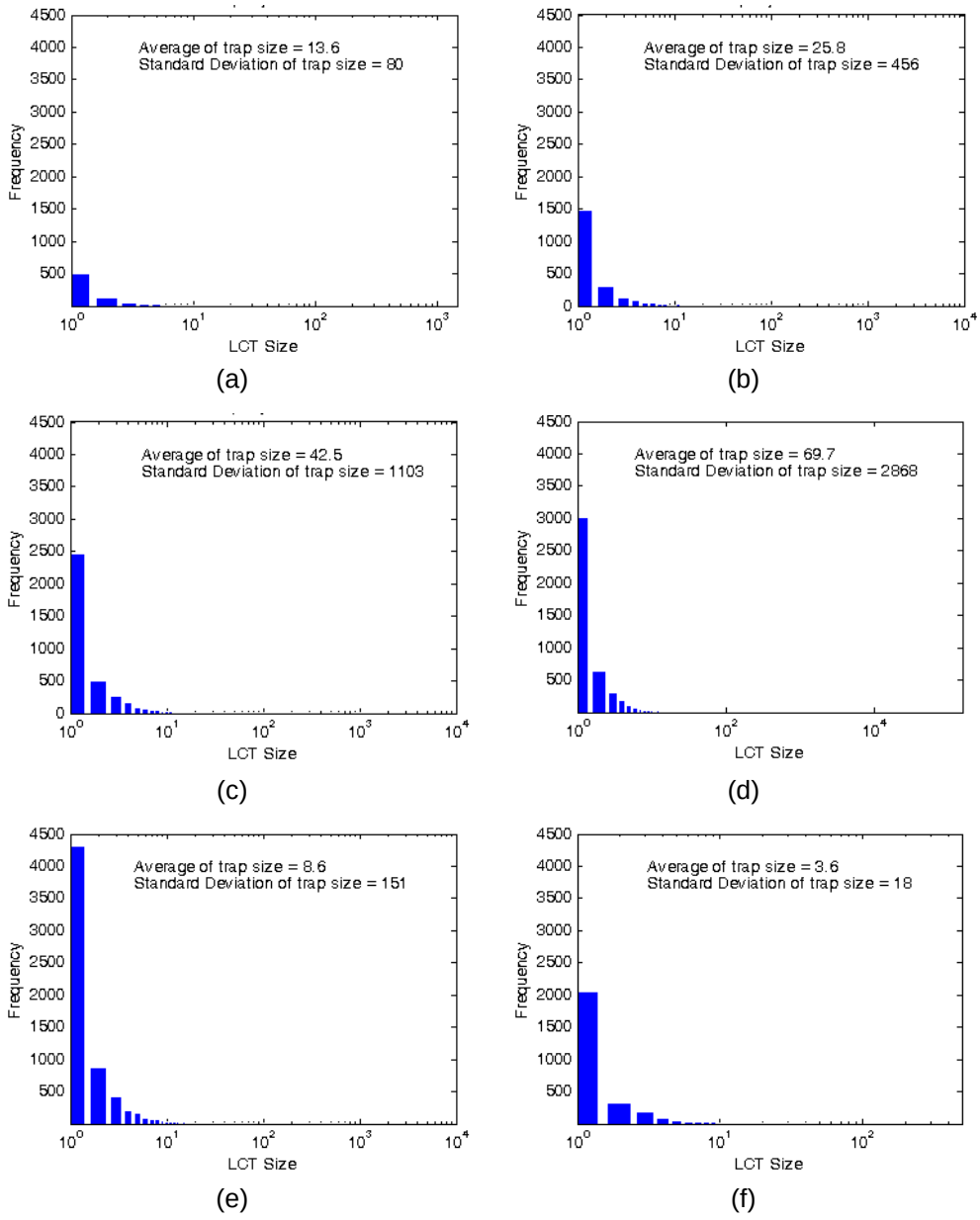

Figure 104: Histogram of size of local capillary traps of the base case using critical entry pressure of (a) 2.1 kPa, (b) 2.8 kPa, (c) 3.4 kPa, (d) 4.1 kPa, (e) 5.5 kPa, and (f) 8.3 kPa.

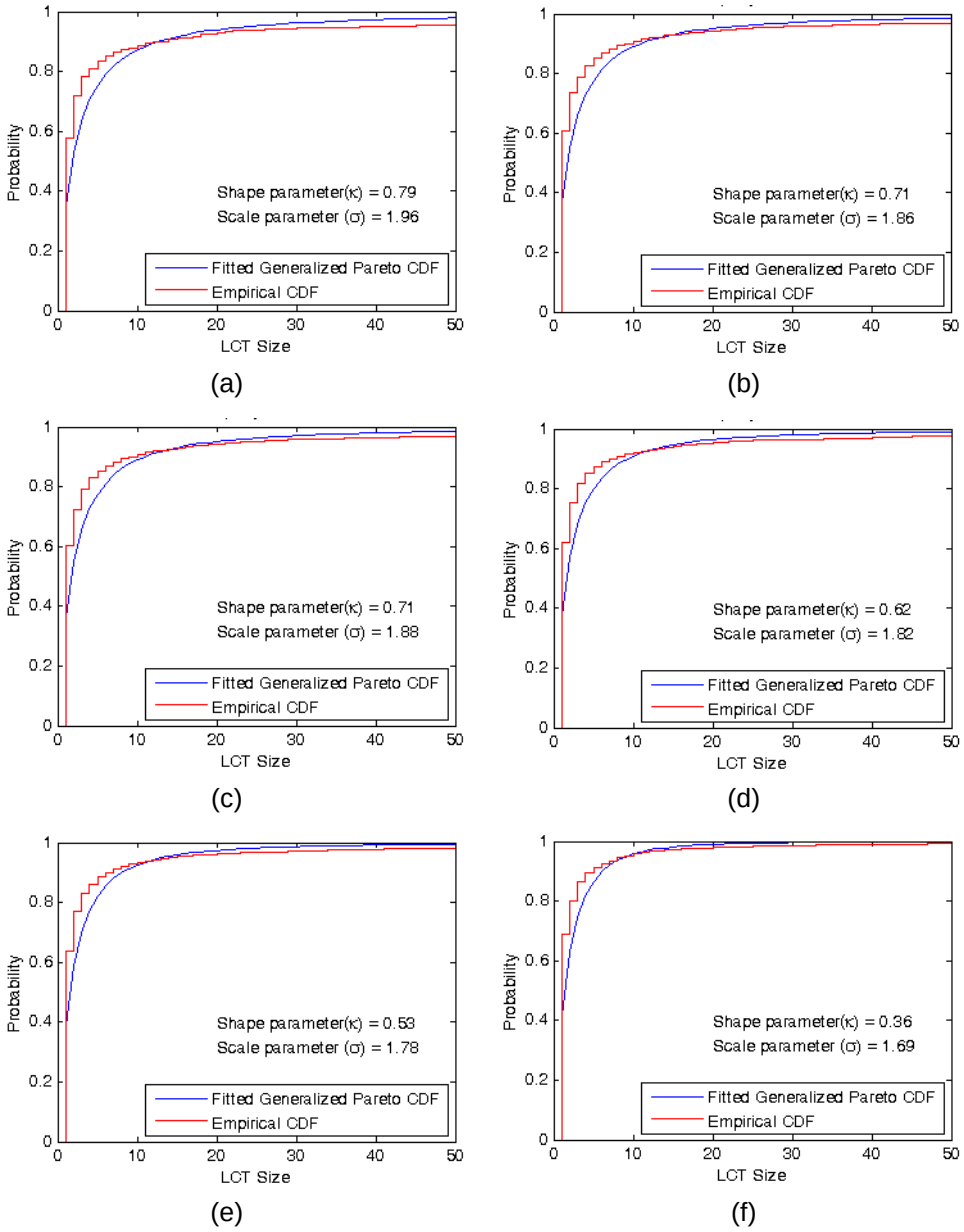

Figure 105: Comparison of the empirical and fitted Generalized Pareto CDF for size of local capillary traps of the base case using critical entry pressure of (a) 2.1 kPa, (b) 2.8 kPa, (c) 3.4 kPa, (d) 4.1 kPa, (e) 5.5 kPa, and (f) 8.3 kPa.

Table 15: Standard Errors for the Parameter Estimates Resulted from Fitting a GP Distribution to Local Capillary Trap Size Data for Different Critical Entry Pressure Values

	$P_{c,entry}^{crit}$, kPa					
	2.1	2.8	3.4	4.1	5.5	8.3
Standard error for k	0.0486	0.0270	0.0208	0.0176	0.0139	0.0175
Standard error for σ	0.1038	0.0569	0.0443	0.0379	0.0308	0.0413

Effect of Horizontal Correlation Length

We continue with the base case (78 m × 78 m × 78 m with grid block size of 0.3 m × 0.3 m × 0.3 m) and study the effect of horizontal correlation length on local capillary traps. We set up several cases by varying the correlation length, ranging from 0.3 m (i.e., uncorrelated) to 30 m in x-direction and y-direction, but all cases are uncorrelated (range 0.3 m) in vertical direction. Capillary entry pressure field is lognormally distributed and has mean value of 8.3 kPa with standard deviation of 4.1 kPa. We use critical entry pressure of 2.8 kPa since it is located more than one standard deviation below the mean. As discussed in previous section, this value of critical entry pressure will give a local capillary trapping volume in the expected range of volumes from flow simulation.

Figure 106 and Figure 107 show the barrier map and local capillary trap map of different cases in layers 8 using $P_{c,entry}^{crit}$ = 2.8 kPa. In these figures, parts (a) through (f) have horizontal correlation length of 0.3, 1.5, 3.0, 7.6, 15, and 30 m, respectively. For the smaller correlation lengths, the local capillary traps are scattered inside the domain. As the correlation length increases, the local capillary traps become less dispersed and more lumped, therefore the number of the local capillary traps decrease while their lateral size tend to increase. This behavior can be seen in histogram of the size of local capillary traps in Figure 108. Each histogram shows the data of number of trap clusters and the mean and standard deviation of the trap size. We can see that for longer correlation length, the number of local capillary trap clusters decreases while the average size of clusters increases. The standard deviation of the size of clusters also increases which shows that the new sizes larger than the most frequent size of one will appear in the domain.

Figure 109 shows the local capillary trapping volume for different correlation lengths for the base case. Since the horizontal correlation length only changes the connectivity of similar grid blocks in horizontal direction and not in vertical direction, it should not have any effect on the percolation threshold. With changes in horizontal correlation length, the grid blocks will still need same amount of critical entry pressure to overcome enough capillary barriers and make a connected path through layers from bottom to the top. However, as discussed in previous section the horizontal correlation length seems to changes the percolation threshold for local capillary trapping volume. As we saw in Figure 100 through Figure 103 in a domain with finite size, increasing the correlation length will increase the percolation threshold of the domain. This happens especially when the correlation length becomes comparable with size of the domain. The reason is that with larger correlation lengths in a finite-size domain the connected batches of non-barrier blocks increase in size, but decrease in number and become less dispersed throughout the layer. Therefore, the probability that two local traps in two consecutive layers become connected to each other decreases. As a result, the percolation threshold needs to increase in order to make a percolating path throughout the whole layers. Nevertheless, if the size of the domain approaches infinity the correlation length becomes less effective. Figure 109 shows that for the large domain with lateral size of 78 × 78 m the correlation length does not affect the percolation threshold of the domain (cf. correlation lengths 0.3, 1.5, 3, and 7.6 m). Note that for correlation length of 30 m the percolation threshold starts to increase from its original value.

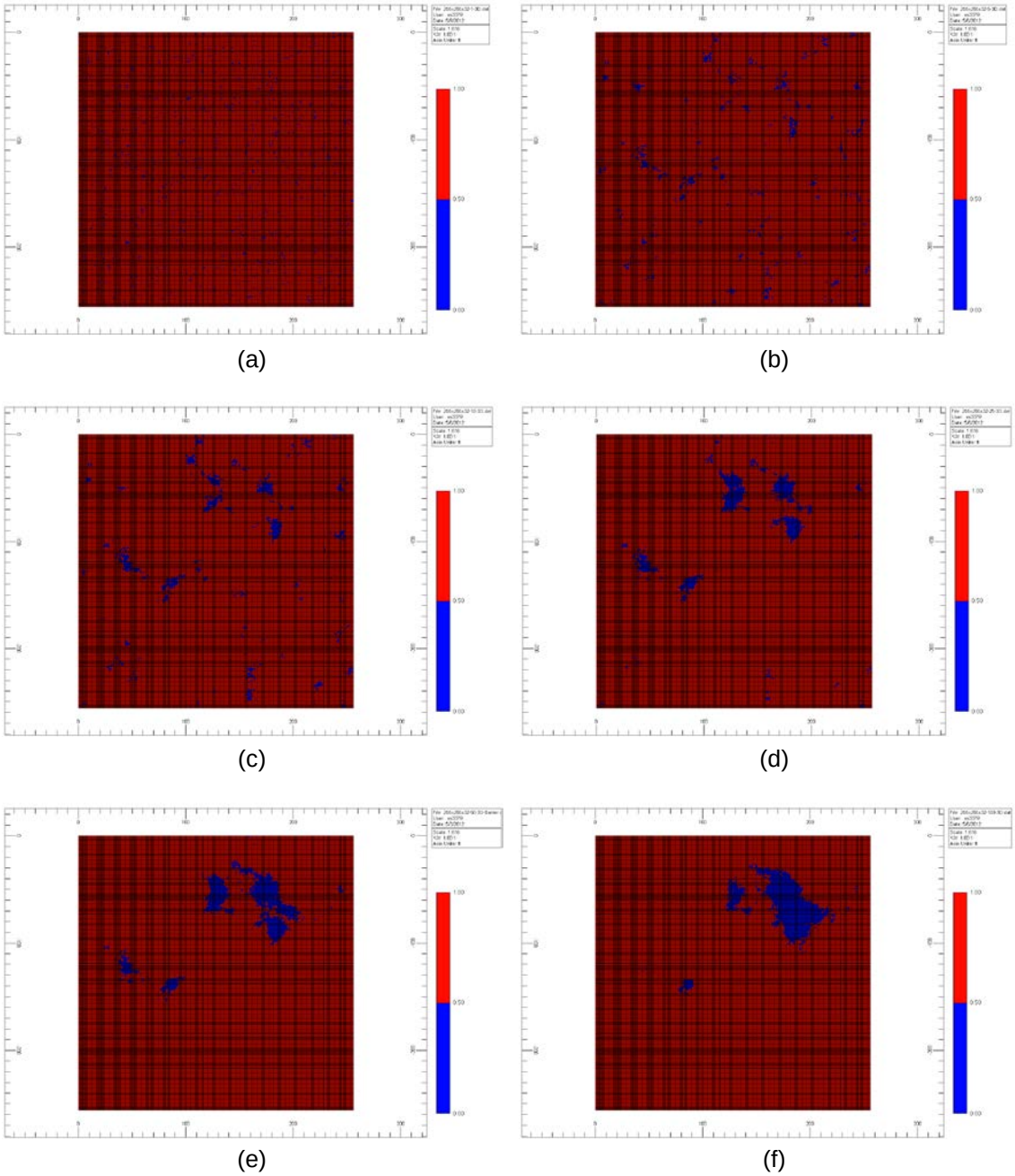

Figure 106: Top areal view of barrier map of the base case at layer 8 using critical entry pressure of 2.8 kPa. The horizontal correlation length is (a) 0.3 m, (b) 1.5 m, (c) 3.0 m, (d) 7.6 m, (e) 15 m, and (f) 30 m.

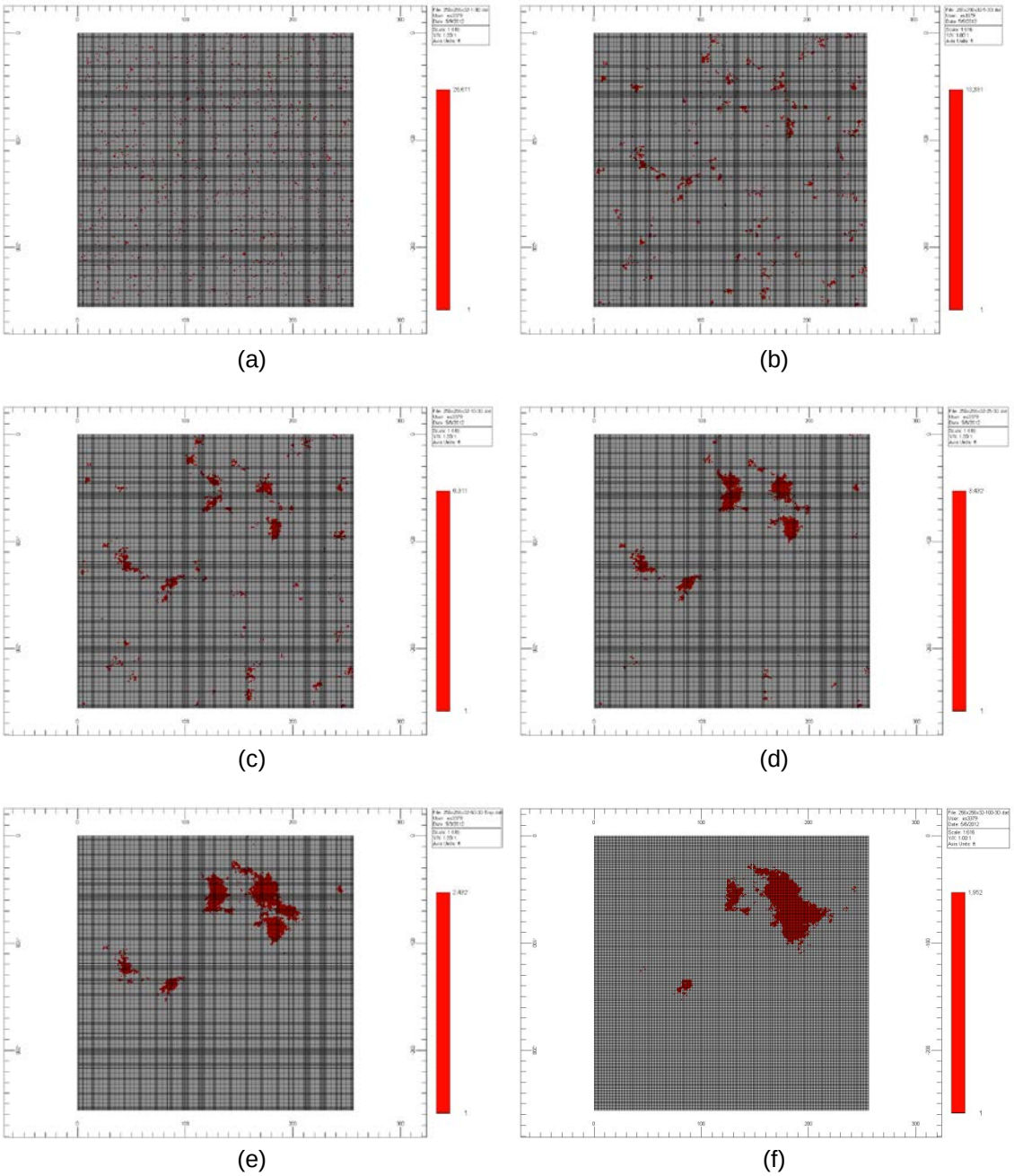

Figure 107: Top areal view of local capillary trap map of the base case at layer 8 using critical entry pressure of 0.4. The horizontal correlation length is (a) 0.3 m, (b) 1.5 m, (c) 3.0 m, (d) 21.5 m, (e) 15 m, and (f) 30 m.

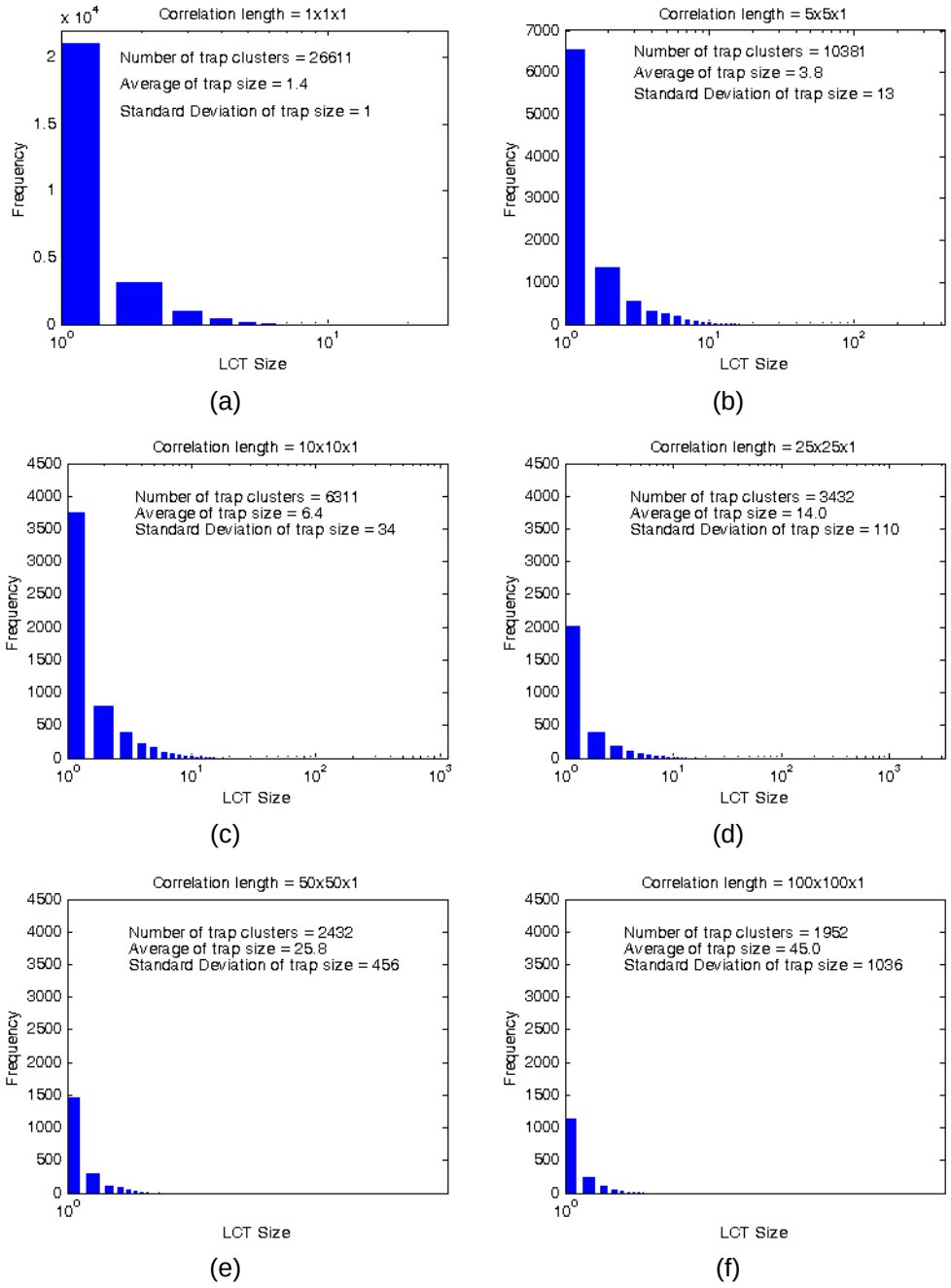

Figure 108: Histogram of size of local capillary traps for the base case using critical entry pressure of 0.4. The horizontal correlation length is (a) 0.3 m, (b) 1.5 m, (c) 3.0 m, (d) 21.5 m, (e) 15 m, and (f) 30 m.

Also, the total volume of local capillary traps slightly increases with longer correlation length. The reason is the same as explained above. Due to longer horizontal correlation length, the probability that two local traps in two consecutive layers become connected to each other decreases. This causes less connection between the local capillary tarps in the first few top layers and therefore, more of these traps are counted as effective traps by the code. Hence, the total volume of local capillary traps increases. This effect also decreases as the size of the model goes to infinity or the ratio of correlation length to the size of the domain becomes very small.

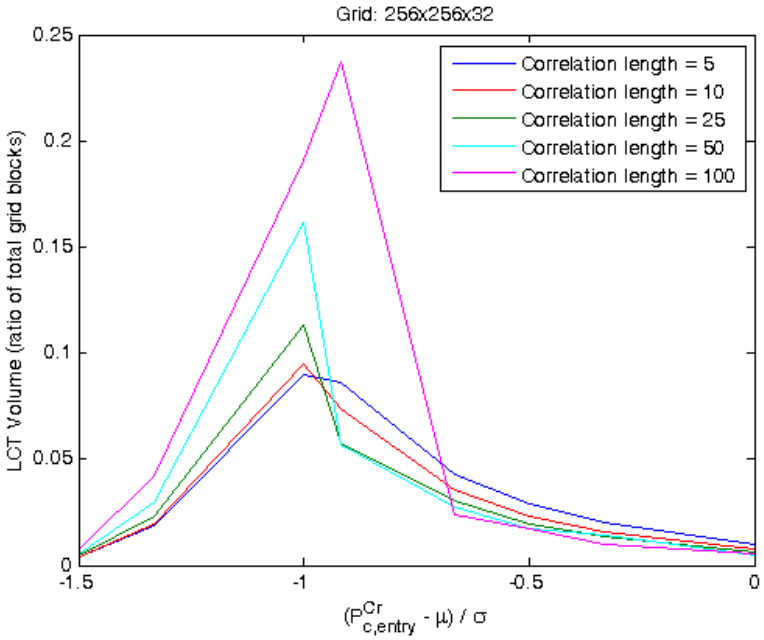

Figure 109: Evolution of the local capillary trapping volume with normalized critical capillary entry pressure for base case with different horizontal correlation lengths.

Effect of Vertical Correlation Length

Since the vertical correlation length affects the connectivity of similar grid blocks in vertical direction, we expect it to have some effect on the local capillary traps. We consider the base case with 256 × 256 × 32 grid block of size 0.3 m × 0.3 m × 0.3 m and study the effect of vertical correlation length on local capillary traps. The entry pressure field is assumed to have 15 m correlation length in x-direction and y-direction and be lognormally distributed with mean value of 8.3 kPa and standard deviation of 4.1 kPa. We set up several cases by using the vertical correlation lengths of 0.3 m, 0.6 m, 1.2 m, and 9.8 m.

Figure 110 shows the IK cross sectional view of local capillary trap map of different cases at J layer 123 using $P_{c,entry}^{crit}$ = 2.8 kPa. As in previous section, we use critical entry pressure of 2.8 kPa to give a local capillary trapping volume in the expected range of volumes from flow simulation, since it is located more than one standard deviation below the mean. In this figure, parts (a) through (d) have vertical correlation length of 0.3 m, 0.6 m, 1.2 m, and 9.8 m, respectively. The length of the local capillary traps has not changed between different figures, but the vertical height of the traps increases with increase in vertical correlation length. In fact, this is like nesting several traps in a longer one. Therefore, the local capillary traps become more elongated in vertical direction and hence, the average size of local capillary traps increases. This behavior can be seen in histogram of the size of local capillary traps in Figure 111. Each histogram shows the mean and standard deviation of the trap size. We can see that for longer correlation length, the average size of clusters increases. The small traps with size one are still the most frequent size that appear in the domain.

The local capillary trapping volume for different vertical correlation lengths for the base case are shown in Figure 112. Since the longer vertical correlation length increases the connectivity of similar grid blocks in vertical direction, the non-barrier blocks will more easily connect to each

other in vertical direction and the probability that two local traps in two consecutive layers become connected to each other increases. Therefore, a smaller amount of capillary entry pressure is needed to make a connected path through layers from bottom to the top. As a result, a smaller percolation threshold will be able to make a percolating path. Figure 112 shows that for the base case with lateral size of 78 × 78 m, increase in the vertical correlation length decreases the percolation threshold of the domain.

Note that for critical entry pressures below the percolation threshold, the total volume of local capillary traps slightly increases with longer correlation length. But, the maximum possible value for the local capillary trapping decreases for the longer correlation lengths. The reason is the same as explained above. As a result of longer vertical correlation length, the probability that two local traps in two consecutive layers become connected to each other increases. This causes more connection between the non-barrier blocks in the consecutive layers and therefore, if the fluid can enter one of these non-barrier regions it will easily go vertically up to a much higher distance. Therefore, it will find the opportunity to trap less gas before penetrating to the top of the domain.

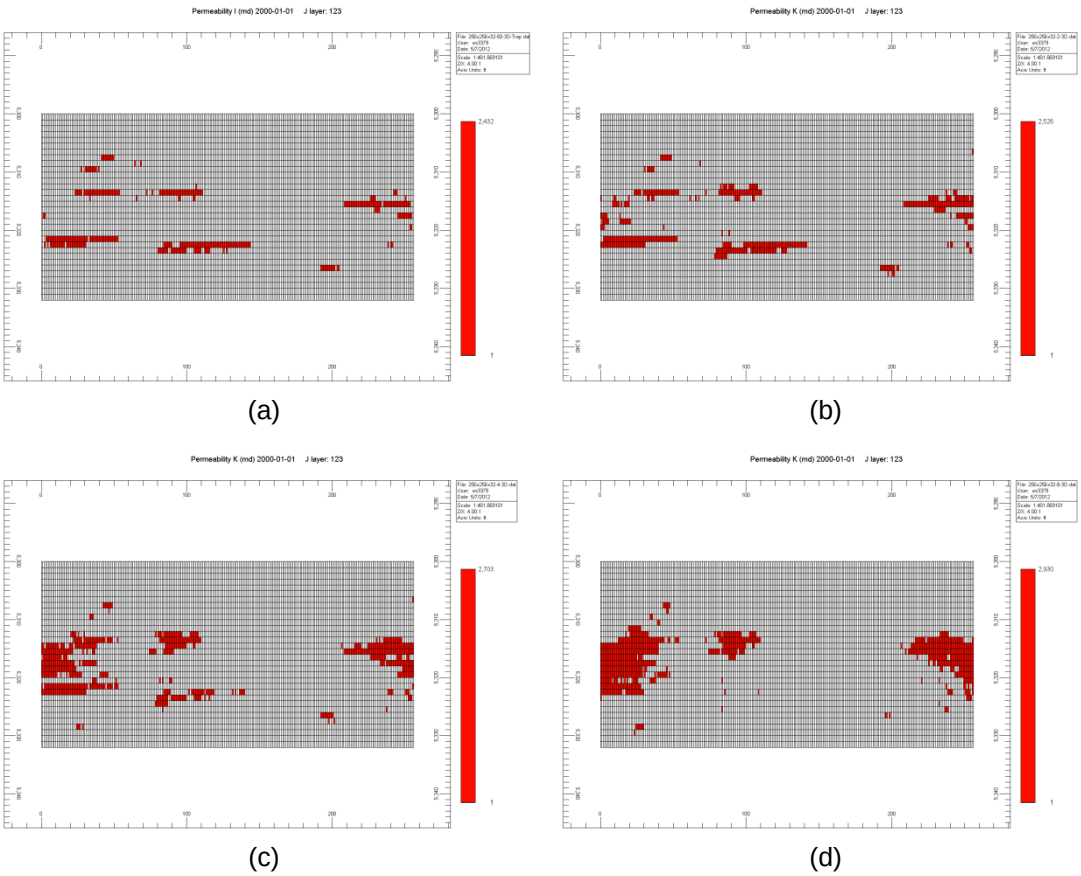

Figure 110: IK-2D cross sectional view of local capillary trap map of the base case at J layer 123 using critical entry pressure of 0.4. The horizontal correlation length is 15 m and the vertical correlation length is (a) 0.3 m, (b) 0.6 m, (c) 1.2 m, and (d) 2.4 m.

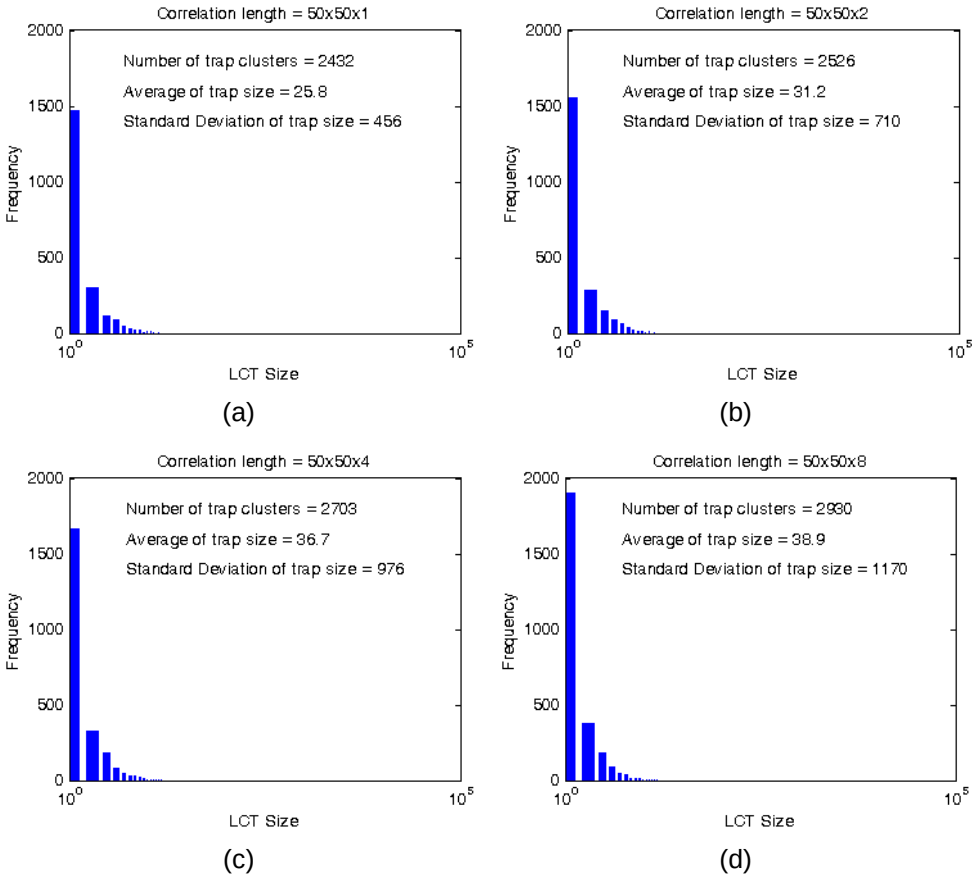

Figure 111: Histogram of size of local capillary traps for the base case using critical entry pressure of 0.4. The vertical correlation length is (a) 0.3 m, (b) 0.6 m, (c) 1.2 m, and (d) 2.4 m.

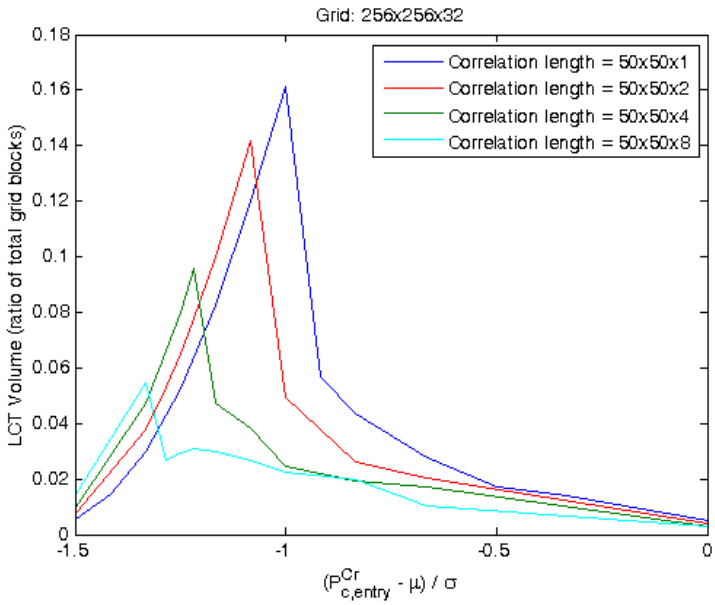

Figure 112: Evolution of the local capillary trapping volume with normalized critical capillary entry pressure for base case with different vertical correlation lengths.

Effect of Standard Deviation (Heterogeneity)

Generally, reservoir rocks are heterogeneous and this variability of rock properties must be considered in any reservoir performance assessment. Variance or standard deviation are the most useful measures of variability around the central value and hence, are measures of heterogeneity. In this section, we are going to evaluate the effect of standard deviation on local capillary trapping.

The base case (78 m × 78 m × 9.8 m) with the lognormally distributed entry pressure field with mean value of 8.3 kPa is used. The entry pressure field has 15 m correlation length in x-direction and y-direction and is uncorrelated in vertical direction. The standard deviation of the entry pressure field is taking values of 0.7, 1.4, 2.8, 4.1, and 8.3 kPa.

Figure 113 shows the change of local capillary trapping volume with critical entry pressure for different values of standard deviation. We can see that the larger standard deviation stretches the curve to the left side of the x axis. First, this means an increased range of critical entry pressures that can lead to local capillary trapping (which is a trivial result of larger standard deviation.) So the possibility of entrapment of gas in the form of local capillary trapping increases in a more heterogeneous domain. Also, this implies that the percolation threshold decreases with more heterogeneity. An increase in the standard deviation causes more values smaller than the mean to appear throughout the domain. This increases the possibility that with smaller values of critical entry pressure, a connected path of non-barrier blocks is achieved from bottom to the top. That is, in fact, a smaller value of percolation threshold.

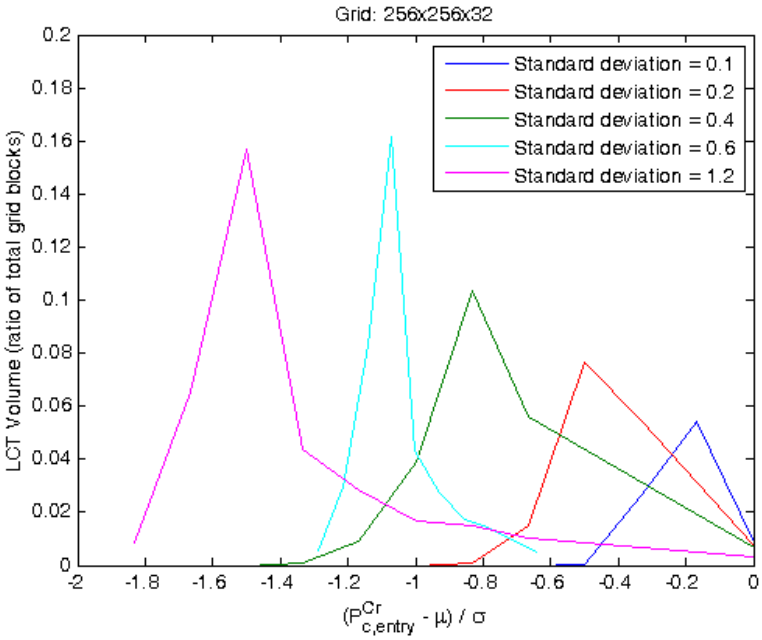

Figure 113: Evolution of the local capillary trapping volume with normalized critical capillary entry pressure for base case (correlation length = 50×50×1) with different standard deviations.

3.1.4 Summary of Influence of Geologic Parameters on Volume of Local Traps

The overall objective of this project is to determine the extent of local capillary trapping, i.e., CO_2 immobilization beneath small scale capillary barriers, which can be expected in typical heterogeneous storage formations. The algorithm described above can estimate the structure of local capillary traps in a domain based on its geologic model, without doing the costly simulations. The algorithm provides valuable qualitative insight into the controls on local capillary trapping. For example, the correlation length of heterogeneities within the storage domain has a first order effect on the number of potential local capillary traps within a storage structure. The 'critical capillary entry pressure' is a measure of the relative ease with which a buoyant plume of CO_2 can displace brine from a (small) region of rock. The interplay of heterogeneity structure in the reservoir and critical capillary entry pressure lead to two competing percolation processes that determine the volume fraction of the domain that could serve as local capillary traps.

The practical implication of the percolation phenomena is that the potential for local capillary trapping exhibits a strong maximum with respect to the value of critical entry pressure. The location of the maximum depends on the correlation length of the domain. Thus if the value of critical entry pressure that applies to a given storage domain can be independently assessed, then a simple estimate of the relative importance of local capillary trapping can be readily obtained.

Using a single value of critical capillary entry pressure, the algorithm provides reasonable though not perfect predictions of the local capillary trapping obtained in full-physics simulations of buoyancy-driven CO_2 migration from an initial emplacement at the bottom of a heterogeneous domain. The main reason for the imperfect prediction is that not all potential local capillary traps get filled by the rising CO_2. This indicates that the concept of critical capillary entry pressure is reasonable, but that the dynamics of the migration may be more complicated than can be captured in a single, constant value. No method currently exists to estimate the critical capillary entry pressure *a priori*, and because the algorithm is tractable for large domains where full-physics simulations are not, seeking such a method is an appropriate topic for future research.

The cases examined in this section represent one limiting case of storage scenarios, in which relatively small amounts of CO_2 (of order 10% of the pore volume of the storage reservoir) are emplaced in the reservoir. Because this scenario enables maximum storage security (all CO_2 held in local capillary traps, in residual saturation at bottom of reservoir, and dissolved in brine in the invaded region, with no CO_2 held beneath a top seal), it is of interest when minimizing the possibility of leakage is the primary concern of the operator. As discussed in Section 3.3 of this report, when greater volumes of CO_2 are emplaced in a reservoir, or when typical injection scenarios are carried out, almost all the local capillary traps in the zone swept by moving CO_2 phase get filled. In this limiting case, the choice of appropriate critical capillary entry pressure may be simpler, and future research should seek to determine this value.

3.2 Experimental Assessment of Local Capillary Trapping

Having demonstrated the theoretical concepts underlying the phenomenon of local capillary trapping, we seek empirical demonstration of these concepts.

The experiments in this research work arrange for a buoyant nonwetting phase to rise through a heterogeneous domain, displacing wetting phase, mimicking the rise of CO_2 in an aquifer with spatially varying capillary entry pressures. Figure 3.1 below presents a simple illustration of this experiment concept.

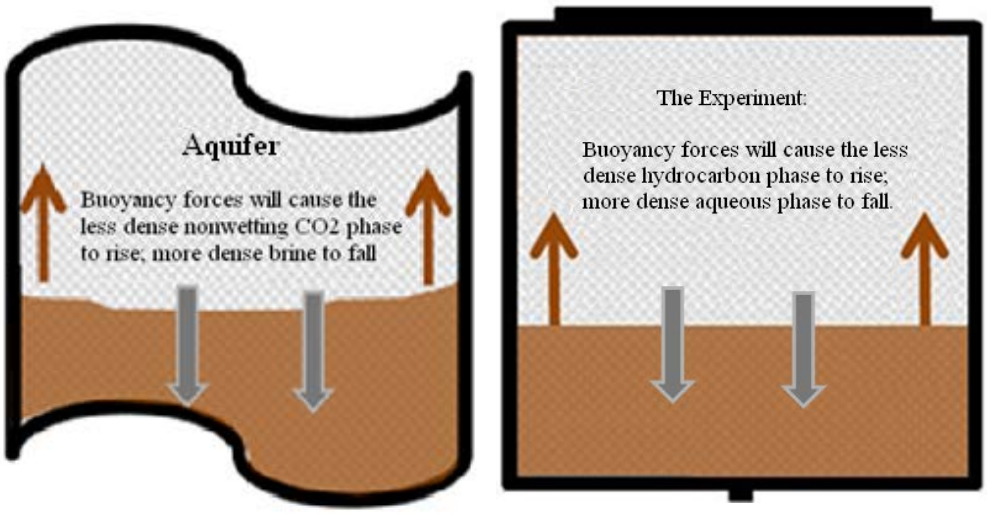

Figure 114: The concept for the experiment. The experiment set up enables two phase immiscible buoyancy-driven counter-current displacement. The porous medium is designed to account for heterogeneity of capillary entry pressure at the cm scale.

Far from an injection well, the CO_2 being stored in a reservoir will migrate primarily because of buoyancy. As shown in Figure 114, in a typical storage aquifer, buoyancy forces will drive the less dense non-wetting CO_2 phase to rise and the wetting more dense brine phase to fall. Similarly, in the experiments conducted in this research, buoyancy forces will drive the less dense non-wetting hydrocarbon phase to rise and the denser wetting aqueous phase to fall. From the point of view of immiscible displacement, the nonwetting hydrocarbon phase rising in the hydrophilic lab apparatus is equivalent to nonwetting CO_2 rising in the hydrophilic aquifer. This forms a countercurrent buoyancy displacement movement in the laboratory apparatus because of the boundary conditions (closed sides), and in the reservoir when the CO_2 plume extends across a wide area; when the area is wide, lateral displacement of brine is slow and the brine instead sinks through the CO_2 countercurrently.

The two types of porous media domains relevant to this research work and their wettability properties are summarized in Table 16.

Table 16: Relevant Domain Wettability Overview

Porous Media Domain	Non-Wetting Phase	Wetting Phase
Nature: Saline aquifer (hydrophilic)	$scCO_2$ ρ = 500-700 kg/m^3 μ = 0.05 mPa-s	brine ρ = ~1000 kg/m^3 μ = 0.3-0.4 mPa-s
Experiment: Hydrophilic container walls and hydrophilic glass beads	90% decane + 10% Mineral oil ρ = 724 kg/m^3 μ = 0.9 mPa-s	60% H_2O + 40% glycerol ρ = 1084 kg/m^3 μ = 7.0 mPa-s

A porous medium made of optically favorable and hydrophilic glass beads was made to represent the storage reservoir. The following section explains the experimental set up in more detail.

3.2.1 Experimental Apparatus[7]

When fully assembled, the apparatus forms a transparent quasi two-dimensional domain which enables the observation of the fluids' behaviors within the bead/grain packing.

The complete experimental apparatus consists of four separate parts:

1. Pyrex glass containment box ("the envelope")
2. Steel caps (top and bottom)
3. Pivoting steel frame
4. Fluid flow system

and is shown in the following Figure 115.

The dimensions for the experimental apparatus are 0.6 m x 0.6 m x 0.03 m To provide an airtight seal, a gasket custom cut from 1/8" (0.003 m) thick neoprene is layered between the glass envelope and its metal caps. Each of the metal caps has twelve (12) 1/2" (0.013 m) threaded holes for a total of twenty four (24). All of them are utilized for a secure attachment by means of 1-1/2" (0.038 m) tightened bolts. The steel frame allows for seamless pivoting of the experimental apparatus. Attachment of apparatus to frame is by means of two steel plates, both of which are secured on two opposing sides.

To enable fluid flow into the experimental apparatus, there are four (4) two-way valves on each of the top and bottom caps (8 valves in total). The valves serve as the inlets and outlets for oil based nonwetting fluid and aqueous based wetting fluids. All valves and connectors are 1/8" (0.003 m) and utilize 1/8" (0.003 m) plastic tubing. Those in the fluid flow tubing system are nylon Swagelok and those directly connected to the experimental apparatus are stainless steel Swagelok.

[7] This section and its following sections constitutes Project Deliverable 4.1 Procedure for establishing saturation distribution resulting from buoyant displacement of wetting by nonwetting phase in heterogeneous porous medium

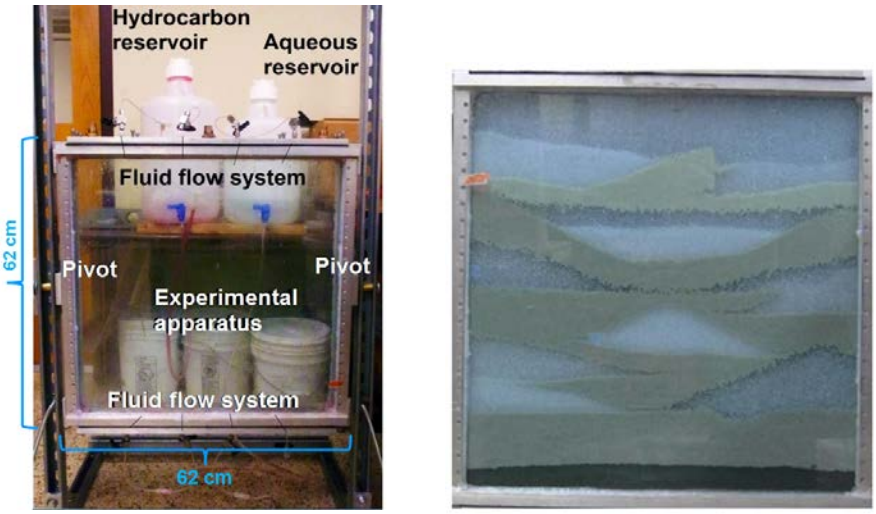

(a) (b)

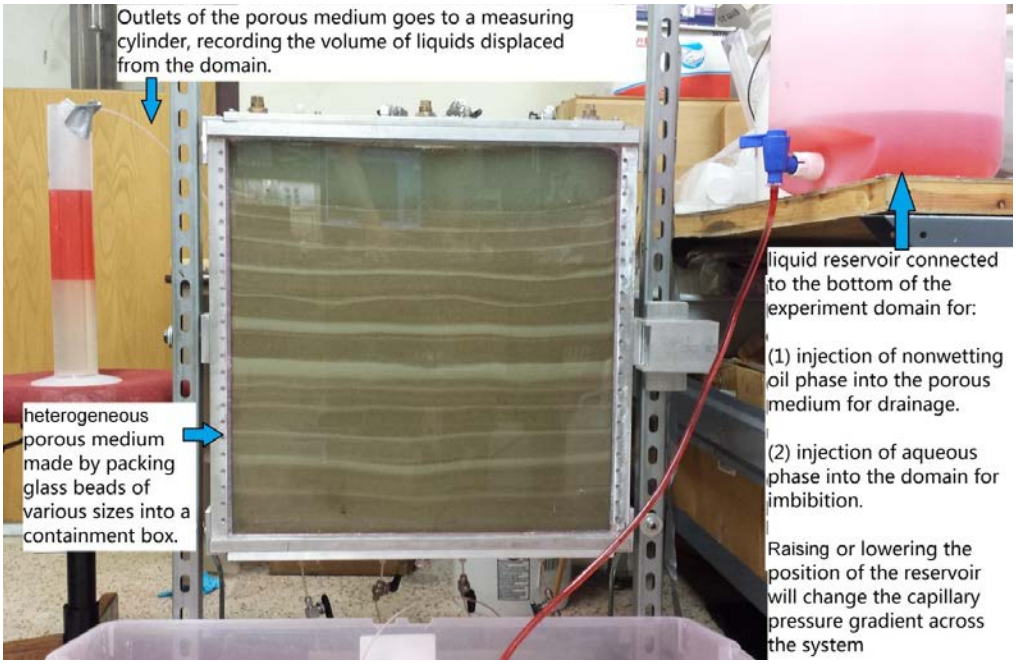

(c)

Figure 115: Experimental apparatus. (a) A 0.6 m by 0.6 m by 0.03 m Pyrex glass containment box with steel caps tapped with fluid entry/exit ports and valves (top and bottom). Box is mounted on horizontal pivots in a metal support frame. Total inside volume of the containment box is about 700 cubic inches (11.33 liter). The pivots enable the easy flipping of a gravity stable initial condition by 180 degrees to start the experiment. (b) Example of packed domain. Various sizes of water-wet silica beads are packed into the glass containment box with desired patterns, to create a porous medium with heterogeneity of interest. Different color corresponds to different sizes of beads, as each type of beads has its own optical characteristic. (c) A fully assembled, operating experimental set up. Liquid reservoir attached to the bottom can be replaced either with oil reservoir or aqueous reservoir, serving different purposes of drainage (entry of nonwetting phase into the domain while simultaneously displacing water) or imbibition (entry of water into the system simultaneously displacing oil). The outlet from the domain is not submerged in to the measuring cylinder, but is open to atmosphere and kept at the same height as the top of the domain for maintaining hydrostatic pressure.

By opening and closing the attached control valves and manipulating the position of attached reservoirs, different types of boundary conditions to the porous media can be achieved. These are shown in the following Figure 116 (migration in closed domain after nonwetting phase emplacement) and Figure 117 (migration in open domain during nonwetting phase emplacement):

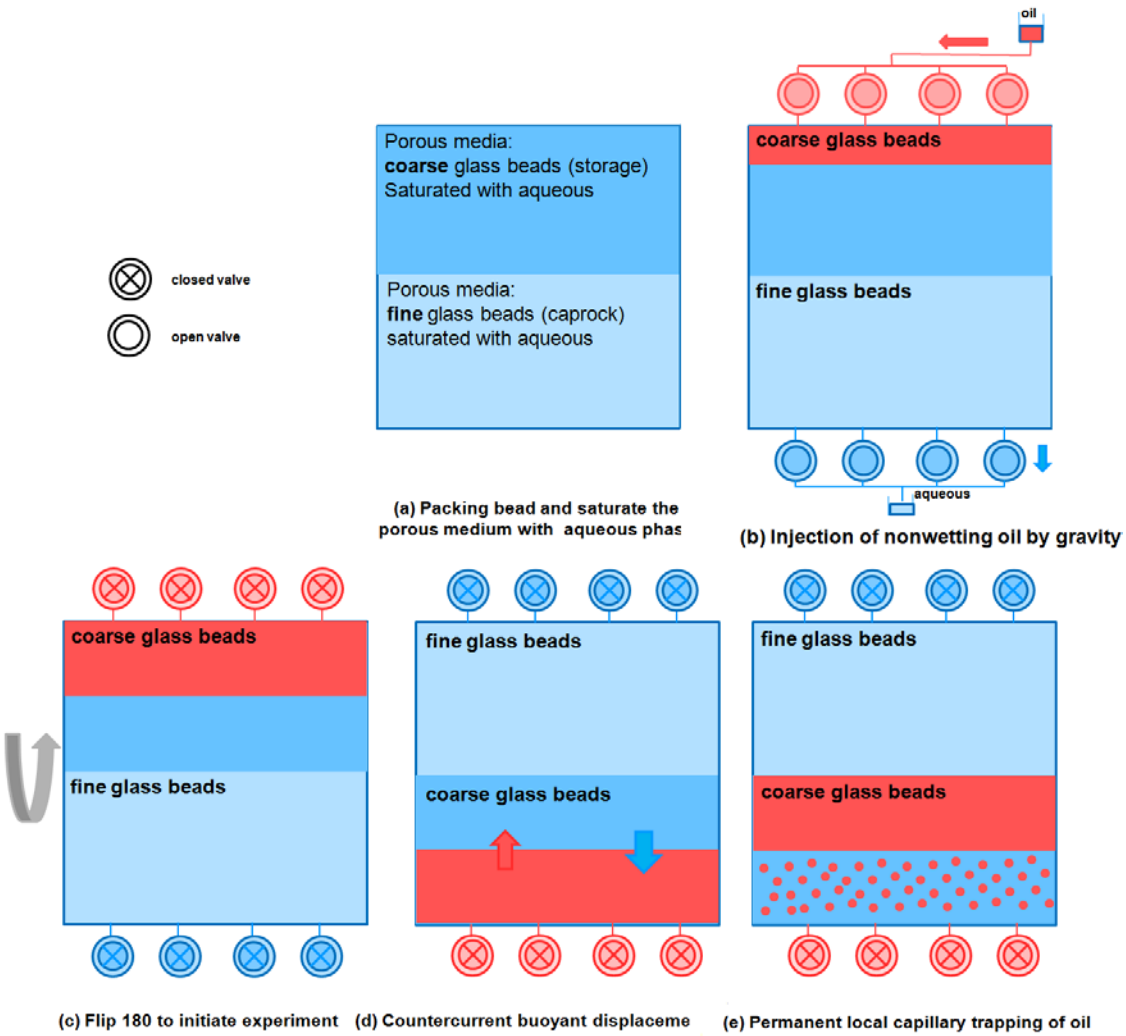

Figure 116: Lab arrangement for a two phase, immiscible, closed-boundary, counter-current displacement. (a) Pack beads with different sizes (here: coarse for storage reservoir, fine for the caprock) to achieve desired heterogeneity, and saturate the entire domain with wetting phase (blue). (b) Inject nonwetting oil phase from the top via gravity, displacing wetting phase from the bottom. (c) Close all valves (circles at top and bottom of domain) and rotate the containment box about the horizontal axis through middle of the domain such that the fine beads region is at top of domain to form the caprock (a capillary barrier to the buoyant nonwetting phase in the storage reservoir). (d) Density difference between the wetting and nonwetting phases will drive the buoyant immiscible counter current movement in a closed environment. (e) Mobile nonwetting phase accumulates beneath the capillary barrier, locally trapped. Part of the nonwetting phase are trapped in the original section as residual (red dots).

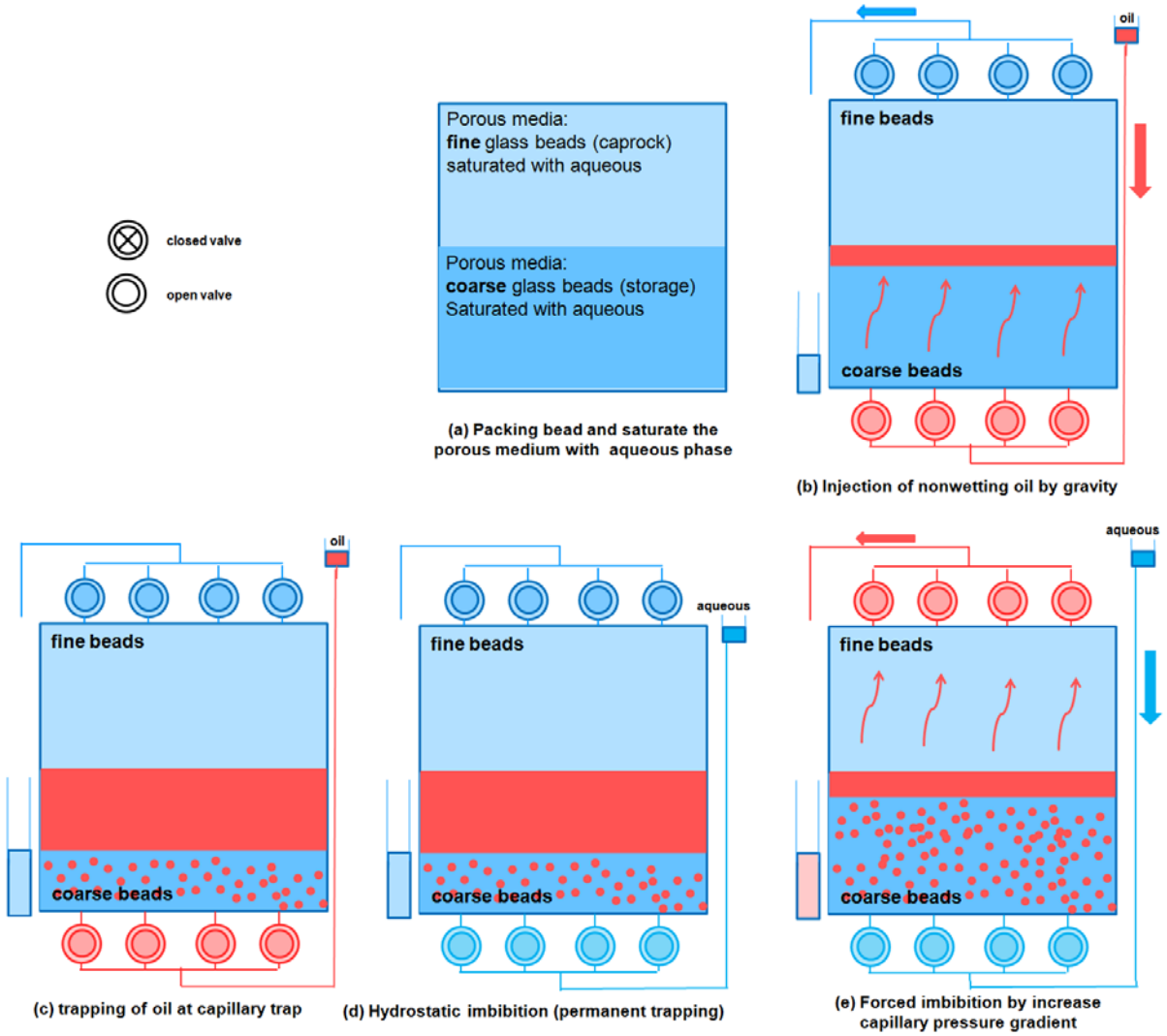

Figure 117: Lab arrangement for a two phase, immiscible, open-boundary, counter-current displacement movement. (a) Pack beads with different sizes to achieve heterogeneity, and saturate the entire domain with wetting phase. (b) Inject nonwetting oil phase from the bottom via gravity, displacing wetting phase from the top. (c) Less dense nonwetting phase rises and trapped permanently beneath capillary barriers. (d) Replace the oil reservoir with an aqueous one at the same height as the top of the domain for hydrostatic potential gradient. (e) Raise the aqueous reservoir to increase the capillary pressure gradient across the domain.

Manipulating the open (circle)/close ('X') state of valves, and positions of reservoirs (red = nonwetting oil; blue = wetting aqueous) create various types of boundary conditions and features (hydrostatic potential, forced imbibition, artificial fractures, etc). Different size of beads corresponds to different capillary entry pressure.

3.2.2 Experimental Design Considerations

Two objectives drove the design of these experiments and each objective involved the assessment of immiscible two-phase buoyancy driven flow in porous media, with practical application to track CO_2 migration in a saline aquifer:

1. to determine the influence of geological and petrophysical characteristics (particularly heterogeneity) on the persistence of local capillary trapping, and
2. to mimic and demonstrate how leakage, e.g. if the top seal is compromised, could affect the mobile phase in a local capillary trap.

CO_2 and Brine Relationship

The relationship of physical properties of supercritical CO_2 and brine was discussed above. It is crucial to have an experiment that is as analogous as possible to in situ conditions. Matching the viscosity, density and interfacial tension relationships is of particular importance. The viscosity ratio has an effect on the stability of immiscible displacement. The density difference between CO_2 and brine drives the buoyant movement of the CO_2 plume in the aquifer. The interfacial tension governs the capillary pressure associated with the fluid flow in such porous media. Therefore the final experimental design should not only match these relationships but also be able to initiate buoyant movement easily and consistently.

Saline Aquifer Environment

Saline aquifers are an aqueous environment in which brine is the wetting fluid and CO_2 is the non-wetting fluid. The experimental apparatus used by previous researchers (Hernandez 2011) was made of polycarbonate which is hydrophobic. It proved difficult to obtain reliably hydrophobic granular material to use in that apparatus, so a new apparatus was constructed from Pyrex glass. The glass has an affinity for water and thus is hydrophilic, which mimics the natural environment when filled with a hydrophilic porous medium.

Ambient Conditions

The experiment is performed at ambient conditions for safe, convenient observation and digital capture (by means of a high definition video camera) of the progress in the open laboratory setting. Experiments run at storage formation temperatures ($T > 300$ K) and pressures ($P > 20$ MPa) are challenging and the imaging reported in this work would not be available. The existing experimental apparatus is not designed to withstand conditions other than ambient.

Qualitative Analysis

Due to the novelty of this research topic and concept, at this stage observations of local capillary trapping and residual trapping made by this experimental set up are qualitative, based on visual indicators, rather than quantitative. The non-wetting oil phase used in this experiment, which represents the rising stored CO_2 in the saline aquifer, is dyed red with trace amount of oleic acid ($C_{26}H_{24}N_4O$). Therefore, when the nonwetting oil phase entered the porous media, more redness means greater saturation. Future work will attempt to quantify the nonwetting phase saturations in the experimental domain.

Final Experimental Design

The final experimental design incorporated the refining of the previous experimental apparatus so that the seal is robust (no fluids leaked out) and the bead packing fills the entire domain without any settling, such that the experiment is convenient and repeatable.

For these experiments, the aqueous phase will act as wetting brine does in the storage aquifer and the hydrocarbon phase will act as the non-wetting CO_2 phase does in the aquifer. Mimicking the density relationships of supercritical CO_2 and brine in nature with convenient fluids in the lab, the buoyant movement to be observed occurs when the aqueous phase falls while the hydrocarbon phase rises.

3.2.3 Fluids

In order to perform the experiments at ambient conditions, it was necessary to develop a fluid pair that was as analogous as possible to that of CO_2 and brine at aquifer conditions. In the temperature and pressure range expected for many storage aquifers (depths of 1 km or more) the density of the CO_2 phase will be 500 to 700 kg/m^3. Thus the density difference driving CO_2 movement will be 300 to 500 kg/m^3. For typical storage conditions the CO_2 viscosity is about 0.05 mPa-s and the brine viscosity is about 0.3 to 0.4 mPa-s. The ratio of viscosities of nonwetting and wetting phases is therefore about 0.05/0.35 or 1:7 (Hernandez, 2011).

The fluids used to match the supercritical CO_2-brine viscosity and density relationship are water/glycerol mixture and a light mineral oil/decane mixture; the latter are both Fisher brand chemicals and were bought online from Fisher Scientific. The fluid properties were obtained experimentally.

The density of the water/glycerol mixture was obtained through a simple experiment in which a graduated cylinder was weighed before and after a known fluid volume was poured. Due to the hydrophilic nature of the experimental apparatus, brine/glycerol mixture serves as the wetting phase and a light mineral oil/decane mixture serves as the non-wetting phase. The density difference between brine/glycerol (ρ_w = 1084 kg/m^3) and the light mineral/decane oil mixture (ρ_o = 724 kg/m^3) is about the same than that of CO_2 and brine at aquifer conditions (Cinar *et al.* 2009). Of greater concern is matching the viscosity ratio. Viscosity ratio of the immiscible fluids determines their migration pattern. If the viscosity ratio of the surrogate fluid pairs used in these experiments deviates from the value of 1:7, the flowing pattern of the fluids in the domain will not resemble the true migration pattern of rising CO_2 in the actual storage saline aquifer. Therefore the accuracy of estimating the total storage capacity of such storage formation will be compromised, and the assessment of the persistence of trapping mechanism, such as Local Capillary Trapping, will be also influenced adversely.

A Fann 35 model rotational viscometer was used to obtain the final Newtonian viscosity of the mixture. With a R1-B1-F1 rotor, bob and spring combination running at 300 rpm and 600 rpm, the viscosity is the difference between the two values read directly from the dial readings and corrected according to the user manual guide.

Figure 118 depicts the viscosity of a mixture of light mineral oil (μ = 44 mPa-s) and decane (μ = 0.92 mPa-s) as a function of decane fraction according to the quarter power mixing rule:

$$\mu_{mixture} = \left(x_a \mu_a^{-\frac{1}{4}} + x_b \mu_b^{-\frac{1}{4}} \right)^{-4} \tag{22}$$

where

μ_i = the viscosity of pure component i

x_j = the volume fraction of component j in the mixture

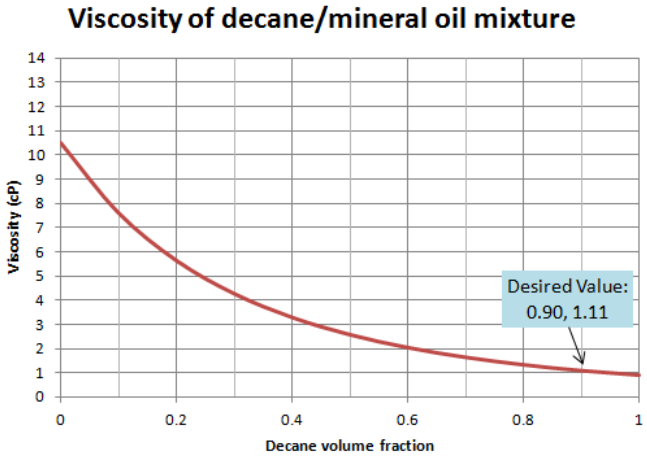

Figure 118: Quarter-power mixing rule applied to a decane/mineral oil mixture at ambient conditions. The actual viscosity of the mixture agrees to this prediction well (Hernandez, 2011).

Experimentally, the desired viscosity of 1.1 mPa-s was achieved with the addition of a certain amount of decane to the original volume composition. This value is indicated in Figure 118 above. In line with the experimental results, for the buoyant displacement experiments we used a mixture of 0.1 light mineral oil/0.9 decane by volume to represent the CO_2 phase. The target composition of the brine/glycerol was also determined using the quarter-power mixing rule (Eq. (22)). In line with the experimental results, for the buoyant displacement experiments we use a mixture that is 0.591 brine/0.409 glycerol by volume to represent the brine phase in an aquifer. The measured viscosity values and calculated values are summarized in the following Table 17. This information is also plotted in the Figure 119.

Table 18 provides a summary of the individual fluid properties and the relationships between the fluid pairs respectively. To match the viscosity ratio of CO_2 and brine, the mixture compositions were adjusted as indicated in the table.

Table 17: Viscosity of Water/Glycerol Mixture at Ambient Conditions*

Component Fraction		Experimental (using the Fann 35 viscometer)			Calculated
H_2O	Glycerol	Reading @ 600 rpm	Reading @ 300 rpm	Viscosity (mPa-s)	Viscosity (mPa-s)
1	0	6	4.8	1.2	1.0
0.9	0.1	7.5	5	2.5	1.4
0.8	0.2	10	6.5	3.5	2.1
0.7	0.3	13	7.5	5.5	3.1
0.6	0.4	19	12	7	5.0
0.5	0.5	35	21	14	8.5
0.4	0.6	59	31	28	15.8
0.3	0.7	141	81	60	32.5
0.2	0.8	Out of range	Out of range	N/A	78.5
0.1	0.9	Out of range	Out of range	N/A	244.4
0	1	Out of range	Out of range	N/A	1200.0

*Pure water and glycerol have viscosities of 1 mPa-s and 1200 mPa-s respectively. The experimental value was obtained by subtracting the 300 rpm reading from the 600 rpm reading and adjusted according to the user guide. The calculated value is based on "quarter power mixing rule."

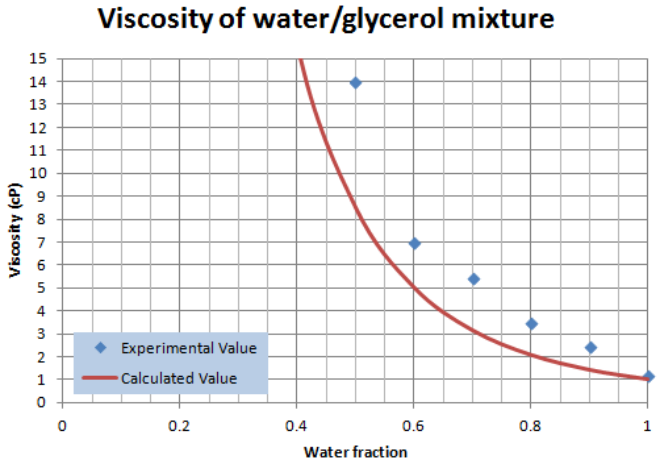

Figure 119: Quarter-power mixing rule applied to a brine/glycerol mixture at ambient conditions (red curve) predicts the trend of the measured viscosity of the mixture (blue points).

Table 18: Convenient Fluid Pair w/Properties Analogous to CO_2/Brine

Fluid	Viscosity (cP)		Density (kg/m^3)	
Typical Storage Aquifer				
Supercritical CO_2	0.05	1:7	500-700	Δρ= 300-500
Brine	0.3-0.4		~ 1000	
Ambient conditions:				
Brine	1.0		1000	
Decane	0.92		720	
Light Mineral Oil	44		800	
90% Decane + 10% Mineral Oil (non-wetting phase, surrogate for CO_2)*	1.1	1:7	724	Δρ=360
60% Brine + 40% Glycerol (wetting phase)*	7.0		1084	

*Fluids used in the experiment

3.2.4 Wettability and Contact Angle

It is expected that Pyrex glass used to construct the transparent faces of the containment box is hydrophilic. To verify this, a transparent water tank was filled with the mixed aqueous wetting phase. A pair of rubber pieces of equal height were placed and submerged at the bottom of the tank, with about 5 cm apart. The glass material to be tested was then placed on the two rubber pieces, and submerged.

Hydrocarbon phase droplet (dyed with red food coloring) was then transferred via a transfer pipette to the cavity formed by the glass material and the two rubber blocks. Due to density difference between the two liquid phases, buoyancy drove the hydrocarbon droplet to rise, to which was then trapped at the lower surface of the glass material and formed a contact angle.

A high definition video camera recorded the image from a level parallel to the glass piece and the contact angle was measured. Results from different combinations of fluid pairs are summarized in the following Figure 120.

Adding mineral oil into decane will increase the contact angle. Adding glycerol into water will decrease the contact angle. The larger the contact angle, the more hydrophobic the non-wetting phase is, the better for the objective of achieving largest capillary pressure according to Young Laplace Equation. Taking viscosity, density difference and interfacial tension into consideration, the fluid pair that best suits the experiment is 60% water 40% glycerol (as wetting phase) and 90% Decane 10% mineral oil (as non-wetting phase).

It is also important to note that the two phases are immiscible during the time period range of the experiments (several hours to days).

(a)

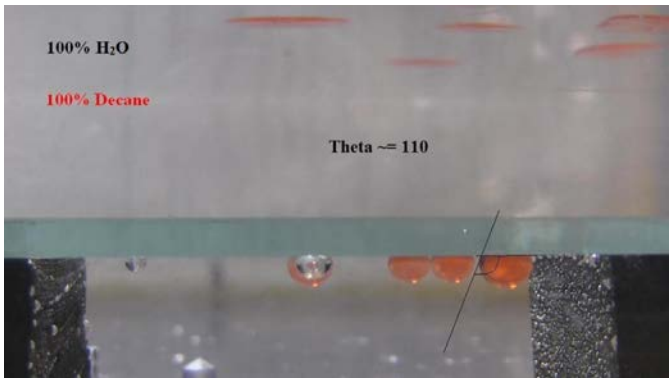

(b)

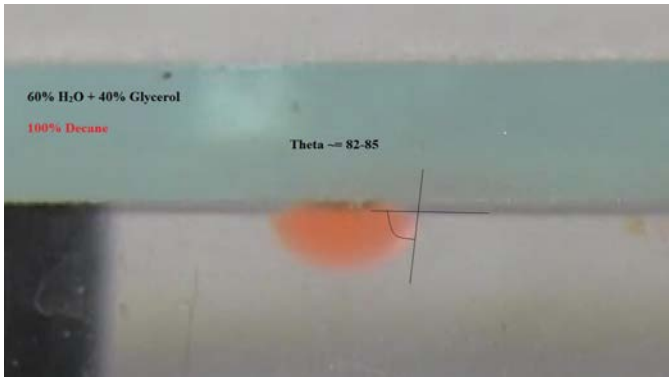

(c)

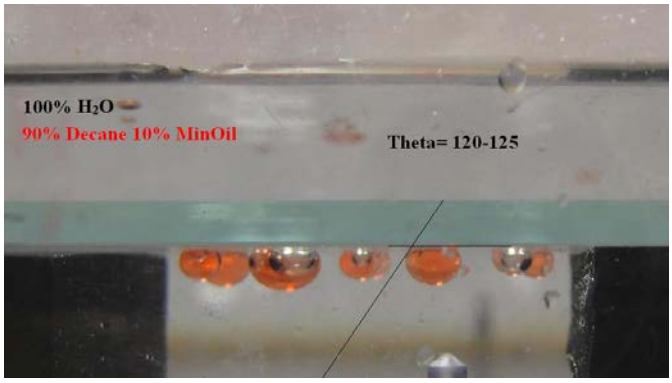

(d)

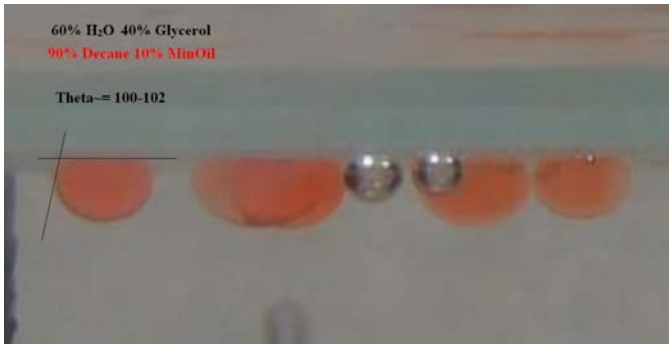

Figure 120: Different fluid pair combinations and their contact angles on hydrophilic Pyrex glass surface, non-wetting phase is dyed in red. (a) Pure decane droplets (dyed in red) surrounded by pure water form a 110 degree contact angle on Pyrex glass surface. (b) Pure decane droplets (dyed in red) surrounded by 60% water 40% glycerol mixture form an 82 degree contact angle on Pyrex glass surface. (c) 90% decane 10% mineral oil mixture droplets (dyed in red) surrounded by pure water form a 120-125 degree contact angle on Pyrex glass surface. (d) 90% decane 10% mineral oil mixture droplets (dyed in red) surrounded by 60% water 40% glycerol form a 100-102 degree contact angle on Pyrex glass surface.

A ring tensiometer is used to measure the interfacial tension (IFT) between the non-wetting phase (90% Decane + 10% Mineral Oil) and wetting phase (60% Water + 40% Glycerol). Assuming perfect wetting (zero contact angle), the IFT between the two phases is measured to be 30.4 dynes/cm. With a 100 degree contact angle, the IFT is calculated to be 27.8 dynes/cm according to Eq. (23), while the actual interfacial tension of brine-CO_2 system under reservoir condition is averaged to be 30-35 dynes/cm (Chalbaud *et al*., 2006).

$$\sigma = \sigma' \cdot cos\theta \tag{23}$$

where

θ = the contact angle between the fluid/fluid interface and the solid surface

σ = the actual interfacial tension between the two fluids with a contact angle θ

σ' = the interfacial tension between the two fluids with perfect contact (θ = 180°)

3.2.5 Beads

The experimental apparatus is a hydrophilic glass containment box packed with hydrophilic glass beads and/or sand. Glass beads all come freshly from manufacturer, Potters Industries Inc. Average bead size distribution and theoretical capillary entry pressures for a column of packed beads are calculated (using interfacial tension of 27.8 dynes/cm for the brine/glycerol—decane/mineral oil interface and a contact angle of 100 degrees). The beads properties are summarized in Table 19.

Table 19: Properties of Beads Used in Experiments

Bead Name	Approximate Bead Diameter Distribution (mm)	Average Bead Diameter (mm)	Capillary Entry Pressure (Theoretical) (Pa)	Capillary Entry Pressure (Experimental) (Pa)	Maximum Possible Trapped Oil Column Height (cm)
P-5 mm	4.7 - 5.3	5.0	67	104	2.9
P-3 mm	2.8 - 3.2	3.0	111	143	4.0
P-2 mm	1.8 - 2.2	2.0	167	208	5.9
P-0230	0.43 - 0.60	0.5	667	887	25.1
P-0120A	0.28 - 0.22	0.25	1334	1735	49.1

As shown in Table 19, the capillary entry pressure of the bead packs is inversely proportional to the diameter of the beads. This is because for monodisperse beadpacks the characteristic pore throat size r_{throat} (which determines the capillary entry pressure) is proportional to the bead size R_{bead} (typically $r_{throat} \approx 0.3 R_{bead}$). Thus halving the bead size doubles entry pressure, according to Young Laplace Equation:

$$P_c = \frac{2\sigma \cdot cos\theta}{r} \tag{24}$$

where

P_c = capillary pressure

σ = the interfacial tension between the two fluids

θ = the contact angle between the fluid/fluid interface and the solid surface

r = the radius of the pore throat

Detailed calculations for the contents of Table 19 are shown below. Notice that all values in the table are for dense random packing of single bead size.

Calculation of Capillary Entry Pressure of Bead Packs (Theoretical Values)

The radius of the pore is related to the radius of the beads by a factor of 3, i.e. $r_{pore}=r_{bead}/3$. When viscous and body forces are negligible, the configuration of two fluids is governed by Young-Laplace equations.

$$P_c = \sigma C \cos\theta \tag{25}$$

where

P_c = the capillary pressure to the curvature of the interface between the two phases

σ = the interfacial tension between the nonwetting and wetting phases

C = the sum of the two principal curvatures, or twice the mean curvatures of the interface, $C=1/r_1+1/r_2$

θ = the contact angle between the solid surface and the interface between nonwetting and wetting phases

A sample calculation of capillary entry pressure and maximum possible trapped oil column height of a dense random packing of the 0.5 mm diameter beads is shown in the following section.

Sample Calculation

Diameter of beads = 0.5 mm,

r_{bead} = 0.00025 m,

$r_{pore} = r_{bead}/3=8.33\times10^{-5}$ m,

$C = 1/r_{pore}+1/r_{pore}=24000$ m^{-1}

Measured interfacial tension = 30.4 dynes/cm = 0.0304 N/m.

Contact angle of 100 degree.

Product of interfacial tension and cosine of contact angle
= 0.0304 N/m × *cos*(100°) = 0.0278 N/m = 27.8 dynes/cm.

Capillary entry pressure of the random dense bead pack
= P_c = 0.0278 N/m × 24000 m^{-1} = 667 Pa.

Maximum possible trapped oil column height
= P_c / $\Delta\rho$ / g = 667 Pa / 360 kg/m^3 / 9.81 N/kg = 0.189 m = 18.9 cm.

Calculation of Capillary Entry Pressure of Bead Pack (Experimental Values)

For comparison with the theoretical values, the actual capillary entry pressures of bead packs were also measured experimentally. Figure 121 illustrates the experiment schematic.

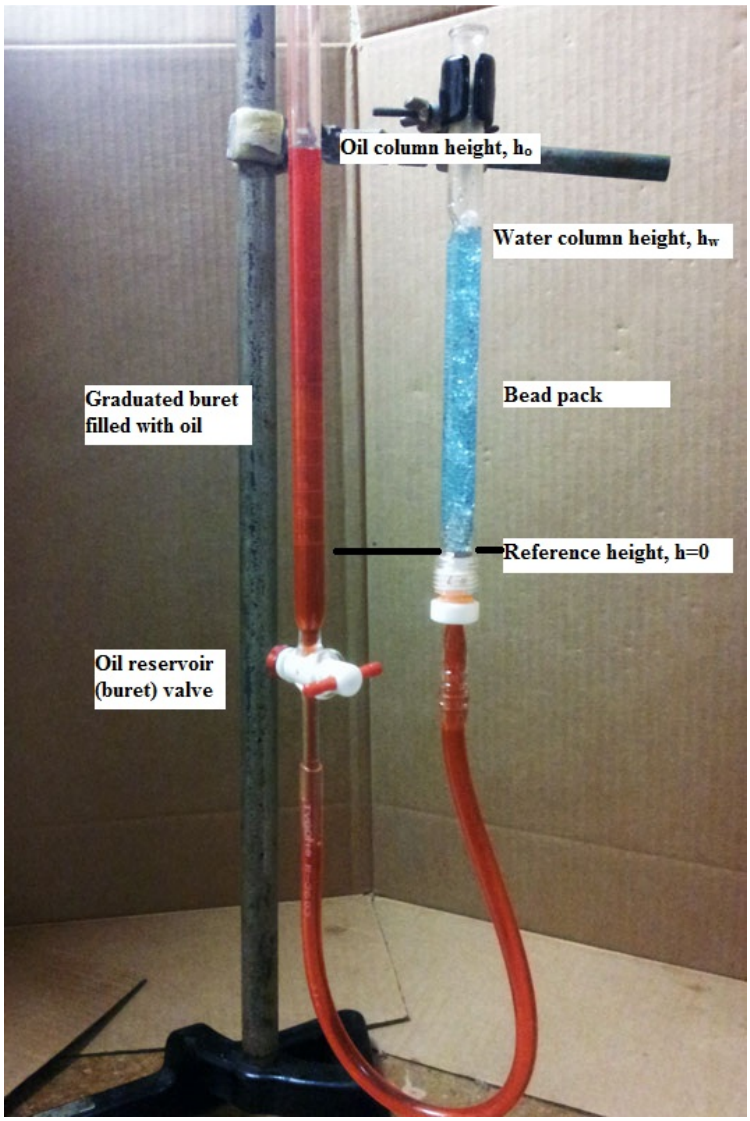

Figure 121: A labeled schematic of the wettability experiment. A bead pack (right) is saturated with water (dyed blue) and connected to an oil (dyed red) reservoir. An increase in oil pressure (accomplished by raising the oil reservoir height) is initiated in increments until oil displacement into the bead pack occurs.

The initial step is to set up the bead column in the glass tube; the column is then saturated with blue-dyed water. Bead pack saturated with food coloring (blue) dyed water is connected to an oil reservoir, in this case a graduated burette. Once saturated, the height of the oil column can be measured relative to the reference height indicated in Figure 121. This reference height starts at the bottom of the bead pack and marks the water-oil interface; it also aligns with the beginning of the graduations on the burette serving as the oil reservoir. The height of the oil column is then calculated using the equation for capillary pressure, denoted by:

$$P_c = g\left(\rho_o h_o - \rho_w h_w\right) \tag{26}$$

where

g = gravity in m/s^2

ρ_w = the density of water in kg/m^3

ρ_o = the density mineral oil in kg/m^3

h_w = the height of the water column relative to the reference height in m

h_o = the height of the mineral oil column relative to the reference height in m

Solving the equation for zero capillary pressure, the only unknown is the height of the oil column. The gravity is divided out and the height of the oil is calculated as the density of oil multiplied by the height of the oil column divided by the density of the water. For example, the density of water is 1000 kg/m^3 and the density of light mineral oil is 800 kg/m^3, thus when the relative height of the water is 80% of the relative height of the oil then the capillary pressure at the oil-water interface at the reference height is zero.

The opening of the valve on the oil reservoir initiates the experiment at this state of zero capillary pressure. Any movement in the water column, oil column or fluid interface is recorded. If there is no movement, the oil reservoir height is increased by a small increment by raising the burette. Typical increments are 1.2 cm as the major graduations on the burette are 1.2 cm apart and using the graduations as markers aids in keeping the experiment consistent. After the system is allowed to reach equilibrium, any movement in either fluid column heights and/or the fluid interface is recorded. The process is continued until the bead column is entirely saturated with oil and all the water is displaced out and accumulated at top of it. The higher the increase required for initial displacement of oil into the water saturated bead pack, the more water wet the medium (or the smaller the beads) and hence the higher the calculated displacement pressure. The expected displacement pressure can be estimated using the Young Laplace equation for capillary pressure.

The Young Laplace equation for capillary pressure for two immiscible fluids in contact with a solid surface is given by Eq. (25) .

A contact angle less than 30º indicates a water wet medium. A contact angle greater than 90º indicates an oil wet medium; oil will not enter the water saturated water-wet bead pack until the displacement pressure is exceeded.

The results of experiments for different bead sizes are shown in Table 19. The agreement with the theoretical expectation is reasonably good.

3.2.6 Experiment Procedures

Each experimental sequence begins with the cleaning and drying of the experimental apparatus. A residual-free soap, water and ethanol are all used along with thick paper towels to wipe down all surfaces of the experimental apparatus, including the gasket, caps and containment box. After cleaning, the gasket is then aligned and positioned in place, then followed by the cap. They are tightened by screws afterwards.

Closed-Boundary Experiments

Figure 122 illustrates the procedures for conducting a closed-boundary experiment.

Figure 122: A graphical representation of the closed-boundary experimental design. The design calls for emplacing the nonwetting phase in a gravity-stable manner (filling from the top), closing valves, then flipping the apparatus to start the buoyancy-driven displacement.

Step 1: Packing the Experimental Apparatus. Packing begins with the glass containment box in the vertical position where the bottom cap is tightened, and the top of the box remains open. Dry beads are introduced into the apparatus via a plastic funnel and settled to the bottom by gravity. The use of a hand held vibrator wrapped in soft material is held against the apparatus to initiate more settling and results in a more uniform pack. Beads of different sizes were placed in sequenced layer to achieve desired patterns of homogeneity or heterogeneity. Once the "envelope" is completely filled with beads, the top cap is then positioned and secured.

Step 2: Saturate with the Aqueous Phase. The experimental apparatus is now rotated to the position that has the oil flow system positioned at the top and aqueous phase flow system positioned at the bottom. The fluid flow system is connected to two reservoirs, two carboys filled with the aqueous phase and the hydrocarbon phase, placed on a small table behind the experimental apparatus. To initiate aqueous phase flow into the bead pack, the aqueous reservoir valve is opened then the valves designated for aqueous phase flow are opened. Flow into the bead pack is gravity driven. Time to reach complete saturation varied from minutes to several hours according to grain size, and the height of the aqueous reservoir. Air is displaced via the ports from the top. Ports at the bottom are closed once the aqueous phase saturates the entire domain.

Step 3: Displace with the Hydrocarbon Phase. Hydrocarbon phase is then introduced into the domain from the top four ports, by gravity feed; at the same time open two valves at the bottom for displaced aqueous phase to leave the system. The hydrocarbon non-wetting phase will build up at the upper portion of the domain till a predetermined volume while aqueous wetting phase has left the system.

Step 4: The Experiment. All valves and ports are closed, so the buoyant displacement in this step occurs in a closed domain, requiring countercurrent movement of the fluids. Note that Steps 1-3 establish a gravity-stable configuration, as the denser aqueous phase rests below the less dense hydrocarbon phase. To initiate the buoyancy driven displacement, the gravity-stable configuration at the end of Step 3 is reversed by pivoting the apparatus 180 degrees in the frame. The subsequent fluid displacement will be physically analogous to the rise of CO_2 non-wetting phase in a saline aquifer as water descends to fill the space vacated by the rising CO_2.

For selected experiments, after the migration of oil stops, top and bottom ports are opened and connected to reservoirs to impose a prescribed hydraulic potential across the domain. This enables various boundary conditions, for example, forced imbibition of aqueous phase from the bottom, with accompanying displacement of fluids from the top, or hydrostatic conditions in which no aqueous phase flows into or out of the domain, unless buoyancy-driven outflow of hydrocarbon phase occurs.

The Initial Condition

The initial condition is a packed experimental apparatus which was initially saturated with an aqueous phase that has had a third of that aqueous phase displaced by a hydrocarbon phase. The configuration is gravity stable, as the denser aqueous phase rests below the less dense hydrocarbon phase. Figure 123 depicts an example of the initial condition.

Figure 123: Initial condition of the closed-state experiment. After packing granular medium of hydrophilic beads in the apparatus, aqueous phase (blue) (the brine/glycerol mixture) was slowly injected from the bottom to fill entire medium, followed by slow injection of light mineral oil/decane mixture (red) from the top to displace aqueous phase through the bottom. To initiate the buoyancy driven displacement, the gravity-stable configuration shown in this photograph is reversed by pivoting the apparatus 180 degrees in the frame (a rotation around a horizontal axis through the middle of the domain in the photograph), thus the denser aqueous phase is placed above the less dense hydrocarbon phase.

Open-Boundary Experiments

Notice that the initial condition of the previous section only appears in **closed-boundary** experiments where a 180 degree rotation of the experiment domain is required to set the less dense buoyant oil phase from the top to the bottom, allowing it to rise. **Open-boundary** experiments do not have such initial condition as the buoyant nonwetting oil phase is injected from bottom and rises simultaneously as soon as it enters the domain. Figure 124 depicts the sequence of an open-boundary experiment.

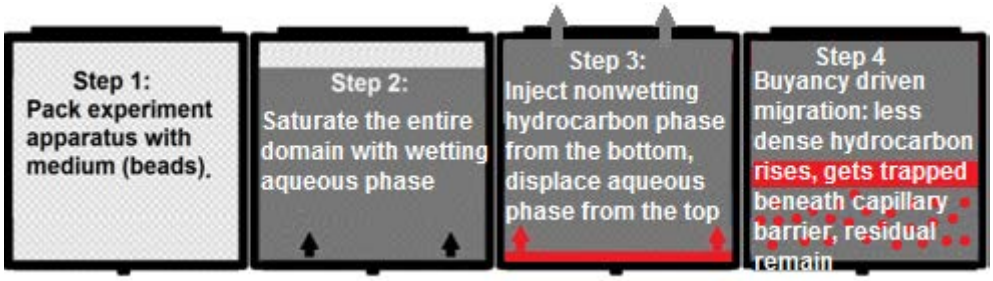

Figure 124: A graphical representation of the open boundary experimental design. The design calls for emplacing the nonwetting phase in a gravity-unstable manner (continuously filling from the bottom), open valves, then buoyancy drives the less dense nonwetting phase to move up until it reaches the capillary barrier and gets trapped.

Step 1: Packing the Experimental Apparatus. Packing procedure is similar to the step listed in Section *Closed-Boundary Experiments*. Beads of different sizes were placed in sequenced layer to achieve desired patterns of homogeneity or heterogeneity. Once the "envelope" is completely filled with beads, the top cap is then positioned and secured.

Step 2: Saturate with the Aqueous Phase. The fluid flow system at the bottom is connected to an aqueous phase reservoir, placed on a small table behind the experimental apparatus. To initiate aqueous phase flow into the bead pack, the aqueous reservoir valve is opened then the valves at the bottom of the envelope are opened. Flow into the bead pack is gravity driven. Time to reach complete saturation varied from minutes to several hours according to grain size, and the height of the aqueous reservoir. Air is displaced via the ports from the top.

Step 3: Inject the Hydrocarbon Phase (Drainage). The aqueous phase reservoir connected to the bottom is replaced by a hydrocarbon phase reservoir. So this red-dyed nonwetting hydrocarbon phase is then introduced into the domain from the bottom four ports, by gravity feed; at the same time the displaced aqueous phase leaves the system through the top valves and gets collected in a measuring cylinder via a tube. The hydrocarbon non-wetting phase will build up beneath the capillary barrier till a predetermined volume. The volume of hydrocarbon injected should equal to the volume of aqueous phase displaced (collected in the measuring cylinder). The subsequent fluid displacement will be physically analogous to the rise of CO_2 non-wetting phase in a saline aquifer as water displaced to fill the other spaces.

Step 4: Maintain/Manipulate the Pressure Boundary Conditions. All valves and ports remained open. The hydrocarbon reservoir connected to the bottom of the domain is then replaced by an aqueous reservoir, whose liquid level is at the same height as the top of the domain to maintain a hydrostatic pressure gradient across the system. Positions of the aqueous reservoir can be raised to increase the hydraulic potential gradient, and consequently the capillary pressure gradient across the system. Depending on the accumulated oil column height, the capillary pressure against the barrier is changing. Once the capillary pressure exerted by the oil column exceeds the entry pressure of the capillary barrier, oil invades the barrier and escaped from the system.

3.2.7 Types of Experimental Domains

Several types of homogeneous and heterogeneous domains were examined. Theoretically, the rising non-wetting phase should accumulate at a boundary between regions of different bead

sizes (if and only if the smaller beads are in the higher elevation region) until the height of the continuous oil column below the boundary imposes a capillary pressure equal to the entry pressure of the smaller beads in the region above the boundary. If more oil joins this column from below and thus increases the continuous column height, oil will leak through the boundary until the column height decreases to the critical height. The oil that remains below the boundary is an example of the local capillary trapping phenomenon.

Table 20 summarizes the characteristics of the different experimental domains used in this research and their objectives.

Table 20: Summary of Different Experimental Domains Studied in This Work

Exp	Beads Diameter (mm)	Domain Description	Objectives	Observation/Summary
1	0.5, 2, 3, 5	Patchy (closed system)	Influence of heterogeneity on LCT (closed system)	Accumulated oil column applies a P_c that cannot exceed the P_{c_entry} of top seal. LCT trapping is permanent.
2	0.045 sand, 0.25, 0.5, 2, 3, 5	Layered (closed system)	Influence of increased lateral length on LCT (closed system)	Maximum lateral correlation maximizes trapping. All the oil gets trapped in the closed system. Trapped oil column cannot escape the 0.25 mm seal because its applied P_c is less than P_{c_entry} of seal.
3	0.25, 0.5, 2, 3, 5	Patchy/ Layered (closed system), aqueous resvr raised to 84 cm higher than top of domain (open)	Persistence of LCT, forced imbibition	Increase lateral correlation increases trapping. Bead pack boundaries serve as preferential flow paths for rising fluids. Residual trapping is obvious, some LCT persisted after 10X increase in applied hydraulic gradient.
4	0.25, 0.5	Layered, Syncline seal, aqueous reservoir same level at the top, oil reservoir on floor.		Syncline seal combined with corner effect allowed some escape of trapped oil. LCT seal hold 90% of oil predicted. Via corner artifact the system lost much of the trapped oil under forced imbibition.
5	0.25, 0.5	Layered, anticline seal, fracture in seal, both reservoirs at the same level as the top.	Persistence of LCT, influence of fracture in seal.	Fracture in the seal serves as the preferential flow paths for rising oil.
6	0.25, 0.5, 2	Layered anticline seal, switching at long time from closed state to open state with hydrostatic potential boundary condition	Persistence of LCT, influence of shape of seal.	Long settling time made corner effect obvious. Thick 2 mm layer "stored" much oil which escaped from seal and should have been displaced out.
7	0.25, 0.5, 2	Layered anticline seal, switching at short time from closed state to open state with hydrostatic potential boundary condition		Short settling time reduces corner effect in the time frame of the experiment. Both reservoirs at the same level as the top. Permanence of LCT.
8	0.25, 0.5, 2	Anticline seal, closed state first, then open state when rising oil reached seal, influence of edge effect obvious		Corner effect is obvious. Local heterogeneity in the "store" section of the domain.
9	0.25, 0.5, 2	Anticline seal, open state for hydrostatic pressure gradient. Raising the aqueous reservoir gradually.	Persistence of LCT, threshold of breakthrough P_c.	Threshold escape pressure of oil from experiment is in agreement with the calculation. Corner effect is reduced.
10	0.25, 0.5, 2	Multiple anticline seal, fill and spill, open state, point source, artificial fracture in the seal	Persistence of LCT when the caprock is fractured.	Locally trapped non-wetting phase remain secure even when there is a fracture induced in close proximity in the caprock. Leakage in one part of the caprock does not affect the adjacent traps.
11	Seal: 0.25 (67%), 0.5 (33%), Store: 0.5 (50%) 2 (25%), 3 (25%)	Layered, anticline shaped seal. Both seal and store are made with mixture of different size of beads	LCT: Influence of degree of heterogeneity. Multi-distributed grain size in both seal and store region.	Closer step to mimic Nature, which has complicated heterogeneity. Coarser beads in the seal serve as leakage pathways for the trapped nonwetting phase. Initial step for quantification.
12	Seal: 0.25 (33%), 0.5 (67%), Store: 0.5 (50%) 2 (25%), 3 (25%)			
13	Seal: 0.25 (67%), 0.15 (33%), Store: 0.5 (50%) 2 (25%), 3 (25%)			

3.2.8 Experimental Observations[8]

Main observations from those experiments suggest that, when managed properly, almost all of injected nonwetting phase was immobilized locally by the capillary traps present in the heterogeneous porous media. Results show that the total nonwetting phase immobilized by local

[8] This section (Experiments 1-13) constitutes Project Deliverable 5.1 Experimental evaluation of extent of local capillary trapping that persists in heterogeneous porous media after top seal is ruptured

capillary trapping (LCT) mechanism in an open domain with hydrostatic pressure boundary condition could remain indefinitely.

Moreover the results demonstrate that local capillary trapping mechanism is persistent when the hydraulic potential is increased for the open boundary condition domain. This has huge and positive impact on the safety and security for storage.

In the following sections, each section header includes bead sizes and qualitative description of heterogeneity and boundary conditions, followed by a brief statement of objective of that particular experiment. For each experiment, the results are shown in time lapse series, to provide the reader a better understanding of the actual migration pathway of the fluids in the heterogeneous porous media.

In the text of this section, "seal" generally implies a continuous lateral region of small (fine) beads and "reservoir" or "store" implies a region of large (coarse) beads below the "seal."

Experiment 1 (0.5 mm, 2 mm, 3 mm and 5 mm, Patchy, Closed System)

Objective: Demonstrate Accumulation of Buoyant Phase in Local Capillary Traps

Four types of silica beads of different sizes are present in this packing in regions indicated in Figure 125 below; the darker colored beads are 0.5 mm in size while the lighter colored beads are 2 mm, 3 mm and 5 mm in diameter. The "patches" of larger-bead regions beneath 0.5 mm beads are expected to act as local capillary traps for the nonwetting phase as it rises from its initial emplacement at the bottom of the domain.

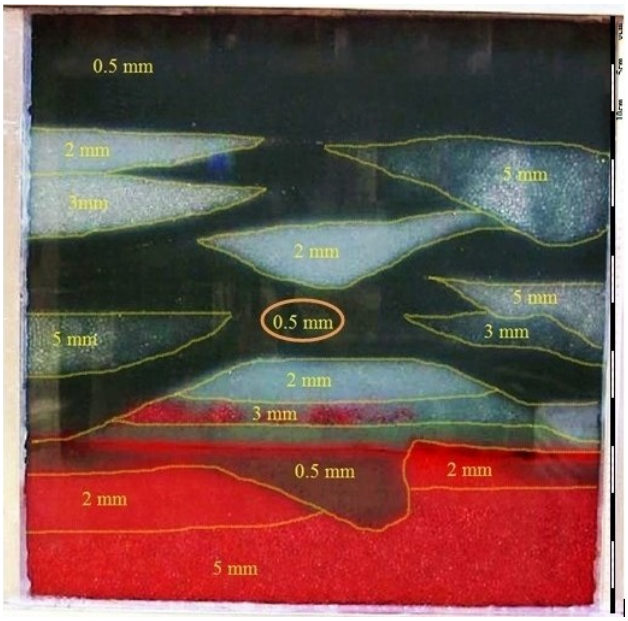

Figure 125: Initial condition of experiment in a heterogeneous domain with region boundaries outlined in yellow. Less dense non-wetting hydrocarbon phase (red-dyed) is about to rise and the denser wetting aqueous phase is to fall simultaneously.

Figure 126 shows a timed sequence of the buoyancy-driven countercurrent migration of the two immiscible fluids in a closed-boundary heterogeneous porous medium.

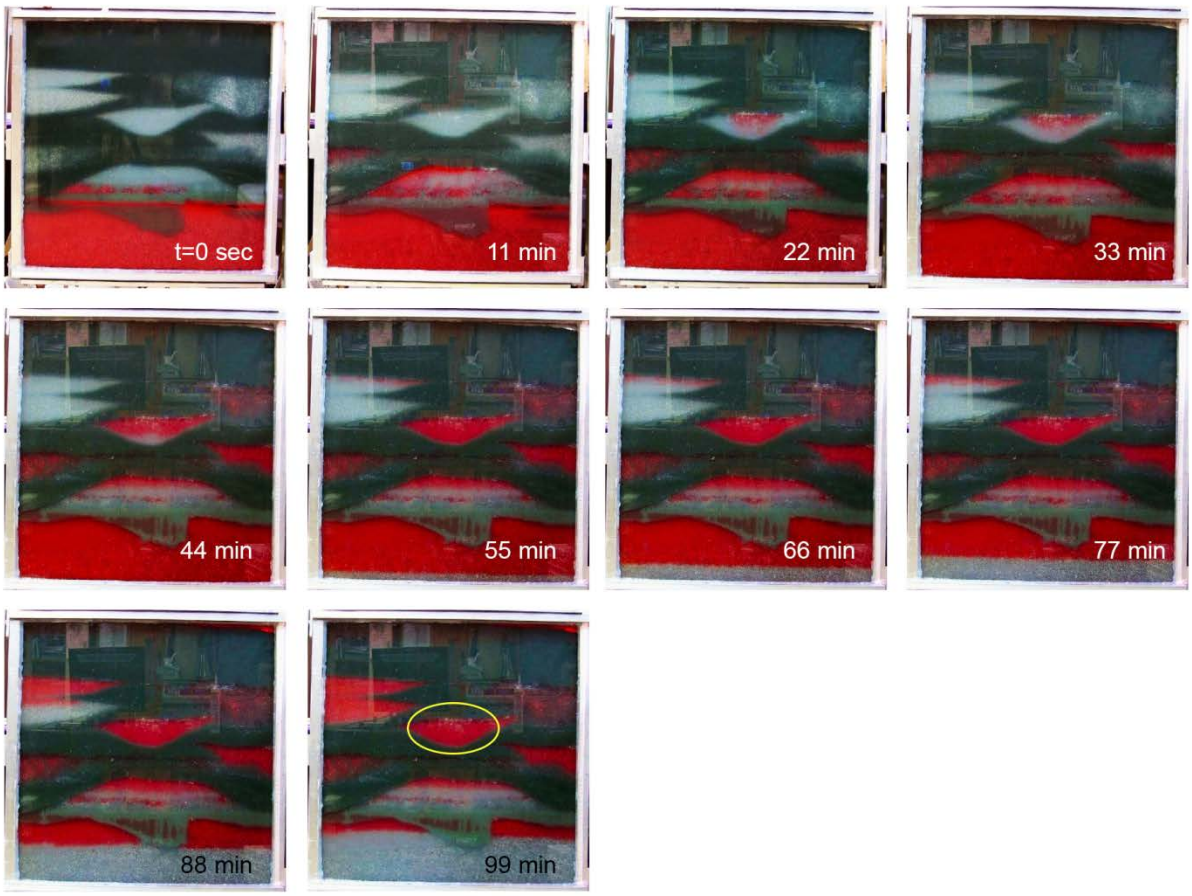

Figure 126: The sequence of snapshots chronicling the oil movement over a series of several hours, with 11-minute intervals between each snapshot in (a), and longer intervals in (b). Initially the hydrocarbon movement appears to prefer one preferential flow path (circled section in (a)). The total movement is fast at the beginning, and then slowed down. The most interesting observation is the accumulation of oil at the boundary of the bead sizes.

In this experiment, the rise of the hydrocarbon phase was fast for the first 100 seconds after flipping (the start of the experiment), then the migration slows down as the rising front

encountered the region of 0.5 mm beads (circled in Figure 125). It took 56 minutes for the hydrocarbon front to pass through entire domain and reach the top. It took about 150 minutes for the migration of fluids to stop.

The corresponding capillary pressures at the top of each oil column are smaller than the entry pressure of the capillary barrier above, as expected. For example, Area A in Figure 126(b) has an accumulated nonwetting phase column height of about 12 cm beneath the 0.5 mm bead layer. The column will exert $P_c = \Delta\rho gh$ =360 kg/m^3 × 9.81 N/kg × 0.12 m = 852 Pa, which is smaller than the entry pressure of the 0.5 mm barrier of 887 Pa (see Table 19).

After the migration of the red-dyed nonwetting phase stopped completely, the experiment domain was allowed to sit for a long enough period of time to make sure the trapped nonwetting phase stays in the trap permanently. A final snapshot was shown in the following Figure 127.

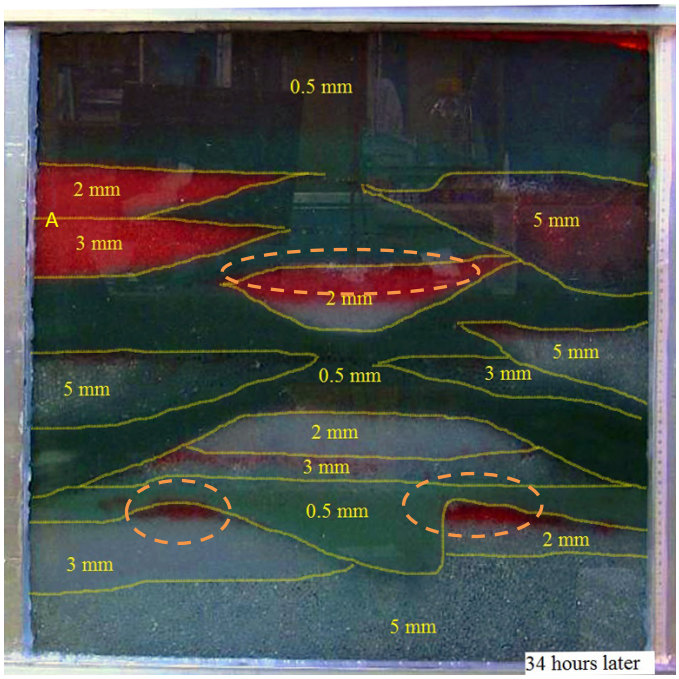

Figure 127: Oil migration almost completely stopped 3 hours after the experimental began. Oil has been trapped in coarse bead regions below boundaries with regions of sufficiently smaller beads. The circled sections appear to be where Local Capillary Trapping occurs. The configuration shown here from 34 hour is unchanged from the 3 hour observation. The circled sections illustrate local capillary trapping of nonwetting phase beneath boundaries of regions of smaller beads above larger beads.

Figure 127 shows that 34 hours after the flipping, the fluids remained at the same position as they did at the end of 3 hours; this confirmed that the oil accumulated at circled regions was trapped locally and permanently by the capillary barriers.

Previous work (Hernandez, 2011) suggested that the 0.5 mm beads may serve as an effective capillary barrier in this experiment. Nonetheless, a significant amount of oil migrated to the top of the domain (darker portion in the topmost section of 0.5 mm beads, Figure 127). The 0.5 mm beads can hold, in theory, a 25 cm oil column, if the beads are uniformly and tightly packed. In area A (top left in Figure 127), however, the observed oil column height is half the theoretical

value. This is because the entry pressure is smaller at the walls of the apparatus. The pores formed between beads and the walls at the left and right sides of the apparatus (where side wall meets front wall and back wall) are about twice the size of pores between beads. The hydrocarbon phase migrated along the side walls into the uppermost portion of the porous medium, establishing sufficient column height to backfill that part of the medium.

The results from this experiment offer promising and interesting insight. A geologic change to a finer grain size serves as a barrier to fluid flow; as explained in previous section, this is a result of capillary entry pressure. Finer grains create smaller pore sizes which result in higher capillary entry pressures. Nonwetting fluid cannot enter into the finer grain medium until the capillary entry pressure is exceeded. Thus a temporary barrier is formed; whether fluid held by this barrier can subsequently escape is an important characteristics of local capillary trapping.

Experiment 2 (0.045 mm, 0.25 mm, 0.5 mm, 2 mm, 3 mm and 5 mm, Layered, Closed System)

Objective: Demonstrate Extent of LCT Beneath Laterally Extensive Barriers

This experiment examines LCT beneath laterally extensive barriers. From Figure 128, when hydrocarbon phase rises from a coarser beads region to a finer beads region, the increasing entry pressure is sufficient to act as an barrier to hinder the flow temporarily, but insufficient to stop the flow. This causes the temporary build up of large saturations beneath each region. The overall migration of the oil phase is fast through the 5 mm, 3 mm and 2 mm region, but slows down in the 0.5 mm region, and completely stopped by the 0.25 mm layer. Figure 128 shows the beginning of the experiment.

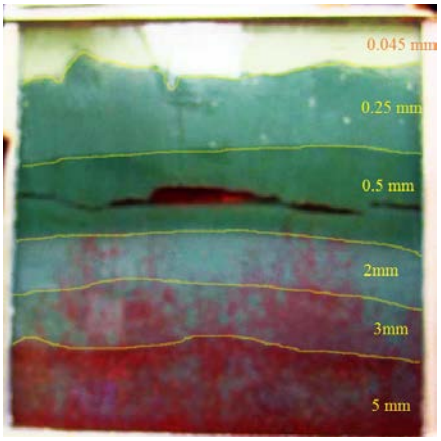

Figure 128: 4 seconds after the apparatus is flipped. Channeling of nonwetting phase is evident in the 5 mm, 3 mm and 2 mm regions. The cavities in the 0.5 mm region are artifacts due to the settling of the beads. Hydrocarbon phase (red) rises through a brine/glycerol mixture (1084 kg/m^3 and 7 mPa-s) saturated domain of hydrophilic (silica) beads. The beads vary in diameter, packed into a quasi-2D domain (0.6 m by 0.6 m by 0.03 m). Several preferential flow paths are observed. The cause is most likely non uniform packing.

Figure 129 shows the timed sequence for the migration of nonwetting phase through the experiment domain.

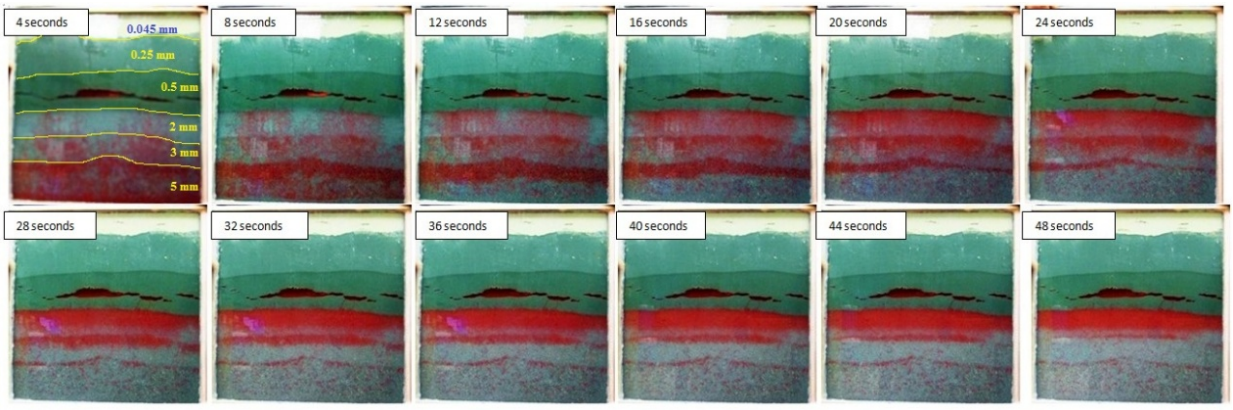

(a)

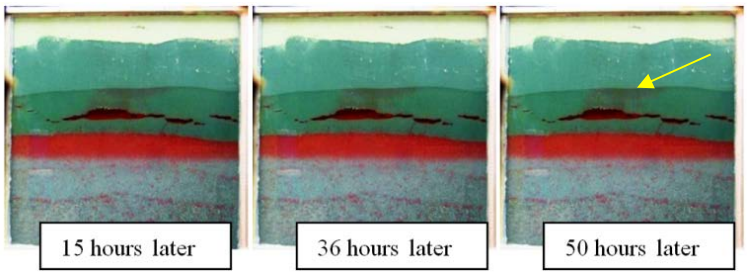

(b)

Figure 129: Timed sequence of images of Experiment 2. (a) First 48 seconds of the experiment. The cavities in the 0.5 mm region are formed by settling of the beads after apparatus was flipped at time zero. Several preferential migration paths are evident, likely due to heterogeneities introduced during settling; (b) Long time equilibrium states.

The system was nearly stabilized after 4 hours. Most of the hydrocarbon phase was trapped at the boundary between 2 mm and 0.5 mm layers. Over the course of two days, hydrocarbon migrated through the 0.5 mm beads to the boundary with 0.25 mm beads (see yellow arrow in Figure 129(b)).

Accumulation of oil at the boundary between 2 mm and 0.5 mm has an average column height of approximately 6 cm, corresponding to a capillary pressure of 212 Pascal, which is smaller than the entry pressure of 0.5 mm bead pack (667 Pa), as well as the entry pressure of 0.25 mm bead pack (1334 Pa). Oil entered cavities that formed in the 0.5 mm layer after the apparatus was flipped, and stayed there throughout the entire experiment period. The movement of beads that caused the cavities also created defects suggestive of shear bands, which evidently have a smaller entry pressure than the beads, especially where the defects contact the front wall of the apparatus. Oil migrated along these defects to the cavities.

Take a closer look at the last snapshot of the equilibrium state, as shown in Figure 130.

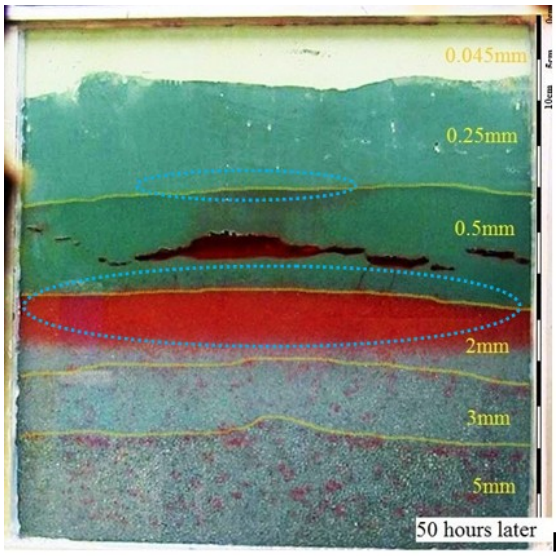

Figure 130: The circled sections illustrate local capillary trapping beneath boundaries where smaller beads lie above larger beads. Long lateral extent boundary provides a good trapping capability.

Migration also occurred to the 0.25 mm/0.5 mm boundary, apparently from the cavity in center of layer through the larger pores at the bead/front wall boundary. However, the oil column did not exert a capillary force that is greater than the entry pressure for the 0.25 mm bead pack and its boundaries.

Because 0.25 mm bead pack serves as a seal, the accumulation of oil beneath the 0.5 mm bead layer cannot be unequivocally attributed to local capillary trapping. That is, the oil in the 2 mm bead layer may be there only because the top of the oil column can migrate no further. If the seal at the 0.25 mm layer were compromised, some of the oil currently in the 2 mm layer may leak into the upper layers. The next experiment illustrates a method to test apparent local trapping for permanence, i.e. for being truly trapped locally.

Experiment 3 (0.25 mm, 0.5 mm, 2 mm, 3 mm and 5 mm, Patchy and Layered Heterogeneous Domain – Closed Counter Current Displacement)

Objective: Demonstrate Persistence of LCT Under Forced Imbibition

Part 1: Closed System

The porous medium in the third experiment was a hybrid of layers and regions of different bead sizes. The counter-current displacement of the two phases was initiated as in the previous experiments. After 30 hours, local capillary trapping is observed at various spots in the system, where buoyancy driven uprising oil has accumulated beneath the region of higher capillary entry pressure (see Figure 131).

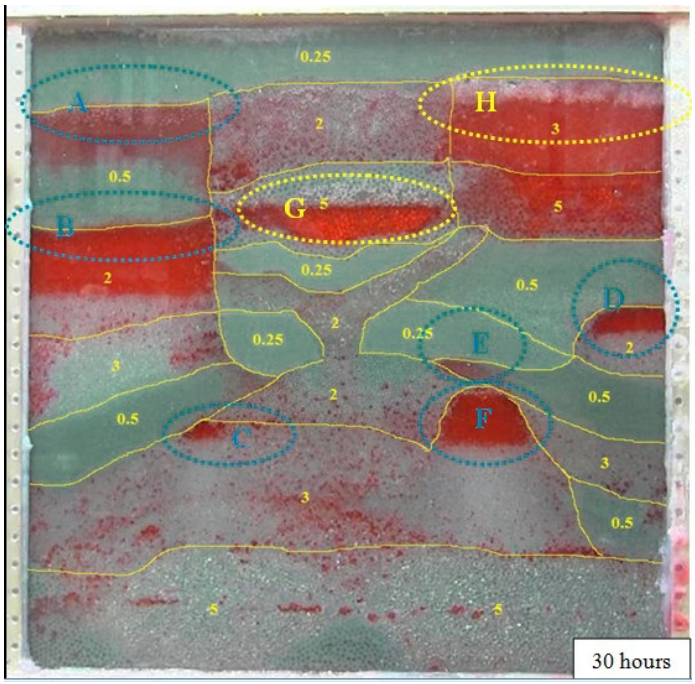

Figure 131: Nonwetting phase migration stopped within 30 hours after Experiment 3 began. The circled sections illustrate local capillary trapping of nonwetting phase beneath boundaries of regions of smaller beads above larger beads. Shorter lateral extent boundaries provide less trapping capability, compared to Figure 130. Numbers indicate bead sizes in mm.

The aqueous hydrostatic pressure gradient across the domain is $\rho_w g$ = 1084 kg/m^3×9.81 N/kg = 10.6 kPa/m and oil hydrostatic pressure gradient is $\rho_{nw} g$ = 724 kg/m^3×9.81 N/kg = 7.1 kPa/m. The system is at a closed state, which has a capillary pressure gradient of 10.6-7.1 = 3.5 kPa/m across the domain, such that the denser aqueous phase falls down and less dense oil phase moves up (counter current displacement) and finally reaches equilibrium. At equilibrium, the capillary pressure at top of an accumulated oil column is less than or equal to capillary entry pressure of beads above the oil column. The capillary pressure exerted by an oil column is equal to h_{oil_column}×3.5 kPa/m. For example, in Figure 131 region B, the oil column height is about 2.5 inches (0.0635 m), so the capillary pressure exerted by this oil column at its top is 0.0635 m×3.5 kPa/m = 222 Pa, which is less than the entry pressure of the 0.5 mm beads above (887 Pa, Table 19). Therefore accumulation occurs.

Late in this experiment, air entered the porous medium because of a leak on the lower right side of the apparatus. The air migrated to the upper portion of area G and H in Figure 131. Thus the trapping in area G and H involved a more complicated 3-phase interaction, not just the intended grain size variation as in Experiments 1 and 2. Nonwetting phase column heights are less than the nominal height that the corresponding bead layer could hold, consistent with edge effects at the walls of the domain controlling upward migration.

Part 2: Forced Imbibition of Wetting Phase From Bottom

After the migration of non-wetting phase stops (equilibrium was reached, Figure 131), top and bottom ports are opened and connected via Teflon tubings to reservoirs to impose a constant hydraulic potential across the domain. This enables, for example, forced imbibition of aqueous

phase from the bottom, with accompanying displacement of fluids from the top. This procedure measures the permanence of local capillary traps established during the earlier buoyancy-only displacement. That is, any nonwetting phase held in some region of the beadpack only because of boundary conditions such as closed valves will be able to migrate, whereas nonwetting phase truly trapped by local capillary barriers will not. Figure 132 depicts the schematics of the forced imbibition.

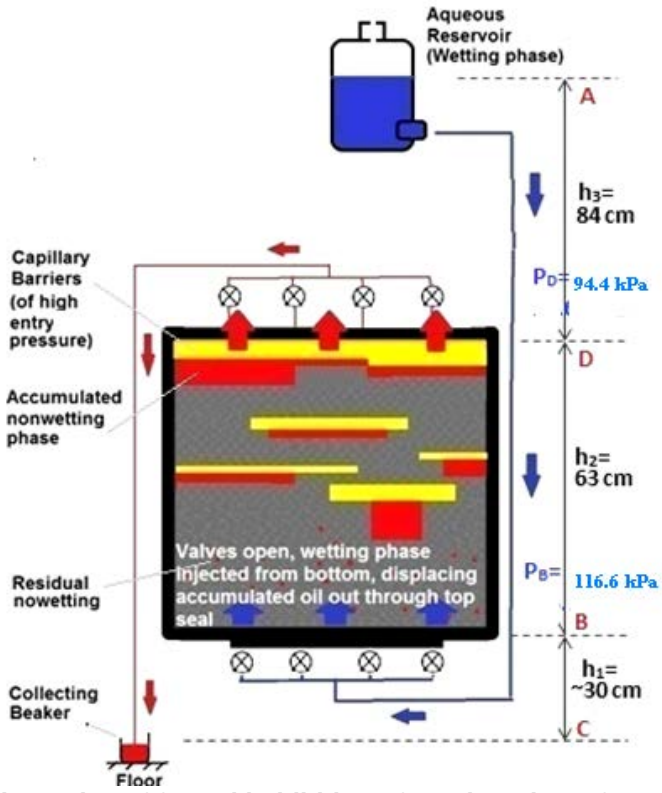

Figure 132: Schematics of forced imbibition of wetting phase from bottom. Valves at top and bottom are closed during the countercurrent movement of wetting and nonwetting phase, and after reaching steady state, the valves are opened to impose a prescribed hydraulic gradient across the domain.

After the valves are open, the aqueous reservoir provides a hydraulic potential difference across the domain. If the reservoir is positioned above the top of the domain, this hydraulic potential exceeds the original hydrostatic potential and thereby alters the capillary pressure gradient. For example, in this experiment the aqueous reservoir was positioned 84 cm higher than the top of the domain (Figure 132). The domain itself is 63 cm tall and is 30 cm above the floor. So the aqueous reservoir is 84 + 63 + 30 = 177 cm above the floor, and is open to atmosphere so P_A = 101 kPa. Pressure at bottom of the domain, $P_B = P_A+(h_A-h_B)g\rho_w$ = 101 kPa+(177 cm -30 cm) ×9.81 N/kg×1084 kg/m^3 = 116.6 kPa. The oil reservoir is placed at the floor and open to atmosphere, so h_C = 0 and P_C = 101 kPa. Similarly the pressure at the top of the domain is given by $P_D = P_C-(h_D-h_C)g\rho_{nw}$ = 101 kPa-(93 cm) ×9.81 N/kg×724 kg/m^3 = 94.4 kPa. Therefore the pressure gradient in the water phase across the domain = (116.6 kPa – 94.4 kPa)/ 0.63 m = 35.3 kPa/m (this will cause upward flow of water through the domain since it exceeds the hydrostatic gradient for the aqueous phase which is 9.81 N/kg×1084 kg/m^3 = 10.6 kPa/m). The capillary pressure gradient within oil phase held motionless in a local capillary trap is the water pressure

gradient less the oil hydrostatic gradient = 35.3 kPa/m – 7.1 kPa/m = 28.2 kPa/m. The accumulated oil column height multiplied with this capillary pressure gradient will give the capillary pressure exerted by the trapped oil column. For instance, the capillary pressure in a region of trapped oil that is 10 cm in height would be 2.8 kPa in the open system with these reservoir heights, much larger than its original value of 0.35 kPa in the closed system. Thus in addition to driving water through the domain (forced imbibition), this large increment of capillary pressure causes the locally held oil accumulations to exceed the seal capacity for most of local capillary trapping accumulations (see Table 19: capillary entry pressure of bead columns), and most of local traps got disrupted and only short columns survived (except where the presence of air helped block the advance of the oil phase).

Fluids were displaced through the ports of the top fluid flow system. In the following 22 hours, 1000 ml aqueous phase and 375 ml of hydrocarbon phase were displaced. No more oil was displaced after 22 h. The local capillary trapping of oil phase stabilized, as shown in Figure 133. Despite the much larger capillary pressure gradient, some oil remained trapped; this is consistent with the basic principle of local capillary trapping, namely that it occurs when P_c at top of oil column is less that $P_{c,entry}$ of porous medium above oil column. Figure 133 shows the equilibrium state for open boundary forced imbibition.

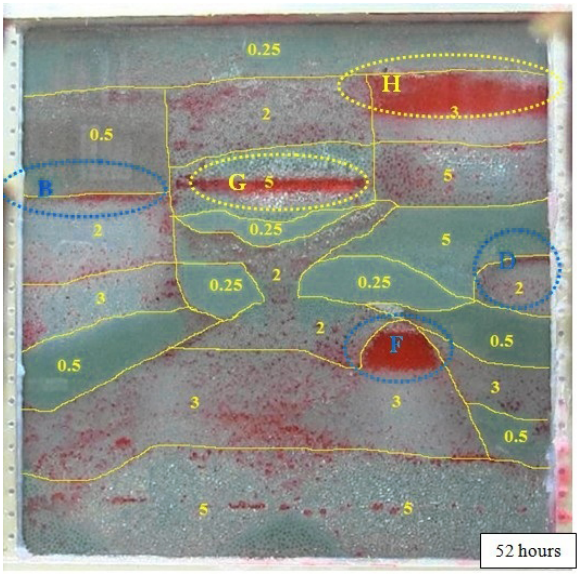

Figure 133: Oil migration stopped within 22 hours after boundaries were opened and a hydraulic pressure was applied to the stabilized configuration at 30 hours. The circled sections illustrate local capillary trapping that persists even during forced imbibition, which induces a larger capillary pressure in the oil phase. Inset gives elapsed time since start of buoyancy-driven displacement in closed system.

As explained before, the amount of oil held beneath the capillary barrier depends on the relationship between oil column height and P_c. The increased capillary pressure of most oil columns during forced imbibition causes most of the oil trapped at closed, hydrostatic conditions to flow out of the domain (compare Figure 133 to Figure 131). However, about 2 inches (5.08 cm) of accumulated oil still survived in Region H of Figure 133. The capillary pressure exerted by this remaining oil column = 5.08 cm × 28.2 kPa/m = 1432 Pa, which is still less than the entry pressure of 0.25 mm beads (1735 Pa, Table 19). This is consistent to the expectation and

demonstrates that LCT can persist after a large increment of capillary pressure, though the mass of buoyant phase trapped necessarily decreases.

Local capillary trapping holds buoyant phase below a capillary barrier, so theoretically it should be possible to move a large amount of nonwetting fluid from local capillary traps if the P_c is large enough (exactly what happened here). But even at the much larger P_c gradient, short columns of oil are still held in region B, D, F, G, and H, proving the persistence of local capillary trapping even with a significant amount of external force. It is also possible that the vertical boundaries between bead patches of different sizes served as preferential flow paths for the migration of rising liquids. In region B of Figure 131 and Figure 133, accumulated oil in the 2 mm bead layer did not penetrate the 0.5 mm bead layer when the forced imbibition was applied. Instead the oil migrated upwards along the vertical boundary of the two bead patches. The entry pressure of the vertical boundary between different bead patches is smaller than the bead patch itself, due to non-uniform contact of different sized beads, leaving larger inter-granular spaces. Therefore the rising nonwetting phase finds it easier to enter those spaces and flow along the vertical boundary with assistance from buoyancy.

Findings from Experiments 1, 2 and 3

The buoyancy driven migration path of the non-wetting phase is significantly influenced by the heterogeneity of the domain. Experiments show that the uprising oil plume will selectively fill up the regions with smaller capillary entry pressure (coarser bead patches) first, and accumulate beneath the capillary barrier formed by a region of smaller beads. Migration of buoyant phase through the barrier occurs when the phase column height times the capillary pressure gradient exceeds the entry pressure of the smaller beads, or the entry pressure of defects within the packing (e.g. caused when regions of beads settle after rotating the apparatus). Migration past a barrier can occur when the phase column height exceeds the entry pressure of the boundary between porous medium and wall of apparatus, which is smaller than the entry pressure of a region filled with beads (no edge effect).

Orientation of boundaries between regions affects the local trapping behavior (compare Figure 130 and Figure 131). Lateral boundaries serve as good barriers, while vertical bead boundaries serve as a connection between trapped regions and became the preferential paths for migrating flows. The observations validate predictions that increasing lateral correlation will yield more local trapping, while increasing vertical correlation will cause less local trapping. Experiment 2 (Figure 130) has the longest correlation length, and therefore the capillary barrier trapped most of the nonwetting phase. Experiment 1 (Figure 127) and Experiment 3 (Figure 131) have longer vertical correlation length than Experiment 2, and thus less nonwetting phase was trapped.

Because continuity of the non-wetting phase column along defects and walls can be difficult to discern, some observed accumulations of non-wetting phase cannot be unequivocally attributed to local capillary trapping. It could be the case that oil formed a continuous path all the way to the top of the domain and stopped flowing only because the ports at the top of the domain were closed. In other words, the valves at the top of the domain were acting as a “sealing formation” rather than regions of smaller beads in the domain. To test this idea, the boundaries of the apparatus were opened after reaching steady state and a constant hydraulic gradient much larger than hydrostatic was imposed. A significant fraction of the hydrocarbon was displaced, but a

substantial amount remained in the accumulations. This indicates that this trapping mechanism is indeed a capillary phenomenon.

Experiment 4 (0.25 mm and 0.5 mm, Layered Heterogeneous Domain)

Objective: Demonstrate Extent of LCT Under a Syncline-Shaped Seal with Hydrostatic Potential Gradient Followed by Forced Imbibition

Part 1: Closed System

The porous medium in the fourth experiment simply consists of only 2 types of beads: 0.25 mm and 0.5 mm. The 0.25 mm beads at the top of the domain form an effective seal. Dry packing was used in which the upper portion of the domain was initially dry when nonwetting phase was injected (compared to previous experiments where the entire domain was saturated with aqueous wetting phase first, injected nonwetting phase then displaces the wetting phase out), so that the entry of non-wetting phase into the top of the domain required air to be displaced simultaneously from valves at the top. This may facilitate trapping of air in the domain, and the clustering of beads at packing flaws. After the initial saturation, the closed boundary experiment started and is shown in Figure 134.

As shown in Figure 134, the oil migration in finer bead pack (0.5 mm) in this experiment exhibits less fingering than in previous experiments 1, 2 and 3, in which coarser beads (2 mm and 5 mm) were used. The plume rises in a relatively smooth front. The edge effect along the side wall, where beads meet the flat surfaces and the corner between them to form relatively large pores, is significant. Some oil “slipped” through the corners/edges of the apparatus which has smaller capillary entry pressure than the bead pack. This oil reaches the seal from the sides first (see frame at 30 min, arrows in Figure 134) and starts accumulating there. This is interesting because it means that the “edge effect” pores for the small beads, though larger than pores in the matrix of small beads, are still small enough to form a capillary barrier to the rising oil.

The boundary in the middle of the domain (blue arrow in Figure 134) was due to packing artifact, where the bottom half of the beads was saturated with oil (from dry fresh beads), and top half was saturated with water/glycerol (from dry fresh beads), resulting in a well-defined boundary (blue arrow in Figure 134, first frame). But the two distinct layers of oil are uniformly packed and considered connected, because there is no capillary barrier in the 0.5 mm layer.

As shown in Figure 135 the nonwetting fluid rests below the capillary barriers for over 10 days (245 hours) and migrates no farther, suggesting that this configuration is stable, which proves that the 0.25 mm bead pack served as an effective capillary barrier (seal). No oil migrated through this capillary barrier, which is a strong evidence of local capillary trapping. P_c exerted by the total 50 cm of oil column in the closed system = 0.5 m × 3.5 kPa/m = 1700 Pa, which is less than the entry pressure of 0.25 mm beads (1734 Pa, from Table 19).

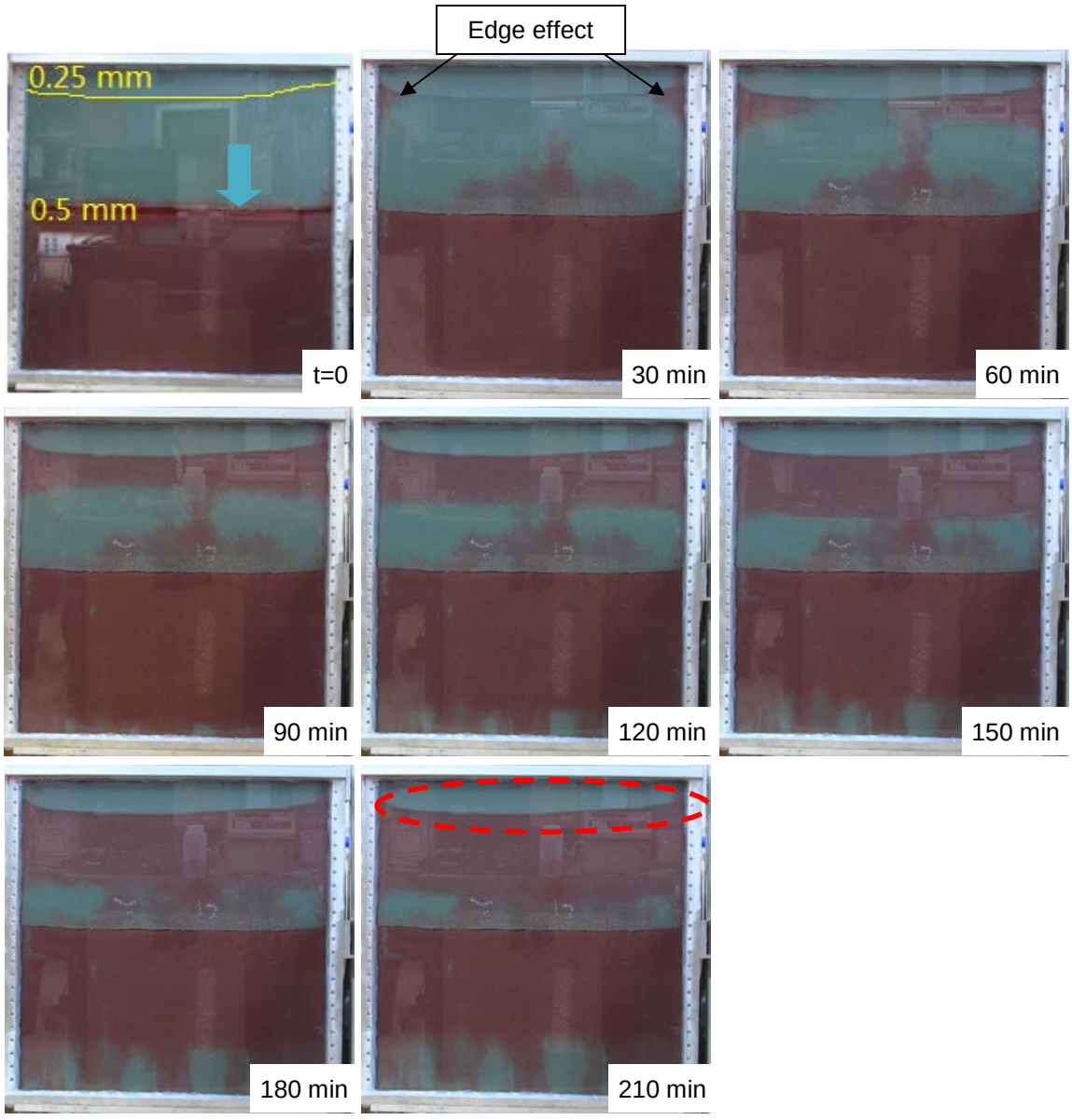

Figure 134: Photographs of first 3.5 hours of Experiment 4 (30 min interval). Oil was emplaced in bottom half of the domain, with initial oil phase/aqueous phase boundary (blue arrow pointing) within the 0.5 mm beads (t = 0). Subsequent oil migration driven by buoyancy stopped within 24 hours. Most oil was trapped beneath the boundary of 0.25 mm beads. Additional migration through these beads occurred because of packing artifacts (edge effect, see text above). The red dashed circle indicates local capillary trapping phenomenon in a closed domain.

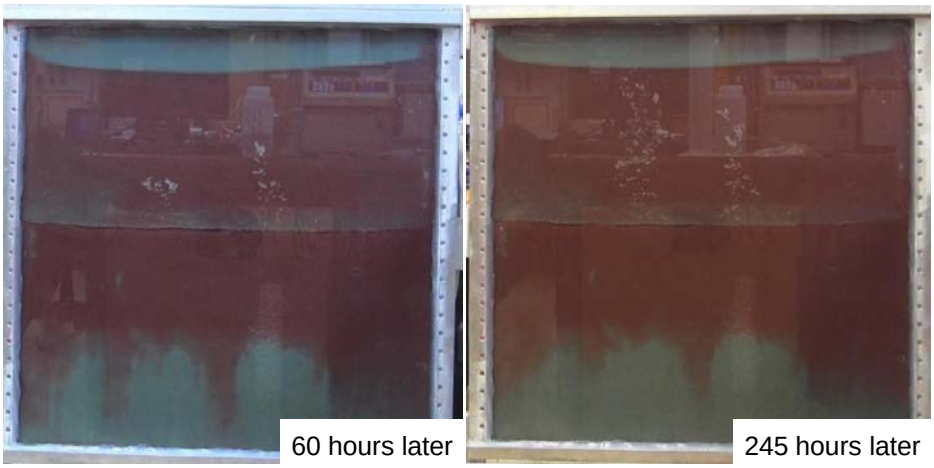

Figure 135: Late time / final fluid distribution of Experiment 4. No oil entered the 0.25 mm beads, consistent with predictions of local capillary trapping.

Part 2: Open Boundary Imbibition

At the end of the 245 hours, the top and bottom boundary were opened as indicated in Figure 136, and wetting phase is allowed to flow into the system from the bottom ports. The aqueous reservoir liquid surface was kept at the same height as the top level of the domain, such that the hydraulic potential provided by the aqueous reservoir is zero, i.e. no change from the hydrostatic state in the closed domain. The oil reservoir is at floor level and connected to the top ports, therefore the pressure at the top of the domain (outlet) is lower than the aqueous phase hydrostatic pressure. The oil phase in the outlet tube is continuous to oil phase inside the domain, therefore by analysis similar to previous experiment, there is driving force for aqueous phase to enter bottom and flow out from top, along with any mobile not trapped oil. Figure 137 shows results for the open boundary imbibition, which proves the driving force for the aqueous phase to enter from the bottom and flow out through the top exits.

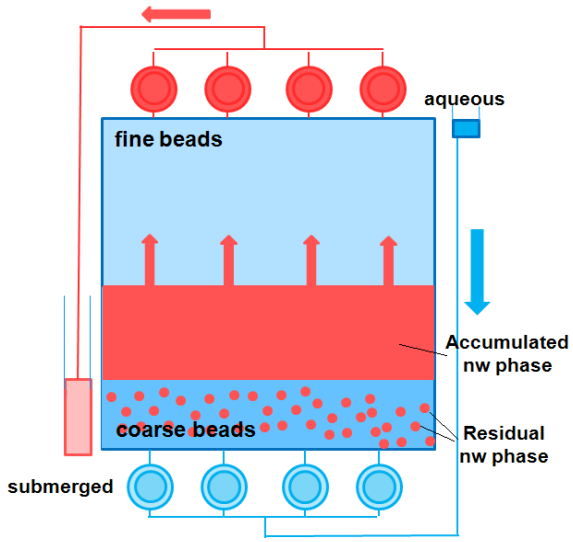

Figure 136: Schematic of the open boundary imbibition setup applied in part 2 of Experiment 4.

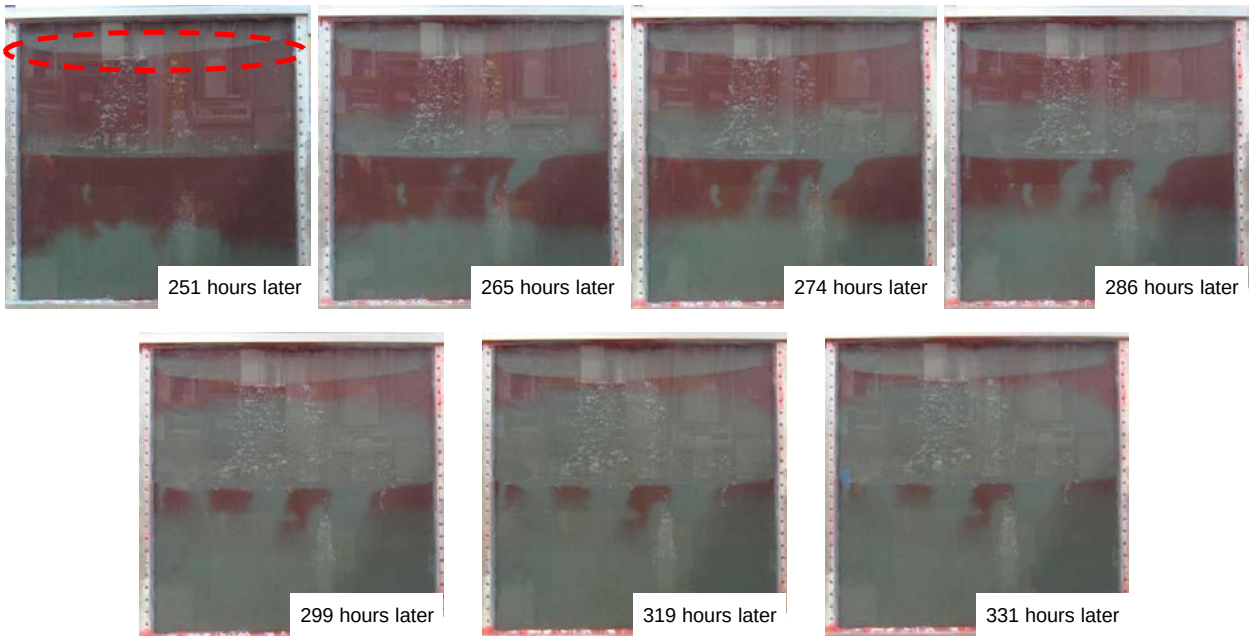

Figure 137: Snapshots of the open boundary imbibition of Experiment 4. Insets give elapsed time since start of buoyancy-driven displacement in closed system. Dashed ellipse (top left panel) indicates capillary barrier that held oil column during closed-boundary portion of the experiment, cf. Figure 135.

Due to the density difference between oil phase in the system and aqueous phase in the aqueous reservoir, oil still got displaced out of the system from the top of the domain, until equilibrium was reached. The exit line was filled with oil. The entering pressure at the bottom of the domain = 101 kPa + (93 cm – 30 cm) × 9.81 N/kg × 1084 kg/m^3 = 107.7 kPa. The exit pressure at the top of the domain = 101 kPa – (93 cm) × 9.81 N/kg × 724 kg/m^3 = 94.4 kPa. Capillary pressure gradient across the domain = (107.7 kPa – 94.4 kPa)/0.63 m – 7.1 kPa/m = 14.0 kPa/m (7.1 kPa/m is the oil hydrostatic pressure gradient).

In the next 80 hours of open boundary imbibition, most of the oil escaped the trapped region (see Figure 137). Capillary pressure exerted by the 50 cm oil column at the new capillary pressure gradient = 0.5 m × 14 kPa/m = 7000 Pa, which is much greater than the entry pressure of 0.25 mm beads (1735 Pa). Therefore capillary barrier is no longer effective to hold a 50 cm column of oil. With the aid from edge effect and the syncline shape of the barrier, oil was continuously leaving the domain until the 331st hour, when the configuration became stable. However, a considerable amount of oil still gets trapped at the boundary at the top; this again demonstrates that local capillary trapping has a certain level of persistence even when capillary pressure gradients change from initial emplacement conditions. The much shorter oil column compared to the closed state is consistent with the much larger capillary pressure gradient.

Experiment 5 (0.25 mm and 0.5 mm, Layered, Anticline-Shaped Seal, with Fracture in the Seal)

Objective: Demonstrate Persistence of LCT Under Influence of a Fracture in the Seal

The seal is a layer of fine beads (0.25 mm diameter) above the 0.5 mm beads which act as the storage formation. This time, instead of injecting oil into dry fresh beads, the entire domain was saturated with wetting phase first, such that the oil injected later will displace some aqueous wetting phase. Half of the domain was then filled with nonwetting hydrocarbon phase, displacing out equal volume of wetting phase. The beads settled during emplacement of initial wetting phase saturation. Upon flipping the apparatus 180 degrees (when Figure 138 was generated), a crack developed in the porous media on the left hand side and cavities developed on the right hand side (indicated by arrows in Figure 138), as the result of beads settlement. Upon flipping, less dense nonwetting phase quickly fills into the packing defects, as soon as the crack and cavities developed. Remaining nonwetting phase then starts to rise (t = 0). In the photograph the apparatus is in a closed state.

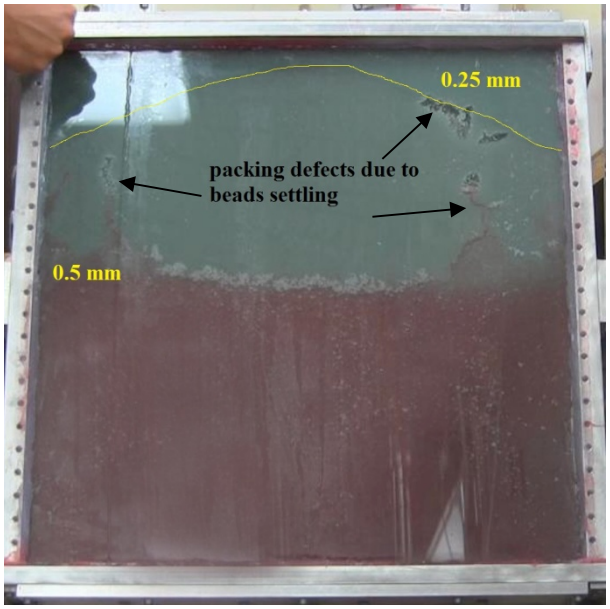

Figure 138: Initial condition of Experiment 5.

Part 1: Closed System

Preparing Initial Condition. After packing, two valves at the bottom were opened allow wetting phase to drain while non-wetting phase is directed via gravity into the domain through all 4 valves at the top. This creates a similar saturation and displacement environment as the actual storage aquifer where initially the entire formation is water-saturated and water wet, and then a nonwetting phase enters a portion of the formation, establishing its saturation by displacing wetting phase. This is an improvement to the previous experiment in reducing trapped air in the domain upon injection of wetting phase.

Countercurrent Buoyancy-Driven Displacement. After establishing the initial state in Figure 138, the domain is flipped so that the less dense oil phase rises in the porous medium. All valves are

closed, so that water descends in the medium as oil rises. As shown in Figure 139, the oil migration stops at the boundary between fine beads and coarse beads about 12 hours after beginning the experiments. The apparatus was left unaltered for another 10 days (240 hours), during which time no movement of oil was seen.

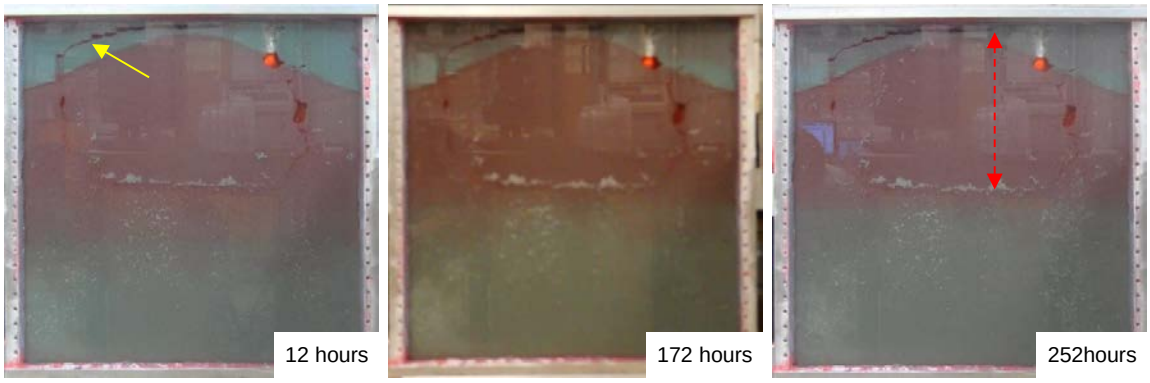

Figure 139: After the apparatus (Figure 138) is flipped, buoyancy-driven oil migration continued until oil gets trapped completely by the seal near the top of the domain. The yellow arrow (left panel) indicates the packing defect that is analogous to a fracture that would compromise the ability of the seal to contain buoyant fluid. The red arrow (right panel) indicates column height of oil phase held by the capillary entry pressure of the fine beads.

Almost all the oil gets trapped beneath the anticline shaped seal, even with a "crack" extending into the seal. The crack is visible in Figure 138 and Figure 139 as a dark streak within the fine-bead layer towards the top left part of the domain. It resulted from the settling of the saturated beads when the domain was flipped. Oil filled up the crack but could not enter the fine beads bounding the crack. The height of the accumulated oil column (as indicated by the double-headed arrow in right panel) is 28 cm, which corresponds to a capillary pressure of 824 Pa, which is smaller than 1334 Pa, the entry pressure of a matrix of 0.25 mm beads for these fluids.

This is a good indication that even if a defect developed in the seal, the storage is still safe, as long as the defect did not extend all the way through the seal, which in this experiment is the continuous lateral region of small beads.

A very little amount of oil "slipped" past the sealing formation via edge effects (smaller entry pressure where beads meet the side walls) to the top of the apparatus.

Part 2: Open Boundary Imbibition

At the 252nd hour, the valves connected to external fluid reservoirs were opened, such that the aqueous wetting phase reservoir is connected to the bottom of the domain while the nonwetting oil phase reservoir is connected with the top. Both reservoirs are open to atmosphere, and their liquid surfaces were at the same height as the system's top. Thus the gradient in potential in the aqueous phase within the domain remained unchanged from hydrostatic when the valves were opened. As shown in Figure 140, the position of the aqueous phase reservoir is chosen so that the aqueous phase potential at the bottom of the domain is the same whether measured through the aqueous phase domain or through the tubing connected to the reservoir. Though the gradient in potential in the aqueous phase does not change, the open valves now enable any immobilized oil due to boundary conditions (i.e. closed valves) from Part 1 to move. Oil that was immobilized

during Part 1 because of local capillary trapping, on the other hand, should not move simply because the valves are open.

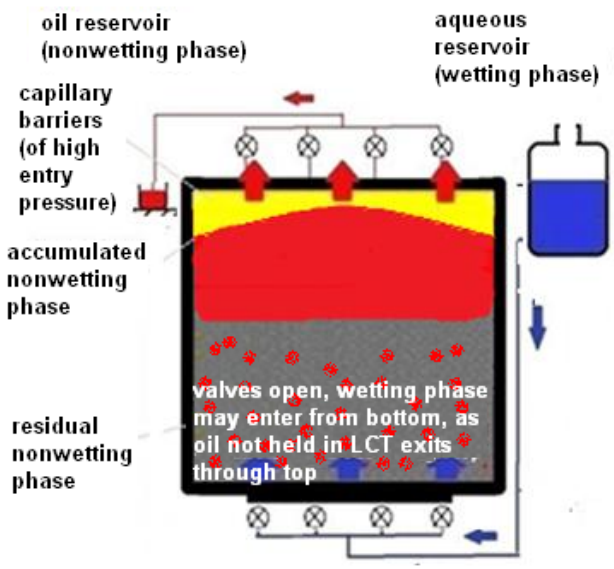

Figure 140: Open boundary portion of Experiment 5. The top and bottom valves are opened after buoyant migration ends in Part 1 of the experiment (see Figure 139). The liquid surfaces from both reservoirs are kept as the same height as the top of the system so that the hydraulic potential gradient in the domain does not change when the valves are opened. Any oil that was not immobilized by local capillary trapping during Part 1 can leave the domain through the open top valves.

The objective of this part of the experiment is to verify what would happen if the entire system becomes open. In Nature, the actual storage aquifer and the layers above and below it constitute an open system. The results are summarized in Figure 141 and Figure 142.

It took 12 hours for the system to re-equilibrate when it is switched from closed to open. Much of the oil phase that was immobile when boundaries were closed (Figure 139) leaves the domain through the open valves at the top. However the layer of fine beads was not invaded by any of this mobile oil (the region remains a translucent blue throughout the experiment), and some of the oil held beneath the sealing layer remains in place.

Two factors contributed to the movement of the oil phase when the valves were opened. One is the artifact of the “corner effect,” the second is the presence of a crack in the seal filled with fluid.

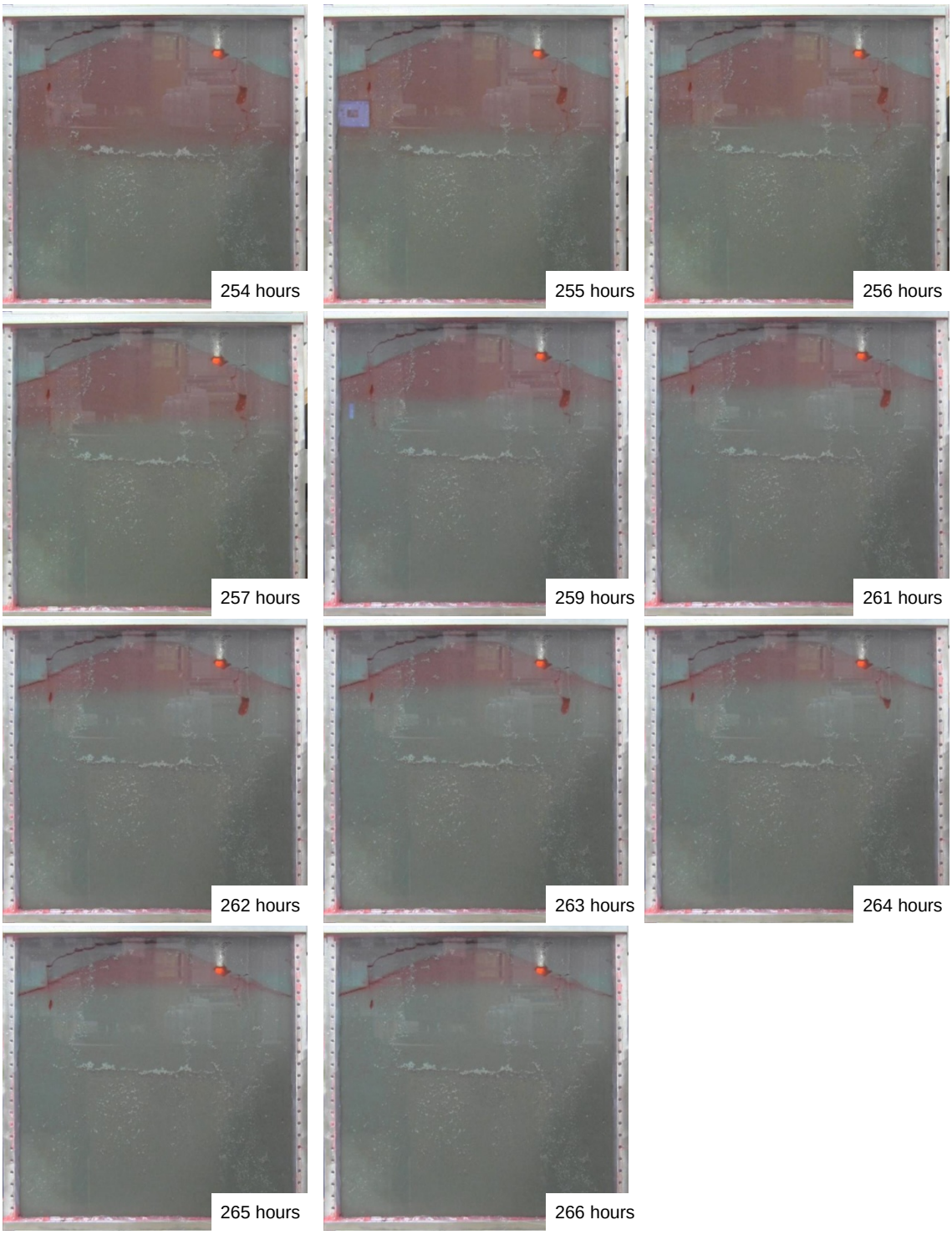

Figure 141: Snapshots of the open boundary imbibition of heterogeneous experiment with the anticline-shaped seal (Experiment 5). Insets give elapsed time since start of buoyancy-driven displacement in closed system.

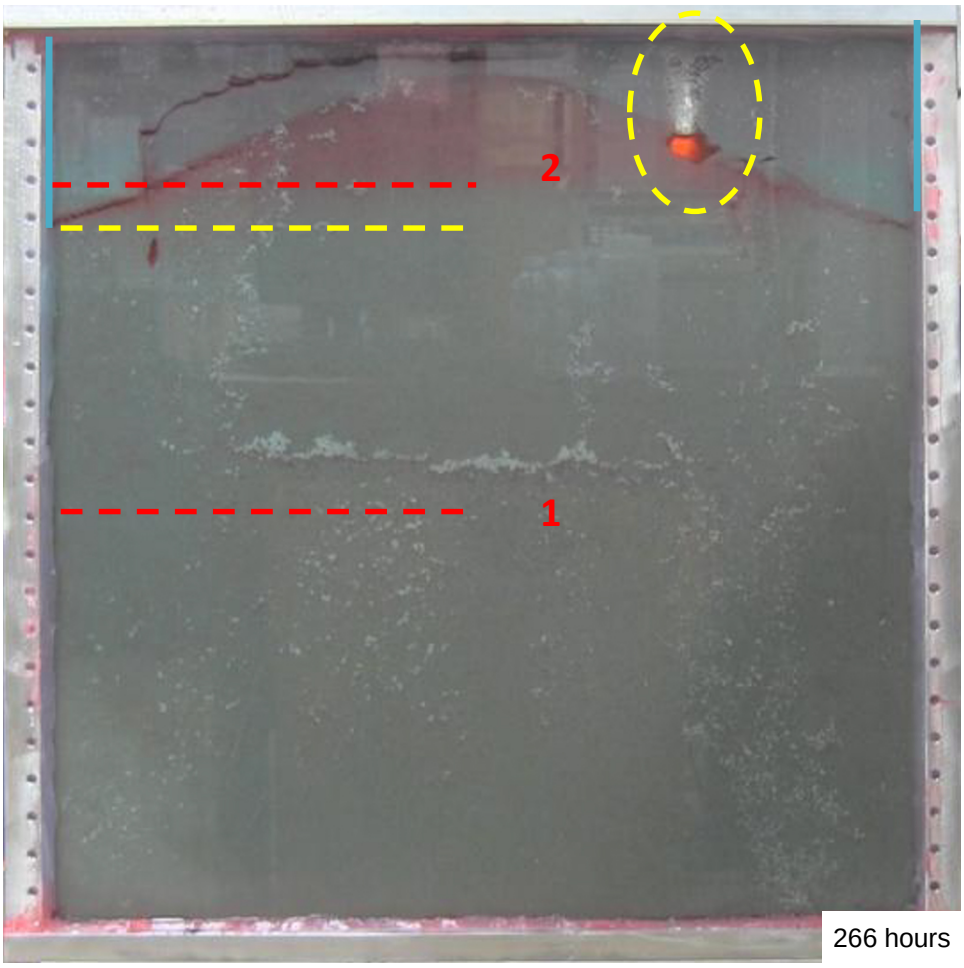

Figure 142: A closer look at the final stage (at 266 hours) of the open boundary imbibition when the system again reached equilibrium.

Corner Effect. Beads pack much less tightly in the corners at the left and right sides of the domain (two vertical blue lines in Figure 142). Consequently the capillary entry pressure into the upper part of the domain is significantly smaller at the corners. Thus the oil phase likely formed a connected path to the top of the domain along these corners during the closed-boundary buoyant migration (Part 1 of the experiment), though the oil was not able to drain into the layer of fine beads from the corners. When the system becomes open, oil can flow out the top along the corners. As long as oil in the 'storage formation' spans the width of the domain, that oil is connected to the corners, and leakage by this pathway can continue until the oil/water boundary reaches the level marked by the yellow dashed line in Figure 142. This is the level at which the coarse bead layer no longer extends across the entire width of the domain. The fact that some oil migration continues is discussed next in item (2).

We note that the connected path of oil in the corners effectively 'short-circuits' the capillary barrier of fine beads, and the fluid motion is controlled by basic hydrostatics. Due to density difference of the oil and aqueous phases, there should be spontaneous adjustment of liquids level to reestablish the equilibrium. This concept is summarized in Figure 143.

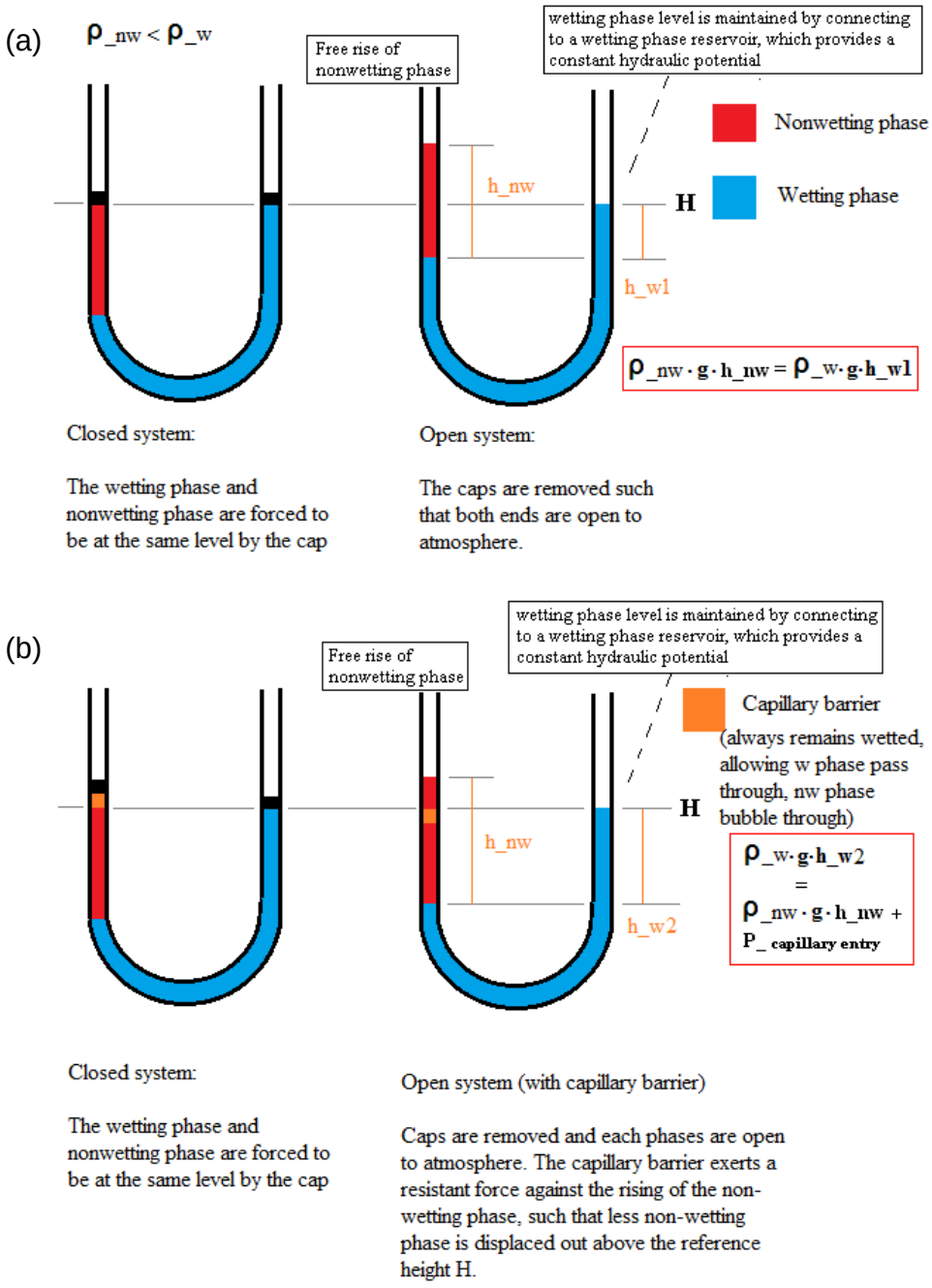

Figure 143: (a) Re-equilibration of liquid columns in a U-tube when the system is switched from closed to open. The tube radius is large so capillarity is negligible. Due to density difference ($\rho_{nonwet}<\rho_{wet}$), in the open system, $\rho_{wet}/\rho_{nonwet} = h_{nonwet}/h_{wet}$. (b) With a porous medium inserted to act as a capillary barrier in one arm of the tube (orange), the nonwetting phase in the open system does not rise as high above its level in the closed system as in (a). The principle of the porous medium is that it remains wetted and only allow nonwetting phase to bubble through (when the capillary pressure just below the porous medium exceeds the entry pressure $P_{c,entry}$. If wetting phase remains in the capillary barrier, then the nonwetting phase above the barrier won't be connected to nonwetting phase below. The example works only if the initial height of oil in the closed system gives a P_c in the closed system larger than the P_{c_entry} of the barrier.

The final extent of oil into the corners of the domain will depend on the level of oil held in the external reservoir. If the connected path of oil in the corners effectively 'short-circuits' the capillary barrier of fine beads, the situation is analogous to Figure 143(a), where the level of oil in the corner in the domain, $h_{nw} = \rho_w h_{w1}/\rho_{nw}$. If the oil in the corner doesn't "short circuit" the capillary barrier, accumulated oil column is disconnected by the capillary seal, and the oil level above the barrier should be lower than that without the barrier, because hydrostatic pressure at the bottom of the barrier decreases by an amount equal to the capillary entry pressure of the barrier. In Figure 143, the corner effects and the crack both 'short circuit' the capillary seal, therefore readjustment of the liquid in the system assisted the escape of nonwetting oil phase out of the domain.

The crack through the seal on the upper left part of the domain. After the valves are opened the oil/water interface keeps rising from its initial location (red dashed line 1 in Figure 142) until it reaches the level marked by red dashed line 2. The level corresponds to the intersection of the crack with the 'storage formation' of coarse beads. This suggests that some portion of the nonwetting phase flowed through the crack to the top of the domain (between the top cap and seal) as the experiment progresses, and was able to leave the domain when the valves at the top were opened. The cavity circled in yellow on the right proves this as well since no nonwetting phase flowed from this cavity out of the system. Nonwetting oil remains in the crack because the crack doesn't extend through the 0.25 mm beads all the way to the top of the apparatus. If the crack connected to the port at the top, oil should have kept flowing out of the crack because the entry pressure of the crack is smaller than the seal bead pack. There must be seal grains present between the top of the crack and the top of the apparatus, cutting off the crack.

This experiment shows the principles of local capillary trapping work in practice as well as in theory. Oil phase was held beneath the layer of fine beads in the open system. Oil phase that was originally located in the storage formation below the level where the crack intersects the storage formation escaped when the system was opened. The escape pathways were the relatively open (small entry pressure) regions at the corners of the domain and the crack (very small entry pressure) within the sealing layer. Though the seal integrity was compromised by these pathways, not all the oil escaped. Some oil remained trapped in the region below the undisturbed sealing formation even as water imbibed into the storage formation from below to replace the oil migrating out the top of the domain. This simple observation is representative of a region that would correspond to a single local capillary trap in a storage formation. Once CO_2 was held in such a region, it would not escape, regardless of what happens elsewhere in the domain.

The amount of nonwetting phase trapped beneath the seal varies from the closed system to the open boundary system. It is possible that in the closed system, when the oil gets trapped beneath the seal (Figure 139), the aqueous phase at the top of the domain (between top cap and seal) did not have flow paths available for counter-current displacement movement and thus remained held above the nonwetting phase; while in the open system, the aqueous phase at the top doesn't have to fall down (it can flow out the top), and the amount of oil trapped beneath the seal in open system may reflect the more accurate storage capacity by local capillary trapping of the particular formation. Therefore it is very important to apply the hydrostatic open boundary condition when estimating the total storage capacity and extent of persistence of the trapping mechanism. A confined closed-state storage space is seldom seen in Nature, while it is possible in the quasi-2D experimental apparatus. Therefore in the subsequent experiments, results

obtained with open boundary hydrostatic condition applied are of primary importance for studying LCT.

Findings from Experiment 4 and 5

Compared to Experiments 1, 2 and 3, where bead sizes range from 5 mm to 0.25 mm and the degree of heterogeneity is high, Experiments 4 and 5 used less bead variety (only 0.5 mm and 0.25 mm, and degree of heterogeneity is low). Reducing the bead size resulted in a smoother rising front of the non-wetting phase in the storage reservoir (Figure 134), instead of fingering through domains with large bead sizes observed previously (Figure 129). The smoother front increases storage efficiency, as reducing the preferential flow will increase the total amount of non-wetting phase stored beneath the capillary barrier.

The small beads (0.25 mm) are very effective seal for the dimensions of this apparatus (which limit the height and therefore the maximum capillary pressure in an oil-saturated region). Almost all the non-wetting phase is trapped beneath regions formed by these beads.

The local trapping mechanism is still stable even when there is a crack in the seal, as long as the crack doesn't extend all the way through the seal to top of the domain to provide a preferential flow for the rising fluid (Experiment 5).

Experiment 6 (0.25 mm, 0.5 mm and Thin 2 mm Region, Layered, Anticline-Shaped Seal, Switching at Long Time from Closed State to Open State with Hydrostatic Potential Boundary Condition Applied)

Objective: Demonstrate Influence of Open Hydrostatic Potential on LCT

Part 1: Closed System

The configuration of seal/reservoir heterogeneity examined in Experiment 5 was also used in Experiment 6: anticline-shaped capillary seal made of 0.25 mm beads. In Experiment 6 an additional layer of 2 mm beads (larger and transparent) was put at the top of the domain above the 0.25 mm beads to provide visual aid if there is any accumulation of nonwetting phase at the top.

In the closed system, rising nonwetting phase was locally trapped by the seal, and no visible nonwetting phase accumulated in the 2 mm region at the top of the domain in the early stage (first two hours). The results are summarized in Figure 144 and Figure 145.

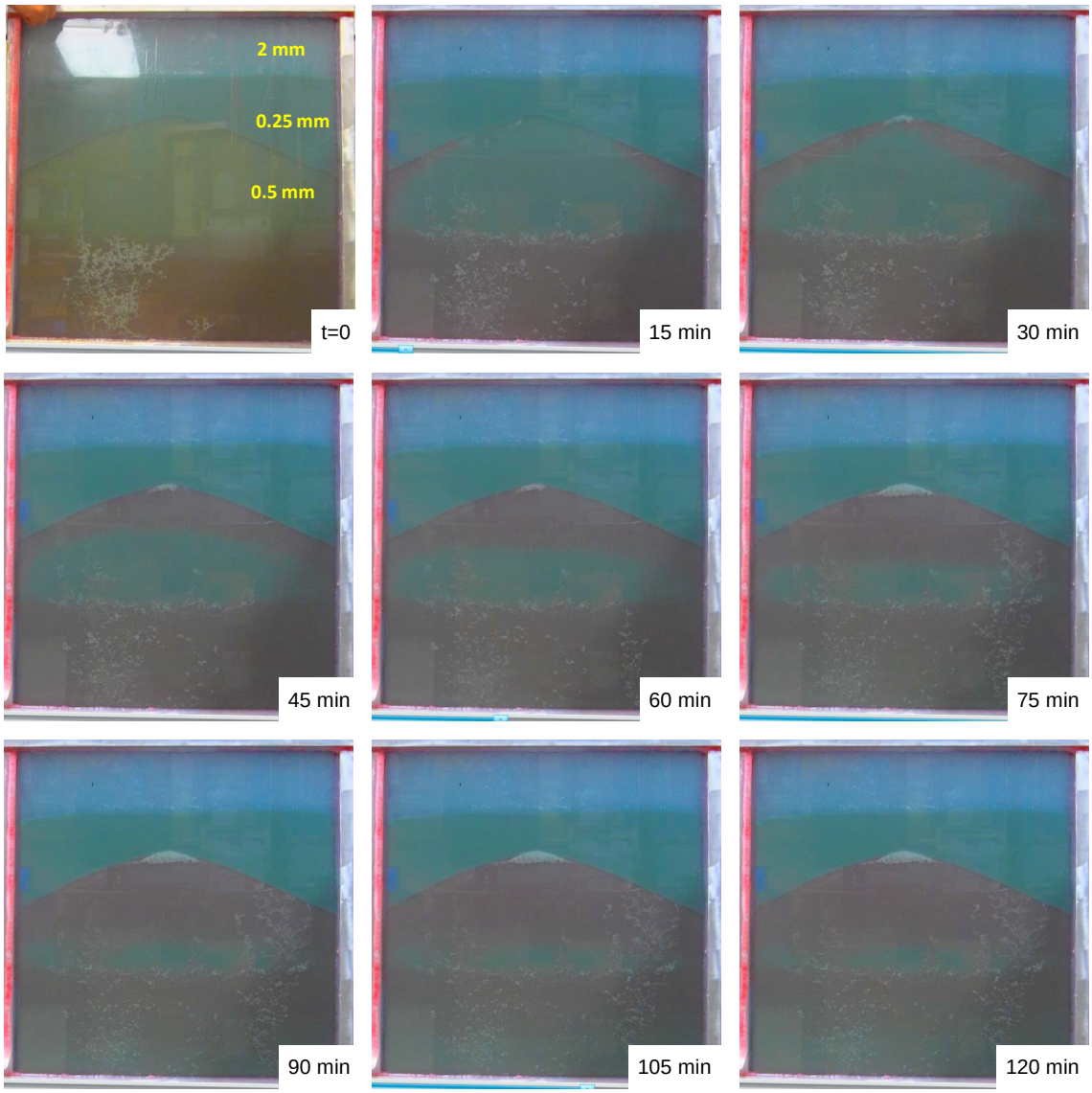

Figure 144: First two hours of Experiment 6 (closed system). Rising nonwetting phase plumes were trapped by the capillary seal (0.25 mm beads) and accumulation beneath the seal happens. No escape of nonwetting phase to the 2 mm layer at the top occurred during this time frame. Insets give elapsed time since start of buoyancy-driven displacement in closed system.

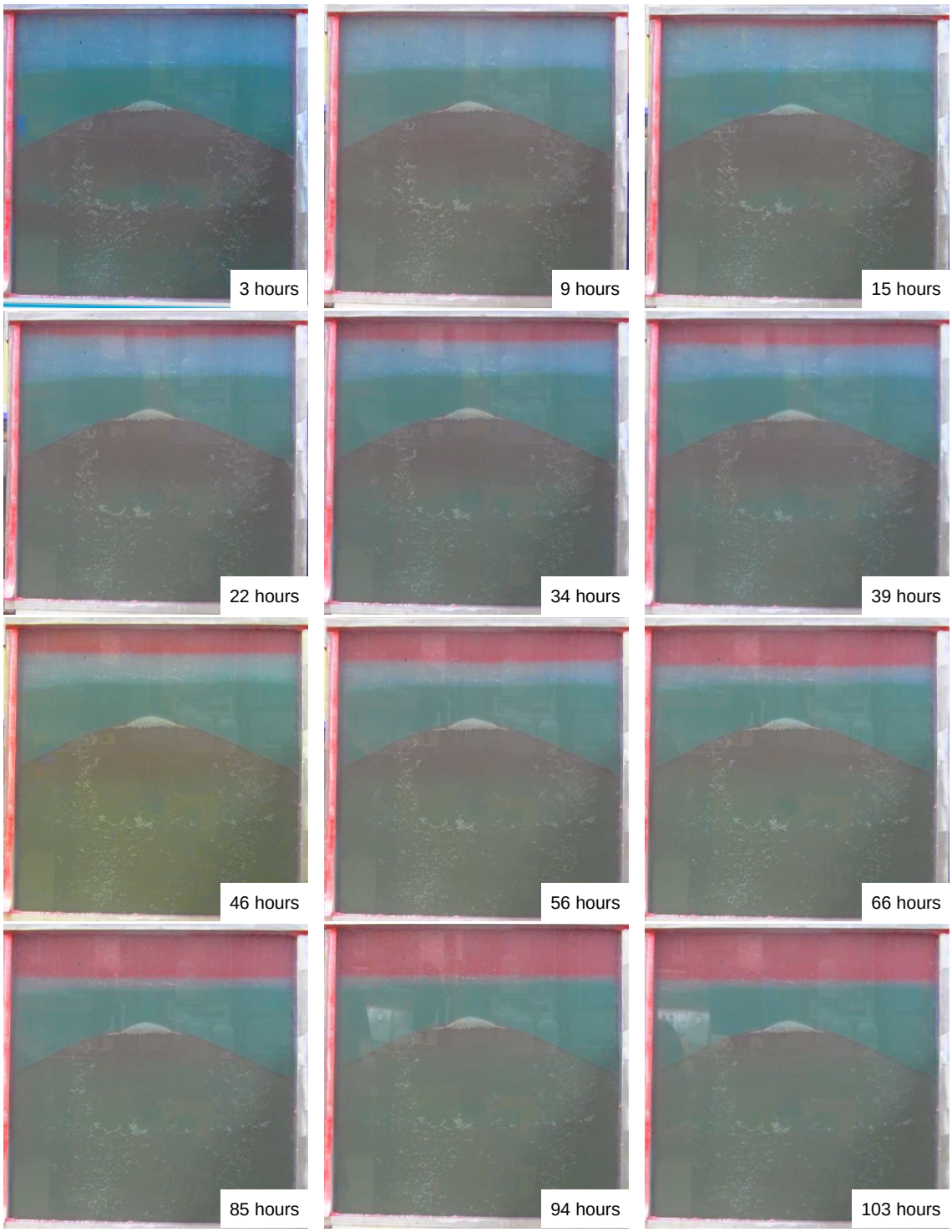

Figure 145: Later hours of Experiment 6 (closed system). System remained closed, but between 9 and 15 hours accumulation in the 2 mm layer increased, suggesting migration of the nonwetting phase along the corners of the domain. Insets give elapsed time since start of buoyancy-driven displacement in closed system.

The accumulation of nonwetting phase in the top layer in the late time period of this experiment (Figure 145) indicates there must be flow paths from the storage formation (beads below the

fine-bead layer) to the top 2 mm layer. However there is no visible crack/fracture found in the fine-bead layer, therefore a reasonable deduction would be the corner effect discussed above for Experiment 5, which enables the slow migration of the nonwetting phase through channels of smaller capillary entry pressure in the corners of the apparatus where the front glass plate, the aluminum side and the beads meet. The oil in the top layer is not held by local capillary trapping, but by the closed ports at the top of the apparatus. Note that oil within the storage formation remains held beneath the fine bead layer and does not invade the fine bead layer from the corners neither from below nor from above via backfilling as oil accumulates in top layer of 2 mm beads. Moreover oil remains held in the 'storage formation' layer of beads beneath the fine-bead sealing layer.

Part 2: Open Boundary Imbibition

At the 200th hour, the valves connected to the reservoirs opened so that potentially mobile nonwetting phase (i.e. not held in local capillary traps) can migrate or escape. As shown in Figure 146, a small amount of nonwetting phase in the top 2 mm layer left the system and entered the reservoir connected to the top ports. In the following 8 hours (until 208th hour), the system re-equilibrates with no more nonwetting phase leaving the system. The cessation of movement of oil out of the domain in this experiment is striking compared to the much greater movement in Experiment 5. The reason is that the 2 mm layer enabled all the oil connected to the corners in the storage formation to rise along the corners while the domain was closed. Thus there was no potentially mobile oil in the 'storage formation' layer of beads when the valves were opened. In this sense this experiment also confirms the local capillary trapping phenomenon. The oil held beneath the capillary seal of the fine-bead layer remained there even when oil held above migrated out of the system and water migrated into the system from below to replace that oil. The trapping is local: as long as the capillary pressure remains below the capillary entry pressure for the local barrier, the movement of fluid(s) elsewhere in the domain does not affect the trapped nonwetting phase.

Figure 146: Open boundary imbibition of Experiment 6. Insets give elapsed time since start of buoyancy-driven displacement in closed system.

Experiment 7 (0.25 mm, 0.5 mm and thin 2 mm Region, Layered, Anticline-Shaped Seal, Switching After Short Elapsed Time from Closed State to Open State with Hydrostatic Potential Boundary Condition Applied)

Objective: Demonstrate Persistence of LCT Under Open Hydrostatic Boundary Conditions

Experiment 7 was conducted with the same bead arrangement as Experiment 6: the 0.5 mm beads comprises the 'store', 0.25 mm beads comprises the 'seal', and the large 2 mm beads formed a top layer above the seal to visualize any un-trapped nonwetting phase bypassing the seal. The only difference is that this top 2 mm bead layer is thinner compared to Experiment 6, which would "store" less amount of escaped nonwetting phase while still providing visual aid to accumulation.

The entire domain was first saturated with wetting phase, and then non-wetting phase was injected from the top, displacing about half of the wetting phase. After nonwetting phase injection finished, all valves are closed. And the domain is in its initial condition, for which a 180 degree rotation will start the experiment.

Part 1: Closed System

In the first hour, rising plumes of nonwetting phase hit the seal layer and accumulated beneath it. See Figure 147 and Figure 148.

The closed system reached equilibrium in about 3 hours, meaning no more liquid movement. Countercurrent displacement of wetting and nonwetting phases stopped. As shown in Figure 148 almost all nonwetting phase was trapped in the coarse-bead region beneath the capillary barrier formed by the fine-bead region. In addition, a fair amount of nonwetting phases remained trapped as a residual saturation in the lower portion of the initially saturated region of 0.5 mm beads.

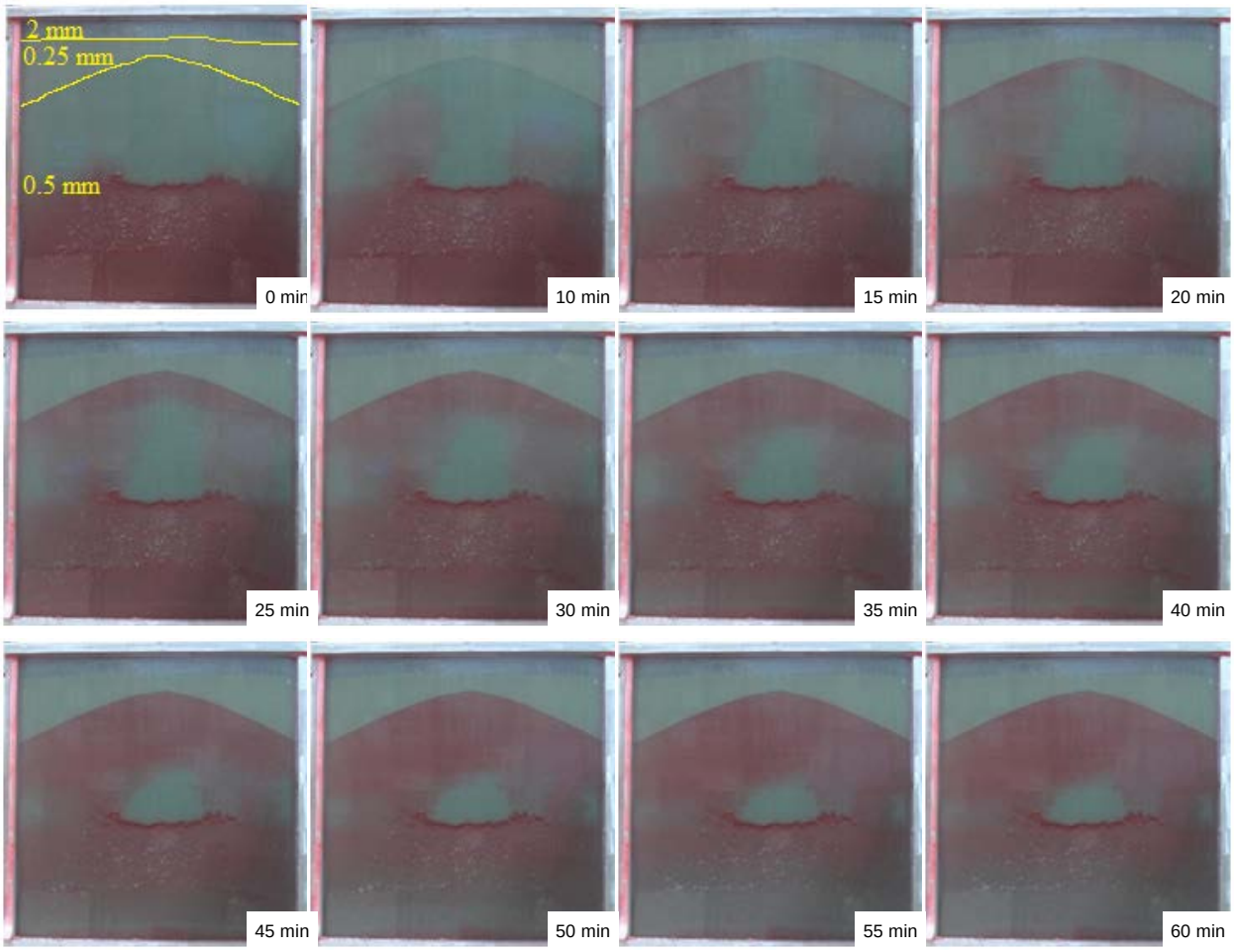

Figure 147: First one hour of experiment 7 (closed system). Insets give elapsed time since start of buoyancy-driven displacement in closed system.

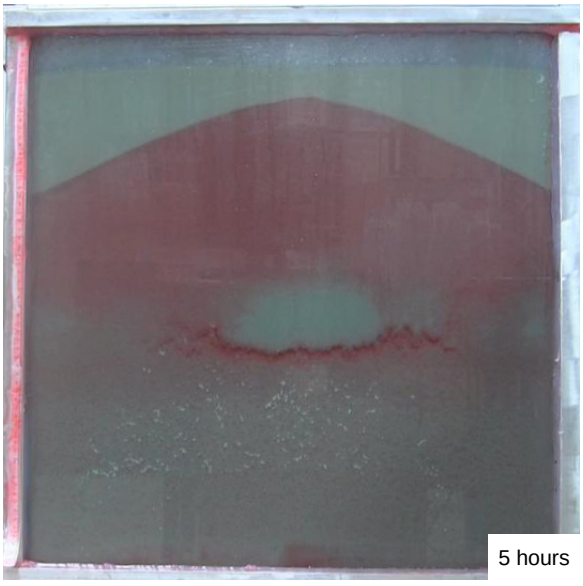

Figure 148: Equilibrium state of the closed system. System reached equilibrium in 3 hours. Insets give elapsed time since start of buoyancy-driven displacement in closed system.

Part 2: Open Boundary Imbibition

From Experiment 6, the corner effect became apparent at about 9 hour. To reduce this artifact, the open boundary imbibition stage of Experiment 7 was conducted starting from the 9th hour. Hydrostatic pressure boundary condition was applied by connecting the aqueous reservoir to the bottom of the domain and keeping its liquid level the same as the top of the domain. Results are summarized in Figure 149.

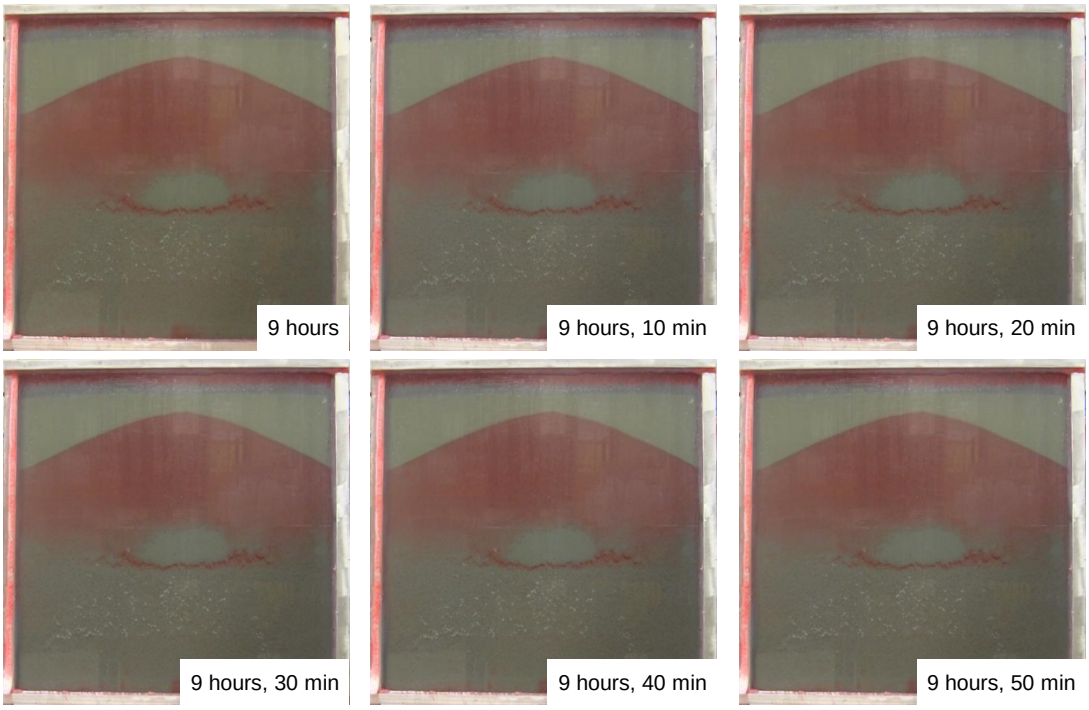

Figure 149: (a) First hour of the open boundary imbibition. (b) Stabilized open system under hydrostatic potential. Insets give elapsed time since start of buoyancy-driven displacement in closed system.

Although migration of oil from the 'storage formation' to the topmost layer of 2 mm beads was facilitated by the opening of the valves, very little amount of nonwetting phase was displaced out of the apparatus. No migration of oil from the storage layer through the interior of the sealing layer occurred. This confirms that 0.25 mm bead layer served as a good capillary barrier, and

local capillary trapping is persistent even in open systems in which the fluids are at hydrostatic potential gradient, i.e. buoyancy-driven displacement is possible but no pressure-driven flow of either phase is imposed.

Experiment 8 (0.25 mm, 0.5 mm and thin 2 mm Region, Layered, Anticline-Shaped Seal, Closed State at First, Then Open State when Rising Oil Reached Seal, Corner Effect Obvious)

Objective: Demonstrate Extent of LCT in a Direct Open Boundary Domain

As shown in previous experiments, interpretation of the extent and the durability of local capillary trapping in these experiments has been complicated by the ability of the nonwetting phase to rise through packing defects (larger than average pore throats) at the corners of the container holding the beads. In an effort to reduce this effect, the apparatus (the Pyrex glass containment box) was sent for modification. Two quarter-inch-wide (0.635 cm) two-feet-long (60.96 cm) hydrophilic metal (aluminum) bars with square cross section were cut diagonally and glued to the inner corners of the glass containment box using silicone gel. Figure 150 shows the modification. The idea is that the oblique angle between the aluminum piece and the glass wall will enable the glass beads to pack more tightly than in the right-angle corners of the earlier version of the containment box.

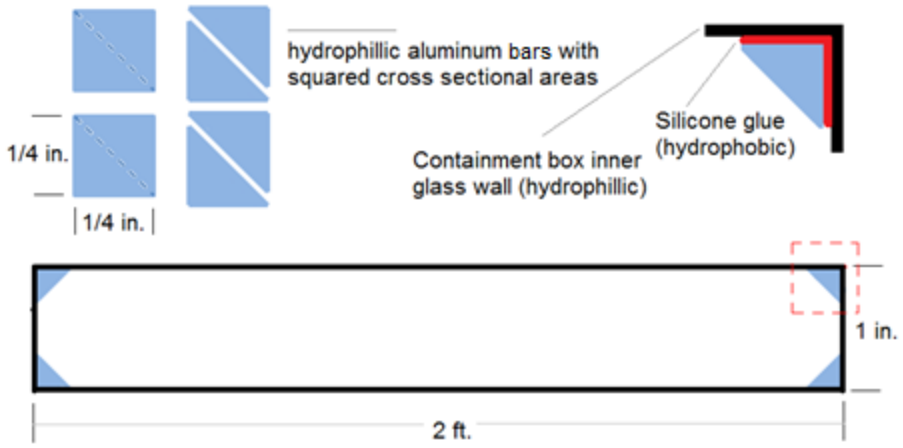

Figure 150: Modification to the experimental apparatus for reducing corner effects. Square corners in original apparatus allow beads to pack loosely and thus introduce regions with relatively large pore throats, through which nonwetting phase can migrate even when it is being held by beads acting as capillary barrier elsewhere in the apparatus. Reducing the angle between flat boundary faces at the corners should reduce the size of pore throats between beads and those faces, making nonwetting phase migration less likely.

Experiment 8 was then conducted with the same beads arrangement as previous experiments: the 0.5 mm beads comprises the ‘store’, 0.25 mm beads comprises the ‘seal’, and the large 2 mm beads formed a top layer above the seal to visualize any un-trapped nonwetting phase bypassing the seal. Difference is that the apparatus now has been modified, intended to reduce the edge/corner effect.

The entire domain was first saturated with wetting phase, and then non-wetting phase was injected from the top, displacing about half of the wetting phase. After nonwetting phase injection finished, all valves are closed. And the domain is in its initial condition, for which a 180 degree rotation will start the experiment.

Part 1: Closed System

Experiment 8 was conducted with a thin top 2 mm beads layer, a 0.25 mm beads seal and a 0.5 mm beads store. The anticline store is proven to be effective for trapping. Figure 151 presents a series of photographs of the closed boundary buoyant counter-current movement.

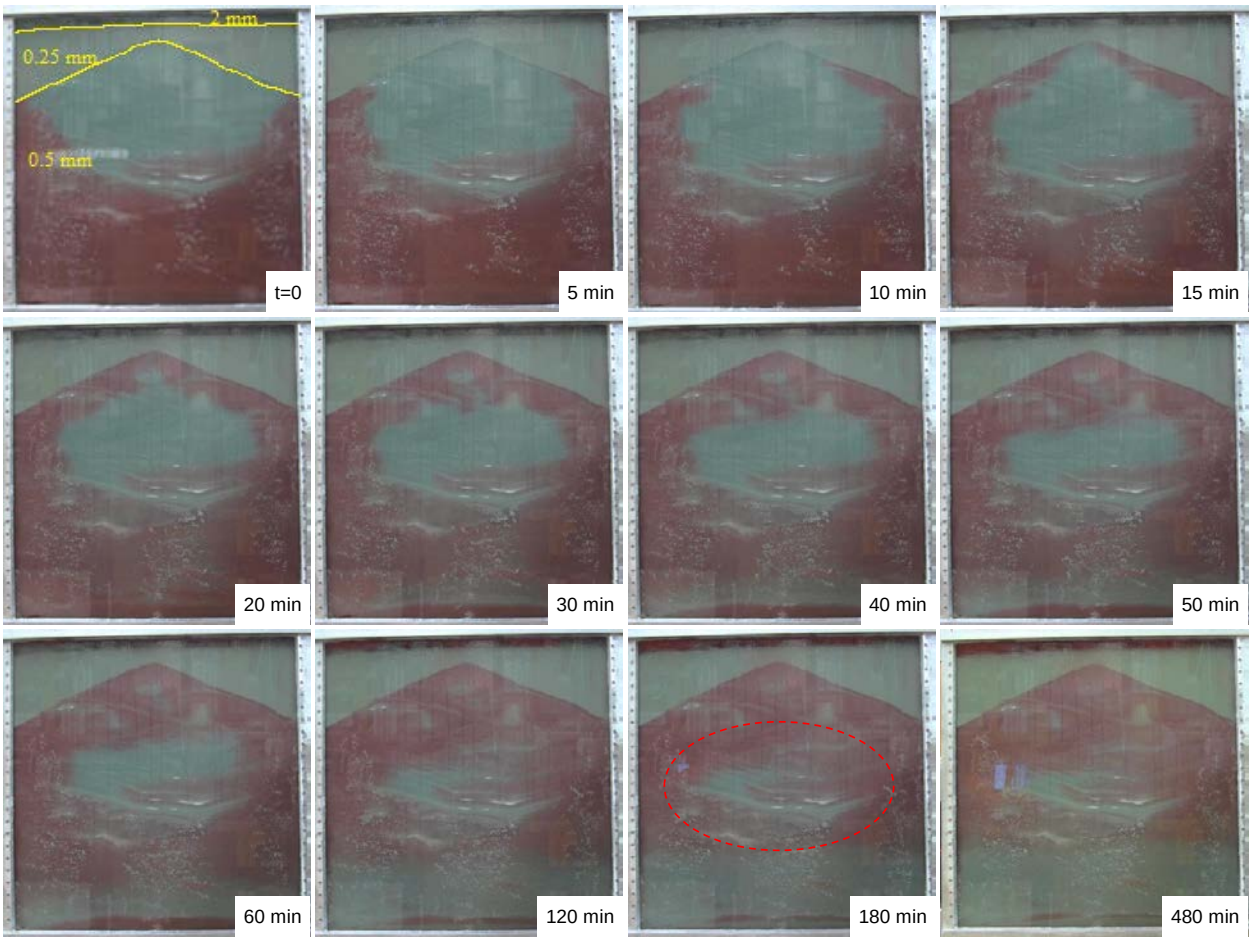

Figure 151: Progress of buoyant migration of nonwetting phase (red) during Experiment 8. Insets give elapsed time since start of buoyancy-driven displacement in closed system. The system was closed throughout the period of migration shown here. The "seal" of fine beads successfully held back the mobile nonwetting phase and caused it to backfill the pore space in the anticline of coarse beads. Though the capillary entry pressure along the corners was larger than in previous experiments, the nonwetting phase nevertheless migrated along the corners of the apparatus and backfilled a small portion of the top of the domain.

The silicone used to glue the aluminum pieces in the corners swells with prolonged direct contact with hydrocarbon phases. This creates a greater surface area of hydrophobic material, creating easy migration pathways for the red-dyed nonwetting phase. This was observed even at the

initial backfilling stage; hence corner effect was, in fact, enhanced in this situation, which contradicted the intention of the modification.

Figure 151 shows the first 8 hours of the experiment at closed state. Despite the corner effect at the two sides, the system still reached equilibrium in about 3 hours, which is consistent with previous results.

The beads came fresh from the manufacturer and contained some dust (even finer particle) which contributed some heterogeneity within the 0.5 mm bead pack region (circled region in Figure 151). The rising nonwetting phase could not reach those regions due to high capillary entry pressure of such bead/dust packs, and accumulated beneath them. This is another manifestation of local capillary trapping, and is a possible direction to proceed when we seek to study finer particle heterogeneity.

Part 2: Open System

At the end of the 8th hour, the system was opened; constant potential equal to hydrostatic (i.e. $\Psi = P - \rho_w g z$) was applied to both the top and bottom of the domain by positioning the reservoirs (one connected to top ports, one connected to bottom ports) such that the liquid surfaces are at the same level as the top of the domain. Since the nonwetting phase reached equilibrium in the closed system with hydrostatic potential within the aqueous phase, no movement of fluid is expected when the system is opened, since the hydraulic potential does not change. Indeed, the system reached equilibrium in a short time. Mobile nonwetting phase migrated from the lowest portion of the domain along the corners and increased the saturation in the top portion of the domain. In this experiment the nonwetting phase backfilled into the seal, as becomes clear at 18 and 31 hours in Figure 152. The reason for this is unclear as the seal formation has never been invaded in other experiments, but the silicone may have facilitated the invasion. The nonwetting phase at the very top of the domain can flow out ports at the top of the apparatus when opened, and it did so. However the nonwetting phase within the coarse beads in the anticline was held by capillary forces and did not migrate, as shown in Figure 152.

Figure 152: Late time equilibrium state (insets give elapsed time since start of buoyancy-driven displacement in closed system) of the open system of Experiment 8. Constant hydraulic potential equal to hydrostatic was applied at top and bottom ports at the 8th hour elapsed time.

The open hydrostatic imbibition was followed by a forced imbibition, and results are summarized in the following Figure 153. Notice that the time has been reset.

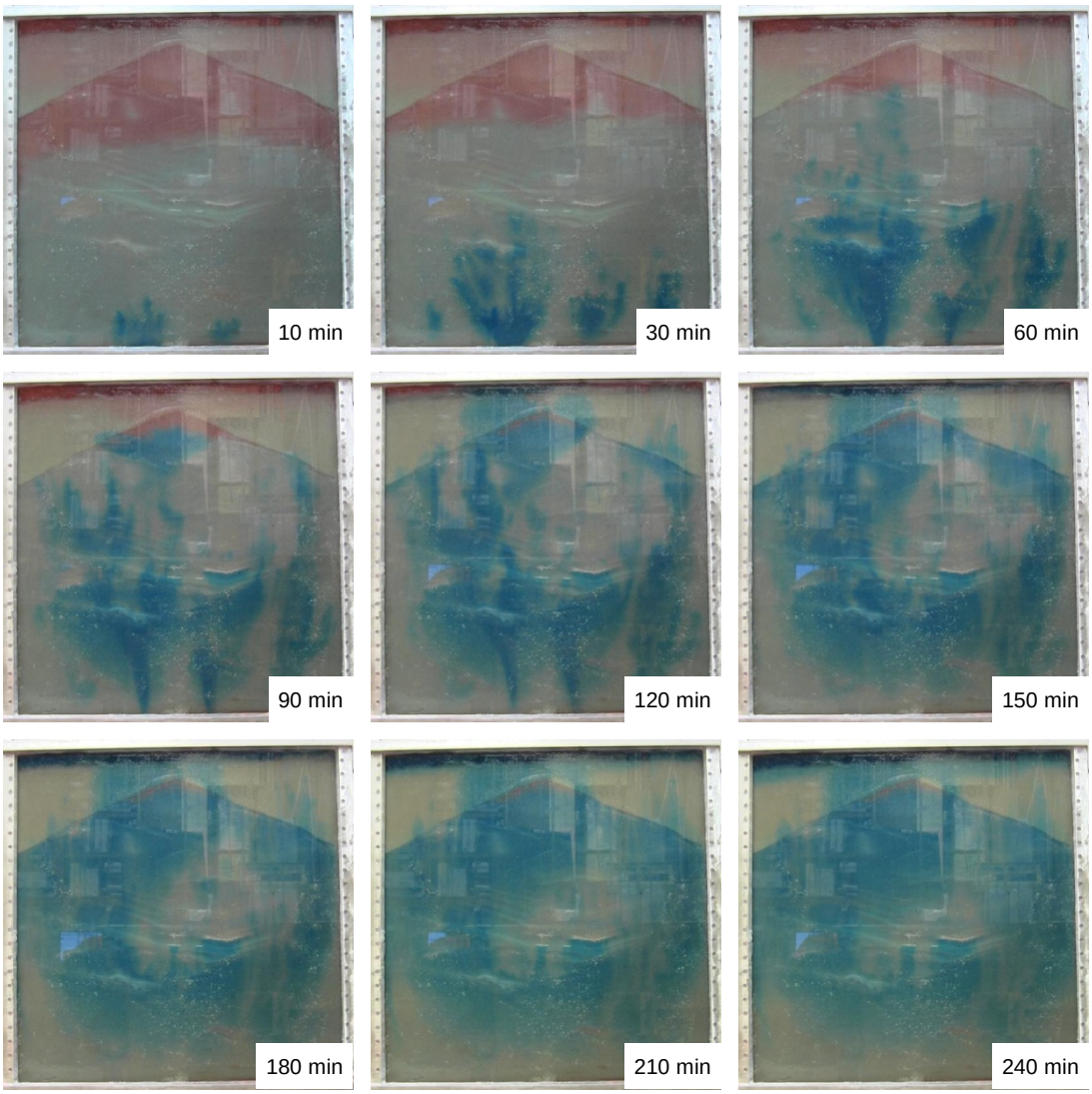

Figure 153: Forced imbibition of the wetting phase (blue) displaces non-wetting phase (red) through the capillary sealing layer. The aqueous reservoir liquid surface connected to the bottom ports was raised 35.6 cm higher than the top of the domain, causing the capillary pressure at the top of the oil column to exceed the capillary entry pressure of the sealing layer. Insets give elapsed time since start of forced imbibition (the clock has been reset at the beginning of the forced imbibition, when the aqueous reservoir is raised).

At the 85th hour, the system remained open, the reservoir connected to the top of the apparatus was not moved, and the aqueous phase reservoir connected to the bottom of the apparatus was raised 14 inches (35.6 cm). The entering pressure at the bottom of the domain = 101 Pa + (35.6 cm + 63 cm + 30 cm – 30 cm) × 9.81 N/kg × 1084 kg/m^3 = 111.5 kPa. The exiting pressure at the top of the domain, assuming oil phase fills up the exiting line, = 101 Pa - (93 cm – 93 cm) × 9.81 N/kg × 724 kg/m^3 = 101 Pa. This imposed a pressure gradient of (111.5 kPa – 101 kPa)/0.63 m = 16.6 kPa/m across the aqueous phase in the apparatus, and therefore a 16.6 – 7.1 = 9.5 kPa/m capillary pressure gradient within the oil phase. Consequently the effective capillary pressure at the top of the accumulation of nonwetting phase beneath the “seal” layer increased considerably; recall the capillary pressure gradient the first stage of migration was 3.5 kPa/m. At the increased gradient, the remaining 9 inches (0.227 m) continuous oil column beneath the

"seal" at the beginning of the 85th hour (see rightmost panel in Figure 152) corresponds to 0.227 m × 9.5 kPa/m = 2156 Pa of capillary pressure, compared to its original (open system at hydrostatic pressure) values of 0.254 m × 3.5 kPa/m = 889 Pa (at closed system). This value is much greater than the entry pressure of the 0.25 mm seal (1334 Pa theoretical and 1735 Pa experimental). Therefore blue-dyed aqueous wetting phase came into the domain (Figure 153) and displaced the trapped oil through the "seal" beads, then out of the apparatus.

This experiment confirms that local capillary trapping does hold nonwetting phase at saturations above residual, as described in the seminal work by Saadatpoor *et al*. (2010a). Since the trapping is exclusively due to the capillary pressure at the top of the nonwetting phase accumulation being smaller than (or equal to) the capillary entry pressure of the porous medium above the accumulation, it should be possible to displace the locally trapped phase if its capillary pressure increases. This is precisely what happened in the forced imbibition stage of this experiment. The nonwetting phase was trapped at a capillary pressure gradient of 3.5 kPa/m, the value corresponding to buoyancy (density difference between phases) in an otherwise static (no gradients in potential) system and illustrated in Figure 151. Raising the aqueous phase reservoir connected to the bottom of the domain by 35.6 cm increased the capillary pressure gradient three-fold, overcoming the entry pressure of the fine beads and allowing the above-residual oil saturation to enter the fine beads.

To calculate the capillary pressure gradient, P_c *gradient*, across the system at open boundary conditions (assuming the outlet is directly open to air and at the same level as the top of the domain):

- For <u>hydrostatic potential gradient</u>:

$$P_c \text{ gradient} = (P_{\text{bottom of domain}} - P_{\text{top of domain}})/h_{\text{domain vertical}} - P_{\text{oil hydrostatic}}\text{gradient}$$
$$= (P_{atm}+\rho_{\text{inlet\_tube\_fluid}}gh_{\text{domain\_vertical}} - P_{atm})/\ h_{\text{domain vertical}} - \rho_{oil}g$$
$$= (\rho_{\text{inlet\_tube\_fluid}} - \rho_{oil})g$$

- For <u>greater than hydrostatic gradient</u> imposed in the aqueous phase:

$$P_c \text{ gradient} = (P_{\text{bottom of domain}} - P_{\text{top of domain}})/h_{\text{domain vertical}} - P_{\text{oil hydrostatic}}\text{gradient}$$
$$= [P_{atm}+\rho_{\text{inlet\_tube\_fluid}}g(h_{\text{domain\_vertical}}+h_{\text{w\_reservoir\_elevated}}) - P_{atm}]/\ h_{\text{domain vertical}} - \rho_{oil}g$$
$$= \rho_{\text{inlet\_tube\_fluid}}g(1+h_{\text{w\_reservoir\_elevated}}/h_{\text{domain\_vertical}}) - \rho_{oil}g$$
$$= [\rho_{\text{inlet\_tube\_fluid}}\ (1+h_{\text{w\_reservoir\_elevated}}/h_{\text{domain\_vertical}}) - \rho_{oil}]g$$

Experiment 9 (0.25 mm, 0.5 mm and 2 mm, Layered, Anticline-Shaped Seal, Open State When Oil Starts to Rise)

Objective: Demonstrate Persistence of LCT While Determining the Threshold Pc_Entry for the Seal

Due to apparent corner effect in Experiment 8, the experimental apparatus was thoroughly examined before proceeding to the next experiment. It was found that the silicone gel attaching the corner metal slats to the large containment box was swollen due to prolonged exposure to the hydrocarbon organic non-wetting phase. This created a preferential vertical pathway along the corner for the rising nonwetting phase. Therefore, the swollen silicone gel was carefully scraped

and removed from the system before carrying on the next experiment, in the hope to reduce the corner artifact.

In Experiment 9, the same heterogeneous configuration of beads as Experiment 8 was used: layer of fine beads above anticline-shaped layer of coarse beads, all beads relatively small (0.25 mm and 0.5 mm). The entire domain was first saturated with aqueous phase, and then the nonwetting phase was injected from top, displacing about half of the aqueous phase initially in place. When the injection of nonwetting phase is complete, the domain was then rotated 180 degree to start the experiment.

To fully mimic the actual storage condition, we switched to open system (top ports open and connected to one fluid reservoir, bottom ports open and connected to second fluid reservoir) as the nonwetting phase begins to rise, i.e. well before it reached the seal. The wetting aqueous phase reservoir was placed at the same height as the top of the domain, and was connected to the bottom of the domain. Nonwetting phase reservoir was connected to the top of the domain. By setting the reservoirs at the appropriate relative levels, constant hydraulic pressure is applied to the open system. The initial levels are chosen so that the potential gradient corresponds to hydrostatic, and the system reached equilibrium in 3 hours (similar to Experiment 8). Figure 154 shows the first four hours of open state system results.

At 430 minutes after starting the experiment, the aqueous reservoir was raised 2.54 cm higher such that the capillary pressure gradient in the accumulated oil column is about 3.7 kPa/m. (Recall that under hydrostatic conditions the capillary pressure gradient corresponds to density difference between the phases and is 3.5 kPa/m for the fluids used in these experiments.) This gradient created a total capillary pressure of 838 Pa at the top of the oil column. No fluid movement was evident anywhere in the system, as shown in Figure 155. This is consistent with expectations; the original oil column height was less than the value needed to reach the capillary entry pressure of the fine beads, and thus a small increase in the capillary pressure at the top of the column was insufficient to exceed the capillary entry pressure.

The aqueous reservoir was then raised to a series of different levels; after each increment in height, a period of time was allowed to pass in order to determine whether the system was at equilibrium, or to allow it to reach equilibrium if any fluid movement was observed. Each new aqueous reservoir height creates a larger pressure gradient in the continuous aqueous phase within the apparatus. This correspondingly induces a larger capillary pressure gradient, and hence increases the capillary pressure at the top of the accumulated oil column. As long as the capillary pressure remains below the threshold pressure, no fluid movement is expected. Once the threshold is exceeded, as shown in the last two frames of Figure 155, the displacement of red dyed nonwetting phase out of the system by blue dyed wetting phase into the system from the bottom commences.

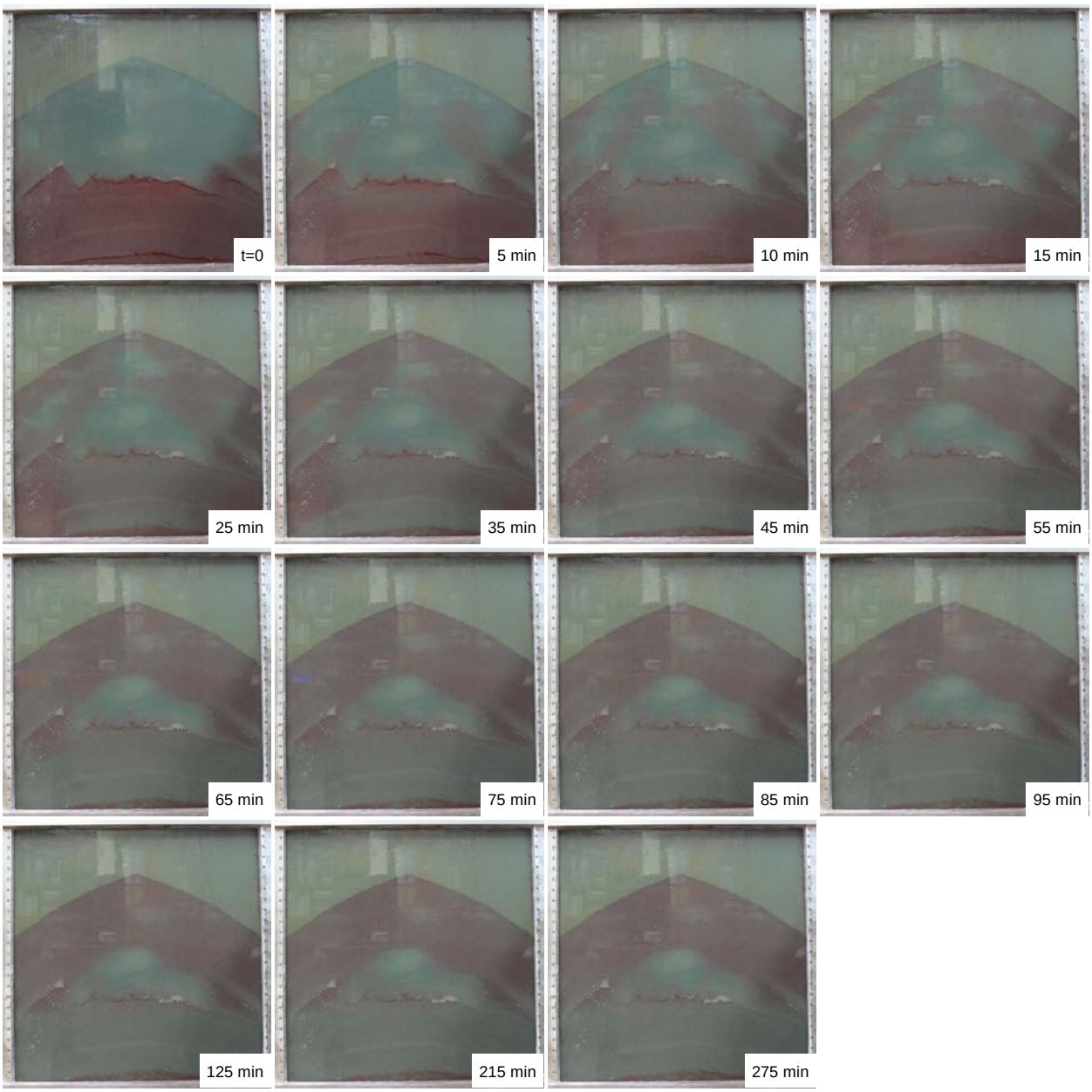

Figure 154: First 275 minutes of Experiment 9. Open state was imposed from the beginning when the red-dyed nonwetting phase was rising from its initial emplacement in the bottom half of the domain. Constant pressure gradient corresponding to hydrostatic was applied across the open apparatus. The system reached equilibrium in 3 hours, and nonwetting phase remained secure below the layer of fine beads.

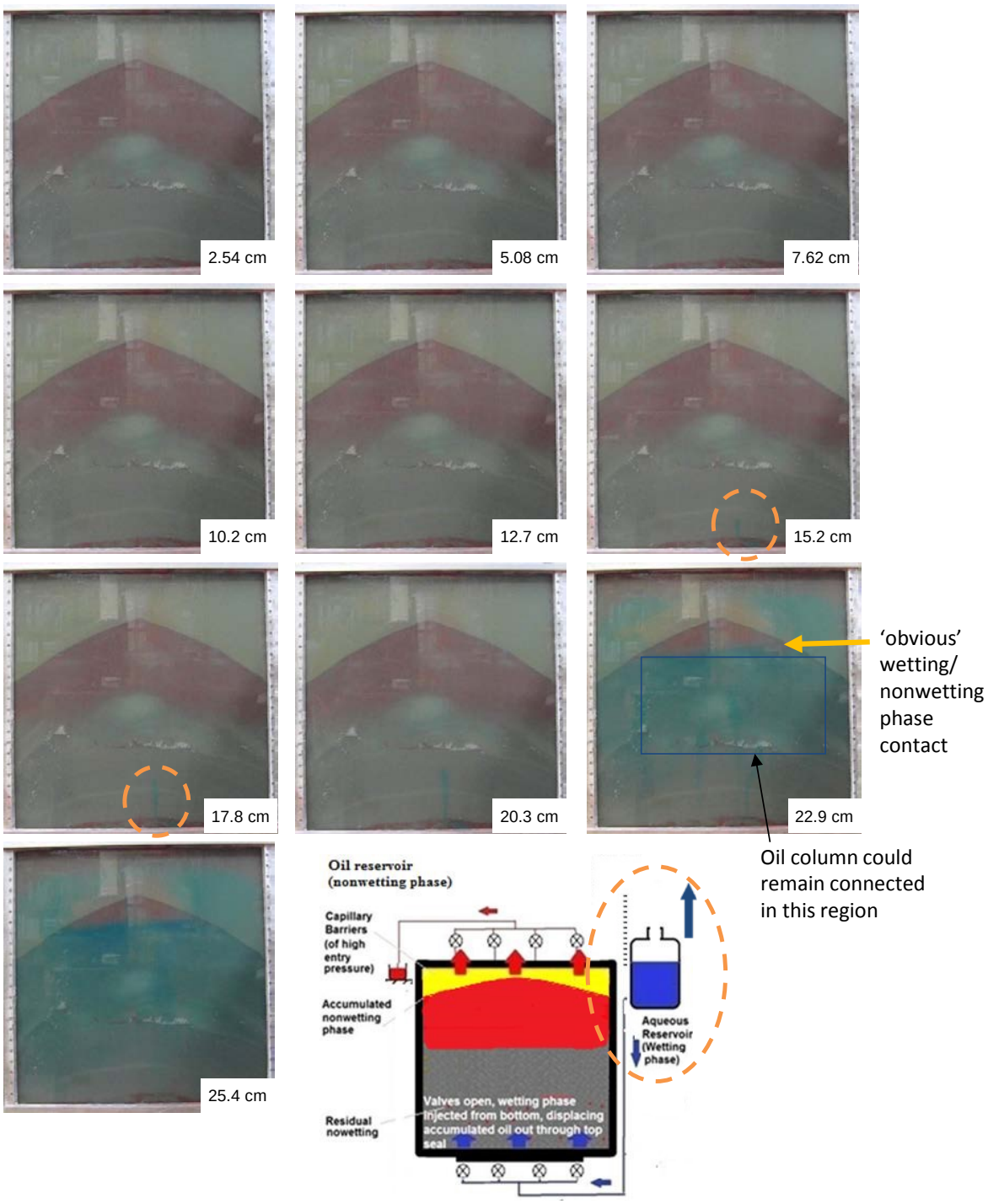

Figure 155: The aqueous reservoir connected to the bottom of the domain (schematic at bottom) was raised in small increments above the top of the domain (height indicated at the bottom right corner of each photograph). Until the increments totaled 38.1 cm, no fluid movement occurred in the system. That is, the red-dyed nonwetting phase remained trapped by capillary forces beneath the fine beads at the top of the domain, even though its saturation was much greater than residual. The blue dyed aqueous wetting phase starts entering the system (indicated by orange circle) when the aqueous reservoir was raised 40.6 cm above the system, and becomes more apparent during subsequent increments.

While blue dyed aqueous phase enters the system, it displaces out the original fluids (both oil and water) in the system though the top ports and tubing. The major displacement of oil occurs when the reservoir is raised from 20.3 cm to 22.9 cm, suggesting that at this point the total capillary pressure due to the trapped oil column height and externally applied hydraulic pressure has exceeded the entry pressure of the capillary barrier, therefore the oil escaped through the seal. Therefore the effective threshold pressure of the capillary seal is determined empirically. Table 21 summarizes the observations.

Table 21: Determination of the Breakthrough Capillary Pressure of the Seal in Experiment 9

Aqueous Reservoir Liquid Surface Above the Top of the Apparatus		Corresponding Hydraulic Potential	Capillary Pressure Gradient	Measured Oil Column Height		P_c Top of the Oil Column	Oil Displaced Out
(inch)	(cm)	(Pa)	(kPa/m)	(inch)	(m)	(Pa)	(ml)
0	0	0					0
1	2.54	270	3.3	10	0.254	838	0
2	5.08	540	3.8	10	0.254	965	0
3	7.62	810	4.2	10	0.254	1067	0
4	10.2	1080	4.6	10	0.254	1168	0
5	12.7	1351	5.0	10	0.254	1270	0
6	15.2	1621	5.4	10	0.254	1372	0
7	17.8	1891	5.8	10	0.254	1473	0
8	20.3	2161	6.2	10	0.254	1575	20
9	22.9	2431	6.6	3	0.0762	503*	370
10	25.4	2701	7.0	2	0.0508	356*	450
11	27.9	2971	7.4	1.5	0.0381	282*	490

*Apparent P_c estimated subject to limitations in the quantification process; refer to assumption (2) below.

Three key assumptions are made when analyzing the image:

1. The entry pressure for the storage formation beads is ignored. When the fluids come from the reservoir connected to the bottom of the domain, they will encounter the beads in the store region first. Those beads also have entry pressure to overcome. Since the beads in the store are twice the size of those in the seal, $P_{c\_entry\_store} = 0.5\ P_{c\_entry\_seal}$. A certain amount of capillary pressure would be required to overcome this $P_{c\_entry\_store}$ value so that oil can enter the domain. However, since the backfilling of the store occurs at the same time that oil rises through the store and water imbibes into the initial (before flipping the apparatus) oil accumulation, it may not be the case that the capillary pressure at the base of the equilibrium (after flipping) oil accumulation is equal to the store entry pressure. The capillary pressure could be close to zero if imbibition were occurring at the base of the accumulation. The calculations in Table 21 assumed that imbibition did occur, and thus that the capillary pressure at the base of the equilibrium oil accumulation was zero. If the base of the equilibrium accumulation were at $P_c = P_{c\_entry\_store}$ then the values of $P_{c\_entry\_seal}$ would be larger than the values reported in Table 21.
2. The oil column is assumed to be disconnected below the level of obvious large oil saturation. This is potentially problematic as the oil approaches the equilibrium accumulation from the initial accumulation, because the imbibition process in the lower

parts of the initial accumulation need not continue all the way to residual oil saturation. That is, oil could still be present at saturations large enough to maintain a connected column but small enough to not be as obviously red (and therefore connected). Accounting for this would require explicitly modeling the capillary imbibition process at the bottom of the initial accumulation. The lower portion of the nonwetting phase will be following imbibition P_c-S_w curve, not drainage curve. So the oil column could remain connected some distance below (blue rectangle in Figure 155) the 'obvious' (to the eye) wetting/nonwetting phase contact line (yellow arrow in Figure 155), making the effective oil column height larger. In this case the P_c at top of oil column would be larger in the first row (2.54 cm elevation) of Table 21. More importantly, the same considerations apply to the displacement that occurs once the threshold capillary pressure is reached (22.9 cm elevation). The implication is that the oil column could be considerably longer than the 7.62 cm of obvious column height in the equilibrium state with 22.9 cm elevation. In fact it is plausible that the column height would be sufficient to provide 1575 Pa capillary pressure at the top of the column. If this were the case it would be consistent with the principle of local capillary trapping. But being able to see and distinguish residual oil from 'not quite residual' oil in the imbibed region is impossible in this experiment. Proper quantification is not achieved.

3. The resistance against the liquid flow is due only to the bead packs. Permeability and capillary force from the porous media are assumed to be the only factors countering the flow of fluids. The apparatus itself (for example, the top cap, the size of the flow lines/valves, etc) does not provide any resistance to counter the applied pressure. This could potentially make the measured P_{c_entry} larger than the true value.

Figure 156 is a graphical presentation of the same information as Table 21. As mentioned above, the capillary pressure on top of the accumulated oil column continues to rise as the aqueous reservoir is raised gradually. At 20.3 cm, the capillary pressure reached its peak at 1575 Pa, which falls in between the theoretical and empirically determined (refer to Table 19) effective capillary entry pressure of the sealing layer of fine beads. The theoretical entry pressure of the fine beads is smaller than the empirical estimate. The theoretical value assumed mono-disperse bead size and a dense, perfectly disordered packing, which are unlikely to exist in the apparatus. The theoretical estimate also assumes the contact angle and interfacial tension are the same as inferred from experiments using these fluids and similar beads. Deviations from these values have proportional effects on the capillary entry pressure.

When the capillary pressure at the top of the oil column exceeded the entry pressure of the fine beads, the accumulated oil column beneath the fine beads started entering the fine bead layer and escaping through the top of the apparatus. Because the system is open, the applied gradient in potential also caused blue dyed aqueous phase to enter the system continuously, and the escaped oil gets displaced out of the system and collected separately. This explains the jump in oil displaced out between 20.3 and 22.9 cm in Figure 156.

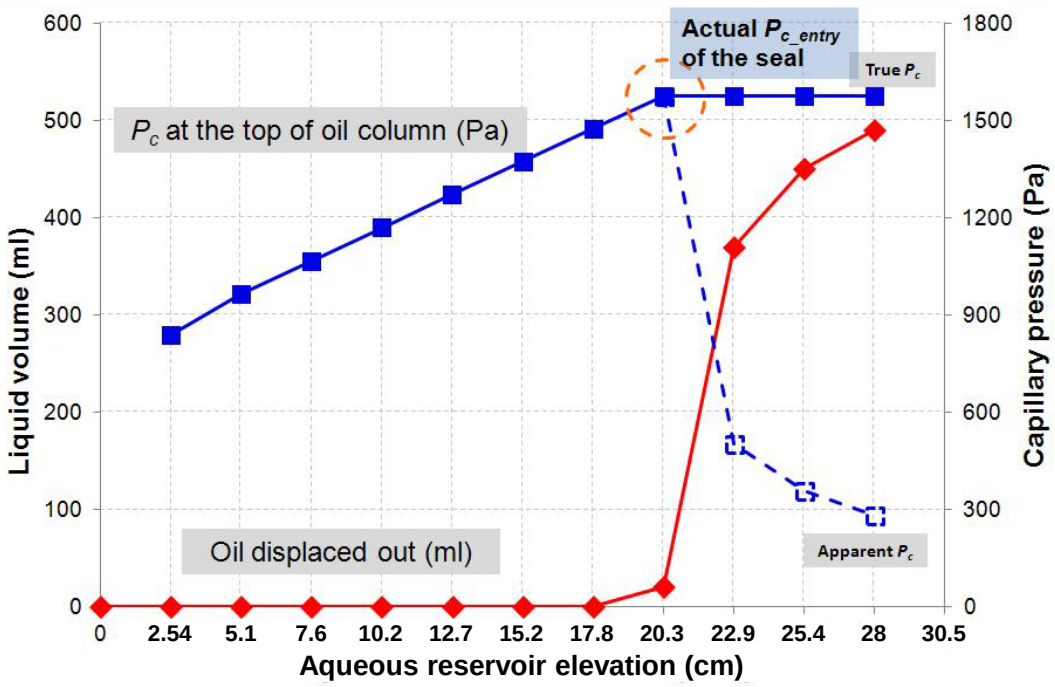

Figure 156: Response of a column of nonwetting phase, originally held within a local capillary trap with only buoyancy forces active (aqueous reservoir elevation = 0), as the effective capillary pressure is incremented by raising an aqueous reservoir connected to bottom of the apparatus. The capillary pressure at the top of the oil column (blue line) increases with each increment in reservoir elevation until the total elevation reaches 22.9 cm, at which point some oil drains through the overlying fine beads, gets displaced out (red line) and reduces the column height remaining in the coarse beads. This provides an empirical estimate of the effective entry pressure of the "seal" (the layer of 0.25 mm beads) of about 1750 Pa (orange dashed circle), somewhat greater than the theoretical estimate based on bead size (1334 Pa, from Table 19).

The peak capillary pressure of 1575 Pa is a good estimate of the effective value of the threshold capillary pressure of the fine bead layer. After this pressure is exceeded, oil column trapped beneath decreased in height; hence the apparent exerted capillary pressure decreased. Based on the apparent oil column height, the capillary pressure decreased to a value considerably smaller than the entry pressure value (1575 Pa). A possible explanation for this is that the imbibition process at the bottom of the oil column was ignored (refer to assumption (2) about Table 21).

The remaining oil in the trap stayed secure for a long time at this particular hydraulic potential / capillary pressure gradient (Figure 157).

To further test whether the persistence of the oil beneath the sealing layer of beads is truly dependent on capillarity, the aqueous reservoir is lowered to the original position (the same level as the top of the domain); the collecting reservoir was raised 12.7 cm higher and a flow line was established from the base of the collecting reservoir to the top ports of the experiment apparatus (replacing the initial outlet line). If any liquid were to flow from the reservoir back into the system at such low height, it would have indicated that the capillary seal was being bypassed and there must have been a connected column for liquids (oil + aqueous phase) backflowing. The results showed that no back flow occurred (Figure 158), which indicated that the persistence and flow of liquid in the domain are solely controlled by capillarity. In other words, the fine beads act like a check valve, allowing the displacement of oil from the coarse beads into the fine beads

only when the capillary pressure exceeds a threshold. The imposition of gradients in hydraulic potential caused viscous flow of connected volumes of fluid, but the viscous flow is not the cause of the oil displacement from the coarse beads. Rather, the viscous flow is one manifestation of the imposed gradient in hydraulic potential, and the increased capillary pressure gradient is another manifestation of the same imposed gradient. Only the latter affects the oil displacement in this experiment. Figure 158 explains this.

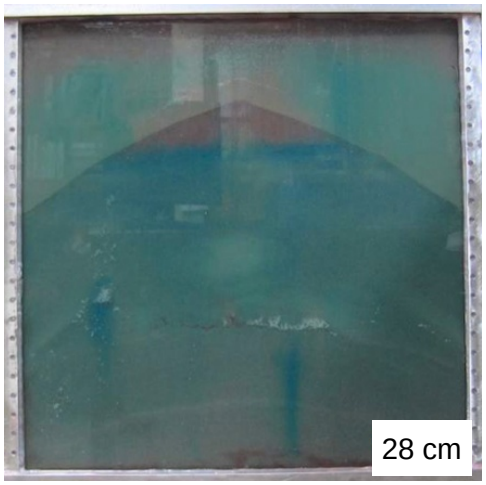

Figure 157: The remaining oil in the capillary trap stayed secure for another 33 hours, while the aqueous reservoir was kept 28 cm (inset) above the top of the domain.

Figure 158: The aqueous reservoir connected to the bottom was brought back to the original position (the same level as top of the domain) while the oil collecting reservoir was raised 12.7 cm higher to drive backflow of oil along connected pathways into the apparatus and into the accumulation remaining in the coarse beads beneath the fine beads. In the absence of such a pathway, no change in the oil accumulation is expected. No back flow occurred, confirming that the oil displacement from the coarse beads into the fine beads is controlled by capillary pressure, not by viscous fluid gradients.

Key learnings from Experiment 9:

1. Systematically proved the persistence of local capillary trapping.

2. Initiated quantification process of experimental parameters, such as volume of oil displaced out and capillary pressure exerted by the oil column, for which more accurate experimental results could be obtained and explained in future experiments.
3. Established experimental protocol to measure the actual entry pressure of any given capillary barrier/seal. This protocol, if studied and improved further, could be potentially developed into a method that could possibly measure and test the limit of any given capillary seal, which is very important in actual CO_2 sequestration and storage processes since the total capacity of the storage could be estimated by better understanding about the seal/caprock.

Experiment 10 (0.25 mm, 0.5 mm and 2 mm, Multiple Anticline-Shaped Seal, Fill and Spill, Open State When Rising Oil Was Injected from a Point Source, Artificial Fracture in the Seal)

Objective: Demonstrate Persistence of LCT When a Fracture is Developed in the Seal

The objective of Experiment 10 was to demonstrate how a fracture, or leakage pathway, in the caprock could affect the locally trapped CO_2 beneath adjacent capillary barriers. To mimic the storage condition in nature, Experiment 10 was designed to show the injection and post-injection during storage in an open system, whose hydraulic potential was always kept constant. Figure 159 and Figure 160 show the schematics of the experiment.

The actual experiment was conducted by following the schematics. The 0.25 mm beads serve as the seal formation, 0.5 mm beads serve as the store, and the 3 mm coarse bead column is to direct flow of the nonwetting phase into the capillary trap. After packing, the entire domain was saturated with aqueous phase. 180 degree rotation is not needed, as the nonwetting phase is directly injected from the bottom of the domain from the beginning.

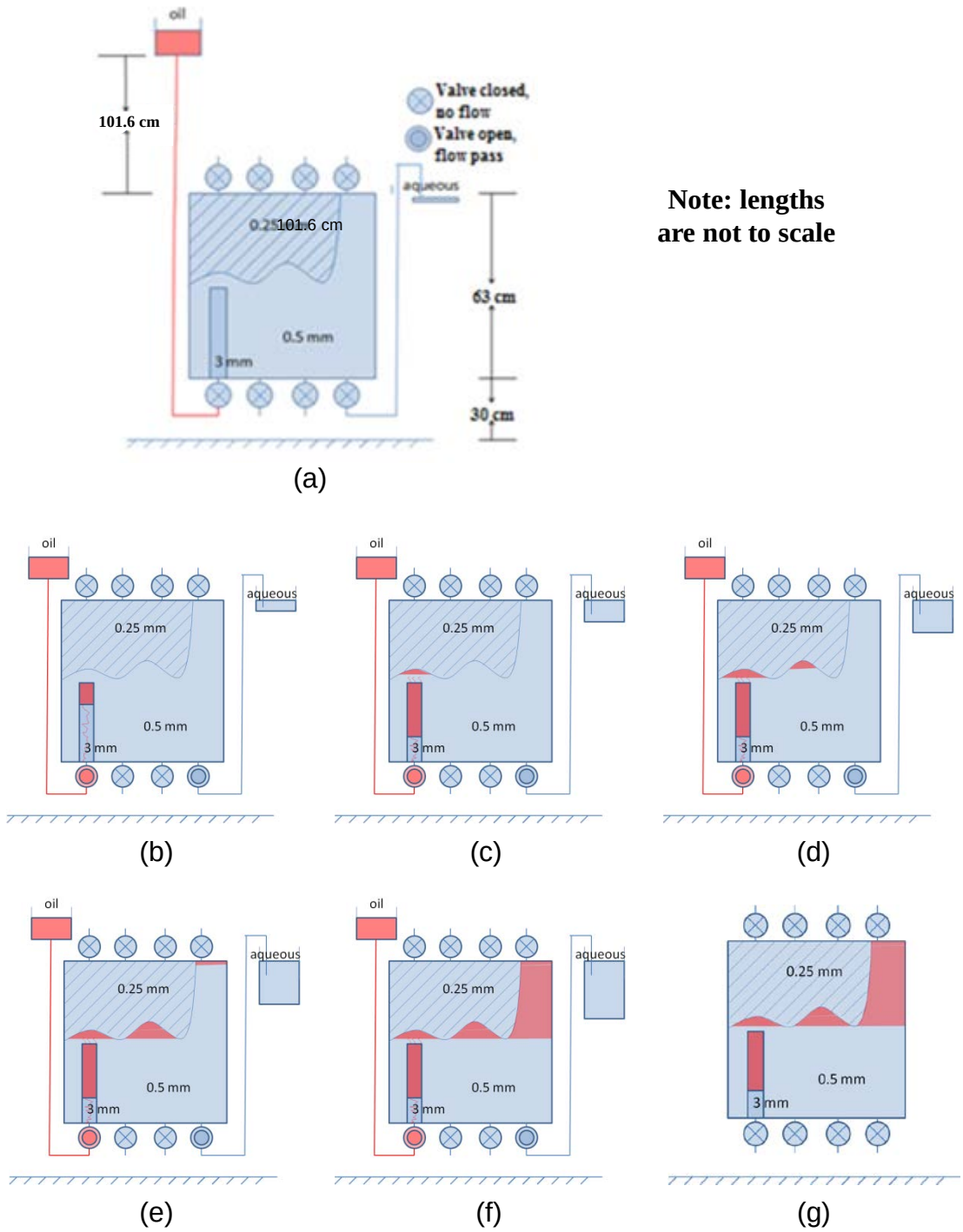

Figure 159: Experiment 10 schematics, part 1 – drainage, fill and spill. (a) Initial setup of the experimental apparatus. Oil reservoir is elevated to provide positive potential to force entry into system when valve is opened. (b) Oil enters the bottom left ports, and first fills up the 3 mm bead column whose capillary entry pressure is least. Aqueous phase leaves the system through the bottom right port. (c) Oil continuously fills up the 3 mm column until the accumulated oil column exerted a higher capillary pressure than the 0.5 mm beads entry pressure; oil started filling up the first trap beneath the seal formation. (d)(e)(f) "Fill and spill". After the first trap was completely filled, oil continues to enter the domain, driven by buoyancy, migrates to the adjacent traps and fills them. (g) When all the traps are completely filled, all valves are closed.

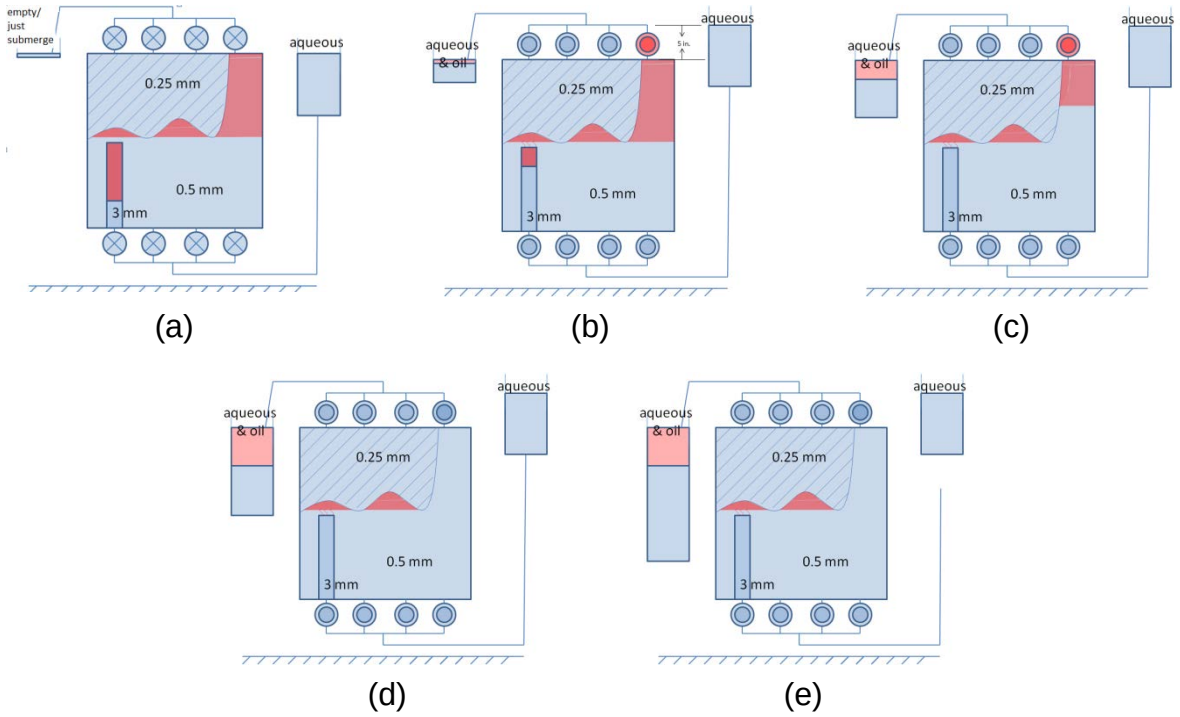

Figure 160: Experiment 10 schematics, part 2 – imbibition when a model fracture induced in the caprock. (a) System was connected to two reservoir kept at the same height as the top of the domain to maintain a constant hydraulic potential. (b) Open all valves, so the aqueous phase could go into the system from the bottom. The reservoir connected to the bottom was raised 5 inches higher to facilitate flow. (c)(d)(e): The accumulated oil in the uppermost "trap" is held back only by the closed valve of the top right port, so opening the valve mimics creation of a fracture through the "seal". Oil is displaced out completely, while the oil in the adjacent traps is expected to remain intact. Aqueous phase continuously enters the system from the bottom as oil and aqueous phase leave through top ports to the collecting reservoir.

The first attempt proved the experiment set up successful, but the results were complicated by edge effects due to prolonged experiment time. So the experiment was repeated to mitigate the adverse impact. Results from both attempts are summarized in the following sections.

Experiment 10, First Attempt

The actual experiment result resembles the expectation of Figure 159 and Figure 160. Figure 161 shows the results in the first stage of the experiment.

The red dyed oil enters the system from the bottom left ports, displacing aqueous phase through the bottom right most port. The rising oil fills the 3 mm column, followed by the first trap in 0.5 mm region, then second, then the last trap which connected to the top right port (serving as an artificial fracture). Between 450 minutes and 1050 minutes, edge effect becomes apparent, such that the oil in the 3 mm column escaped and flowed along the left side of the domain all the way to the top of the system. But the oil in the traps remained relatively intact.

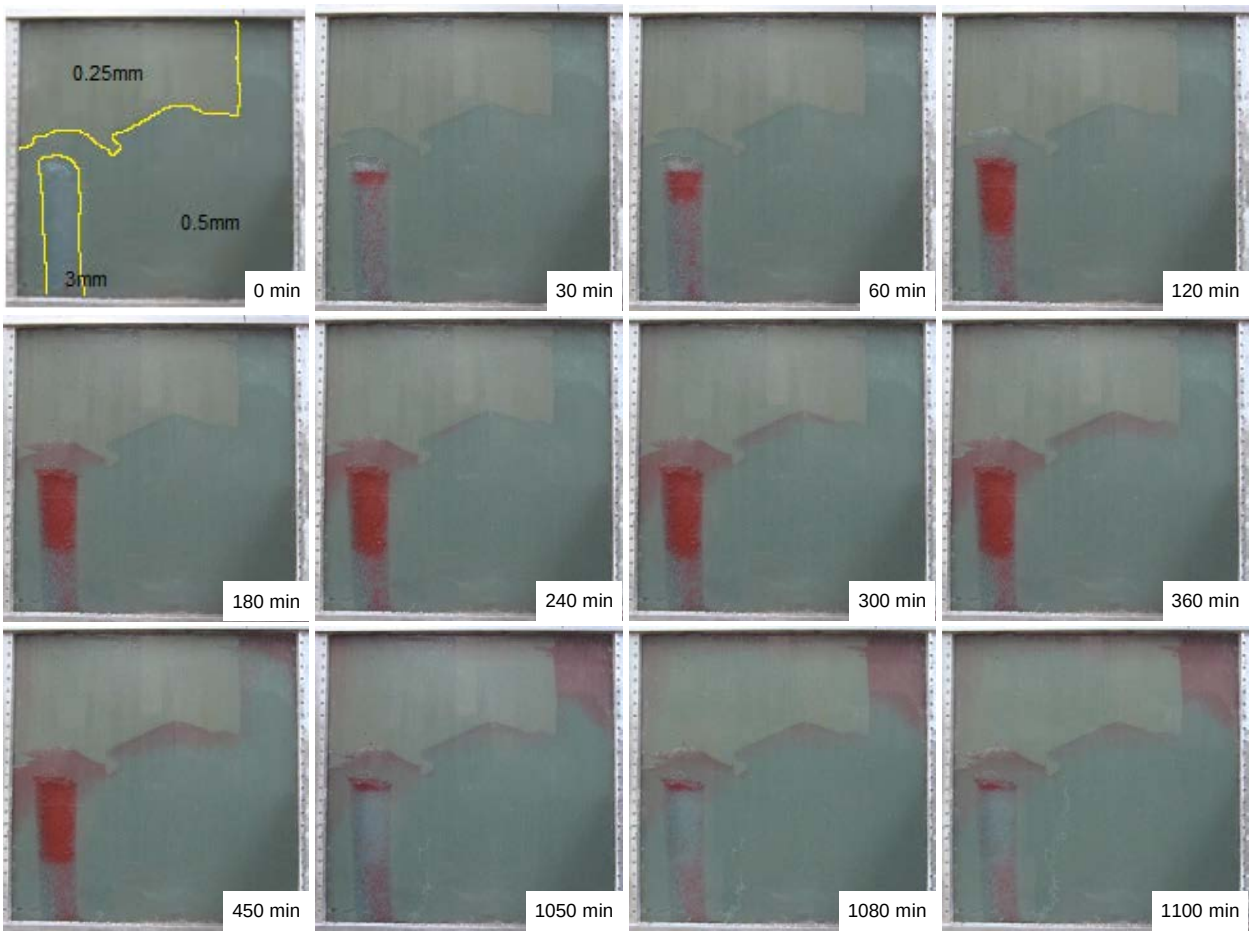

Figure 161: Experiment 10, first attempt results, part 1 – drainage, fill and spill. Only the bottom left most and bottom right most valves are open to oil and to aqueous phase, respectively (cf Figure 159).

At the 1100th minute after starting the experiment, injection of oil stopped since the trap on the top right corner has been mostly filled. The next phase of the experiment, imbibition of aqueous phase, was then initiated. All valves opened, and blue dyed aqueous phase entered from the bottom, displacing liquids (oil and aqueous phase) out of the system through the top. Results are shown in the following Figure 162.

As we can see, the imbibition of blue dyed aqueous phase displaced oil out of the system. While open, the top right port served as an artificial fracture in the capillary seal, through which the accumulated oil escaped via this leakage pathway under pressure exerted by the imbibition.

After all the oil accumulated in the top right trap escaped through the "fracture", a significant amount of oil still remained in the middle trap (indicated by red circle). The system was then left for a week and observed for movement of the fluids. Eventually, the accumulated blue aqueous column in the 3 mm region completely dissipated and distributed to the entire domain. The locally trapped oil remains intact in the middle traps. This shows that even if a fracture occurred in the caprock/seal after storage, it would not affect the stored nonwetting phase in the adjacent traps. This is very important in ensuring the security of stored CO_2 in actual aquifers.

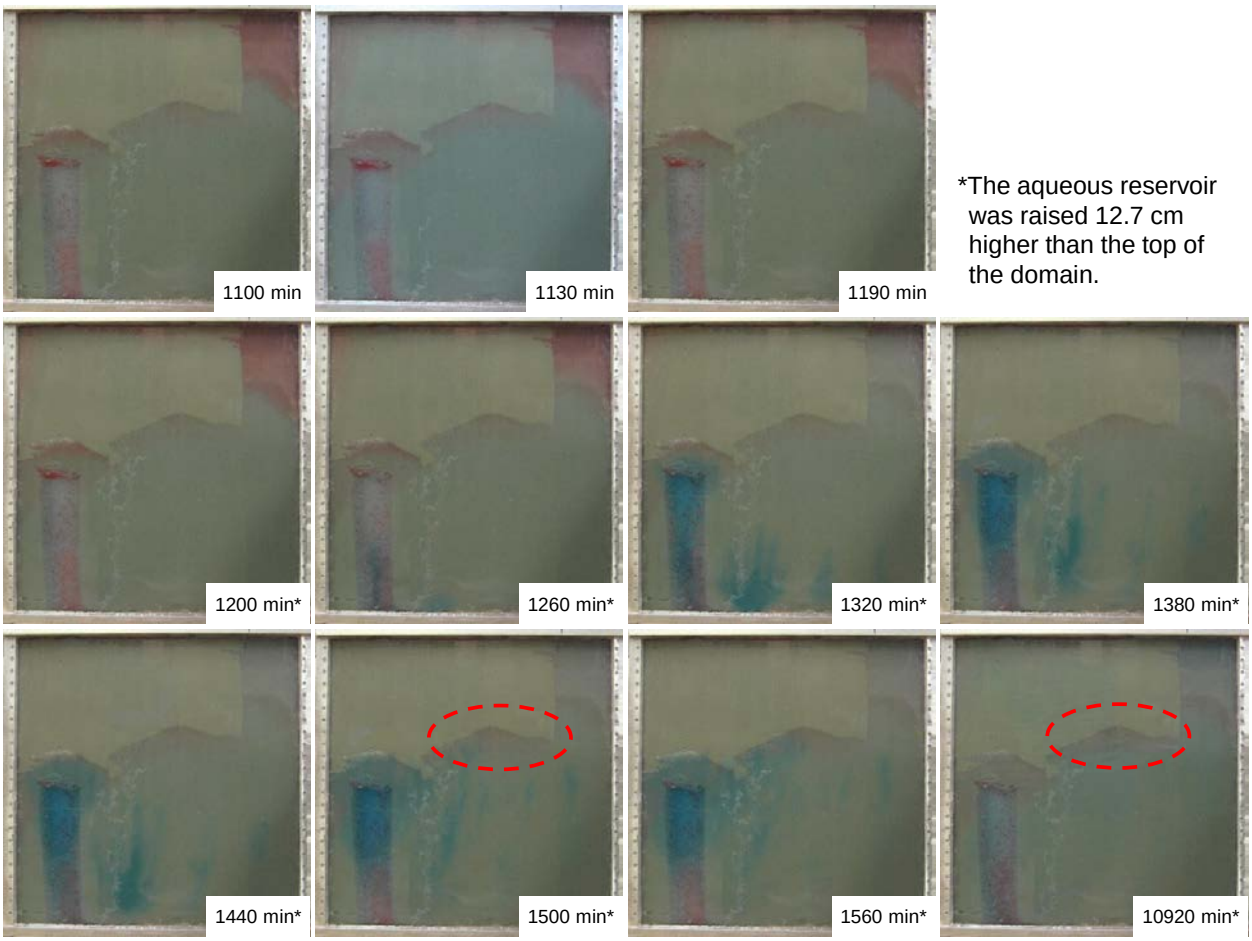

Figure 162: Experiment 10, first attempt results, part 2 – imbibition when a simulated fracture induced in the caprock. All valves are open, aqueous reservoir which is connected to the bottom of the domain was kept at the same height as top of the domain to provide constant hydraulic potential. There was no flow for the first 90 minutes, so the aqueous reservoir was raised 12.7 cm higher to provide a larger potential and to facilitate the flow of blue dyed aqueous phase into the system. At 1440 minutes, the reservoir was lowered to its original position. Finally the system was left for a week, during which no change was observed. The * marks in the time insets indicate that the aqueous reservoir was raised 12.7 cm higher than then top of the domain to facilitate the flow.

Significance of Experiment 10, first attempt:

1. This experimental procedure better mimics the injection and post-injection stages of a storage process. Experiment 10 didn't require a "flipping" stage. The original line source from the bottom could now be transformed to a "point" source. This offers a better analogy to the storage condition, from the moment of injection to post injection.
2. The complex geometry of heterogeneity/capillary barrier systems can be achieved in the relatively simple experimental apparatus. Basically we can mimic natural depositional patterns in our own sedimentary strata.
3. The fracture in the caprock has little to no effect on retaining nonwetting phase in adjacent capillary traps. This is especially important to the security and total capacity of a site selected for CO_2 sequestration and storage.

Experiment 10, Second Attempt

Due to apparent edge effect between 450th minute and 1050th minute the first attempt of Experiment 10, most of oil in the 3 mm column had escaped to the top of the domain. In order to avoid the edge effect and to better understand the flow pattern of the uprising oil, second attempt was made with the same arrangement of beads, except the total experiment time was limited to less than 9 hours to minimize the opportunity for edge effects to affect the behavior. The beads used in the first attempt were discarded. New beads were used to replicate the arrangement for second attempt in order to keep the domain initial saturation condition consistent.

Initially the aqueous reservoir was placed 101.6 cm higher than the top of the domain and connected to the bottom of the domain, such that aqueous phase was injected into the system by gravity and thereby saturated the dry porous media. The entire filling up process took about 1 hour. Upon saturation, the aqueous phase imbibes into regions of finer beads faster. This is expected as the smaller the bead size, the larger the capillary pressure, therefore the higher the saturation front will rise compared to its position in adjacent larger beads. Figure 163 illustrates this process.

The initial saturation step was then followed by drainage, where the oil reservoir was placed 101.6 cm higher than the top of the domain and connected to the bottom left valve (as indicated in Figure 164). The nonwetting oil phase therefore was injected into the system via gravity. The bottom right valve was open to allow displaced water to leave the system. The other valves remained closed.

Red dyed nonwetting oil phase first entered the system, and rose along the 3 mm bead column. Due to the relatively large bead size, 3 mm bead column has the smallest capillary entry pressure, therefore served as a preferential flow path for the rising buoyant oil phase. The nonwetting phase reached the 0.5 mm region, and due to higher entry pressure of the 0.5 mm region than the 3 mm region, oil started to accumulate beneath the 0.5 mm region and in the 3 mm column. The nonwetting phase accumulated to a height where its effective capillary pressure exceeded the entry pressure of the 0.5 mm. The nonwetting phase broke through the 0.5 mm region, and started to enter the first capillary trap on the left, which was an anticline-shaped region beneath a capillary barrier made of 0.25 mm beads.

The 0.25 mm bead pack has a capillary entry pressure of 1735 Pa, which could hold up to about 50 cm nonwetting phase column accumulated beneath it. But the nonwetting phase trapped beneath the barrier in this experiment would never reach such height, because it “spilled” to adjacent traps on the right when the first trap was completely filled. This “fill and spill” propagated to the rightmost “trap”, a region of 0.5 mm beads continuous all the way to a valve at the top of the domain. The seal for this “trap” is a closed valve, not a capillary barrier, so it differs qualitatively from the local accumulations at the left side and middle of the domain.

A total of 650 ml of oil had been injected into the system; the same volume of aqueous phase was displaced out. Then all valves were closed. The oil reservoir connected to the bottom of the domain was replaced by an aqueous reservoir, and connected to all four valves from the top. The bottom valves were connected to another aqueous reservoir (please refer to following Figure 165). Both reservoir liquid levels were kept at the same height as the top of the domain. When

the valves were open, these two reservoirs provided hydrostatic pressure gradient to the system, by means of which an open boundary system similar to Nature was mimicked.

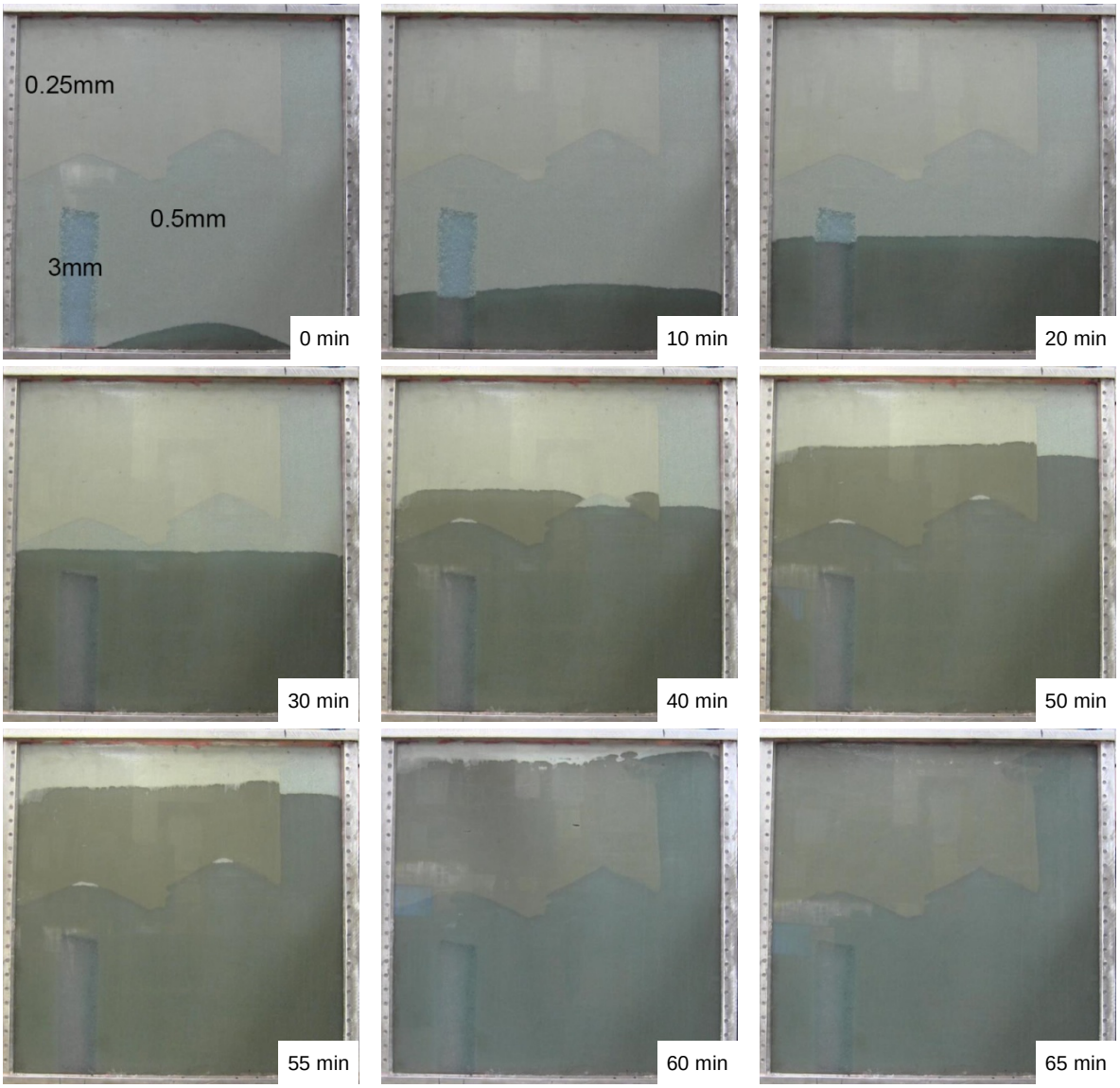

Figure 163: Filling up (initial imbibition with aqueous phase displacing air) of Experiment 10, second attempt.

The nonwetting phase has a smaller density, therefore the pressure gradient in the apparatus was smaller than the one provided by the aqueous reservoir, hence blued dyed water entered the system through all four valves at the bottom and less dense oil rose and tended to leave the system from the top. A large amount of aqueous phase entered the system through the valve at the bottom left corner because of the lowest capillary entry pressure of the 3 mm bead column. The aqueous phase first displaced out the trapped oil phase in the 3 mm column, and then displaced a portion of trapped phase in the first capillary trap on the left. A significant amount of oil was still trapped beneath the capillary barrier. Due to the persistence of local capillary trapping mechanism, the moving aqueous phase could not displace all oil out of the first trap, and moved to adjacent trap to displace oil out there.

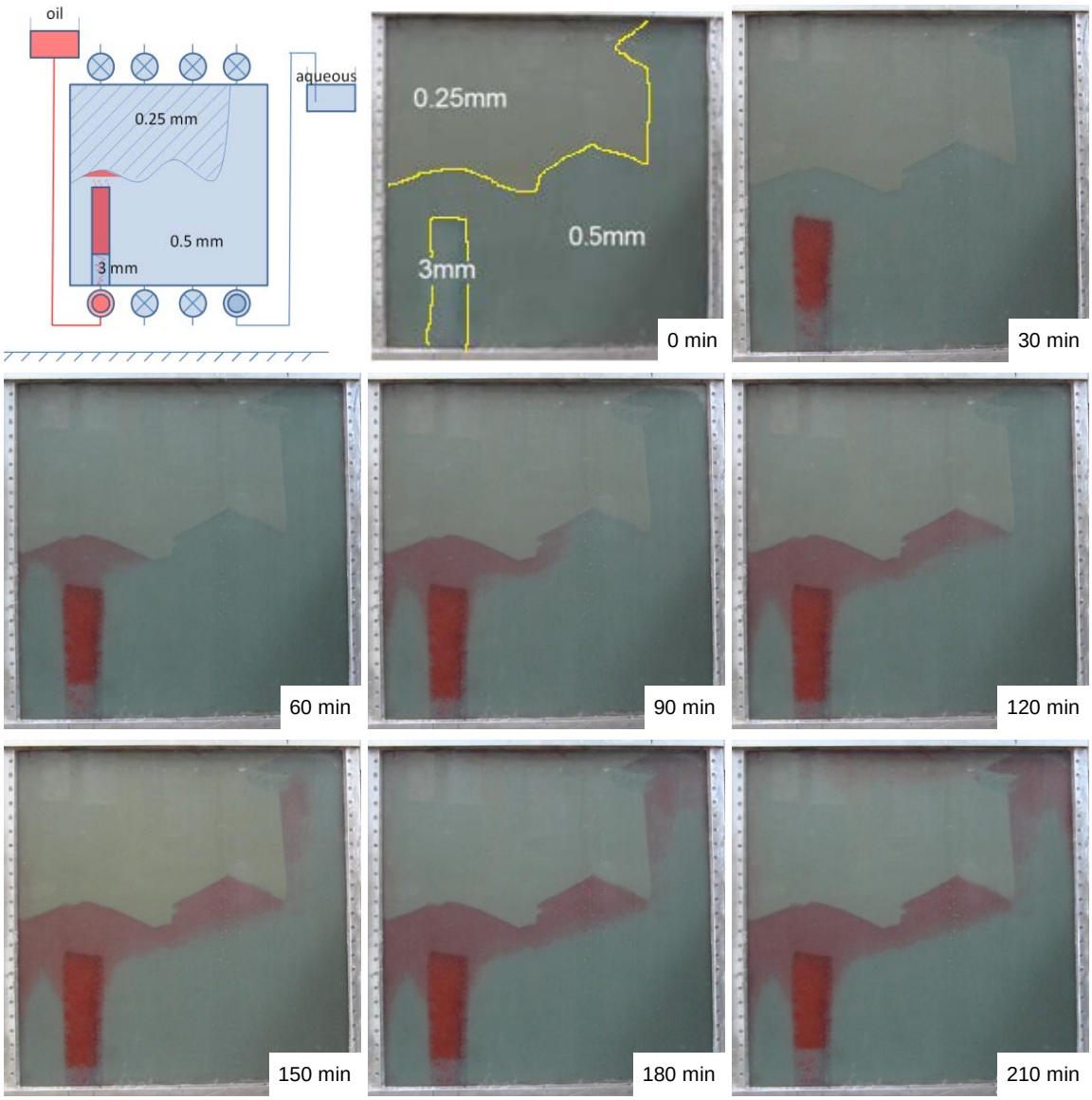

Figure 164: Drainage process of Experiment 10, second attempt.

The top right trap was directly beneath a valve, which served as a leakage pathway when opened. It mimicked the breaching seal situation. As we can see in Figure 165, almost all accumulated oil phase in the right most trap was displaced out of the system through the top valves, leaving only residual oil. But the mobile nonwetting phase in the adjacent traps remained undisturbed. Notice that only oil has been displaced out to this time (note level in the measuring cylinder).

The system reached equilibrium at around 360th minute, as no more aqueous phase entered and no more oil left the system. At 860th minute, the measured displaced oil out of the system is 520 ml, meaning there were 130 ml oil still remained in the system securely. This demonstrated the persistence of local capillary trapping under constant hydraulic potential.

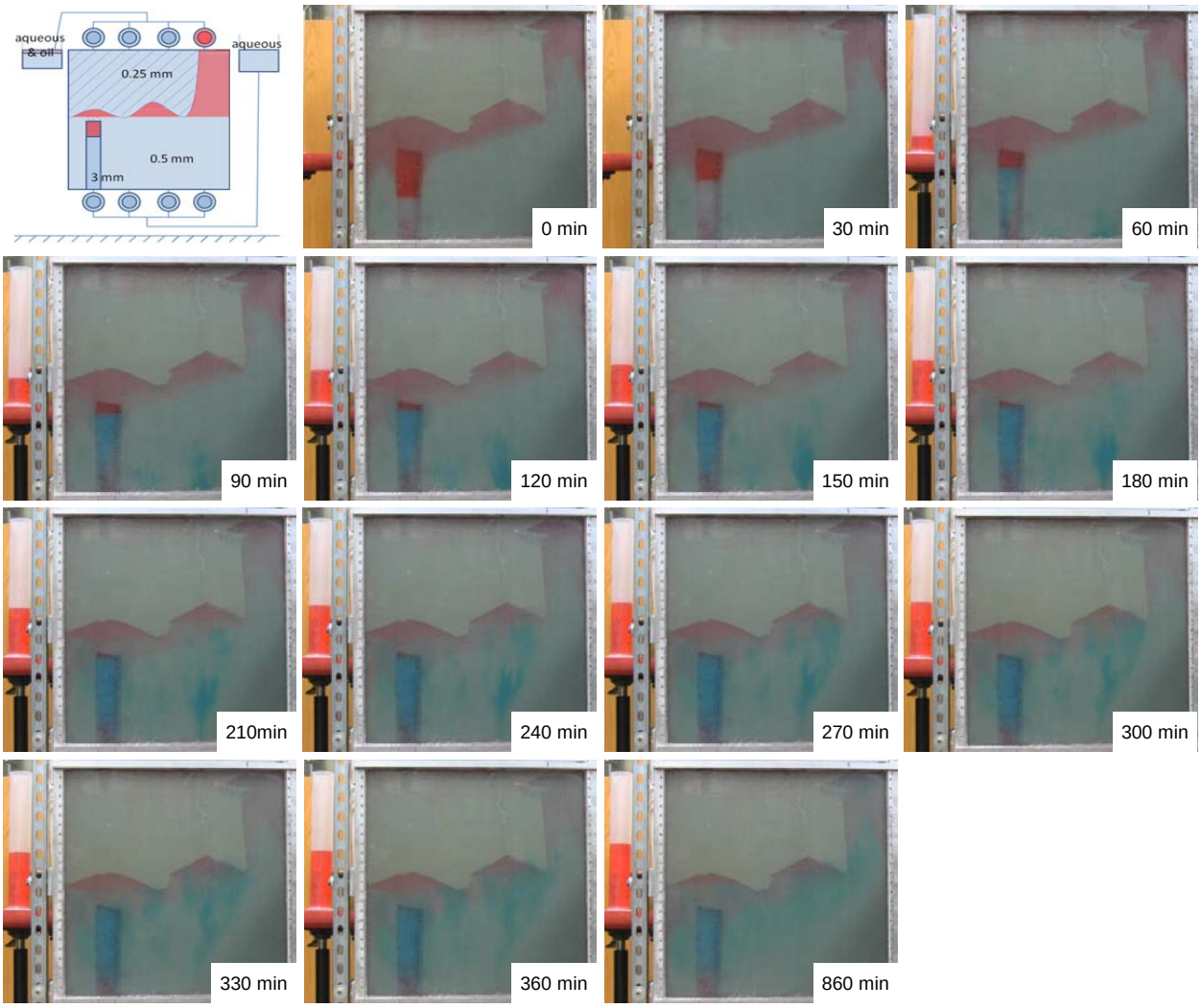

Figure 165: Imbibition under hydrostatic potential of Experiment 10, second attempt. All liquids displaced out of the domain were collected in a measuring cylinder (on the left hand side of each image). The continuous liquid in the exit line terminates at the same height as the top of the domain, but above the oil level in the collection measuring cylinder. By examining the volume in the cylinder at different point of time, the rate of displacement/injection can be calculated.

In order to further test the persistence of local capillary trapping under forced imbibition, at the 1590th minute the aqueous reservoir connected to the bottom was raised 5 inches higher, by means of which the capillary pressure gradient across the domain was increased and a hydraulic potential gradient was established. Therefore aqueous phase again flowed into the system. See Figure 166.

Although the aqueous phase again flows into the system, the oil trapped beneath capillary barriers remained intact. As we can see from Figure 166, only water is displaced out of the system, the volume of displaced oil (in the cylinder on the left) remained constant.

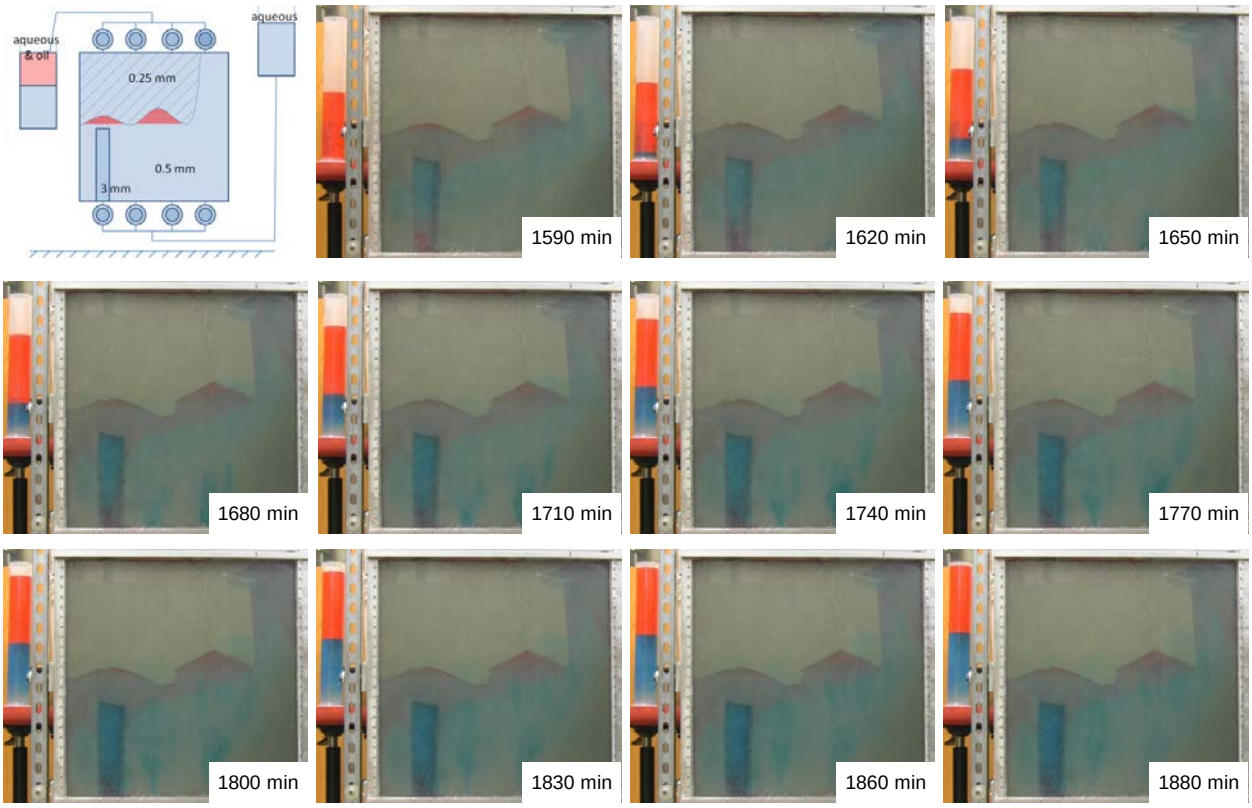

Figure 166: Forced imbibition in open boundary system with a higher applied hydraulic potential, Experiment 10, second attempt.

Significance of Experiment 10, second attempt:

1. This is the first ever unequivocal experimental evidence on persistence of local capillary trapping. It demonstrated that Local Capillary Trapping mechanism remains persistence even under forced imbibition. The persistence could be potentially predictable or even quantified if we successfully manipulated the boundary conditions by changing the hydraulic potential / capillary pressure gradient across the system.
2. Majority of the buoyant mobile phase trapped beneath capillary barriers will remain secure in the case when the caprock integrity is compromised. The breach or fracture in the caprock will serve as a leakage pathway for the mobile phase trapped directly beneath it. But mobile phase in adjacent capillary traps will remain undisturbed. This discovery provides strong support for the safety and security of storing CO_2 via local capillary trapping mechanism.
3. It shows some clues for quantifying the total CO_2 storage capacity in the formation. A sample quantification process for Experiment 10 is shown here:
   - Experimental value:
     - Total injected oil volume in the drainage = 650 ml
     - Total displaced oil volume at the end (when system reached equilibrium) = 520 ml
     - Total oil volume remained in the domain permanently = 650-520 = **130 ml**

- Calculated value:
  - Inner dimension of the experiment apparatus (glass box) = 63 cm × 63 cm × 2.54 cm = 10080 ml
  - Assume a 0.35 porosity of all beadpack regions, so the total pore volume available = 10080 ml × 0.35 = 3530 ml
  - 3530 ml / 650 ml = 0.184 gives the initial pore volume fraction occupied by oil By observation (read from picture, end of drainage), initial total fractional area of oil occupation to the entire domain is about 0.25. Assuming that oil displaces aqueous phase down to an irreducible saturation of about 20%, this is reasonably consistent with the calculated value in previous step, i.e. 0.25 × (1- 20%) = 0.20 ≈ 0.184.
  - Total pore volume occupied by oil = 3530 ml × 0.25 = 882 ml
  - Initial oil saturation = 650/882 = 0.74 (this suggests $S_{w,irr}$ = 0.26)
  - Final oil saturation = 130/882 = 0.15
  - At the end of imbibition, assume fraction of oil in capillary traps (anticlines) = 0.1, fraction of oil in residual = 0.9
  - The amount of oil trapped in the capillary traps = 0.1 × 882 × 0.74 = 65 ml
  - Assume irreducible oil saturation of the domain = 0.1
  - The amount of oil in residual after imbibition = 0.9 × 882 × 0.1 = 80 ml
  - About 30 ml oil trapped at the top of the domain (in between the seal and top cap of the ant-farm, invisible)
  - So the total amount of oil left in the system = 65 + 80 + 30 = **175 ml**

The discrepancy between the calculated value (175 ml) and actual experimental value (130 ml) is likely due to inaccurate estimation of porosity of the porous media as well as the area of oil saturation.

Experiment 11 (Seal = 0.25mm(67%) + 0.5mm(33%). Store = 0.5mm(50%) + 2mm(25%) + 3mm(25%) Anticline-Shaped Seal, Direct Open State When Rising Oil Was Injected From Bottom)

Previous experiments had demonstrated the persistence of local capillary trapping, but all of them consisted of mono-distributed porous media, meaning the "seal" and "store" in each case were only made of one sized beads. In Nature, however, this is never true. In order to fully mimic the actual storage formation with grain distribution, we introduced the degree of heterogeneity into the system.

Before pouring the beads into the containment box, different sizes of beads are mixed mechanically in big plastic buckets to ensure an even distribution of heterogeneity. Figure 167 is an example of beads mixture to make the store in Experiment 11.

Figure 167: Mechanically and evenly mixed beads of 0.5mm (50%), 2mm (25%), 3mm (25%) to form the store with local heterogeneity.

The pouring of beads started from the middle position of the top of the domain, in order to create the anticline-shaped trap. During the falling, larger beads with larger potential energy tended to roll over to the side faster and settle there. This uneven settling process created heterogeneous layers in the "store". But the filling-up process prove that the heterogeneity introduced by these layers did not significantly affect the movement of fluid, as the liquid front remained relatively even and were not affected significantly by the capillary heterogeneity (Figure 168, 0-60 minutes).

Simultaneous imbibition occurred when the aqueous saturation front migrated in to the seal section. Due to uneven settling of beads in the seal, regions with more 0.25mm beads will have a faster saturation than regions with more 0.5 mm beads. (Figure 168, 80 minutes onwards).

Once the filling up process finished, the aqueous reservoir connected to the bottom of the domain was replaced with the oil reservoir which was placed 25 inches higher to increase the capillary pressure and facilitate flow of oil into the system (see Figure 169). All valves are open, such that the gravity driven injection of oil entered the system and rose.

The system reached equilibrium in less than 2 hours, and about 150 ml aqueous phase was displaced out of the system. Then the migration of fluids stopped. Most of the oil was trapped between the seal and store boundary where has a large difference in capillary entry pressures (Region B and green circle in Figure 169).

Some of oil were trapped by the layers in the store, since those areas have more larger beads (2 mm or 3mm) and have lower entry pressure compared to the surrounding 0.5mm beads (Region C and red circle in Figure 169).

Some of oil entered the seal into the region apparently having more 0.5mm beads than 0.25mm beads (Region A and yellow circle in Figure 169). These low entry pressure regions were created at the bead-pouring stage, where beads mixture are dumped in to the domain from the two sides and slid down. Due to different sizes, the sliding speeds are different, therefore created these slanted layers and introduced local heterogeneity into the seal. Whether or not these layers served as channels connecting the store and top of the domain for oil remain unknown.

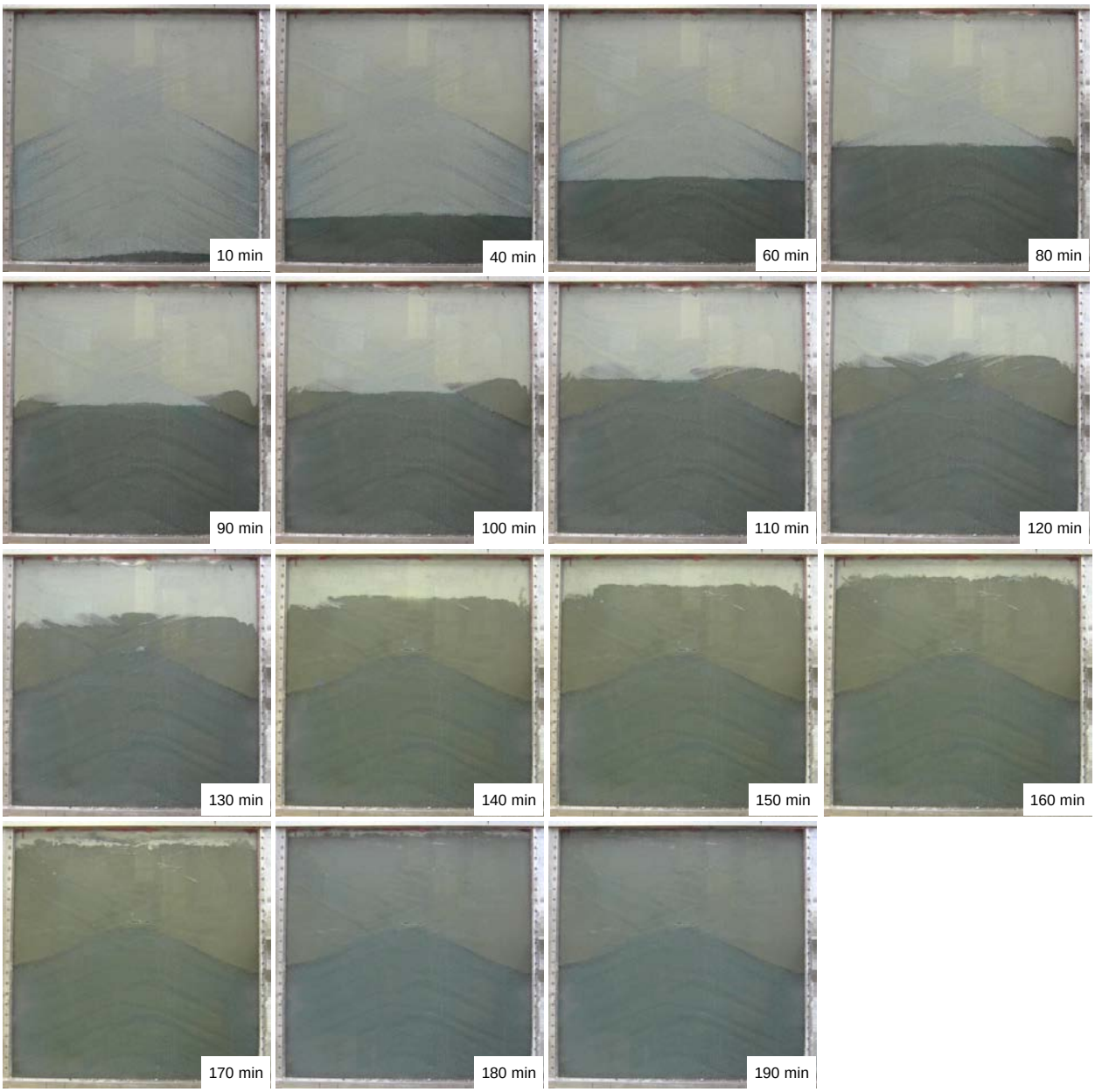

Figure 168: Initial saturation of the porous media of multi-distributed heterogeneity.

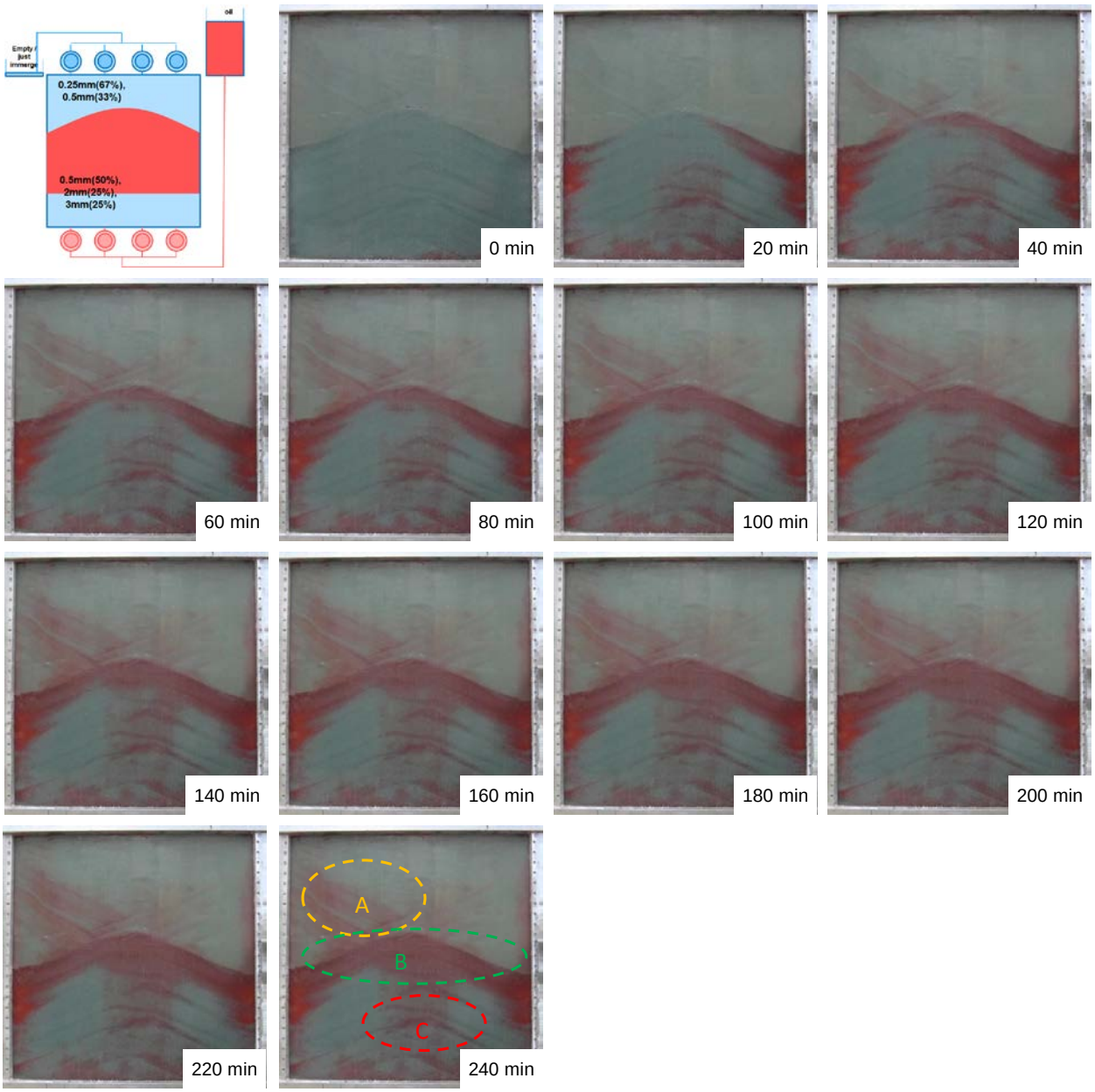

Figure 169: Drainage of Experiment 11.

The significance of Experiment 11 is that it opens a new realm of research area. For the first time we are one step closer to the real Nature where multi-distribution of beads occurring in a single formation. Previous experiments and simulation results are built on the assumption that individual formation is mono-distributed (containing only one size of beads), and distinct boundaries serve as distinct capillary barriers. Better understanding of the local multi-distributed heterogeneity presence as such in individual formation (both for the seal and store) will give us more accurate estimation of total potential storage capacity in the system.

Experiment 12

The overlap of pore size distribution between sealing formation and storage reservoir is smaller in Experiment 12 but is still nonzero. Consequently the seal is still leaky, and connected paths of nonwetting phase between the storage reservoir and the top of the domain are established within the sealing formation during drainage (left side of Figure 170). Much of the nonwetting phase escapes the storage formation when hydrostatic boundary conditions are established, though local capillary trapping does occur in smaller structures within the storage reservoir.

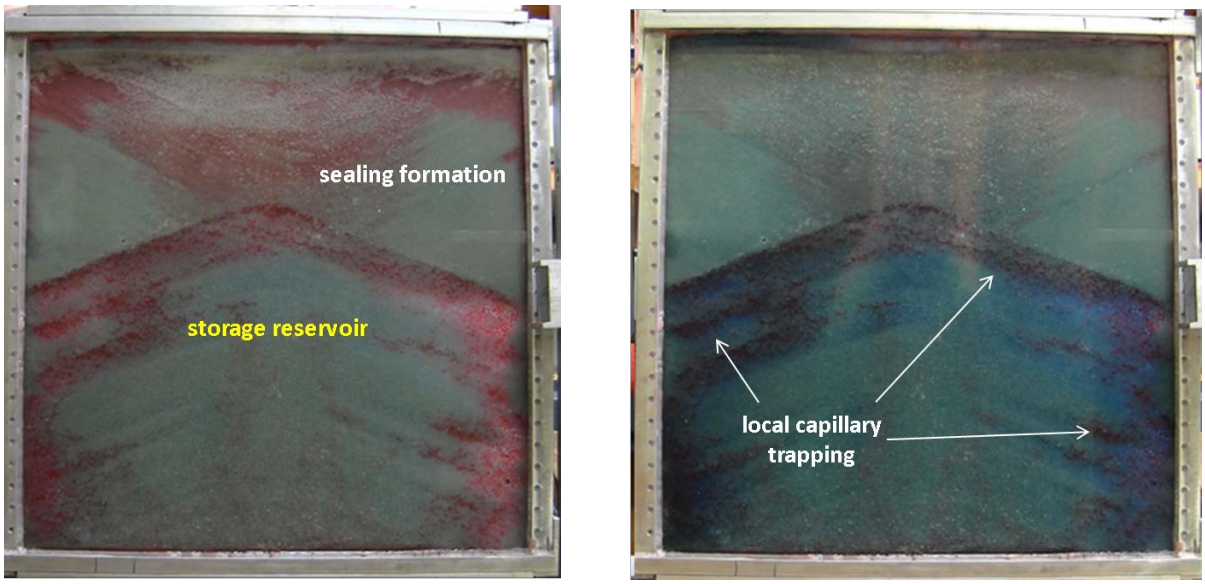

(a) (b)

Figure 170: Experiment 12; see Table 22 for bead size distributions. (a) end of drainage: nonwetting phase (red) driven by gravity enters the domain from bottom left and right as wetting phase (clear) is displaced at the top. Accumulation is evident within thin layers of larger beads (2 and 3 mm) in the storage reservoir, along the boundary between storage and seal, and along tilted regions in the sealing formation. (b) end of imbibition: water at hydrostatic pressure (blue) enters the domain as nonwetting phase leaves the domain due to buoyancy. Residual saturation of the nonwetting phase remains in the storage reservoir and sealing formation. Local capillary trapping is evident within numerous structures formed within the storage reservoir by sorting of the bead mixture during deposition.

Table 22: Grain Size Distributions Used in Experiments 11 Through 13

		0.15 mm	0.25 mm	0.5 mm	2 mm	3 mm
EXP 11	Seal		33%	67%		
	Store			50%	25%	25%
EXP 12	Seal		67%	33%		
	Store			50%	25%	25%
EXP 13	Seal	33%	67%			
	Store			50%	25%	25%

Experiment 13

When the distribution of bead sizes does not overlap between sealing formation and storage reservoir, as in Experiment 13, the behavior is simpler, as shown in Figure 171.

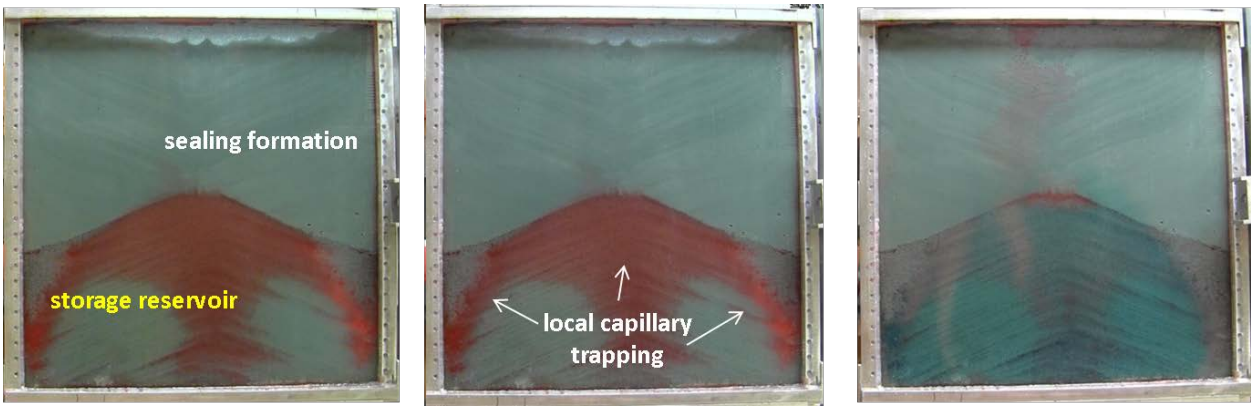

Figure 171: Experiment 13; see Table 22 for bead size distributions. (a) end of drainage: nonwetting phase accumulates in the storage reservoir beneath the capillary barrier of the smaller beads in the sealing formation. (b) end of imbibition: when open hydrostatic boundary conditions are established, none of the nonwetting phase is displaced. This is because all of it is held in a local capillary trap; the capillary pressure at the top of storage formation is smaller than the capillary entry pressure of the sealing formation. (c) end of forced imbibition: water is forced into the domain from the bottom by imposing a larger-than-hydrostatic gradient in the water phase from bottom to top of the domain. At sufficiently large imposed gradients the capillary pressure in the nonwetting phase exceeds the capillary entry pressure of the sealing formation, and the buoyant nonwetting phase leaves the storage reservoir.

The nonwetting phase fills the storage reservoir during drainage (Figure 171(a)). Local capillary trapping occurs throughout the storage reservoir, and no nonwetting phase enters the sealing formation. Consequently there is no displacement of the nonwetting phase under the open hydrostatic conditions representative of storage boundary conditions in real reservoirs (Figure 171(b)). The nonwetting phase is held at above-residual saturations, and this is demonstrated in the right image of Figure 171 when the water phase pressure gradient is held at a value significantly larger than hydrostatic (i.e. forced imbibition). In this situation the capillary pressure gradient within the nonwetting phase increases above the gradient applied during the drainage process (Figure 171(a)). Consequently the nonwetting phase can enter the sealing formation, and it does so. Note that the forced-imbibition boundary condition does not arise under natural storage conditions, where the pressure gradient in the aqueous phase will not deviate significantly from hydrostatic. The forced-imbibition part of the experiment is conducted solely to demonstrate that the trapped nonwetting phase is indeed held at above-residual saturations.

By illustrating the essential principle of local capillary trapping – namely, that any region of locally larger than average capillary entry pressure that is laterally extensive can hold a volume of buoyant nonwetting phase beneath it – in domains that have more realistic, heterogeneous pore size distributions, this set of experiments reduces the uncertainty associated with estimates of local capillary trapping in this project.

3.2.9 Summary of Experimental Observations

The experiments confirm the key physical principles underlying the phenomenon of local capillary trapping: i) the path followed by non-wetting phase migrating under the predominant influence of gravity is dictated by the interaction between the capillary pressure in the plume and the capillary entry pressure of the porous medium in which the plume migrates; ii) non-wetting phase can accumulate beneath barriers to buoyant migration and establish above-residual saturations; iii) the barriers correspond to regions of locally large capillary entry pressure; and iv) the non-wetting phase trapped beneath local barriers cannot be displaced unless the capillary pressure in the nonwetting phase is augmented.

3.3 Effect of Injection Rate on Extent and Persistence of Local Capillary Trapping

Prior to this project, the physical and conceptual examples of local capillary trapping focused on one limiting case of storage scenario: the emplacement of CO_2 in the lower portion of a storage reservoir, which then migrated upwards. For simplicity, the process of injecting the CO_2 was ignored, and the stored CO_2 was simply assumed to be present in the storage reservoir at the beginning of the While this scenario can be achieved at commercial-scale injection rates into the lower portion of reservoirs with large anisotropy (e.g. vertical permeability about one thousand times smaller than horizontal permeability), it is important to examine a wider range of storage scenarios, including smaller injection rates and smaller degrees of anisotropy. The research reported in this section evaluates the influence of the injection process on the filling of local capillary traps.

3.3.1 Effect of Injection Rate on Extent and Persistence of Local Capillary Trapping

It is convenient to discuss the influence of injection rate in the context of the limiting case of buoyancy-only CO_2 migration. For this purpose we introduce the gravity number, a dimensionless ratio of buoyancy forces to viscous forces that drive the CO_2 migration. Several definitions of gravity number are possible; here we use the ratio of nominal speed of vertical flow u_v to nominal speed of horizontal flow u_h combined with the ratio L/H of the characteristic length L and thickness H of the storage reservoir. The nominal vertical flow speed depends on the mean vertical permeability, the buoyancy driving force and the CO_2 viscosity:

$$u_v = \frac{k_v \Delta \rho g}{\mu} \tag{27}$$

The nominal horizontal flow speed is the volumetric flux (volume per unit area per unit time) from the injection well:

$$u_h = Q / A_w \tag{28}$$

where Q is the volumetric injection rate (at bottomhole conditions of pressure and temperature; for convenience these are take to be reservoir temperature and initial reservoir pressure) and A_w

is the surface area of the perforated section of the wellbore (i.e. $A_w = 2\pi r_w L_{perf}$ for a wellbore of radius r_w that has been perforated along an interval of length L_{perf}).

The characteristic rate of vertical flow in the reservoir is u_v/H, and similarly the characteristic rate of horizontal flow is u_h/L. We define gravity number as the ratio of these characteristic rates, writing:

$$N_{gr} = \frac{k_v \Delta\rho g L}{u_h \mu H} \tag{29}$$

For a given storage reservoir and well completion all terms in this expression are fixed except for u_h, which varies with injection rate. Thus gravity number is essentially a dimensionless injection rate (actually, a reciprocal injection rate). Small values of gravity number (10^{-2}) correspond to large injection rates, with correspondingly minimal influence of buoyancy on the CO_2 plume movement. Large values of gravity number (~10^2) correspond to very small injection rates, and CO_2 plume movement is dictated by gravity. For commercial injection rates and typical storage reservoirs, the gravity number is small in the portion of the reservoir near the wellbore. This is the region of primary interest in this research. We note however that for radial flow (expected to be the typical flow field for large-scale CO_2 storage), the gravity number increases with distance from the injection well.

Filling traps during buoyant displacement following CO_2 emplacement[9]

The limiting case of CO_2 migration driven only by buoyancy was discussed in Section 3.1.2. The trend in the extent of filling of local traps can be extracted from the fraction of reservoir pore volume of potential traps, which we determine from the geologic method described above, and the fraction of reservoir pore volume of CO_2 that occupies those traps, as determined by a full-physics simulation of buoyancy-driven migration. The value of critical capillary entry pressure used in the geologic method is taken to be the value that gives the best match of the occupied traps, as discussed in the text of Section 3.1.2. The results are summarized in Table 23.

[9] This section constitutes Project Deliverable 6.1 Trend of the fraction of potential local capillary traps filled as a function of primary controls for displacement driven by buoyancy.

Table 23: Extent of Filling of Local Capillary Trapping Capacity (LCT) when CO_2 Rises Due to Buoyancy from Initial Emplacement*

Domain		$P_{c,entry}^{crit}$	LCT Filled	LCT Possible	Fraction of Traps Filled	Reference
Number Dimensions	Correlation Length (m)	(kPa)	(PV)	(PV)	--	
2D	1.5	6.9	0.089	0.175	0.51	Table 6
2D	15	9.7	0.112	0.243	0.46	Table 8
3D	1.5	6.9	0.05	0.114	0.44	Table 10
3D	4.6	5.5	0.032	0.055	0.58	Table 12

*The value of critical capillary entry pressure (3rd column) is used to determine the possible volume of LCT (5th column) via the geologic method described above.

The results summarized in the sixth column of the table indicate that about half of the possible traps get filled when CO_2 migrates from an initial emplacement in the lower portion of a reservoir. This fraction is not a strong function of the geologic parameters (correlation length within the capillary entry pressure field) nor of the simulation parameters (dimensionality of the domain).

On the other hand the absolute amount of LCT, i.e. the fourth column in the table, ranges from 3% to 11% of the pore volume of the storage reservoir and does depend on dimensionality and geology. More LCT is possible in a 2D domain than a 3D domain, because the percolation threshold at which barriers becomes well connected is lower in 2D than in 3D. That is, the probability of getting a laterally extensive barrier is smaller in a 3D domain than in a 2D domain. More LCT is possible in a domain with greater correlation length because the lateral extent of the barriers is greater. (The simulation for the 3D domain does not show this effect because the size of the domain is only two correlation lengths in one horizontal direction, and this is unlikely to have given a statistically representative number of structures).

The fact that the fraction of the traps that gets filled is roughly constant for the cases summarized in Table 23 is a useful result. We propose that purely buoyancy-driven migration from an areally extensive plume will fill about half of the possible local capillary traps. The fraction of the reservoir pore volume corresponding to the local capillary traps depends on the nature of the heterogeneity of the storage reservoir.

Effect of Emplaced CO_2 Volume[10]

The results summarized above are for relatively small volumes of initially emplaced CO_2. It is instructive to observe the extent of filling of local capillary traps when more CO_2 is emplaced, then allowed to rise under gravity. Intuitively we expect the extent of filling to increase as the amount of emplaced CO_2 becomes large enough for the CO_2 to migrate to the top seal of the reservoir. This is because the CO_2 will begin to backfill the local capillary traps in an areally uniform fashion.

[10] This section constitutes Project Deliverable 6.3.1 Trend of fraction of potential local capillary traps filled under buoyancy as function of primary controls for different volumes of emplaced CO_2

As an example, Figure 172 shows the CO_2 saturation profile at 25 years after CO_2 was emplaced in the bottom 6.7 m of a heterogeneous formation. The rock properties have a 1.5 m correlation length in the horizontal direction. The CO_2 follows capillary-dominated complex patchy flow paths and in this figure, it has just found a connecting path to the top seal. Therefore, the initial volume of CO_2 used in this simulation, which is 20% of the formation pore volume, is the threshold value of stored CO_2 that leads only to local capillary trapping and does not lead to accumulation of gas as bulk phase in the storage formation. Because the flow path is so ramified, the threshold volume of CO_2 in the heterogeneous domain is small.

If three times as much CO_2 is emplaced beneath the heterogeneous reservoir, the rising CO_2 reaches the top of the reservoir along the capillary-dominated flow paths, as seen in Figure 173. Here the injected volume of CO_2 is 41% of the reservoir pore volume , which exceeds the threshold value for CO_2 to accumulate below the top seal as a gas cap. Consequently, all the local capillary traps in the uppermost portion of the reservoir get filled with CO_2. Indeed, all the pore volume that is not a local capillary barrier gets filled, hence the essentially binary distribution of CO_2 saturation in the uppermost portion: yellow/orange (CO_2 saturation equals unity less the irreducible brine saturation) and blue (CO_2 saturation is zero because the capillary pressure was smaller than the capillary entry pressure in that region. Note that not all the CO_2 filled region in the "gas cap" of the uppermost portion of the reservoir is in local capillary traps. That is, the CO_2 is backfilling all the non-barrier grid blocks in the gas cap. But only the fraction of these grid blocks that lie below a convex arrangement of barrier grid blocks (like a local anticline) will act as local traps. Below we discuss what happens to CO_2 in this grid blocks if the seal integrity is lost. For the purposes of this section, the key point is that the backfilling of the gas cap is tantamount to a gravity stable displacement of brine by CO_2. This causes the CO_2 to enter and fill all accessible (non-barrier) grid blocks at any given elevation in the reservoir before entering the next lower elevation. This is the opposite situation from rising CO_2, and consequently complete filling of local traps occurs in backfilled portions of the reservoir, while only partial filling (about 50%) occurs in the portions of the reservoir through which CO_2 rises.

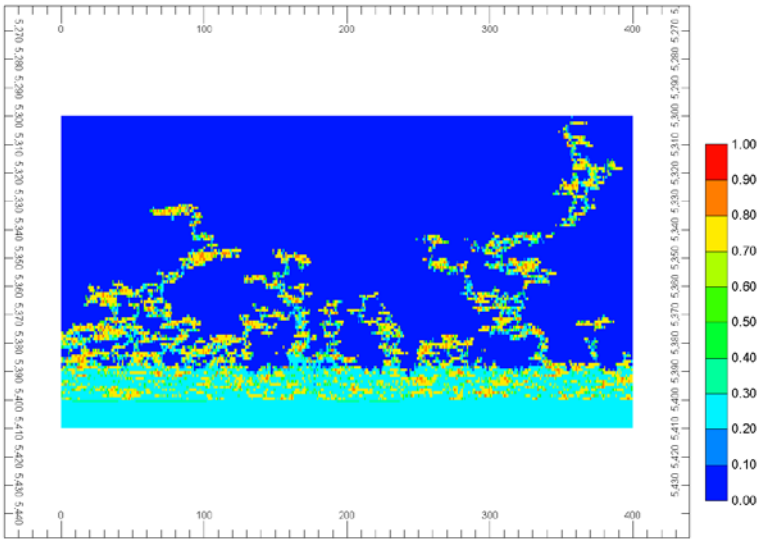

Figure 172: CO_2 saturation profile at steady state in a heterogeneous aquifer with initial emplacement in the bottom 6.7 m of the reservoir. The permeability field of storage formation has a 1.5 m correlation length. The rising CO_2 just reaches the top of the reservoir, filling about half the local capillary traps.

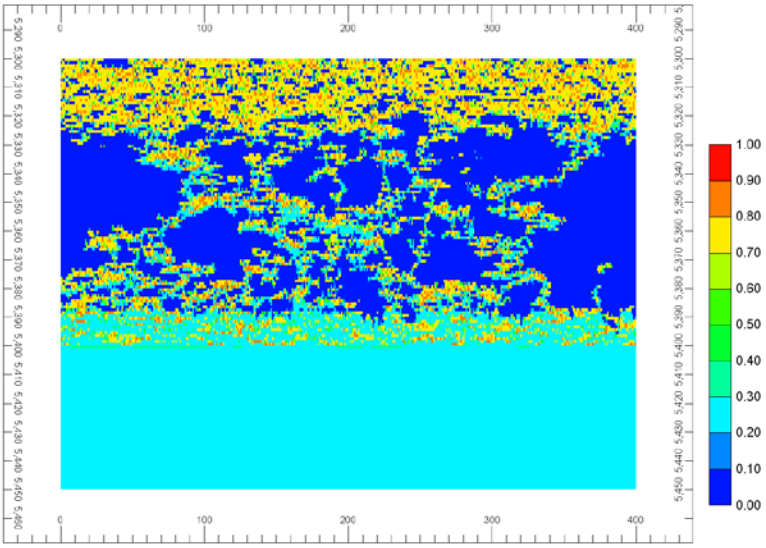

Figure 173: CO_2 saturation profile at steady state for the same reservoir with three times larger initial emplacement of CO_2 than in Figure 172. There is sufficient CO_2 to rise to top of reservoir then backfill all the local traps in the upper portion of the reservoir.

A systematic investigation of this concept is shown next. We increase the volume of CO_2 initially present at the bottom of the domain several-fold to study the accumulation of CO_2 as a bulk phase in the upper part of the storage formation, driven by buoyancy. The heterogeneous part of the domain remains unchanged. We add a thickness h_2 of CO_2-saturated layers to the bottom of the simulation model, representing the result of injection into a greater fraction of a thicker aquifer. New layers are added to the bottom of the domain to hold additional CO_2, as indicated in Figure 174. The new layers are homogeneous, with permeability and porosity equal respectively to the average permeability and porosity of the aquifer.

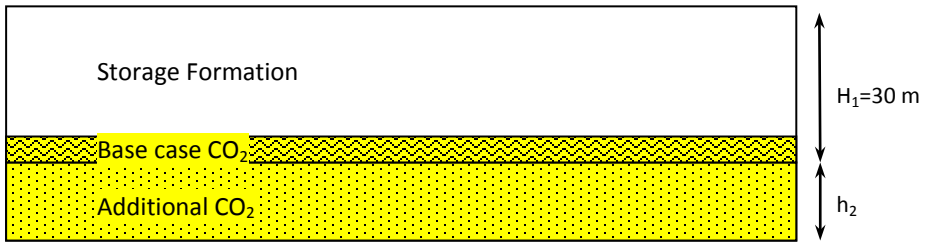

Figure 174: Schematic of the initial condition used to study the accumulation of CO_2 beneath the top seal. The heterogeneous part of the domain (H_1) remains unchanged; the bottom 12% (3.6 m) of this part contains CO_2. New homogeneous layers are added to the bottom of the domain (h_2) to hold additional CO_2.

Reservoir with 1.5 m Correlation Length

In this section results for a reservoir with 1.5 m correlation length are discussed. Figure 175 through Figure 180 show the CO_2 saturation profile at 25 years for h_2 equal to 0, 3, 6, 9, 15 and 30 m, respectively when capillary pressure scaling is used. In these figures, we can see that CO_2 follows capillary dominated flow paths to reach the top seal if adequate amount of CO_2 is provided. As discussed in previous section, in case with h_2= 3 m, Figure 176, the CO_2 has just found a connecting path to the top seal and hence, the initial volume of CO_2 is the threshold value of injection for no-risk-of-leakage scenario. When the injected volume of CO_2 is more than

threshold value, Figure 177 through Figure 180, the excess CO_2 accumulates below the top seal but not uniformly.

Regardless of reaching the top or not, large saturations of CO_2 (70% and more) remain in its flow path. At the end of simulation, the CO_2 exist through a wide spectrum of saturations. Above-residual saturations in the area below the seal are connected along the paths from the initial accumulation. However, still there exist some residual saturation and even un-invaded grid blocks in this upper "gas cap" section. The latter are the consequence of capillary barriers that resisted vertical migration from below and then from above as the accumulating CO_2 pushes downward. In other words, the barriers have been so severe that even pushing the gas downward by more CO_2 (which traveled upward due to buoyancy force) has not led the gas to invade those grid blocks.

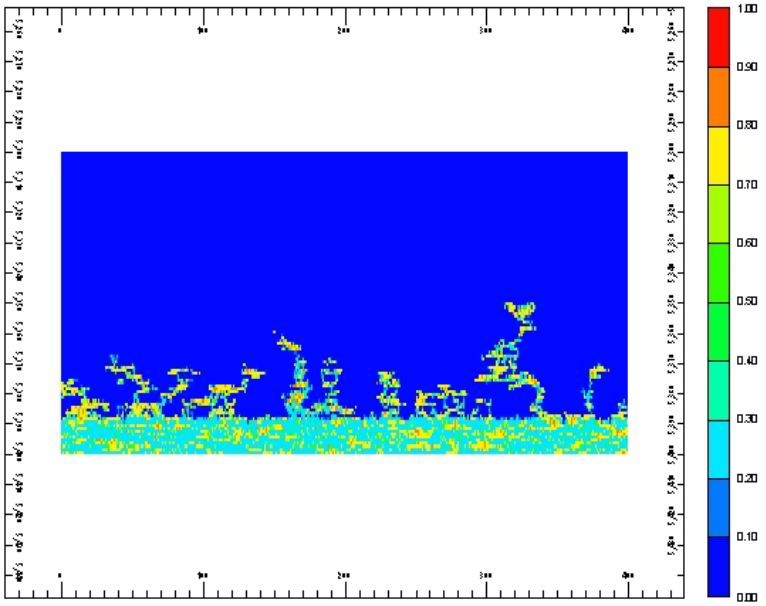

Figure 175: CO_2 saturation profile at steady state for the reservoir of Figure 174 with h_2=0, assigning the reference capillary pressure curve to average (mean) permeability of the field.

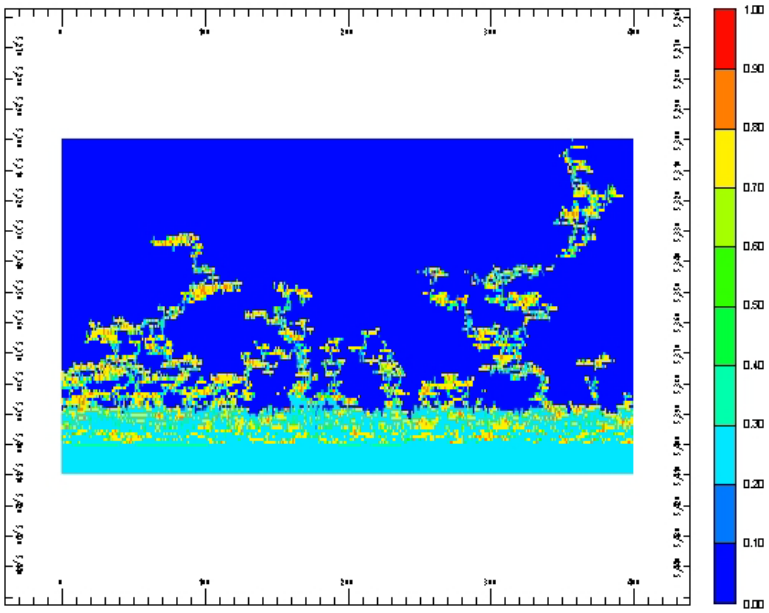

Figure 176: CO_2 saturation profile at steady state for the reservoir of Figure 174 with h_2=3 m, assigning the reference capillary pressure curve to average (mean) permeability of the field.

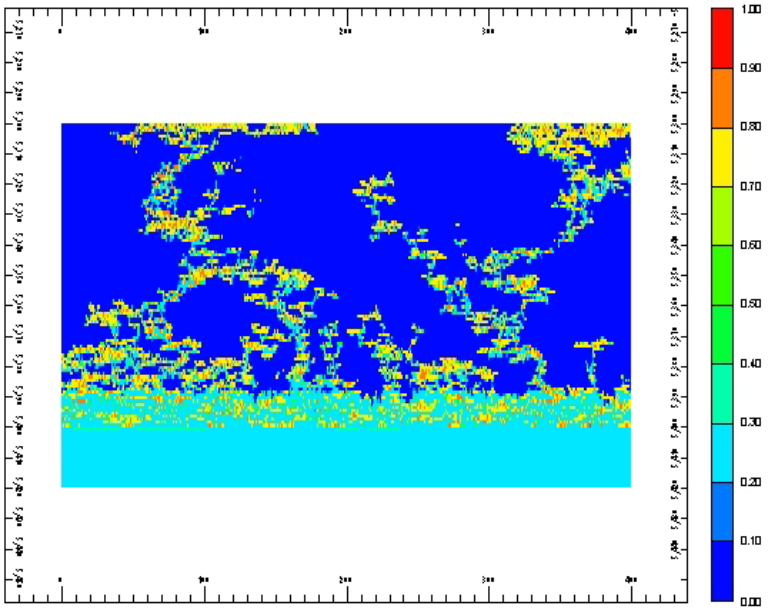

Figure 177: CO_2 saturation profile at steady state for the reservoir of Figure 174 with h_2=6 m, assigning the reference capillary pressure curve to average (mean) permeability of the field.

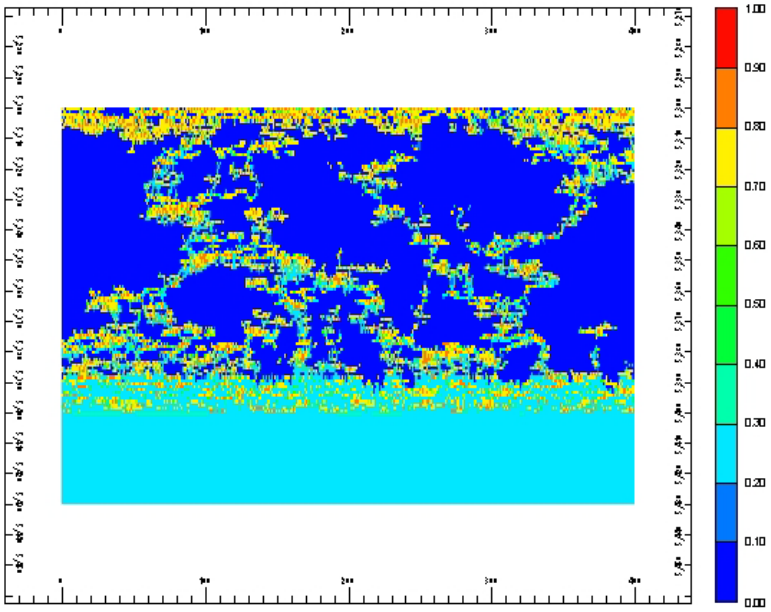

Figure 178: CO_2 saturation profile at steady state for the reservoir of Figure 174 with h_2=9 m, assigning the reference capillary pressure curve to average (mean) permeability of the field.

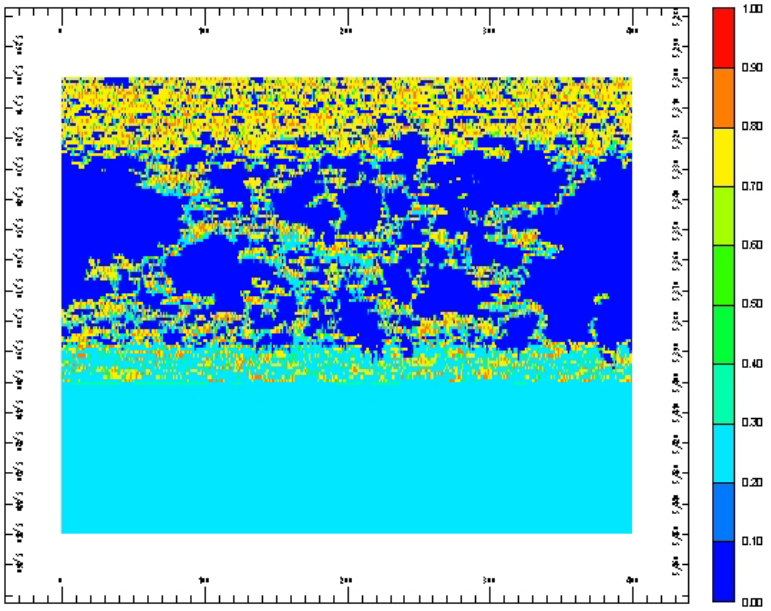

Figure 179: CO_2 saturation profile at steady state for the reservoir of Figure 174 with h_2=15 m, assigning the reference capillary pressure curve to average (mean) permeability of the field.

Figure 180 shows the gas saturation profile at 25 years when h_2=30 m, i.e., the volume of injected CO_2 is more than pore volume of the storage formation. This causes the CO_2 to almost spread over the whole area of storage formation. In fact, CO_2 first rises through capillary dominated flow paths due to buoyancy and then sweeps the aquifer downward due to rise of more CO_2 in those channels. In this case, the aquifer is divided into two parts, with no distinguishable transition zone in between: an upper section (the gas cap) in which CO_2 accumulates in high saturations within the flow channels, and a lower section with residual CO_2 saturation where CO_2 was initially injected.

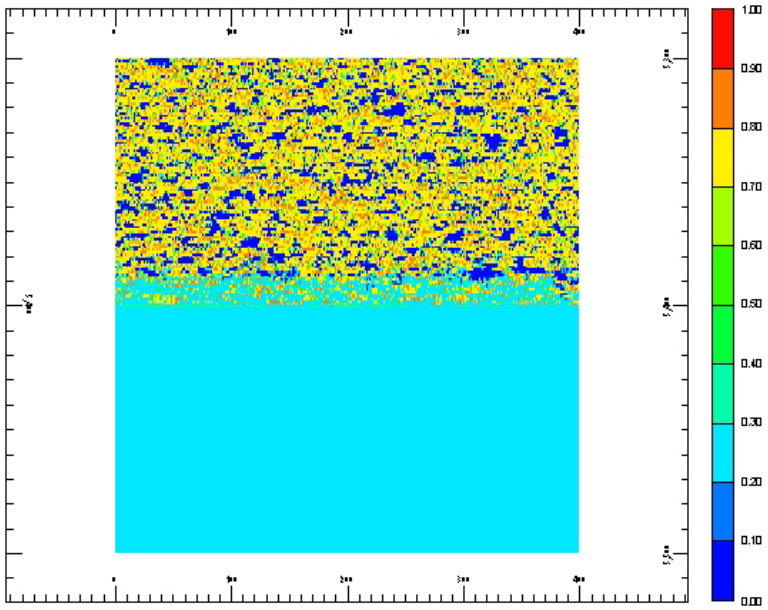

Figure 180: CO_2 saturation profile at steady state for the reservoir of Figure 174 with h_2=30 m, assigning the reference capillary pressure curve to average (mean) permeability of the field.

To verify that the backfilled regions are in fact filling all the traps, the saturation map is recolored, so that black corresponds to above-residual saturation, and then overlaid onto the map of capillary entry pressure in Figure 181. The gas cap in the uppermost 5% to 10% of the reservoir shows extensive regions of large saturation (yellow and orange pixels in upper panel), and these fill all the nonbarrier cells in that part of the reservoir (dense black regions in lower panel separated by warm colors, which indicate large capillary entry pressure in lower panel). Since the local capillary traps are necessarily a subset of the nonbarrier cells, it follows that all the local capillary traps are filled in the gas cap region. In contrast, the transition zone (between the gas cap and the region of initial CO_2 emplacement), where the CO_2 only rose through the domain, many of the nonbarrier cells (blue regions in lower panel) contain no CO_2. That is, the black regions occupy a smaller fraction of the pore volume in the transition zone, and it follows that some of the local capillary traps in the transition zone have not been filled. This is consistent with the results discussed above in Table 23.

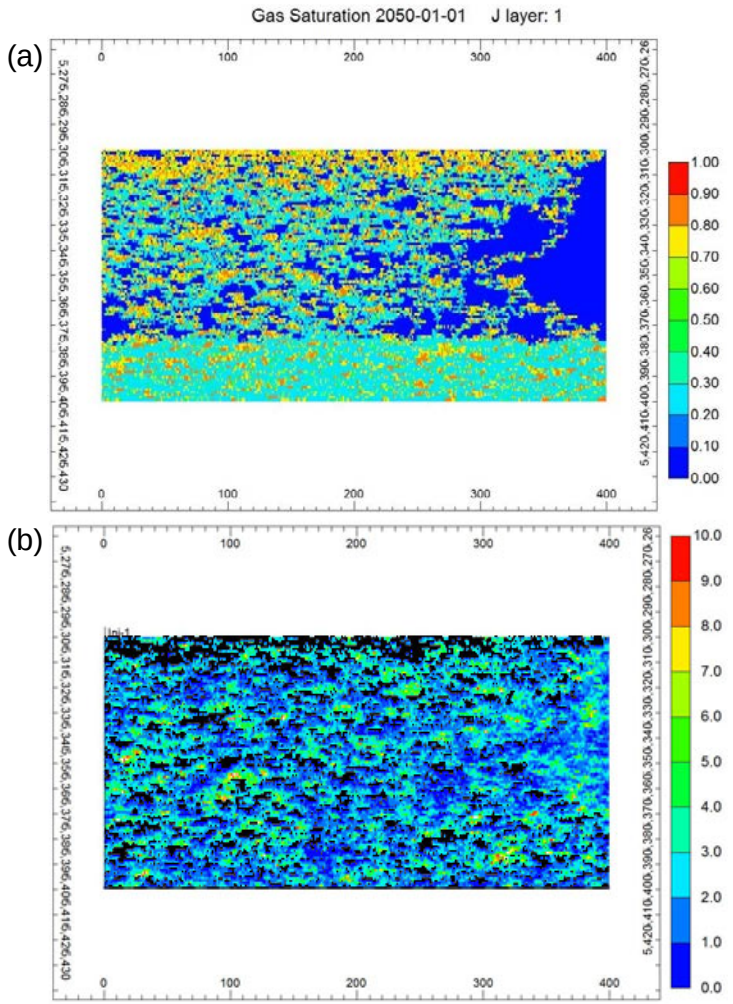

Figure 181: (a) CO_2 saturation profile at steady state when CO_2 is initially emplaced in bottom 25% of the reservoir. Backfilling occurs in the uppermost 10% of the reservoir. (b) Map of capillary entry pressure distribution in the reservoir, with above-residual saturations of CO_2 from the upper panel marked as black pixels. Not all traps are filled in the transition zone (relatively sparse black regions) but all the traps, along with all non-barrier cells, are filled in the gas cap (dense black regions) at the top of the reservoir.

Summary for Buoyancy-Only Displacement. We conclude that the extent to which purely buoyancy-driven CO_2 fills local capillary traps is about 50% in the transition zone (lying above the initial emplacement and below the final accumulated gas cap), where the CO_2 rises through the reservoir, and 100% in the gas cap (region backfilled below the seal overlying the reservoir). The size of the transition zone depends on the amount of CO_2 emplaced.

Filling Traps During Buoyant Displacement Following CO_2 Injection

Having established the behavior in the limiting case of storage scenario in which CO_2 migrates through the heterogeneous reservoir only due to buoyancy, we now examine the influence of flow during in the injection process on the behavior.

Aquifer Model Description

The 2D model is almost the same as before, the relevant important parameters are stated again here for reference. As shown in Figure 182 the domain is a 120 m wide by 30 m high two-dimensional Cartesian grid system with grid blocks 0.3 m by 0.3 m. The initial pressure is 15.6 MPa with constant temperature of 60°C. The geostatistical permeability field has an average of 1.0×10^{-13} m^2 with the Dykstra-Parsons coefficient of 0.7. The permeability is correlated in the horizontal direction with length of 1.5 m and no correlation in the vertical direction. Leverett-*J* function was used to scale the capillary pressure of each grid. The fluid/rock properties are all the same as described above.

We apply an extremely large VOLMOD (1.0E+7) to the right boundary gridblocks. This mimics a constant pressure boundary. Clearly this assumption is not an accurate representation of the pressure response. But here we are concerned only with the extent to which local capillary traps get filled. This assumption is convenient because it prevents pressure buildup during injection without perturbing the injection flow field. Pressure buildup is problematic because it greatly alters the behavior if the overlying seal integrity is compromised, which is explored in the next section.

We set the domain to be anisotropic by considering the vertical component of permeability to be a tenth, hundredth, and thousandth of the horizontal component. Two formation dip angle, 5 and 25 degree were incorporated into the domain to represent moderate and highly deviated saline aquifer formation, respectively.

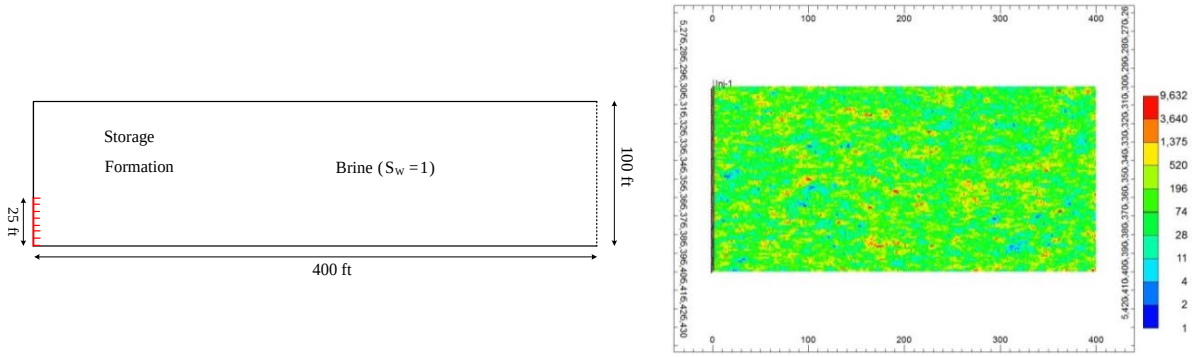

(a) (b)

Figure 182: 2D aquifer model (a) and permeability field (b), vertical well is located in the left boundary of the Cartesian systems with the injection interval height of 25% of the reservoir thickness. Very large volume modifiers (1.0E+7) are applied to the right boundary gridblocks to represent a constant pressure boundary.

Effect of Injection Rate[11]

In this work, the range of CO_2 saturations associated with local capillary trapping is defined as the range from maximum residual saturation ($S_{gr}^{max} = 0.286$) to 100%. So, in the following evaluation on the injection and leakage modeling, gas saturation of the grids in the domain above maximum residual CO_2 saturation would be considered as local capillary trapping. The LCT mass fraction is calculated using the following equation:

$$m_{LCT} = \sum_{S_g > 0.286}^{PV<1} (PV \cdot (S_g - 0.286) \cdot \rho_{g,molar} \cdot Y_{CO_2} \cdot MW_{CO_2}) \quad (30)$$

where, PV is pore volume. S_g is CO_2 saturation; $\rho_{g,molar}$ is gas phase mole density; Y_{CO2} is gas mole fraction of CO_2; and MW_{CO2} is CO_2 molecular weight, 44 g/mole.

Figure 183 shows the CO_2 plume distribution at the end of injection for the different injection rates, the total injected CO_2 mass for the four cases are the same of 189.53 ton. It can be observed that injection eliminates the transition zone, at least in the vicinity of the wellbore, for the isotropic domain. In the section *Effect of Anisotropy* below we try to find out if we can get transition zones from long-term injection, by considering very anisotropic domains.

At large injection rate (N_{gr}=0.039, 0.39), the immiscible displacement is compact and CO_2 could go almost everywhere during injection, Figure 183(a) and Figure 183(b). This leads to widespread residual gas trapping during water imbibition into the tail edge of CO_2 plume, as shown in Figure 184(a) and Figure 184(b). CO_2 immobilized by local capillary trapping is surrounded by CO_2 immobilized by residual gas trapping, which makes local capillary trapped CO_2 much safer provided any leakage occurs.

However, when the small injection rates are employed, corresponding to the large gravity numbers, CO_2 mostly followed channels of correlated large-than-average permeability, Figure 183(c) and Figure 183(d). As the injection rate decreases, buoyancy stands out as the main driving force and the gravity segregation is pronounced, as show in Figure 183(c) and Figure 183(d).

After injection ends, CO_2 would continuously migrate upward and laterally under the driving force of buoyancy. We run the simulation till CO_2 plume is at the steady state, and it is observed that in the post-injection period, CO_2 is either migrating along a path at a low critical saturation or is backfilling and flooding a trap to a higher saturation.

Figure 184 shows the CO_2 plume distribution after 50 year of injection plus post-injection period with 189.53 ton of total CO_2 injected; the gravity numbers are 0.039 (a), 0.39 (b), 3.87 (c), and 38.7 (d), respectively. It can be observed that local capillary traps in the near-well region are fully filled during injection at low gravity numbers (large injection rates). Moreover, they remain

[11] This section constitutes Project Deliverable 6.2 Trend of fraction of potential local capillary traps filled as function of primary controls including effect of the injection period for a range of gravity numbers

filled after post-injection buoyancy-driven flow ends, as indicated by the bright and scattering yellow and green colors in the domain. This is much greater degree of filling than predicted for purely buoyancy-driven migration from a laterally extensive uniform saturation in the lower portion of the aquifer. In the latter, most of the local capillary traps do not get filled because CO_2 migrates along some, but not all, of the channels with small capillary entry pressure, which means CO_2 accesses relatively small volume of local capillary traps. Obviously, the fraction of potential local capillary traps filled for the largest gravity number (Figure 184(d)) is the least in the four cases studied here. Therefore, utilization efficiency on local capillary traps decreases as transition from compact displacement to the capillary channeling flow, i.e. as injection rate decreases.

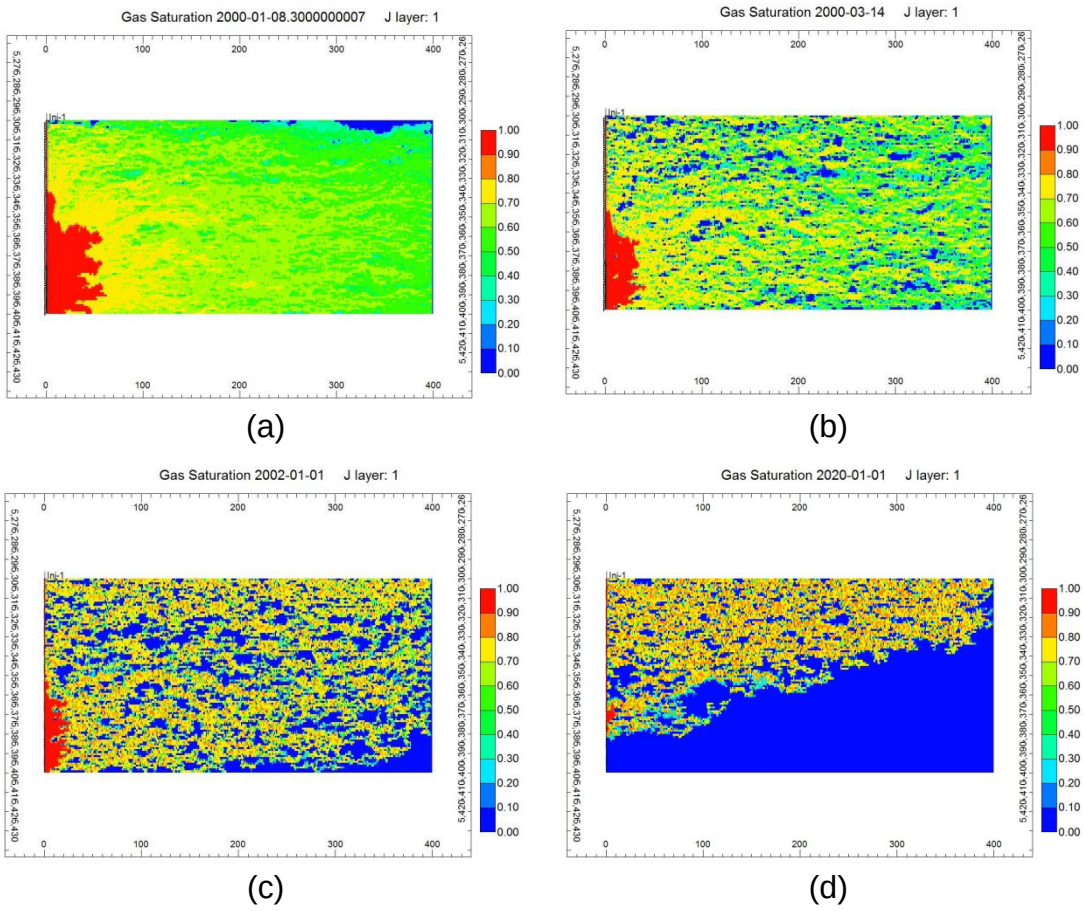

Figure 183: CO_2 plume distribution at the end of injection for the isotropic formation with 189.53 ton of total CO_2 injected, the injection periods for the gravity numbers of 0.039 (a), 0.39 (b), 3.87 (c), 38.7 (d) are 0.02 yr (a), 0.2 yr (b), 2 yr (c), and 20 yr (d), respectively. At the end of the injection period, mass of CO_2 staying in the 122 m × 30 m portion of the domain are 147.6 ton (a), 106.2 ton (b), 92.1 ton (c), and 57.6 ton (d). The difference between the remaining and the injected CO_2 masses has entered the column of very large grid blocks on the right side of the domain.

On the other hand, the filling of local capillary traps *within the region invaded during injection* is essentially the same for all injection rates. That is, if a region contains CO_2 at the end of injection, and that region corresponds to a local capillary trap, then at steady state that trap will contain locally trapped CO_2 at a large saturation, regardless of the gravity number during injection. In other words, while the gravity number strongly influences the fraction of the

reservoir into which CO_2 flows during injection—essentially 100% at small gravity number, falling to about 50% at large gravity number (compare blue regions in Figure 183)—the migration processes that fill the traps to large saturation occur after injection ends, and hence are independent of gravity number.

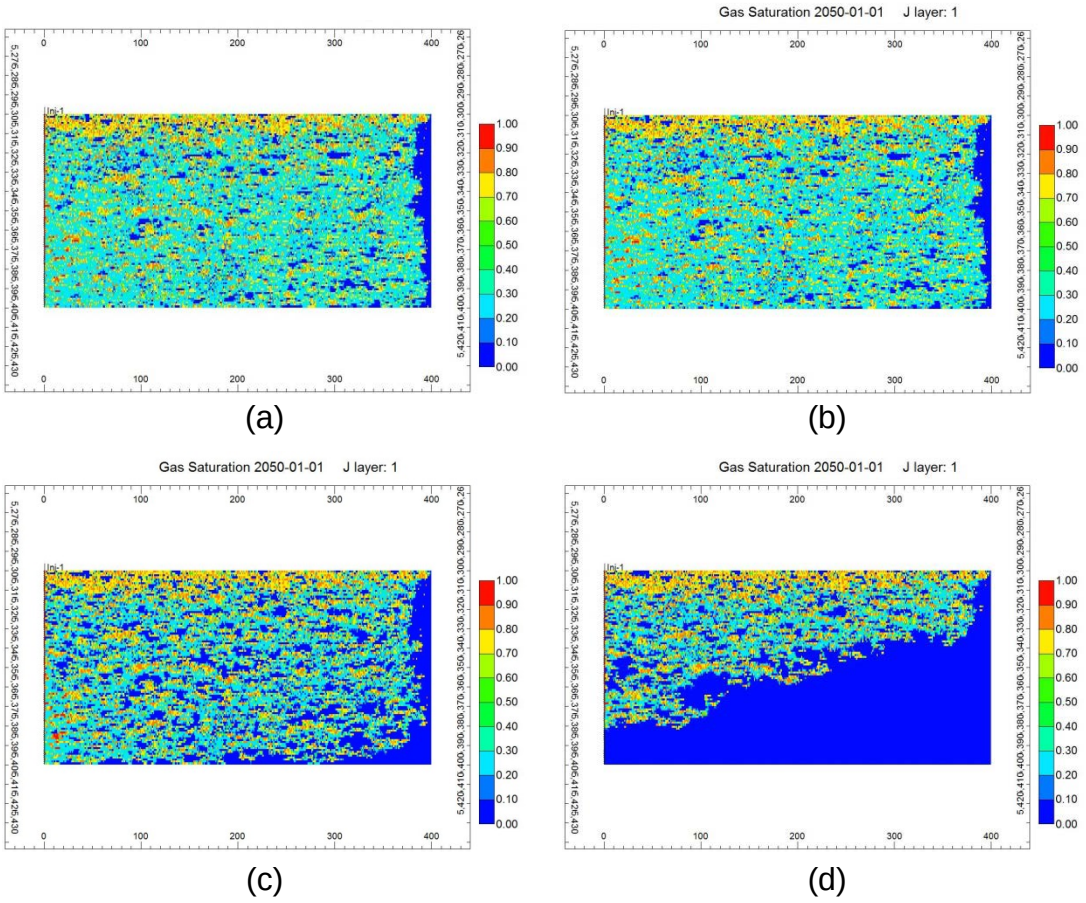

Figure 184: CO_2 plume distribution after 50 year of injection and post-injection period with 189.53 ton of total CO_2 injected, the gravity numbers are 0.039 (a), 0.39 (b), 3.87 (c), and 38.7 (d), respectively.

As in section **Filling traps during buoyant displacement following CO2 emplacement** it is instructive to verify that the steady state post-injection CO_2 distribution occupies local capillary traps. Consider for example the case of largest injection rate (gravity number 0.039). Because viscous forces are large throughout this 2D reservoir at so small a gravity number, CO_2 displaces water from every grid block in the domain by the end of injection, Figure 183(a). Obviously CO_2 has invaded all the regions corresponding to local capillary traps. The CO_2 has also invaded all the regions corresponding to capillary barriers. This is to be expected: the definition of a barrier is with respect to capillary forces, not to viscous forces. None of the grid block have zero permeability, and thus when viscous forces are sufficient to overcome capillary entry pressures, the CO_2 can and does invade the entire domain.

The detailed structure of the heterogeneous reservoir can still be detected in the fine-scale variation of the saturation contours in Figure 183(a). As an aside this is the reason that

simulation of conventional reservoir processes, in which flow at commercial rates is driven by production and injection wells throughout the reservoir, routinely ignores the heterogeneity of capillarity in the reservoir. The solution, in terms of where injected and reservoir fluids go, is dictated by the structure of the permeability field, and this can be determined with sufficient accuracy by ignoring capillarity. However in the application of geologic CO_2 storage, the onset of buoyancy-dominated migration and displacement is a crucial portion of the storage process. This behavior cannot be described correctly unless the heterogeneity of capillarity is explicitly included.

The widespread filling of local capillary traps in the high-rate injection storage scenario is similar to behavior observed in the large-emplaced volume limit of the buoyancy-driven storage scenario. As discussed in the previous section, in the latter scenario all the local capillary traps get filled as the rising CO_2 forms a gas cap, backfilling nonbarrier regions downward from the seal overlying the reservoir. In high-rate injection, viscous forces enable the CO_2 to fill all the rock volume. In both cases, essentially all the traps are filled. Recalling that one challenge of finding a method to estimate critical capillary entry pressure for the small-emplaced-volume storage scenario was that only some of the traps were filled. This suggests that a method to identify the critical capillary entry pressure could be easier for the injection storage scenario, although this was beyond the scope of this project.

The next step of the storage process, when injection ceases, is that the injected CO_2 and the remaining native brine are free to rearrange themselves in response only to buoyancy forces. Because the CO_2 is above residual saturations in the entire reservoir, we expect significant migration to occur. Figure 184(a) confirms this expectation, and moreover demonstrates that large saturations accumulate within the local capillary traps – even when the saturation in the trap at the end of injection was a moderate value. To see this note how many of the yellow/orange pixels in Figure 184(a) correspond to green pixels in Figure 183(a). Evidently post-injection migration enables CO_2 to build to the drainage-curve limit in the local capillary traps. Meanwhile in regions that are neither traps nor barriers the CO_2 present at the end of injection migrates until it leaves residual saturation behind (cyan pixels).

Overlaying the above residual saturations of Figure 184(a) as black pixels on the capillary entry pressure map yields the right panel in Figure 185. This confirms that the steady-state CO_2 distribution has filled essentially every possible local trap. Blue regions still exist in the right panel, as they did in the emplacement storage scenario in Figure 181. But these regions contained no CO_2 in the emplacement scenario; here in the case of high-rate injection these regions contain residual CO_2.

We summarize these observations in a plot of local capillary trapping characteristics in Figure 186.

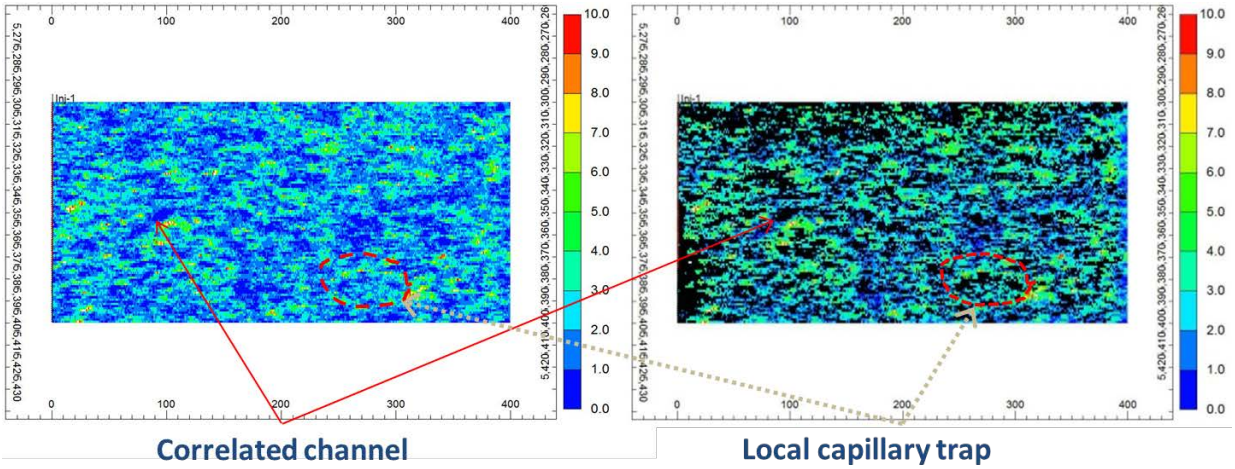

Figure 185: (a) Map of capillary entry pressure distribution in the reservoir used for injection modeling. Blue regions are non-barriers. (b) Same capillary entry pressure map with steady-state CO_2 above-residual saturation map (from Figure 184(a)) overlaid as black pixels. High-rate injection (gravity number = 0.039) into lower portion of the reservoir. The prevalence of black regions beneath warm colors shows that essentially all the local capillary traps in the entire reservoir are filled. Note the contrast with the transition zone of Figure 181.

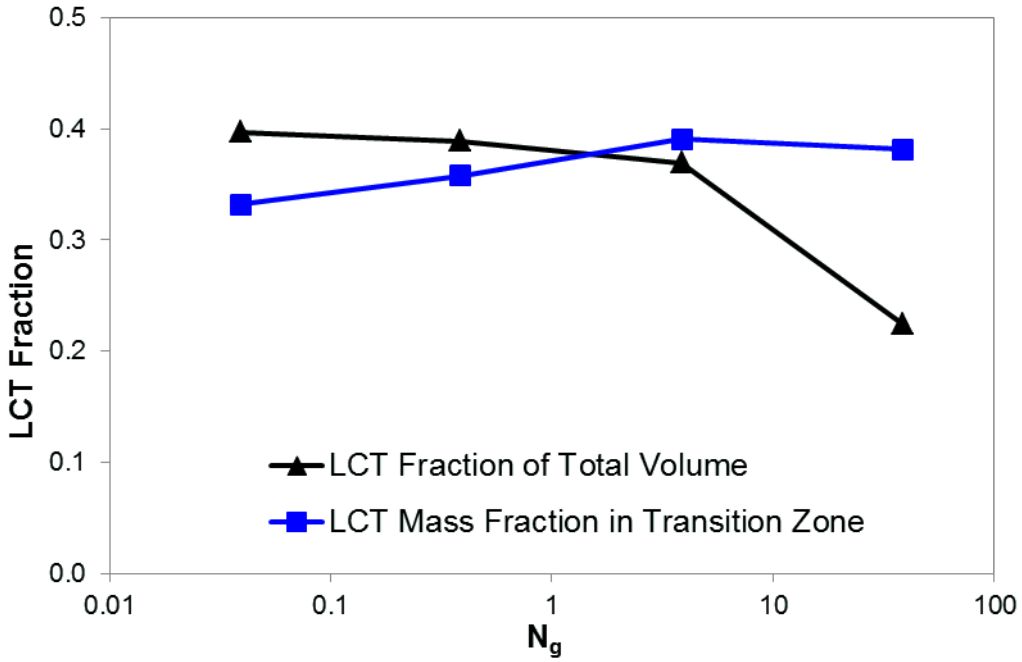

Figure 186: Summary of local capillary trapping (LCT) behavior in Figure 183 and Figure 184. In the transition zone (the volume of the reservoir below the gas cap that accumulates at the top of the reservoir at steady state) LCT is essentially independent of the injection rate. This is because all local traps get filled during injection, either because viscous forces overcome capillary entry pressure barriers (small gravity number) or because the volume of injected CO_2 is large enough to fill non-barrier regions (large gravity number). Expressed in terms of the total reservoir volume, the LCT decreases as gravity number increases, because the dominance of buoyancy causes the CO_2 to sweep only the upper portion of the reservoir.

Finally we remark that the smallest gravity number in the above simulations corresponds to a reasonable commercial scale injection process. The large gravity number scenarios correspond to uneconomically small injection rates (as low as a ton per day) and thus are unlikely to occur in near-wellbore regions of a storage aquifer. However, the difference in behavior (fraction of the reservoir swept during injection) is important, because in 3D reservoirs the gravity number increases steadily with distance from the injection well. Thus the key question will be what fraction of the reservoir gets swept when the CO_2 plume has advanced 100 m from the injector and beyond. Though beyond the scope of this project, the results of the large-gravity-number simulations (panels (c) and (d) in Figure 183 and Figure 184) provide qualitative insight into possible local capillary trapping behavior in more distant regions of the storage reservoir.

Effect of Injected Volume

Figure 187 shows the CO_2 plume distribution after 50 years of injection and post-injection period of flow simulation. Different mass of CO_2 were injected for the above five cases at the constant relatively large injection rate (N_{gr}=0.039). We simulated injection at a fixed rate for several time periods: 0.002 yr (a), 0.004 yr (b), 0.01 yr (c) , 0.02 (d), 0.04 yr (e), with the corresponding injected mass of 18.95 ton (a), 37.9 ton (b), 94.77 ton (c), 189.53 ton (d), and 379.1 ton (e), respectively. Obviously, as the injected CO_2 mass increases, the local capillary traps in the 122 m × 30 m portion of the domain become more fully used.

Recalling that the maximum mass of CO_2 that can be accommodated in the pore volume of the 122 m × 30 m portion is 189.53 ton, it is very instructive to compare the two largest injected mass (189.53 ton and 379.1 ton) in terms of their CO_2 plume distribution at the steady state. As shown in Figure 187(d) and Figure 187(e), the injected CO_2 mass does not affect the local capillary trapped CO_2, and the bright yellow color for the two cases have the same distributions and structures. This implies that local capillary traps are intrinsically determined by the geologic model for injection at low gravity number.

Similarly to the behavior observed at different gravity numbers, Figure 187 shows that the CO_2 occupies all the local capillary traps within the region swept by CO_2. Thus the essential question during injection is what fraction of the reservoir volume “sees” injected CO_2. This depends on gravity number, injected volume and heterogeneity of the permeability field. The gravity driven fluid movement after injection ends enables CO_2 to fill local traps in the swept region to a large saturation.

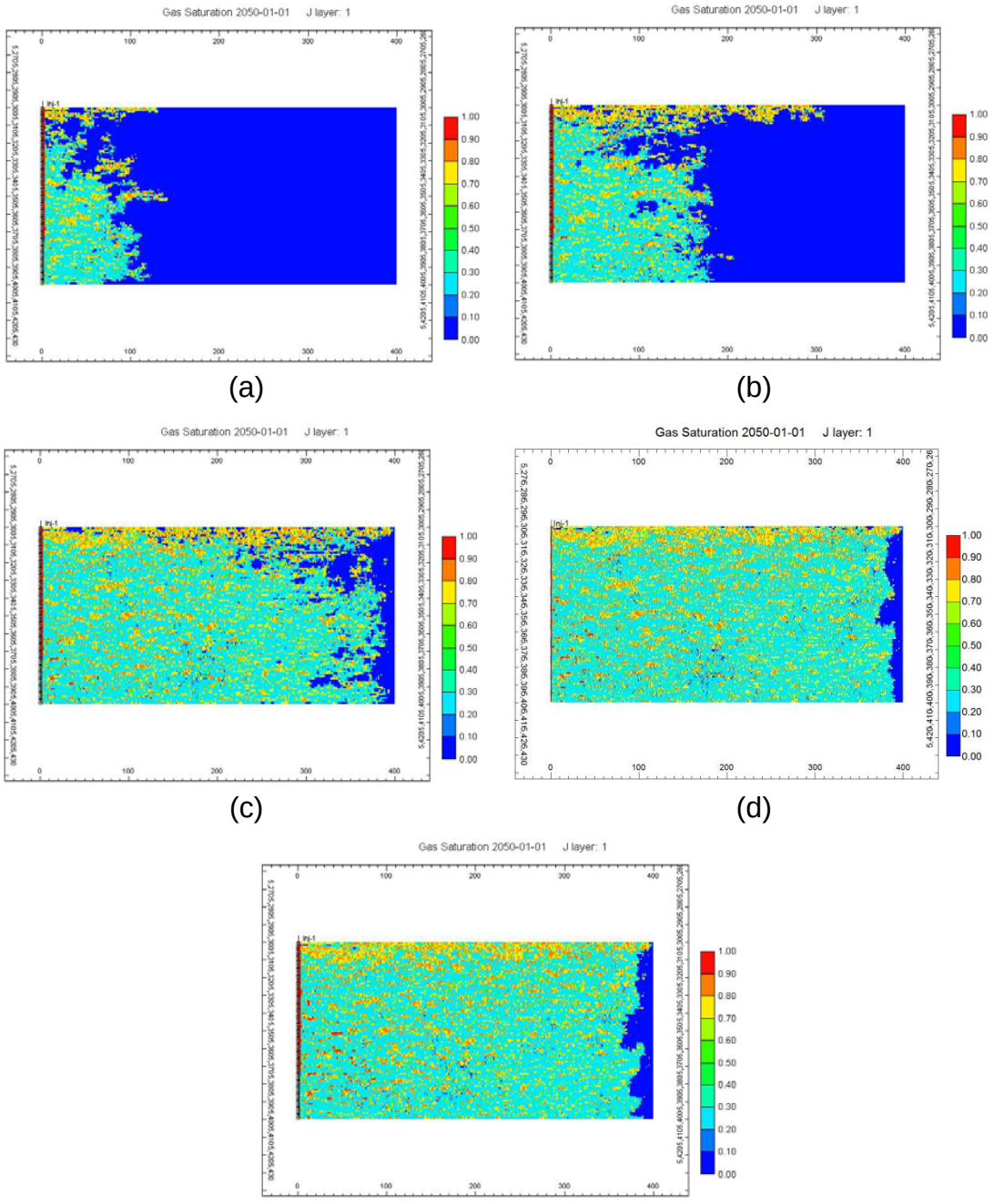

Figure 187: CO_2 plume distribution after 50 years of injection and post-injection period of flow simulation. Different volumes of CO_2 were injected for the above five cases at the constant injection rate (N_{gr}=0.039), The injection periods are 0.002 yr (a), 0.004 yr (b), 0.01 yr (c) , 0.02 (d), 0.04 yr (e), with the corresponding injected mass of 18.95 ton or 0.1 reservoir pore volume (PV) (a), 37.9 ton or 0.2 PV (b), 94.77 ton or 0.5 PV (c), 189.53 ton or 1 PV (d), 379.1 ton or 2 PV (e), respectively.

Effect of dip angle[12]

In this section, we study of the influence of the geologic setting (dip angle) on the potential local capillary trapping structures by selecting dip angles of 0°, 5°, and 25°. They are representative of horizontal formation, moderate dip and highly inclined formations, respectively. Figure 188 shows the CO_2 plume distribution at the end of injection for the above three angles, The total injected CO_2 mass is of 189.53 ton with the injection period of 0.02 yr under the same injection rate (N_{gr}=0.039). At this moment, the mass of CO_2 staying in the 122 m × 30 m portion of the domain are 147.6 ton (a), 147.73 ton (b), and 148 ton (c), respectively. Therefore, when the high injection rate is employed, dip angle does not change the mass of CO_2 remaining in the portion at the end of injection.

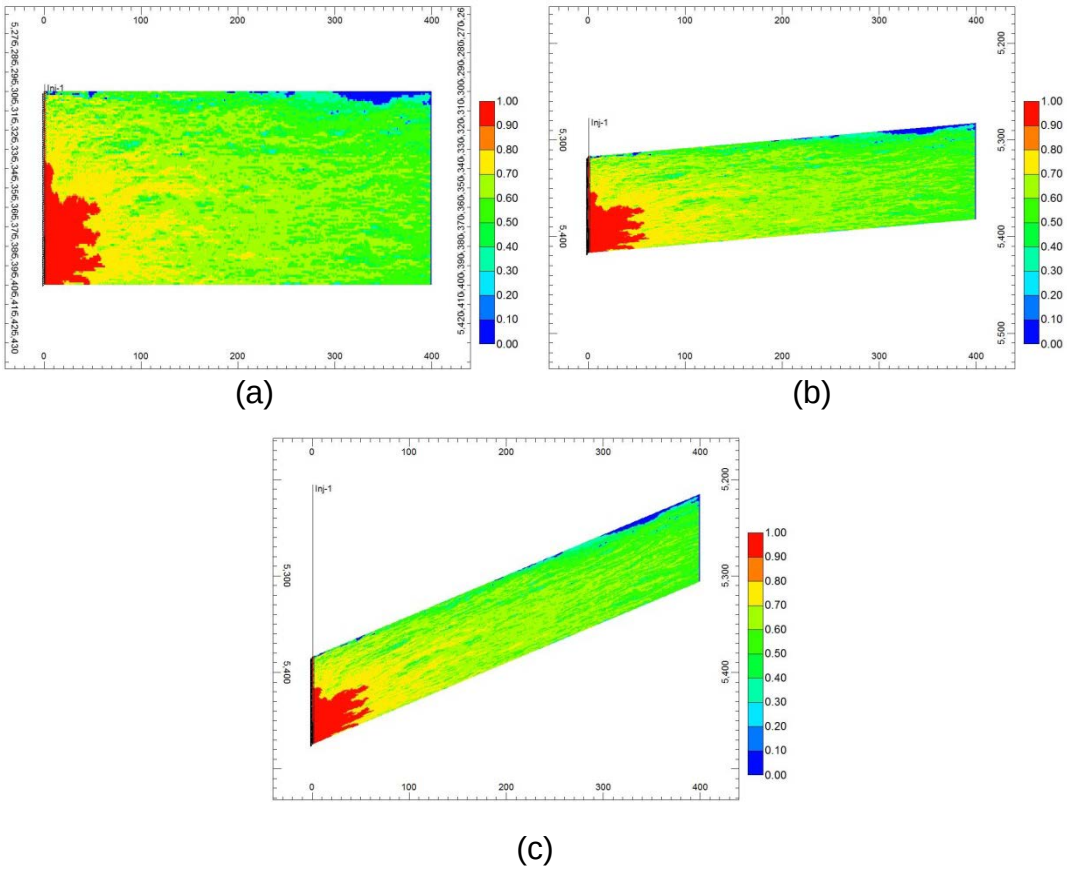

Figure 188: CO_2 plume distribution at the end of injection for the 2D isotropic model with formation dip angle equal to 0 degree (a), 5 degree (b), and 25 degree (c), respectively. They are representative of horizontal, moderate dip and high dip, respectively. The total injected CO_2 mass is of 189.53 ton with the injection period of 0.02 yrs under the same injection rate (N_{gr}=0.039). At this moment, the mass of CO_2 staying in the 122 m × 30 m portion of the domain are 147.6 ton (a), 147.73 ton (b), and 148 ton (c), respectively.

After injection, CO_2 continues to flow upward and laterally, Figure 189 shows the CO_2 plume distribution after 50 years of injection and post-injection flow modeling (at the steady state) for

[12] This section constitutes Project Deliverables 3.1-3.3 on the effect of dip angle on local capillary trapping.

the 2D isotropic model with formation dip angle equal to 0 degree (a), 5 degree (b), and 25 degree (c), respectively. Generally, we can see that the local capillary trapping structures in the moderate dip formation are similar to those of the horizontal formation. However, when the formation is becoming highly inclined, local capillary trapping structures tend to be parallel to the formation. It can be extrapolated that when the formation is vertical, there would be the least amount of local capillary trapping, because the vertical permeability correlation is zero for our 2D horizontal domain, and when the domain is becoming vertical, the vertical permeability correlation length changes into the lateral permeability length. This is consistent with our previous finding by the geologic method that, the local capillary traps decreases as the lateral correlation length is becoming smaller.

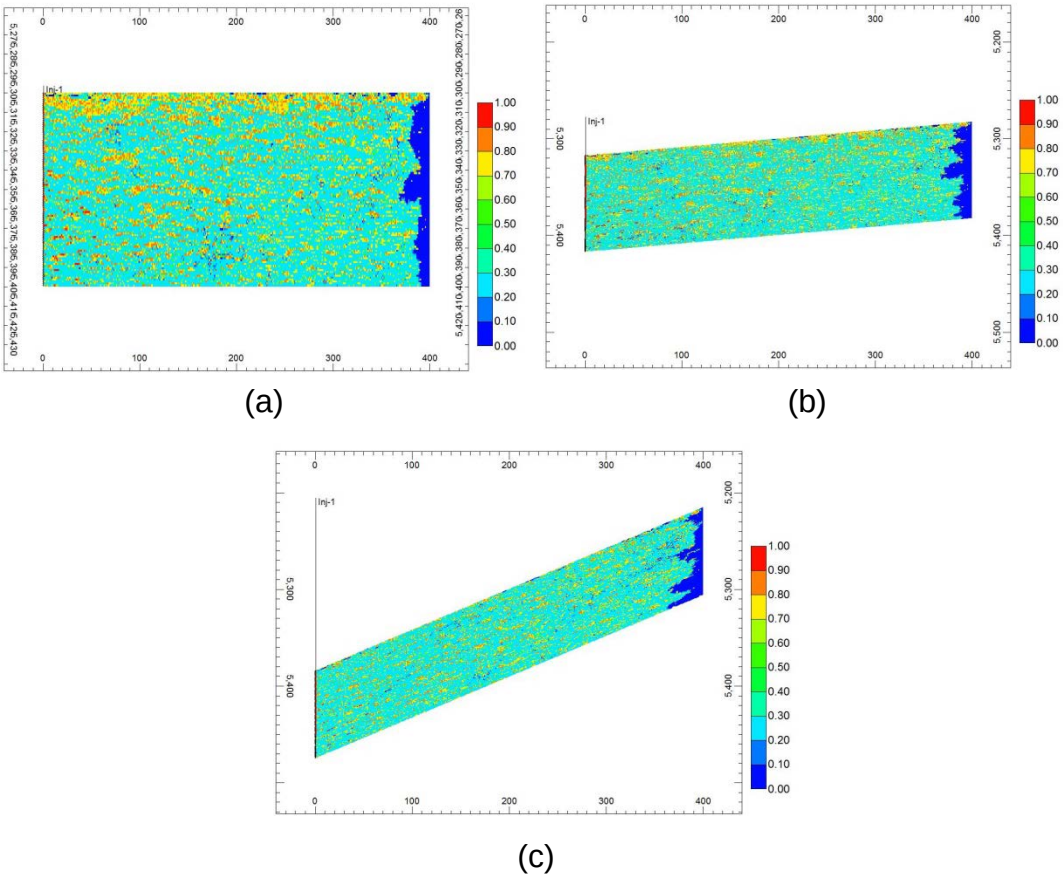

Figure 189: CO_2 plume distribution after 50 years of injection and post-injection period (at the steady state) for the 2D isotropic model with formation dip angle equal to 0 degree (a), 5 degree (b), and 25 degree (c), respectively. The total injected CO_2 mass is of 189.53 ton with the injection period of 0.02 yrs under the same injection rate (N_{gr}=0.039).

Additionally, we inject the same amount of CO_2 into the above three types of domains by using a small injection rate (N_{gr}=38.66). The CO_2 plume distributions at the end of injection and the steady state are shown in Figure 190 and Figure 191 respectively. At the end of injection, the mass of CO_2 staying in the 122 m × 30 m portion of the domain are 57.6 ton (a), 48.6 ton (b), and 25.8 ton (c), respectively. Therefore, formation dip angle changes the mass of CO_2 remaining in our desired portion under the small injection rate.

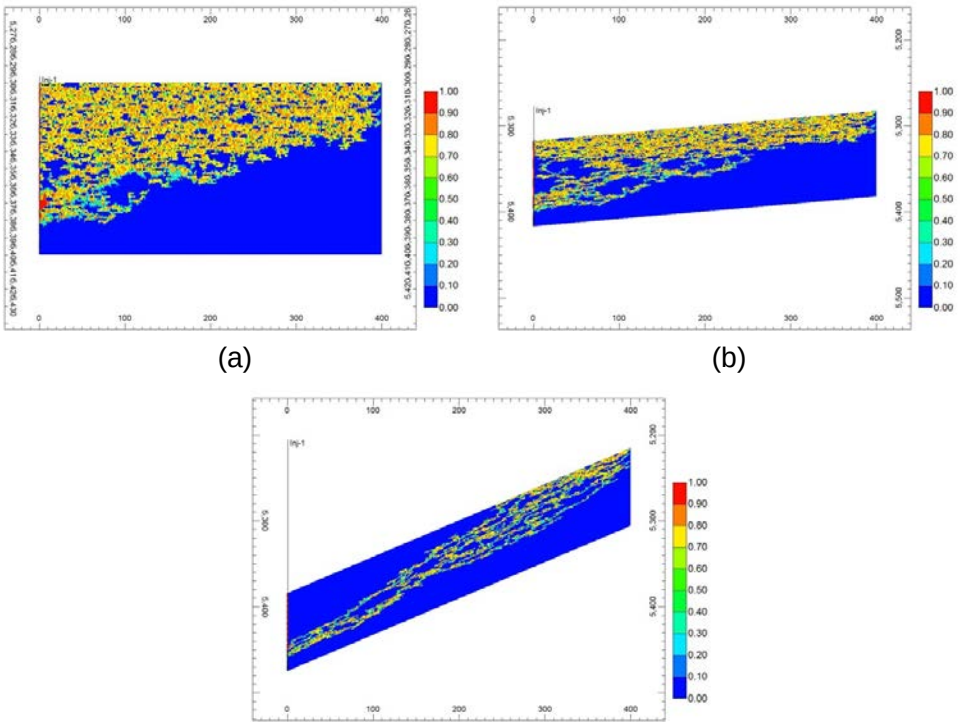

(a) (b)

(c)

Figure 190: CO_2 plume distribution at the end of injection for the 2D isotropic model with formation dip angle equal to 0 degree (a), 5 degree (b), and 25 degree (c), respectively. They are representative of horizontal, moderate dip and high dip, respectively. The total injected CO_2 mass is of 189.53 ton with the injection period of 20 yrs under the same injection rate (N_{gr}=38.66). At this moment, the mass of CO_2 staying in the 122 m × 30 m portion of the domain are 57.6 ton (a), 48.6 ton (b), and 25.8 ton (c), respectively.

The CO_2 plume trail and pressure propagation is very important because it determines the area of review for the injection well. From the above observation, we can conclude that for the highly-deviated formation, large injection rate would be better for the next-step review and monitoring activity since most of the injected CO_2 stays near the wellbore during injection.

Also, it is worthwhile to notice that, when the injection rate is smaller in the highly-deviated formation, CO_2 migration tends to be dominated by several of the capillarity channels. Obviously, most of the local capillary traps potentially existing in the domain cannot be flooded and filled in this situation. However, for the horizontal formation with the low injection rate, as shown in Figure 190(a) and Figure 191(a), although the local capillary traps in the upper portion cannot be flooded by CO_2, they can also be filled by the backfilling of CO_2 from the gas cap. From this aspect, we can further conclude that, if the small injection has to be employed due to the small injection pressure or fracturing pressure, it is better to choose the horizontal saline aquifer as the storage body to make good use of local capillary traps in the formation. On the other hand, the phenomena of backfilled local capillary trapping indicates that perforation interval might have no impact on the local capillary trapping, although it does affect injectivity and bottom-hole pressure.

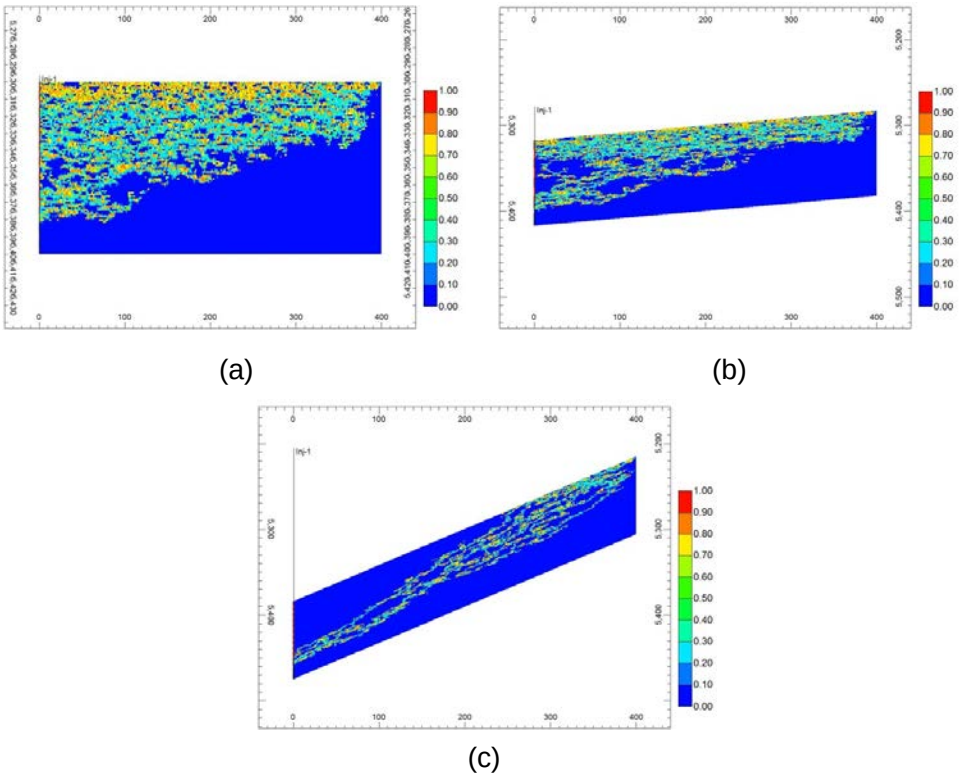

Figure 191: CO_2 plume distribution after 50 years of injection and post-injection period (at the steady state) for the 2D isotropic model with formation dip angle equal to 0 degree (a), 5 degree (b), and 25 degree (c), respectively. The total injected CO_2 mass is of 189.53 ton with the injection period of 20 yrs under the same injection rate (N_{gr}=38.66).

Next, we quantify the LCT mass fractions for the different dip angle formations and compare them under two different injection rates. The result is shown in Figure 192. From the figure, we can observe that local capillary trapping decreases linearly with the increase of dip angle. It can be expected that when the formation dip angle is 90 degree, the local capillary trapping would be the least. This point has been explained previously and has been verified by the simulation result.

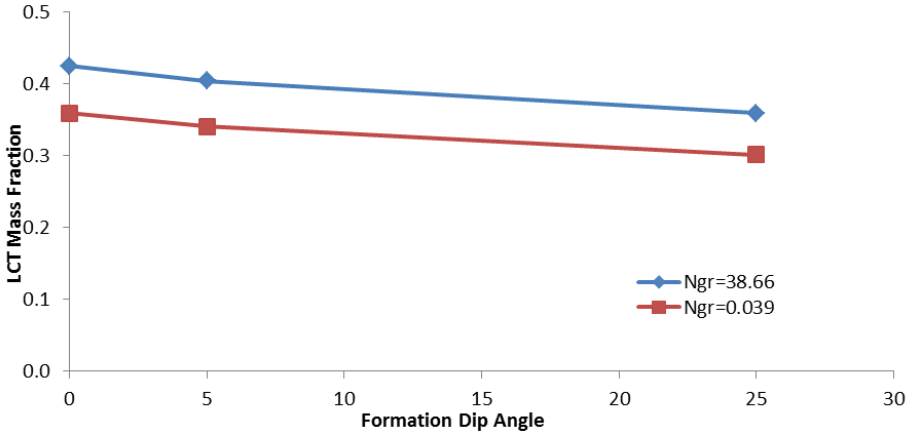

Figure 192: Variation of local capillary trapping mass fraction along with formation dip angle for the injection modeling, here, LCT mass fraction is defined as the fraction of local capillary trapped CO_2 mass of the totally left CO_2 in the 399×100 grids system at the steady state.

Effect of Anisotropy

As stated earlier, injection of large quantities of CO_2 eliminates the transition zone in the isotropic formation, even when perforations are only in the bottom quarter of the domain. On the other hand, such transition zones are an important feature of CO_2 migration from an initial emplacement of CO_2 at the bottom of a storage structure. Therefore, it is important to determine if transition zones arise during long-term injection under other conditions. The condition most likely to lead to this situation is permeability anisotropy. Here we decrease the ratio of vertical permeability to horizontal permeability to 0.1, 0.01, and 0.001, and inject same amount of CO_2 as for the isotropic domain under the gravity number of 0.39. Figure 193 shows the CO_2 plume distribution at the end of injection for the 2D model with K_v/K_h equal to 1 (a), 0.1 (b), 0.01 (c), and 0.001 (d), respectively. At the end of injection, the mass of CO_2 staying in the 122 m × 30 m portion of the domain are 106.2 ton, 110.01 ton, 97.1 ton, and 67.55 ton, respectively. With the increasing level of anisotropy, CO_2 tend to flow along the bottom of the domain and it can be observed from Figure 193(d) that, for the very anisotropic formation with K_v/K_h equal to 0.001, injected CO_2 is located in the bottom of the domain and become the source CO_2 zone for the following buoyancy-dominated flow, during which, transition zones and gas caps were generated. The local capillary trapping in the transition zone and the gas cap are similar to patterns reported by Saadatpoor (2012) for purely buoyancy driven migration in a closed domain.

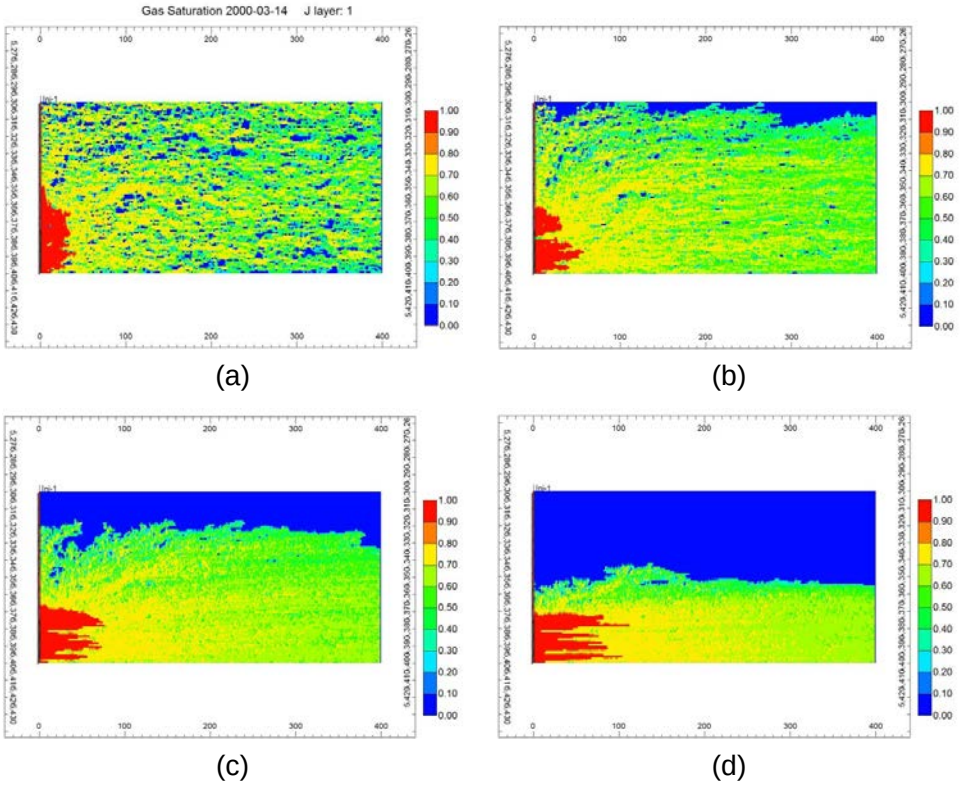

Figure 193: Plume distribution at the end of injection for the 2D model with K_v/K_h equal to 1 (a), 0.1 (b), 0.01 (c), and 0.001 (d), respectively. The total injected CO_2 mass is of 189.53 ton with the injection period of 0.2 yrs under the same injection rate (N_{gr}=0.39). At this moment, the mass of CO_2 staying in the 122 m × 30 m portion of the domain are 106.2 ton (a), 110.01 ton (b), 97.1 ton (c), and 67.55 ton (d), respectively.

This was observed by the continuous flow simulation under the buoyancy-dominated displacement. After 50 years of injection and post-injection flow, the CO_2 plume distribution is at the steady state, which is shown in Figure 194 with the increasing anisotropy. From the figure, we can observe that in the viscous flooded area common for the four cases, local capillary trapped CO_2 structures and distribution are similar, although the LCT CO_2 saturations are a little different. The first three cases with relative large mass of CO_2 left in the 122 m × 30 m portion of the domain tends to have the higher CO_2 saturation in the local capillary traps than the highest anisotropic case with the least left CO_2 of 67.5 ton. In the discussion section, we will compare this case of injection with the emplacement scenario in terms of CO_2 plume dynamics, in which, same amount of CO_2 (67.5 ton) is emplaced at the same bottom portion (122 m × 15 m) of the domain.

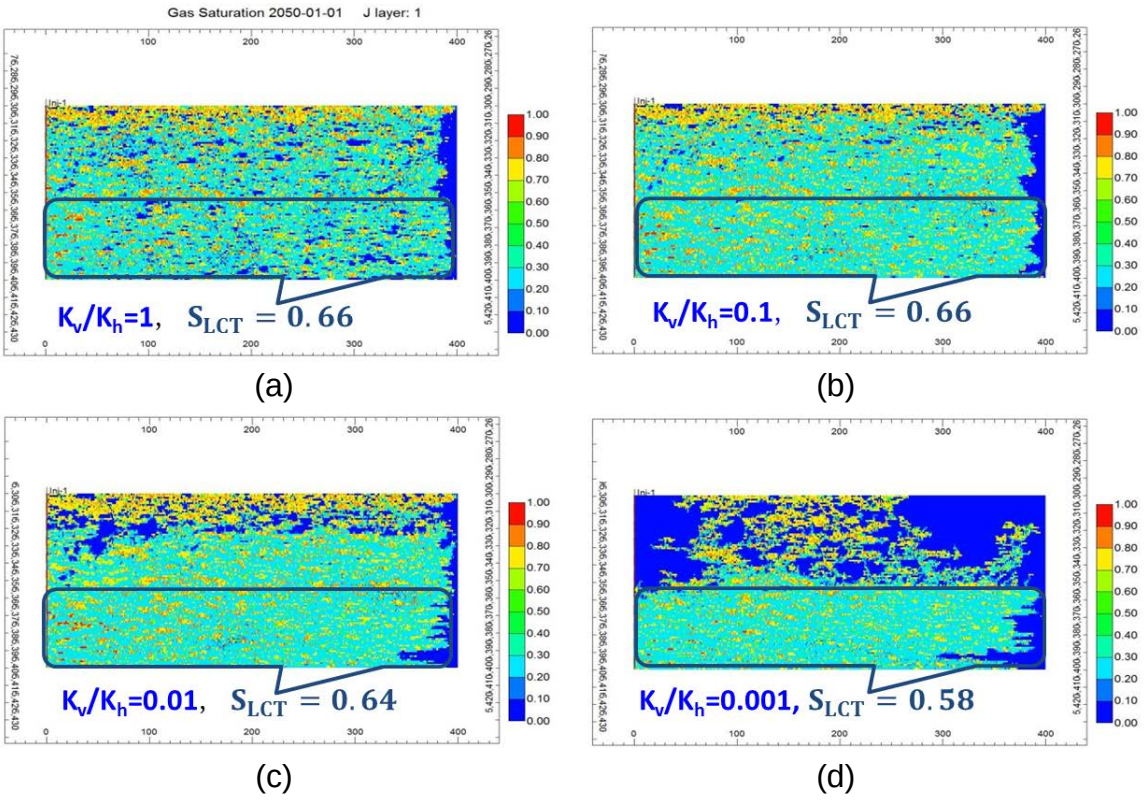

Figure 194: CO_2 plume distribution after 100 years of injection and post-injection period (at the steady state) for the 2D model with K_v/K_h equal to 1 (a), 0.1 (b), 0.01 (c), and 0.001 (d), respectively. The total injected CO_2 mass is of 189.53 ton with the injection period of 0.2 yrs under the same injection rate (N_{gr}=0.39).

In the transition zone, as show in Figure 194(c) and Figure 194(d), CO_2 migrates along some of the capillarity dominated flow paths to reach the top seal, but leaves large saturation of gas in the flow path. Large CO_2 saturations of CO_2 also accumulate below the top seal but not uniformly. At the end of simulation, most of the CO_2 is connected along the preferential paths, but through a wide spectrum of saturations. It is worthwhile to notice that, in Figure 194(d), almost half of the upper portion of the domain is not invaded by the CO_2, therefore, the intrinsically existing local capillary traps in these un-invaded grid blocks are not filled.

We conclude that injection into storage reservoirs with large anisotropy yields essentially the same behavior as the emplacement storage scenario. The emplacement volume essentially corresponds to the thickness of the perforated interval.

Previous research (Saadatpoor, 2012) employs a simple model that has hydrostatic pressure gradient for initial condition and closed domain for boundary condition. The formation pressure close to the injection wells increases during the injection phase. Therefore, assumption of hydrostatic pressure gradient for initial condition is not realistic. One possible remedy would involve finding the more accurate initial conditions by simulating injection phase. Recall that we can generate the transition zone by using very anisotropic formation and the CO_2 plume distribution at the end of injection is shown again in Figure 195(a). Meanwhile, we emplace same amount of CO_2 (67.5 ton) at the same bottom portion of the domain as the end of injection in Figure 195(a), by tuning the initial CO_2 saturation to be 0.76, as shown in Figure 195(b). The pressure buildup induced by the injection is almost 690 kPa for Figure 195(a), so we assign the pressure field at the end of injection to the domain with emplaced CO_2 as the initial pressure. After 100 years of flow modeling, both the injection and emplacement scenarios achieve the steady state and the final CO_2 plume distribution is shown in Figure 195(c) and Figure 195(d), respectively. Comparing these figures shows that local capillary trapping is essentially independent of the mode of CO_2 storage in highly anisotropic reservoirs..

Otherwise, if we do not consider the injection-induced pressure by using the hydrostatic pressure field, simulation shows that it would take a very long time of period (400 years) for the CO_2 migration to achieve steady-state. The CO_2 plume distribution in this case is shown in Figure 195(e). As we can see, under the emplacement scenario in which the acting forces capillarity and buoyancy, CO_2 is more inclined to the move upward rather than laterally. So we can observe more and longer CO_2 clusters in the gas cap at the final steady state. Compared with the emplacement simulation, injection modeling for the post-injection period shows less local capillary traps and less/shorter CO_2 clusters in the gas cap because certain amount of CO_2 migrates to the right boundary under the horizontal injection-induced pressure gradient. Therefore, injection-induced pressure affects both the CO_2 plume dynamics and local capillary trapping structures. Direct emplacement of large saturation CO_2 in the bottom of the domain cannot be representative of what happened in reality during post-injection period.

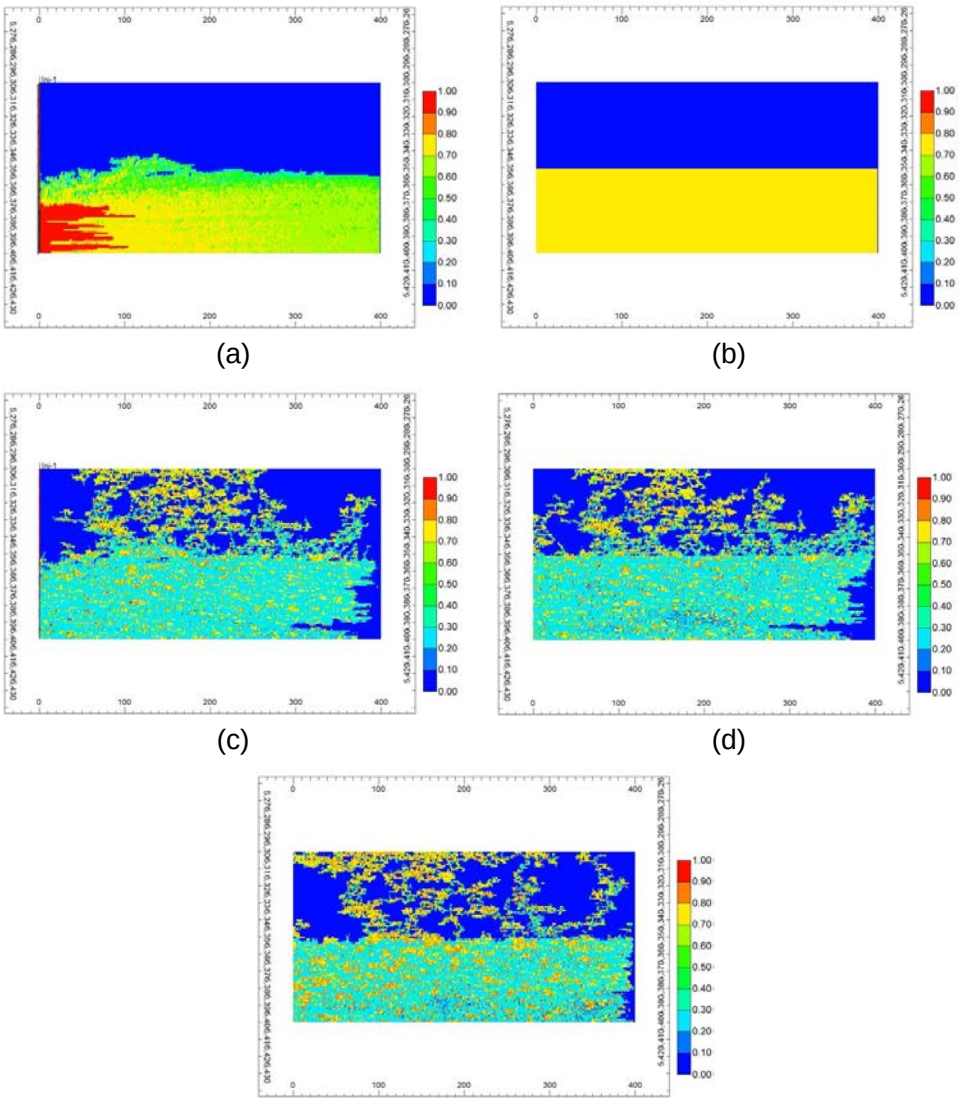

Figure 195: (a) CO_2 plume distribution at the end of injection in the highly anisotropic (K_v/K_h=0.001) formation with the total injected CO_2 of 189.53 ton and injection gravity number of 0.039. The mass of CO_2 remaining in the 122 m × 30 m portion of the domain is 67.5 ton. (b) Same amount of CO_2 as (a) is emplaced in the almost the same portion of the domain as the initial state. (c) is the CO_2 plume distribution at the steady state after 100 years of flow simulation for (a). (d) and (e) are the CO_2 plume distribution at the steady state with the injection-induced pressure field and with the hydrostatic pressure, respectively, as the initial condition.

Persistence of Trapping Following Loss of Seal Integrity

Post-Injection Leakage Scenario

We simulate the sudden development of a leak in the top seal when the initial CO_2 emplaced at the bottom of the domain accumulates below the seal after buoyant flow during the relaxation period (which is typically 25 years in our cases.) The leak is a set of high permeability grid blocks extending through the impermeable layer at the top of the aquifer. This could represent a

damage zone around a fault, defects in the cemented annulus of a well, or a fracture induced during injection. The storage formation containing the CO_2 remains closed, so any CO_2 that leaks out must be replaced by water sinking into the aquifer. This does not prevent the migration of any potentially mobile CO_2 although it does affect the rate at which CO_2 escapes.

As shown in Figure 196, we model the leak as a high permeability (1 Darcy) channel of 1.2 m width at the top seal. The leak has a width of four grid blocks in order to accommodate countercurrent flow within it. We assume that the formation above the leak has large permeability (1 Darcy) and porosity (30%). This facilitates the escape of CO_2 from the storage formation, so that any hindrance to escape should be the result of behavior within the storage formation.

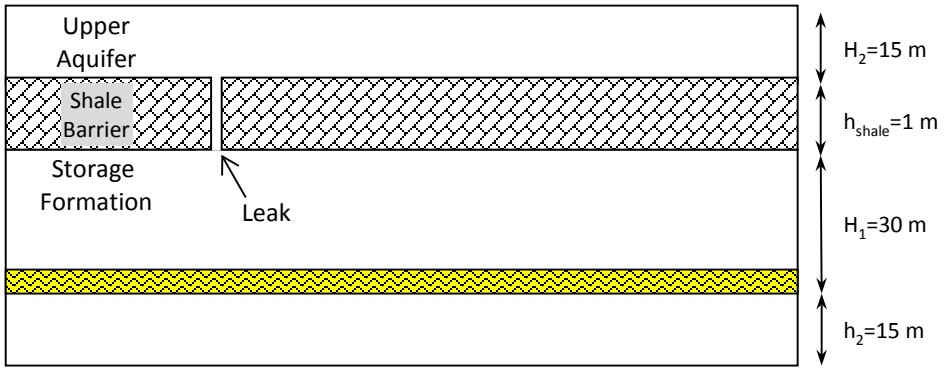

Figure 196: Model of the leak is a high permeability channel of 1.2 m width in the top seal. CO_2 is initially emplaced in the yellow zone and in the 15 m thick section below the yellow zone. The high permeability upper aquifer is located above 1 meters impermeable shale layer at the top of the storage formation.

After the leak opens a path to the upper aquifer, the fluids are allowed to redistribute within the now-connected storage and upper reservoirs. In all the simulations, the saturation profile reaches close to steady state, that is, negligible changes are observed in saturation profile throughout the aquifer for a large period of time. Throughout the rest of this section, this steady state saturation profile at the end of the redistribution period is reported for each case as the CO_2 saturation profile.

Analyzing Leakage Simulations: Security Index

In order to analyze the risk involved in each of the leak simulations, we quantify the CO_2 escaped through the leak by defining a "security index" parameter. First, we calculate the initial mass of CO_2 in the gas cap that is potentially mobile, i.e., that part of CO_2 which is beyond the maximum residual gas saturation. For the simulations shown here, the following equation is used for every grid block with $S_g > S_{gr,\max}$ in the gas cap zone:

$$m_{potentially\ mob\ CO_2} = V_p \cdot \left(S_g - S_{gr,\max}\right) \cdot \rho_{g,\mathrm{mol}} \cdot Y_{CO_2} \cdot MW_{CO_2} \tag{31}$$

where

$m_{potentially\ mob\ CO_2}$ = mass of potentially mobile CO_2 in the grid block

V_p = pore volume of the grid block

S_g = gas saturation

$S_{gr,\max}$ = maximum residual gas saturation

$\rho_{g,\mathrm{mol}}$ = gas phase mole density

Y_{CO_2} = gas mole fraction of CO_2

MW_{CO_2} = CO_2 molecular weight (44 g/mole)

When the simulation of the aftermath of the leak event reaches steady state, the mass of total CO_2 in the upper aquifer is calculated ($m_{escaped\ \mathrm{CO}_2}$). This calculation includes all forms of CO_2: dissolved in water, residually trapped, and accumulated in regions at above-residual saturations. The security index can be defined using the ratio of these two variables as

$$SI = 1 - \frac{m_{escaped\ \mathrm{CO}_2}}{m_{potentially\ mob\ \mathrm{CO}_2}} \tag{32}$$

This is a relative measure of how secure the configuration is if a leak develops. The index varies between 0 and 1, with higher indexes showing higher security. Since the mass of escaped CO_2 will depend on total mass of potentially mobile CO_2 as well as the security index, then the cases are comparable using their *SI* only if they have same mass of potentially mobile CO_2 accumulated beneath their seal. This is the case for all models in following sections. Because the storage formation is heterogeneous, *SI* is a function of location of the leakage path. Clearly, it is of special interest to be able to relate the value of *SI* to other parameters that describe the storage scheme. We now present simulations that provide insight into this relationship.

Emplaced CO_2[13]

The high permeability formation immediately above the top seal, which is a a single narrow sealing layer of thickness h_{Shale}=0.3 m. Figure 197 shows the CO_2 saturation profile at the beginning of leak simulation. The configuration after 25 years of buoyant flow in the lower aquifer without a leak (Figure 179) is set as the initial condition of the leak simulation.

The results 25 years after the leak opens are shown in Figure 198 through Figure 200 and summarized in Table 24. In Figure 198 the leak is placed 33 m from the left boundary of the domain. More than 50% (mass percent) of the above-residual saturation of CO_2 in the gas cap escaped 25 years after development of the leak, forming an accumulation of a few CO_2 saturated

[13] This section constitutes part of Project Deliverable 7.0 Trend of fraction of CO_2 above residual that remains trapped after seal rupture for range of operating conditions in a representative set of storage formations.

layers at the top of the upper aquifer. This gives a security index value of *SI*=0.50. Most of the grid blocks at the upper layers of storage formation only contain the residual gas saturation after the leak. Sinking brine dissolved the residual phase just below the leak. However, as discussed below, much of the CO_2 in the flow channels did not escape.

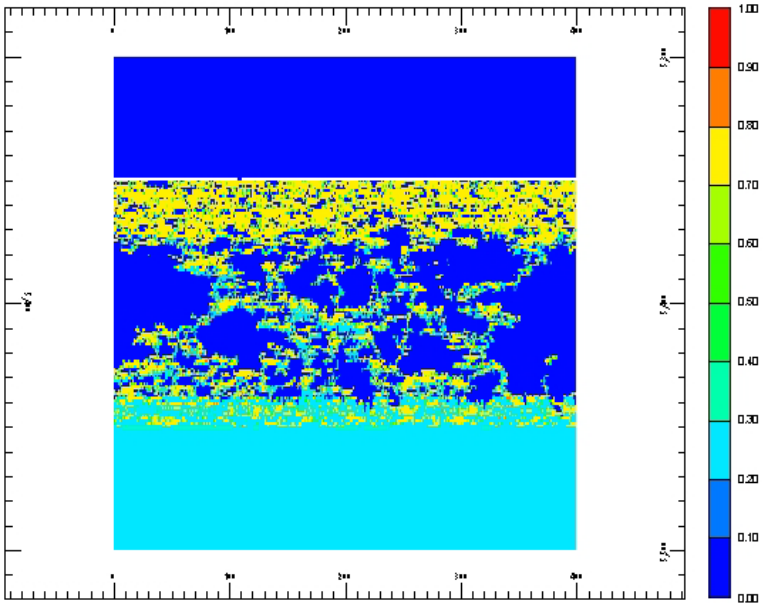

Figure 197: CO_2 saturation profile just before leak evolves. The leak is assumed to emerge instantaneously after 25 years of buoyant flow of the CO_2 initially in the storage formation. In fact, CO_2 saturation profile of Figure 179 is set as the initial condition before the leak opens in the top seal of the aquifer.

In Figure 199 the leak is placed 90 m from the left boundary of the domain. In contrast to Figure 198, only less than 4% of the above-residual saturation of CO_2 in the gas cap has leaked, mostly in form of dissolved gas in brine, and a large fraction of potentially mobile CO_2 has remained in place. The security index is then *SI*=0.96 which shows a highly secure configuration of stored CO_2 if a leak develops at x=90 m.

So, we can conclude that the location of fracturing in the top seal is important in evacuation of CO_2 to adjacent formations when the storage formation is heterogeneous. In other words, not every leak in storage formation in which CO_2 has accumulated in local capillary traps leads to extensive contamination of neighboring waters.

In Figure 200 both leaks in the last two figures are assumed to develop simultaneously after 25 years of buoyant flow, i.e., there are two leaks at 33 m and 90 m from the left boundary of the domain. Calculation shows that about 54% of the above-residual CO_2 in gas cap has escaped through the leak which is equal to sum of the escaped gas in the last two cases. The resulting security index of *SI*=0.46 shows a fairly insecure storage for this leak combination. However, results of simulation show that the rate of escape of the gas through each leak is different from the rate of escape when that leak is the only leak in the aquifer. This can be better understood by comparing Figure 201 and Figure 202. Both figures show the CO_2 saturation profile at 10 years after leaks open. Apparently much more CO_2 is escaping through right-hand side leak in Figure 202 than in Figure 201. The reason is the difference in pressure field in the two cases.

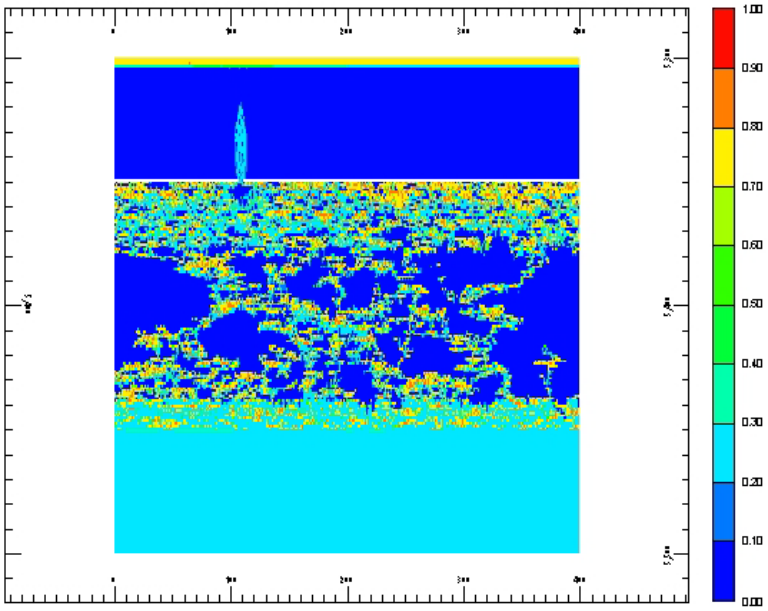

Figure 198: CO_2 saturation profile at 25 years after a leak opens in the top seal of the aquifer. The high permeability formation is immediately above the top seal. The leak is located at 33 m distance to the left boundary.

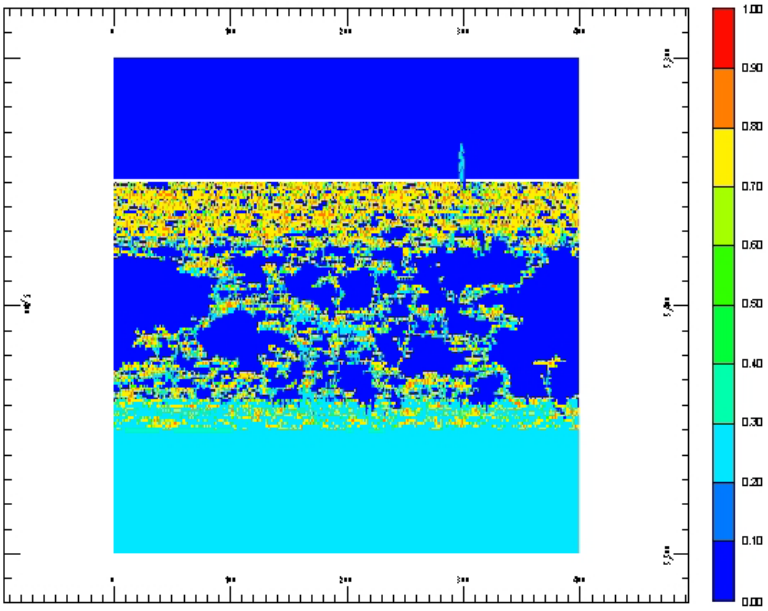

Figure 199: CO_2 saturation profile at 25 years after a leak opens in the top seal of the aquifer. The high permeability formation is immediately above the top seal. The leak is located at 90 m distance to the left boundary.

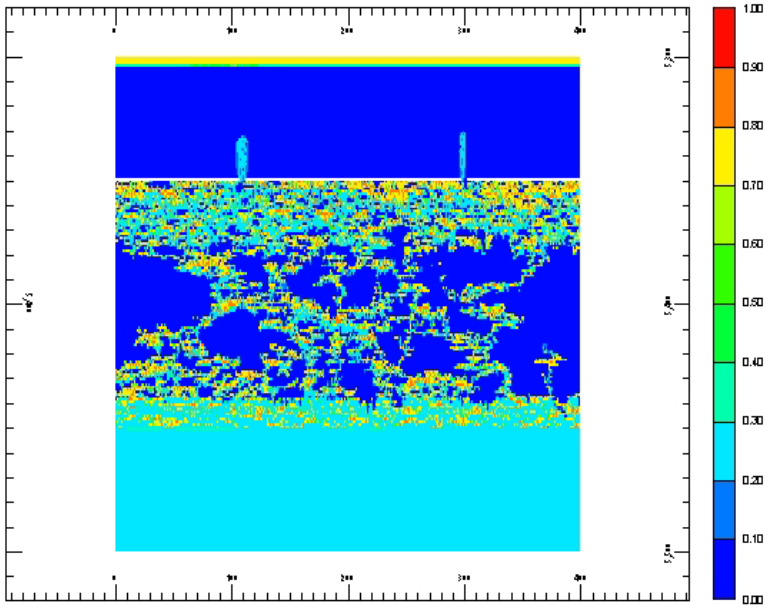

Figure 200: CO_2 saturation profile at 25 years after two leaks open in the top seal of the aquifer. The high permeability formation is immediately above the top seal. The leaks are located at 33 m and 90 m distance to the left boundary.

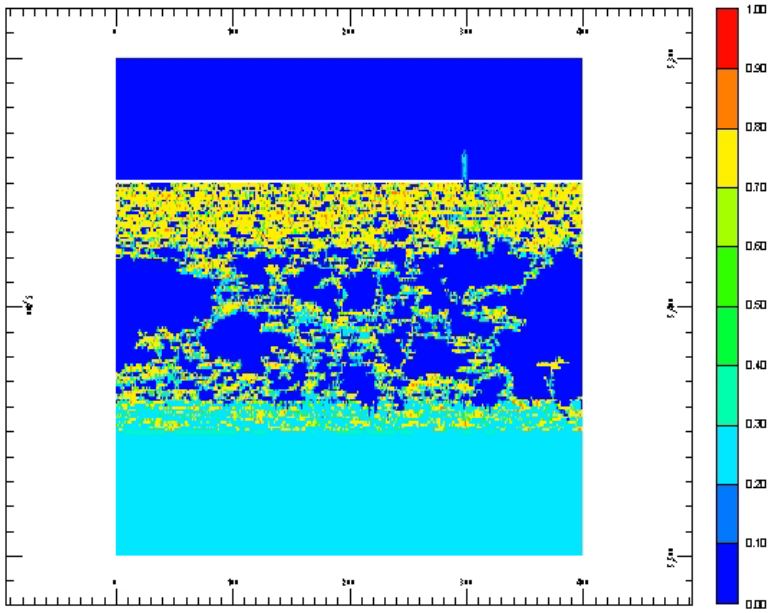

Figure 201: CO_2 saturation profile at 10 years after a leak opens in the top seal of the aquifer. The high permeability formation is immediately above the top seal. The leak is located at 90 m distance to the left boundary.

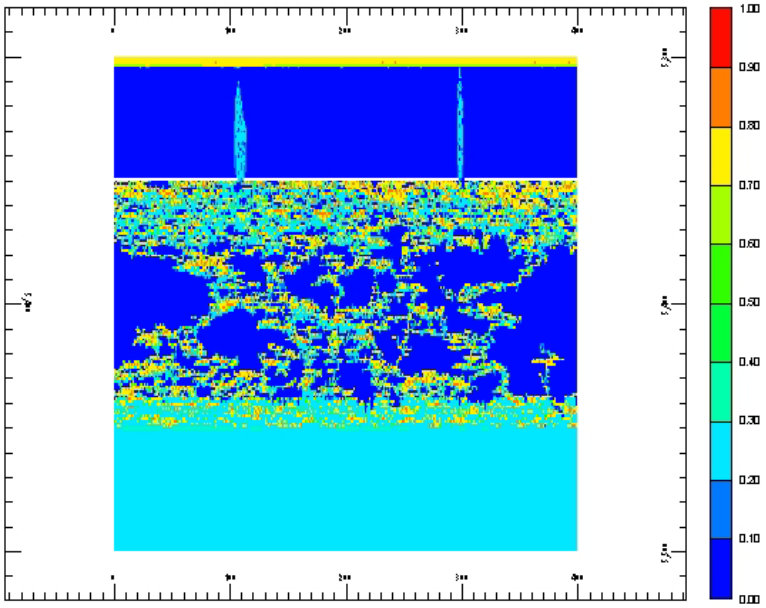

Figure 202: CO_2 saturation profile at 10 years after two leaks open in the top seal of the aquifer. The high permeability formation is immediately above the top seal. The leaks are located at 33 m and 90 m distance to the left boundary.

Regardless of the leak location, above-residual saturations of CO_2 remain trapped by local capillary barriers in several scattered regions throughout the domain. This mode of trapping is analogous to filling a hydrocarbon trap beyond the spill point. Once CO_2 fills the local trap, subsequent migration of CO_2 past the spill point has no effect on the trapped CO_2. It does not matter if the migration is a continuation of buoyant flow from below, or induced by leakage above. This secure mode of CO_2 storage could not be seen when neglecting capillary pressure or using a single capillary pressure curve for the whole aquifer.

Table 24: Summary of Different Simulation Cases and Their Security Index

Case	Emplaced PV of CO_2	Permeability Field	Capillary Pressure Field	Seal Thickness	Leak Position	Upper Aquifer	Security Index
Figure 198	0.41	Heterogeneous	Scaled	*h*=0.3 m	x=33 m	Closed	0.50
Figure 199	0.41	Heterogeneous	Scaled	*h*=0.3 m	x=90 m	Closed	0.96
Figure 200	0.41	Heterogeneous	Scaled	*h*=0.3 m	x=33 m and 90 m	Closed	0.46

Injected CO_2[14]

For the study of the influence of injection on filling of local traps, the security of the local trapping was studied in a manner analogous to the emplacement scenario of the previous section. After injection, leakage was simulated in a way that represents a sudden caprock breach induced by geochemical process, the leakage mode is the same as before and the relevant important

[14] This section constitutes the remaining of Project Deliverable 7.0 Trend of fraction of CO_2 above residual that remains trapped after seal rupture for range of operating conditions in a representative set of storage formations.

parameters is stated as below for reference and illustrated in Figure 203. The leak conduit is a high permeability channel of 1.2 m width at the left top seal ("Shale Barrier"), the formation above the leak ("Upper Aquifer") has large permeability of 1 Darcy and porosity of 0.3. Large pore volume modifier (1.0E+7) are assigned to the right boundary grid blocks of the upper and lower aquifers and left boundary grid blocks of the upper aquifer, to simulate the open aquifer system.

The leakage simulation is treated as a new run in the CMG-GEM. The initial conditions within the storage formation in the new run correspond to the steady state after injection without any leak to the top seal. Thus the global model fraction of gas and water and also reservoir pressure after 50 years of flow in the lower aquifer without a leak are set as the initial conditions of the leak simulation. The leakage simulation lasts for another 50 yrs.

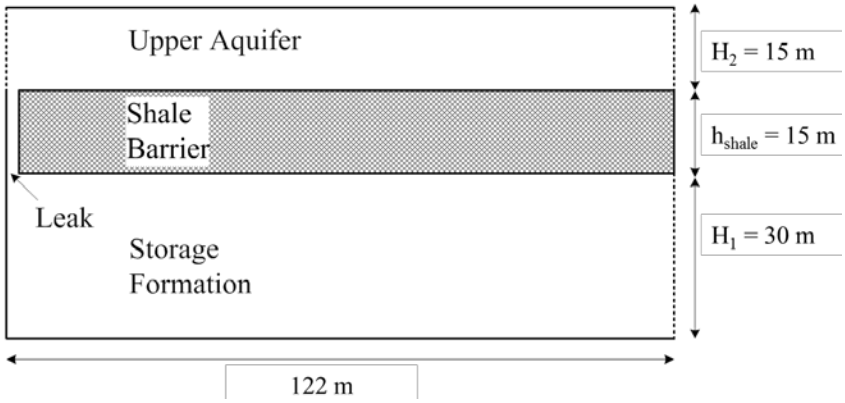

Figure 203: Aquifer Leakage Model: the leak is a high permeability channel of 1.2 m width in the top seal at the left side of the domain, corresponding to location of injection well. The configuration of the lower aquifer is same as the injection model. The upper aquifer is 15 m height with permeability of 1 Darcy and porosity of 0.3. The lower aquifer is open in the right boundary (dotted lines), while the upper aquifer is open in both right and left boundaries (dotted lines).

Effect of Injection Rate

The effect of injection rate on filling local traps was illustrated in Figure 184. Here we apply the leakage scenario to the post-injection buoyancy-driven steady states for each flow rate shown in Figure 184(a) through Figure 184(d).

After 50 years of injection and post-injection flow simulation, a sudden leakage conduit is introduced along the wellbore and then another 50 years of leakage modeling is conducted to look into the robustness of the local capillary trapping under the buoyancy dominated flow. The final CO_2 plume distribution at the steady state for the leakage modeling is shown in Figure 204. It can be shown that most of the bright yellow colors still reside in place; this means that local capillary trapped CO_2 is stable and robust. What leaks from the formation is the CO_2 in the flow path connected with the leakage conduit.

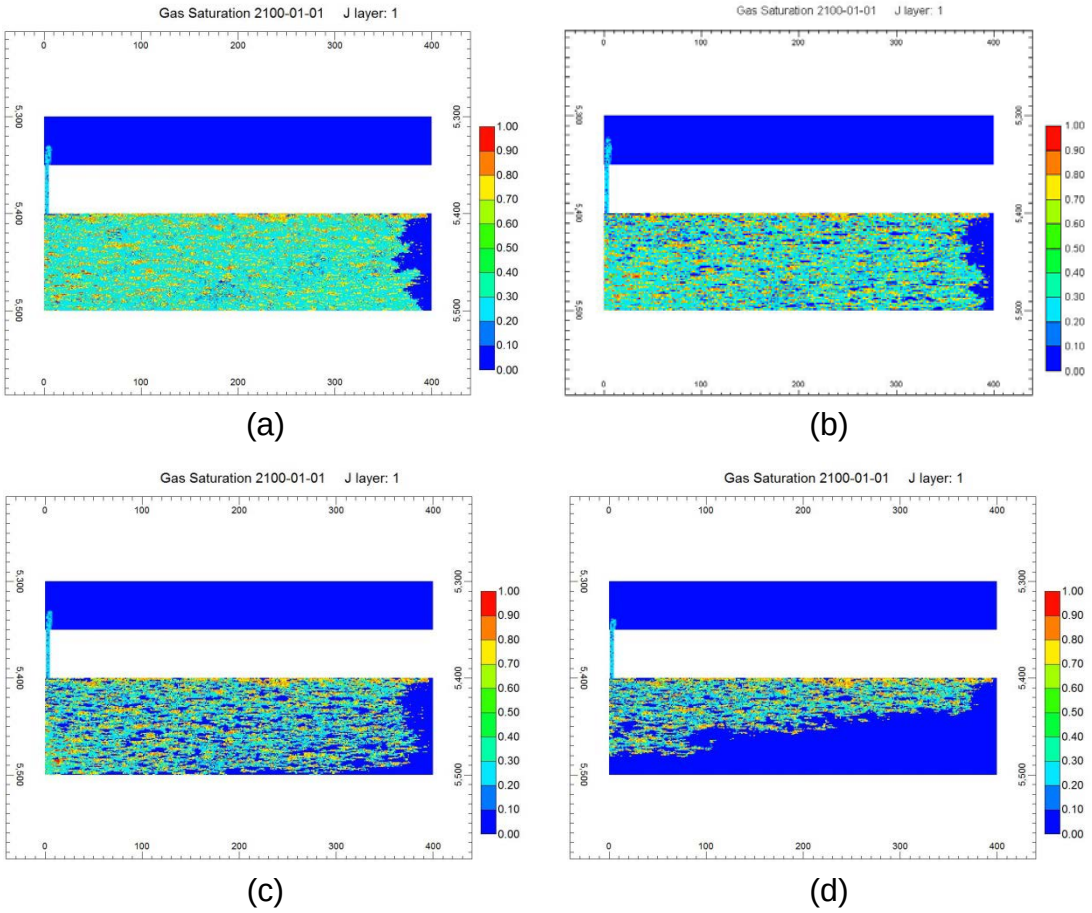

Figure 204: CO_2 plume distribution after 50 years of leakage modeling. A sudden leakage conduit is introduced along the wellbore after 50 years of injection and post-injection period of flow simulation as indicated in Figure 184. The gravity numbers during injection are 0.039 (a), 0.39 (b), 3.87 (c), and 38.7 (d), respectively.

Next, we quantify the local capillary mass and volume fraction for the above cases. Here, LCT mass fraction is defined as the mass of CO_2 in local capillary traps divided by the mass of CO_2 remaining in the 399×100 gridblocks at the steady state. The 400^{th} column of gridblocks acts as a boundary condition (recall the very large VOLMOD multiplier is applied to this column) and thus is not included in the LCT calculation. Local capillary volume fraction is defined as the percentage of the 399×100 grids that occupies CO_2 with saturation larger than residual gas saturation.

At the steady state, the variation of local capillary trapping mass fraction along with gravity number for the injection modeling and leakage modeling is shown in Figure 205. The LCT for injection is computed from the steady state at the end of injection for four injection rates shown in Figure 184. The LCT for leakage is computed from the steady state after the leak is imposed shown in Figure 204. It can be observed that LCT mass fraction is almost insensitive to the injection rate and the LCT mass fraction almost keeps around 40%. It is worthwhile to notice that, although, different injection rate gives rise to different displacement pattern and the local capillary traps utilization efficiency decreases as gravity number decreases, this does not affect the local capillary trapped CO_2 mass fraction.

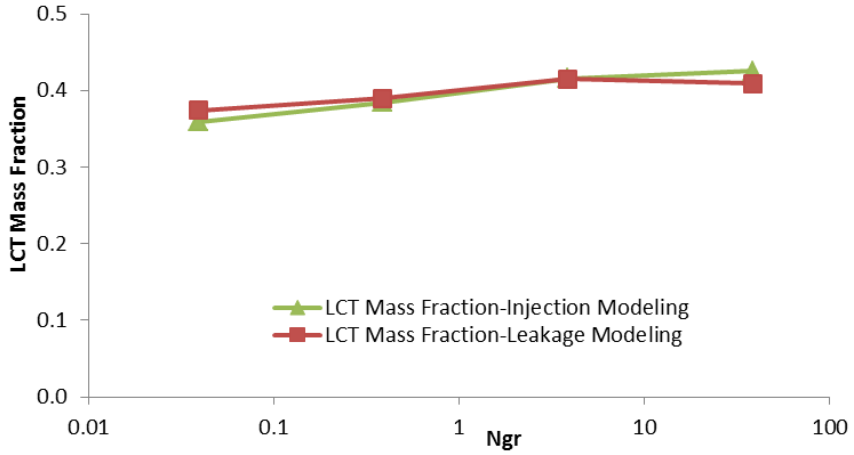

Figure 205: Variation of local capillary trapping mass fraction along with gravity number for the injection (Figure 184) and leakage (Figure 204) modeling, here, LCT mass fraction is defined as the fraction of local capillary trapped CO_2 mass of the totally left CO_2 in the 399×100 grids system at the steady state.

While the mass fraction is the most useful measure of trapping for MVA activities in CO_2 storage, it is useful to account for the differences in the volume of rock through which CO_2 migrates. We measure this by defining a local capillary trapping *volume* fraction in a manner analogous to the local capillary trapping mass fraction given above. This measure of LCT is shown in Figure 206 as a function of gravity number for the injection and leakage modeling. From Figure 205, we can see that, for the injection modeling at the steady state, almost 40% of the grid blocks have the CO_2 saturation larger than residual gas saturation for the large injection rate, and this number decreases little to 35% after 50 years of leakage. However, at the higher gravity number, the local capillary trapped volume fraction decreases by 15% for both the injection and leakage modeling. This is because the rapid dominance of buoyancy on the plume pattern in the large gravity number cases restricts the plume to a smaller fraction of the domain. Local traps in the uninvaded part of the domain never get filled.

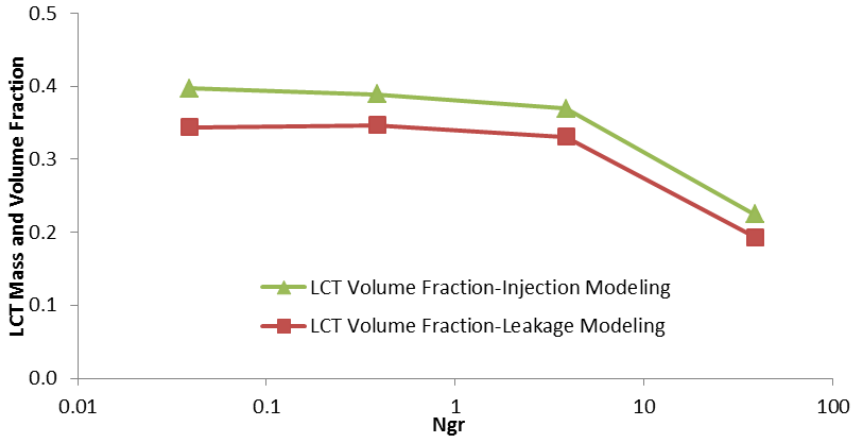

Figure 206: Variation of local capillary trapping mass and volume fraction along with gravity number for the injection and leakage modeling. Here, local capillary volume fraction is defined as the percentage of the 399×100 grids that occupies CO_2 with saturation larger than residual gas saturation.

Overlaying the CO_2 saturation distribution on the capillary entry pressure field, as shown in Figure 207, confirms that CO_2 occupies essentially all the local trap structures within the region of the storage formation that CO_2 invaded.

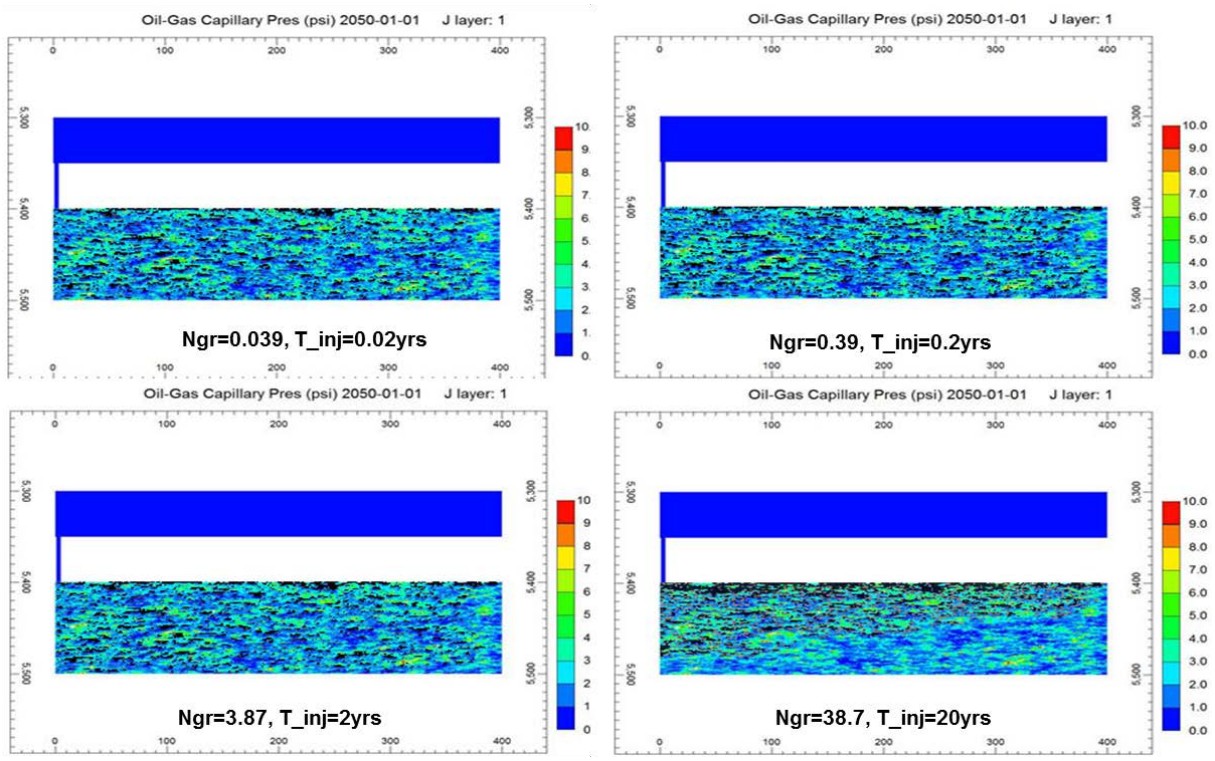

Figure 207: Steady state CO_2 saturation profiles in the storage reservoir from Figure 204 show that above-residual saturations (black) occupy the local traps (beneath local barriers indicated by warm colors) throughout the swept region, regardless of gravity number during injection. Thus the injection rate affects the size and shape of the swept region but not the essentially complete extent of filling of local traps within that region.

Effect of Injected Volume

The effect of injected volume on filling local traps after injection was illustrated in Figure 187, reproduced for ease of reference below as Figure 208. Here we apply the leakage scenario to the post-injection buoyancy-driven steady states for each volume shown in Figure 208(a) through Figure 208(e).

After 50 years of injection and post-injection flow simulation, leakage is imposed along the wellbore with another 50 years of modeling till the CO_2 plume is at the steady state. Figure 209 shows CO_2 plume distribution after 50 years of leakage modeling the above five cases. It can be observed that local capillary trapped CO_2 are very robust irrespective of the injected mass.

Next, we quantify the LCT mass and volume fraction for the different injected CO_2 mass under injection and leakage modes. Figure 210 shows the variation of local capillary trapped CO_2 mass and volume fraction with the different injected CO_2 mass for the injection and leakage modeling. The injection rate keeps constant (N_{gr}=0.039) under different injection periods. Injected pore volume is the ratio of injected CO_2 volume to the pore volume of the 30 m by 120 m portion of the domain. The reference 1 pore volume corresponds to the injected CO_2 mass of 189.53 ton. It

can be observed that, as the CO_2 gradually fill the domain, the LCT volume fraction increases and then keeps almost constant when mass of injected CO_2 exceeds 189.50 ton, for both the injection and leakage modeling. However, LCT CO_2 mass fraction is insensitive to the injected mass and they almost keep at the level of ~36%; the gray and red line corresponding to the LCT mass fraction for the injection and leakage modeling coincides with each other.

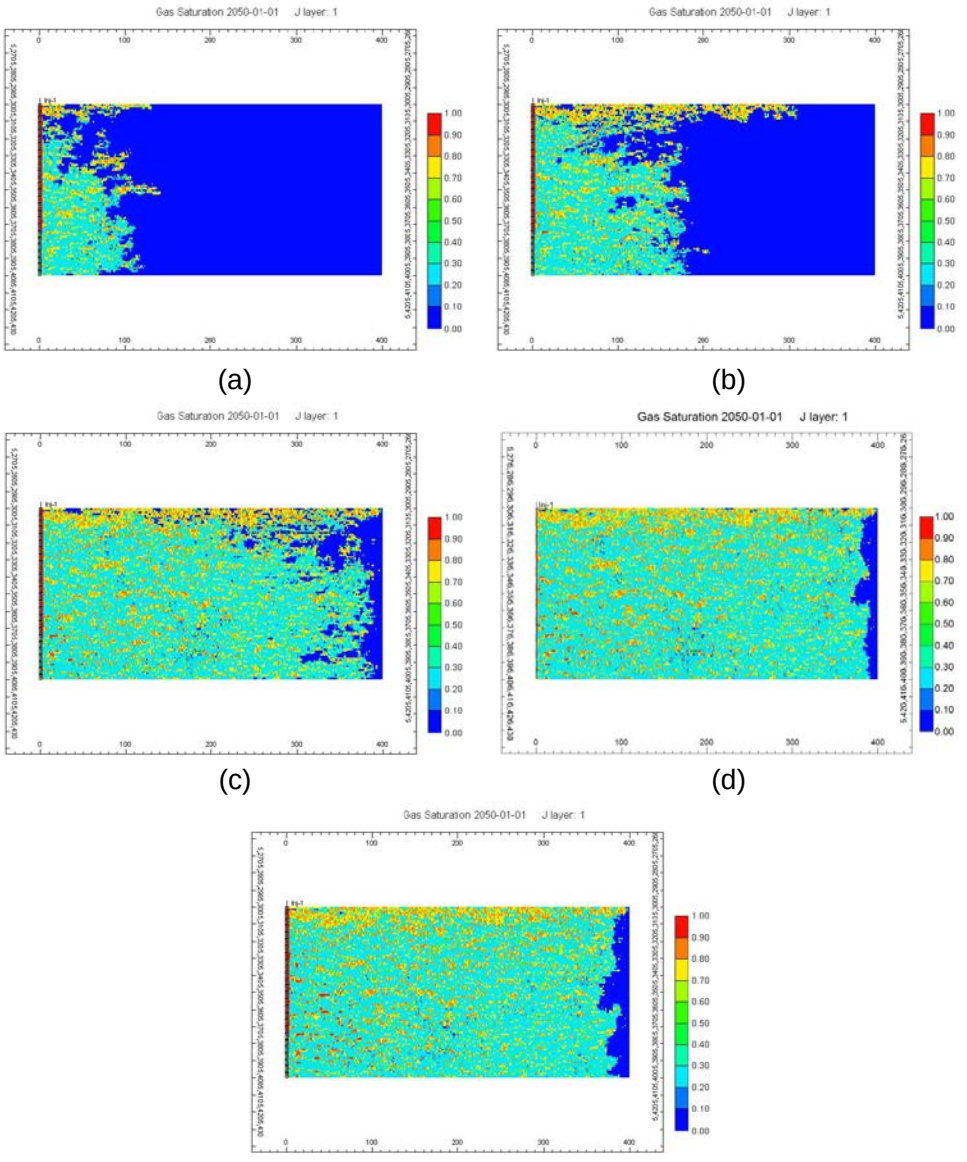

Figure 208: CO_2 plume distribution after 50 years of injection and post-injection period of flow simulation. Different volumes of CO_2 were injected for the above five cases at the constant injection rate (N_{gr}=0.039), The injection periods are 0.002 yr (a), 0.004 yr (b), 0.01 yr (c) , 0.02 (d), 0.04 yr (e), with the corresponding injected mass of 18.95 ton (a), 37.9 ton (b), 94.77 ton (c), 189.53 ton (d), 379.1 ton (e), respectively.

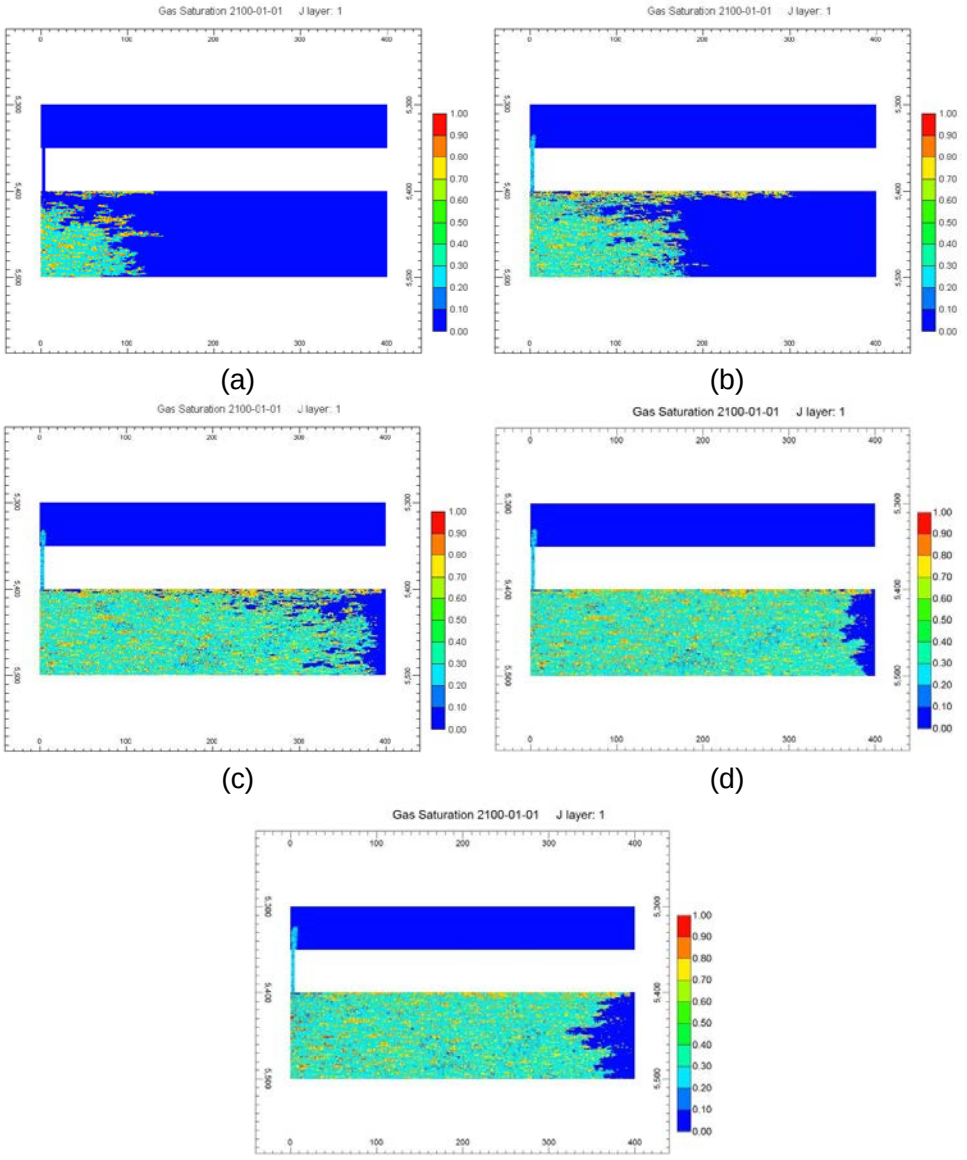

Figure 209: CO_2 plume distribution after 50 years of leakage modeling. A sudden leakage conduit is introduced along the wellbore after 50 years of injection and post-injection period of flow simulation as indicated in Figure 208. The injected CO_2 mass are 18.95 ton (a), 37.9 ton (b), 94.77 ton (c), 189.53 ton (d), 379.1 ton (e), respectively, and the above five cases are at the constant injection rate during injection period (N_{gr}=0.039).

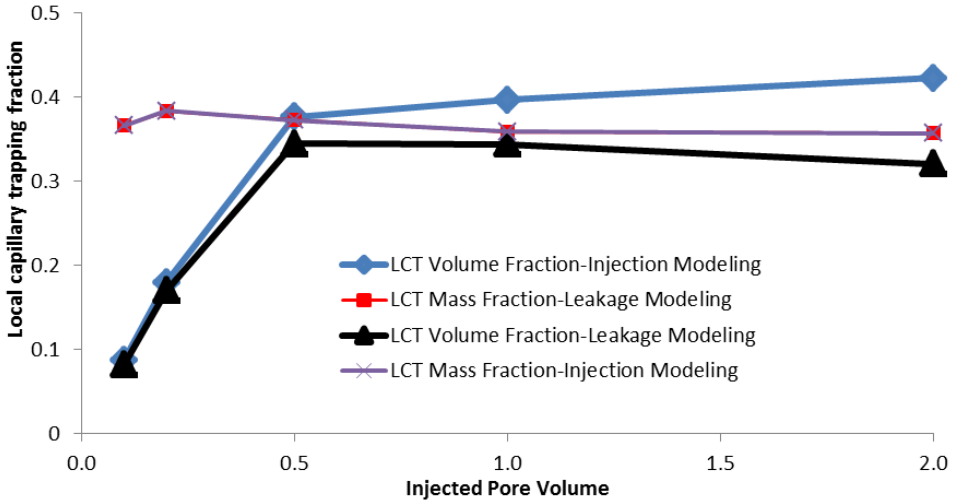

Figure 210: Variation of local capillary trapped CO_2 mass and volume fraction with the different injected CO_2 mass for the injection modeling (steady state after injection ends) and leakage modeling (steady state after leak imposed). The injection rate keeps constant (N_{gr}=0.039) under different injection periods. Injected pore volume is the ratio of injected CO_2 volume to the pore volume of the 30 m by 120 m portion of the domain. The reference 1 pore volume corresponds to the injected CO_2 mass of 189.53 ton.

Effect of Anisotropy

The effect of anisotropy, expressed as the ratio of vertical permeability to horizontal permeability, on filling local traps after injection was illustrated in Figure 194, reproduced for ease of reference below in Figure 211. Here we apply the leakage scenario to the post-injection buoyancy-driven steady states for each ratio of vertical to horizontal permeability shown in Figure 211(a) through Figure 211(d).

To examine durability of the LCT, a sudden leak is introduced along the wellbore after 50 years of injection and post-injection flow modeling with another 50 year of leakage simulation under the buoyancy-dominated displacement. The final CO_2 plume distribution at the steady state of leakage is shown in Figure 212(a) through Figure 212(d) with increasing level of anisotropy. It can be seen that, generally, after seal rupture, local capillary traps are robust and no CO_2 escapes from the highly anisotropic formation during leakage in the intermediate period.

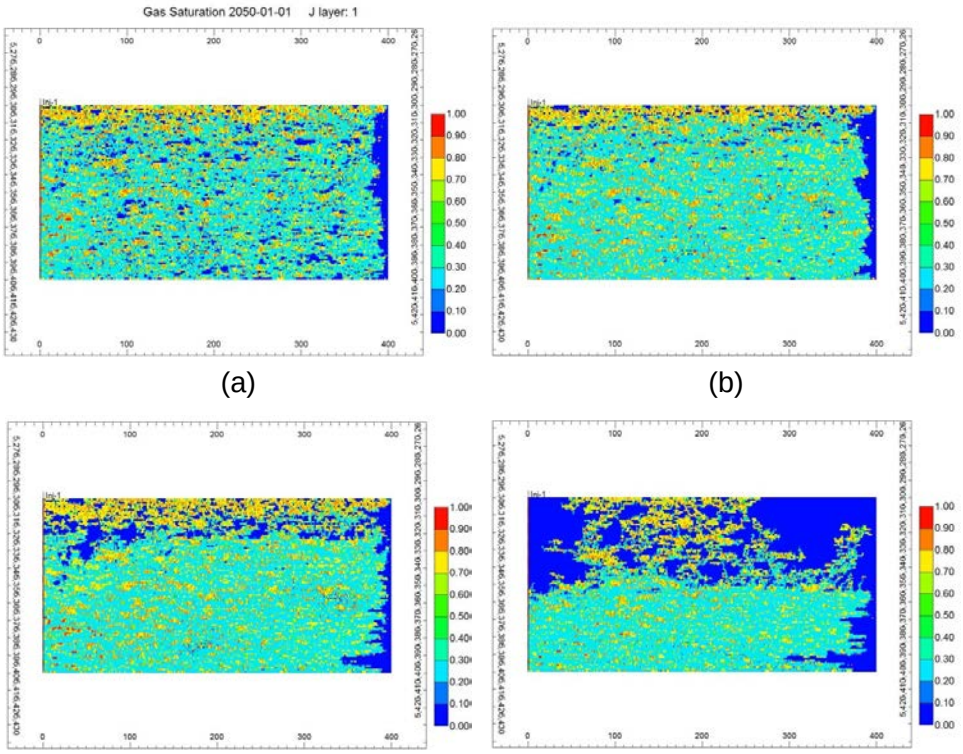

Figure 211: CO_2 plume distribution after 100 years of injection and post-injection period (at the steady state) for the 2D model with K_v/K_h equal to 1 (a), 0.1 (b), 0.01 (c), and 0.001 (d), respectively. The total injected CO_2 mass is of 189.53 ton with the injection period of 0.2 yrs under the same injection rate (N_{gr}=0.39).

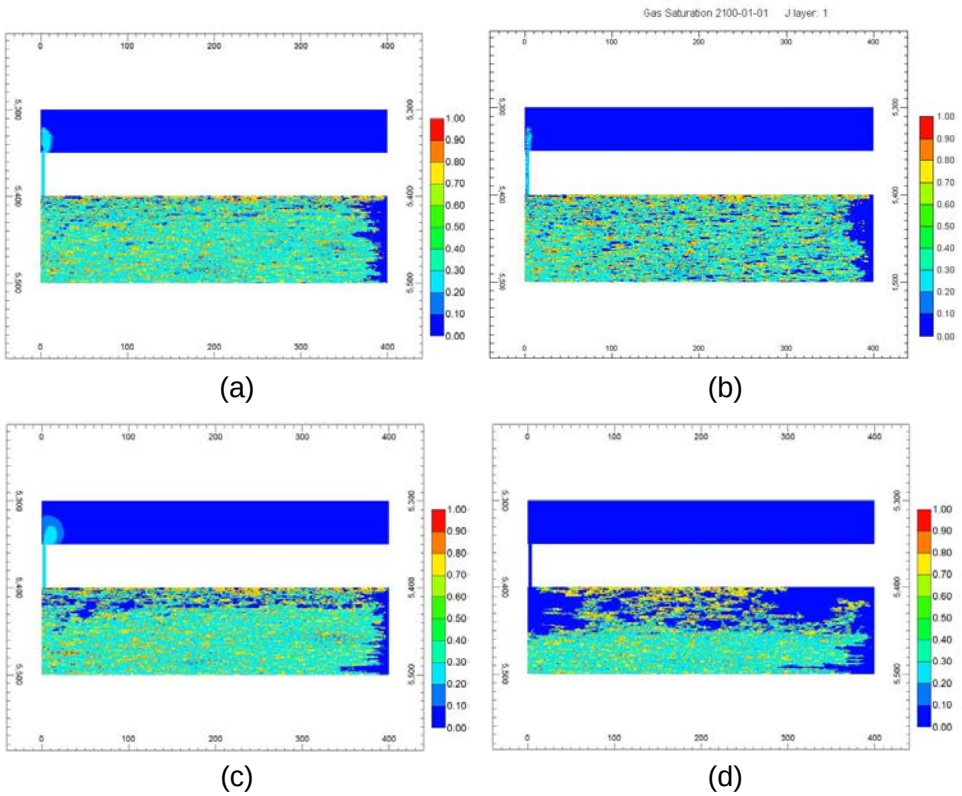

Figure 212: CO_2 plume distribution after 50 years of leakage modeling on the 2D model with K_v/K_h equal to 1 (a), 0.1 (b), 0.01 (c), and 0.001 (d), respectively. A sudden leakage conduit is introduced along the wellbore after 50 years of injection and post-injection period of flow simulation as indicated in Figure 211.

Next, we quantify LCT mass fraction for the four cases with the increasing anisotropy. In the preceding discussion we defined the gravity number as $N_{gr} = \frac{k_v \Delta \rho g L}{u_h \mu H}$; therefore, as the vertical permeability decreases, the gravity number decreases, and the corresponding gravity numbers for the above four cases are 3.9E-1, 3.9E-2, 3.9E-3 and 3.9E-4, respectively. Note that in preceding discussion the gravity number changed only when the injection rate changed; this is physically different means of changing gravity number and thus it is of interest to check whether the same trends of LCT against gravity number are observed. Figure 213 shows the variation of local capillary trapped CO_2 mass fraction along with increasing gravity numbers (decreasing anisotropy), it can be observed that LCT mass fraction has almost no change with four orders of gravity numbers, and it keeps as a constant around 38% for both injection and leakage modeling. This is almost identical to the behavior arising when flow rate varies.

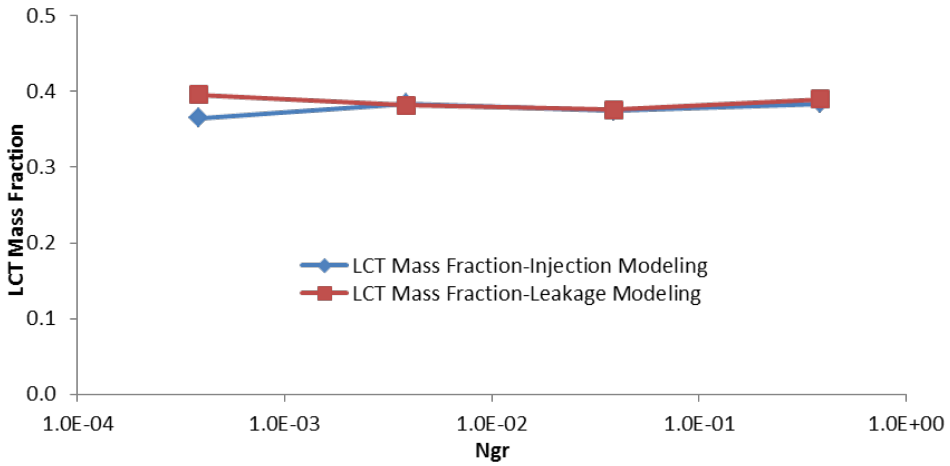

Figure 213: Variation of local capillary trapping mass fraction along with gravity number for the injection and leakage modeling, here, LCT mass fraction is defined as the fraction of local capillary trapped CO_2 mass of the totally left CO_2 in the 399×100 grids system at the steady state.

3.3.2 Upscaling Local Capillary Trapping

Using homogeneous capillary pressure field or even several rock types in a heterogeneous domain fails to capture local capillary trapping. Instead, the displacement front is much more uniform, and consequently residual trapping is overestimated in simulations that ignore capillary heterogeneity. On the other hand, fine-scale simulations that resolve the local heterogeneity have very large run times. A small two-dimensional case of 400×150 grid with 0.3 m by 0.3 m grid blocks takes CPU times in the order of a day to simulate 25 years of buoyant flow on a 3 GHz processor. Fine-scale simulation of a real field case with sizes in the order of miles would be costly and impractical. In addition, the uncertainties associated with the heterogeneity modeling and the need to perform long term predictions (the order of 1000 years) make it more reasonable to assess the initial estimates based on some coarse-grid simulations.

Therefore, there is a clear need for an upscaling method which can decrease the cost of simulation of buoyancy-driven flow. However, since the ultimate goal in CO_2 sequestration simulations is commonly risk analysis, the upscaling method should be able to give similar simulation results that are important from risk analysis point of view. Examples include whether the CO_2 reaches the top seal of the storage formation, the time it takes for CO_2 to reach the top seal, and the amount of CO_2 leakage if a presumptive leak develops in the top seal. Such method would greatly facilitate the assessment of large fields nominated for storage.

In reservoir simulation, upscaling is defined as the process of obtaining petrophysical properties at a coarse-scale grid system equivalent to the properties (e.g., porosity, permeability, and phase saturations) defined at a fine-scale grid system. Here “equivalent” means that the two systems act as similarly as possible (Li, 1995). Because of the heterogeneous characteristics of sedimentary rocks, upscaling should be done carefully such that an optimum balance is achieved between flow simulation time in the coarse grid and preservation of important geologic features in the fine grid reservoir model. Moreover, it is now known that the type of fluid displacement process also affects the quality of the upscaling method. An approach which is accurate for single phase

flow may prove inadequate for viscosity-dominated multiphase flow, and an approach accurate for the latter may not work well when displacement is driven by buoyancy.

For additive properties, like porosity, fluid saturation and component mole fractions, arithmetic average is used for upscaling. This averaging method decreases the standard deviation of the property distribution. The bigger the sample volume, the smaller the standard deviation of the property becomes and hence, more similarity to homogeneous conditions.

But, the main difficulty in upscaling is for nonadditive properties, mainly permeability and multiphase properties. The effective permeability of an upscaled heterogeneous medium is defined as the permeability of an equivalent homogeneous medium that gives the same flux for the same boundary conditions. Thus, the upscaled permeability of a heterogeneous medium depends on both the distribution of heterogeneities and the boundary conditions (Begg *et al.*, 1989). One of the important multiphase properties, especially in applications like CO_2 storage where imbibition occurs, is residual saturation. It strongly affects the mass of CO_2 that remains securely as residual phase in the storage aquifer. It also affects the mass of escaped CO_2 in the case of leakage from the aquifer through a breach in the overlying seal. On one hand, the underestimation of residual saturation in an upscaled system could lead to disqualification of a candidate aquifer due to wrong estimation of storage capacity. On the other hand, overestimation of this parameter may lead to approval of a risky candidate aquifer.

The competition between buoyancy and capillary entry pressure which causes local capillary trapping does not depend on residual saturation. Indeed, the salient feature of local capillary trapping is that the most of the saturations in the accumulations are far above residual. Nevertheless, treating the CO_2 held in local capillary traps as though it were a residual phase has some appeal. If a suitably upscaled or equivalent value of residual saturation can be found, then incorporating that value into commercial and research codes being used for sequestration simulations and risk assessment is straightforward. The challenge here is to account for the range of possible displacement behavior. We anticipate that the correlation length of the small-scale heterogeneity will affect the equivalent residual saturation. More complicated is the behavior of CO_2 in local capillary traps after a leak develops in the overlying seal. If the CO_2 is connected to CO_2 which has risen under buoyancy to accumulate at the top of a structure, then the amount that remains in the trap after a leak is a stochastic function of the leak location (Saadatpoor *et al.*, 2010b). If the CO_2 in the local trap is not connected to the accumulation, then it will not be displaced, regardless of whether or not the seal leaks. Thus, process dynamics for local capillary trapping strongly influence the upscaling method.

In this section, we study the effect of single phase upscaling on buoyancy-driven vertical flow of CO_2. Different degrees of coarsening are considered and results are analyzed based on average gas saturation and distribution of CO_2 into different storage modes. The effect of heterogeneity enters via scaled capillary pressure curves for all grid blocks. Then simulation of a leak at the top seal of the aquifer is upscaled and the results are analyzed. Preferential flow paths, which contain CO_2 trapped at saturations far above core-scale residual, exhibit structures several times larger than the correlation length of the permeability field. A coarse-grid simulation that only upscales heterogeneous permeability and porosity is inaccurate to capture this behavior. Hence, we use simulations and post process the data to compute a new parameter called “effective residual gas saturation” for the whole aquifer domain. Using this corrected value of residual gas saturation in

coarse-grid simulation is shown to give an acceptable result as mass percent of escaped CO_2 is considered. A linear relationship is shown to exist between effective maximum residual gas saturation and mass of CO_2 escaped through leaks. The relationship holds for grid blocks larger than the correlation lengths of permeability field and entry pressure field.

Simulation Model

The simulation model described previously is also used here and summarized in this section. The Computer Modeling Group's GEM simulator is used in this study. Dissolution of CO_2 in brine as well as residual trapping of CO_2 is considered, but geochemical reactions are not used and mineral trapping is neglected.

We use a simplified aquifer model to study the dynamic behavior of buoyancy-driven flow of CO_2 during post-injection phase. The two-dimensional aquifer is 120 m wide. For simplicity, the CO_2 is placed at the bottom of a two dimensional aquifer as h_1 feet of CO_2-saturated layers, shown schematically in Figure 214. This represents the distribution of CO_2 at the end of the injection phase that is designed to place the CO_2 in the lower part of a storage formation. Aquifer temperature is held constant at 60°C and initial pressure is assumed to be 15.6 MPa at 1615 m reservoir depth. Both values are typical values of a conventional deep saline aquifer in the Gulf Coast. The base case is run with a 0.3 m by 0.3 m fine grid system.

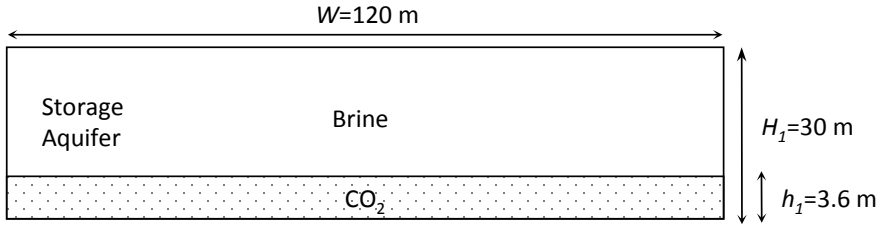

Figure 214: Schematic of the aquifer used for the buoyancy-driven flow simulations. The injection phase has been completed and is simulated here as an initial condition of uniform CO_2 saturation in the lower part (h_1) of the aquifer. Buoyancy-driven flow of CO_2 is about to begin.

The Peng-Robinson equation of state is used to model fluid properties. This equation is tuned for H_2O-CO_2 system by Kumar *et al*. (2005) using experimental data for density and solubility over a wide range of pressures, temperatures, and salinities related to deep saline aquifers. The brine salinity of 100,000 ppm is assumed for the aquifer. The Pedersen correlation (1984) is used for viscosity of brine phase.

Two realizations of synthetic heterogeneous permeability field are generated for 40,000 grid blocks of the base case. Both permeability fields have a log-normal distribution with a mean value of 190 md (i.e. 190×10^{-15} m^2). The standard deviation of natural logarithm of permeability is 1.23. The two realizations are different in their correlation length. Correlation lengths of 1.5 m and 15 m are used in the horizontal direction, but the field is uncorrelated in the vertical direction. The permeability field is assumed to be isotropic. Based on the properties of the permeability field, porosity and relative permeability hysteresis parameters (irreducible water saturation and maximum residual gas saturation) are generated using Holtz (2002) equations.

Porosity is generated for every grid block, but a single value is estimated for relative permeability hysteresis parameters.

The Brooks-Corey (1966) capillary pressure model is used in this study. A reference curve with capillary entry pressure of 8.3 kPa and compatible with relative permeability hysteresis parameters is generated and assigned to the average permeability of the field. Then, this reference capillary pressure curve is scaled for every grid block via Leverett scaling group,

$$P_{c2}\left(S_w\right) = P_{c1}\left(S_w\right)\sqrt{\frac{k_1}{k_2}.\frac{\phi_2}{\phi_1}} \tag{33}$$

Therefore, the permeability and porosity of the heterogeneous domain are affecting the drainage capillary pressure curves, making the capillary entry pressure field heterogeneous. The capillary pressure hysteresis is neglected in this work considering its small impact compared to hysteresis in gas relative permeability.

To study the security of storage, we assume another aquifer is located above the storage aquifer and a 0.3 m shale layer acts as the top seal that separates the two aquifers. (The thin barrier is for convenience; its thickness does not affect the ultimate amount of leakage.) Figure 215 shows a schematic of the leak model. A prescribed amount of CO_2 is emplaced into the storage formation as an initial condition and is allowed to accumulate below the top seal after 50 years of buoyancy-driven flow. Then a fracture appears in the top seal. The CO_2 is now subject to an open path through the upper aquifer. The leak is 0.6 m wide and gives enough space to both the CO_2 and brine to move past each other in different directions, if they do so.

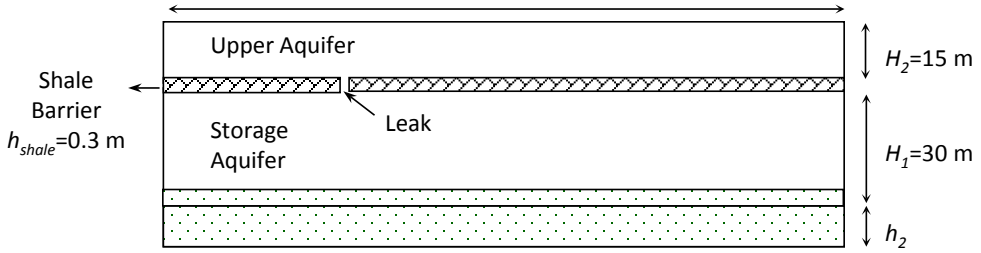

Figure 215: Schematic of the leak model. More CO_2 is initially emplaced (h_1+h_2, cf. Figure 214) such that CO_2 accumulates below the top seal after buoyancy-driven flow. The leak is assumed to exist only after CO_2 accumulation ends.

Upscaling Methods

In this work, we use single phase upscaling to upscale the single phase properties of the model, namely porosity and permeability. The calculated values of porosity and permeability are used to calculate the drainage capillary pressure curve for new coarse grid blocks by scaling the original capillary pressure curve via the Leverett scaling group, Eq. (33). The relative permeability curve and maximum residual gas saturation are assumed to be constant for the whole system regardless of upscaling. This assumption will be shown to be impractical and will need to be changed during the upscaling process.

We use the arithmetic average of the original grid blocks as the equivalent porosity of the coarse grid block:

$$\phi_e = \frac{\sum_{i=1}^{n}\left(V_{Pi}\cdot\phi_i\right)}{\sum_{i=1}^{n}V_{pi}} \tag{34}$$

where ϕ_e is effective porosity of the coarse grid block, V_p is pore volume, ϕ is porosity, subscript i denotes the i^{th} original grid block, and n is the total number of original grid blocks in the coarse grid block.

Several upscaling procedures have been proposed for permeability in the literature. Some examples are power-law average, renormalization, pressure-solver method and pseudofunction technique (Qi and Hesketh, 2005). A Monte Carlo approach was used by Journel *et al*. (1986) to generate realizations of sand/shale environments and derive an effective permeability for them. They proposed the following power-law model:

$$k_e = \begin{cases} \left[\, pk_{sh}^{w} + (1-p)k_s^{w} \right]^{1/w} & , \quad w \neq 0 \\ k_{sh}^{p} k_s^{1-p} & , \quad w = 0 \end{cases} \tag{35}$$

where k_e is effective permeability of the coarse grid block, k_{sh} is shale permeability, k_s is sandstone permeability, p is shale volume fraction, and w is power of average. The power of average (w) has a value between 1 and -1, at which limits it yields arithmetic and harmonic averages, respectively. For w=0, it gives the geometric average. Warren and Price (1961) show that regardless of the type of permeability distribution, the effective permeability can best be approximated by the geometric mean. In practice, arithmetic average is commonly used for horizontal flow and geometric average is used for vertical flow (Begg *et al.*, 1989; Journel *et al.*, 1986). Since we are studying the buoyancy-driven vertical flow of CO_2 we use geometric mean to upscale permeability:

$$k_e = \left(\prod_{i=1}^{n} k_i \right)^{1/n} \tag{36}$$

where k_i is the permeability of the i^{th} fine grid block in the upscaled sample.

Permeability Field with 1.5 m Correlation Length

Three cases are considered to see the effect of upscaling on the behavior of a buoyant plume:

1. Base case as depicted in Figure 214. We want to see how different degrees of coarsening will affect local capillary trapping.

2. Base case with enough initially emplaced CO_2 such that CO_2 rises just far enough to reach the top seal. We want to see if upscaling distorts estimation of the threshold capacity of an aquifer for secure storage of CO_2.
3. Leakage at the top seal of the aquifer. We want to see the effect of upscaling on estimation of escaped CO_2 from an aquifer in case of leakage in the top seal.

Each case considers the original grid with 0.3 m by 0.3 m blocks and compares it as a reference with four coarse grid systems with 0.6×0.6 m, 1.2×1.2 m, 3×3 m and 6×60 m blocks (First number is the vertical size of the block, while the second one is horizontal size.) In the last two grids, some layers have different height than main upscaling size in order to accommodate the same value of initial CO_2 as original fine grid system. Only the single phase flow properties, i.e., porosity and permeability are upscaled here. The relative permeability and Leverett *J*-function are the same as original fine-scale case. Capillary pressure scaling is considered in all the simulations. That is, we impose a drainage capillary pressure curve in each coarse grid block determined from the Leverett *J*-function and the upscaled permeability and porosity in that grid block.

Effect of Upscaling on Local Capillary Trapping

Injection period has caused the bottom 3.6 m of total 30 m thickness of the storage aquifer to be saturated with CO_2. The emplaced CO_2 then rises upward due to buoyancy. Figure 216(a) shows gas saturation profile after 25 years of buoyant flow in original 0.3×0.3 m fine grid. The local capillary trapping can be seen in this picture, as the large saturations (yellow and orange pixels) are accumulated along the specific channels through which the CO_2 rises. These preferential flow paths are capillarity dominated and it is the spatial correlation of the capillary entry pressure field that determines the path of CO_2 flow.

The CO_2 saturation is shown at the same time (25 years) in Figure 216(b) through Figure 216(e) for upscaled system with coarse grid blocks of 0.6×0.6 m, 1.2×1.2 m, 3×3 m and 6×60 m blocks, respectively. In all cases buoyant flow is almost at steady state. Local capillary trapping is still visible in (b) and (c), where the degree of upscaling is smaller than the five-foot correlation length in the permeability field. CO_2 follows the same preferential flow paths as in (a). As the upscaling goes beyond correlation length, the local capillary trapping starts to disappear. In Figure 216(d) the effect of heterogeneity can still be seen. The CO_2 displacement front is similar to a front in a simulation with a single capillary pressure for all grid blocks (Bryant *et al.*, 2008). In contrast, the coarsest grid, Figure 216(e), does not show any evidence of the heterogeneity of the fine-scale domain.

These grid blocks in Figure 216(e) are coarse relative to the fine-scale model, but they are typical sizes in routine field-scale simulations, mainly because they enable manageable computing time (overnight or faster). This illustrates the essence of the challenge for quantifying local capillary trapping at the field scale: the high degree of coarsening has completely averaged out the fine-scale heterogeneity of the domain and hence, the nature of the displacement is essentially one-dimensional within a homogeneous domain.

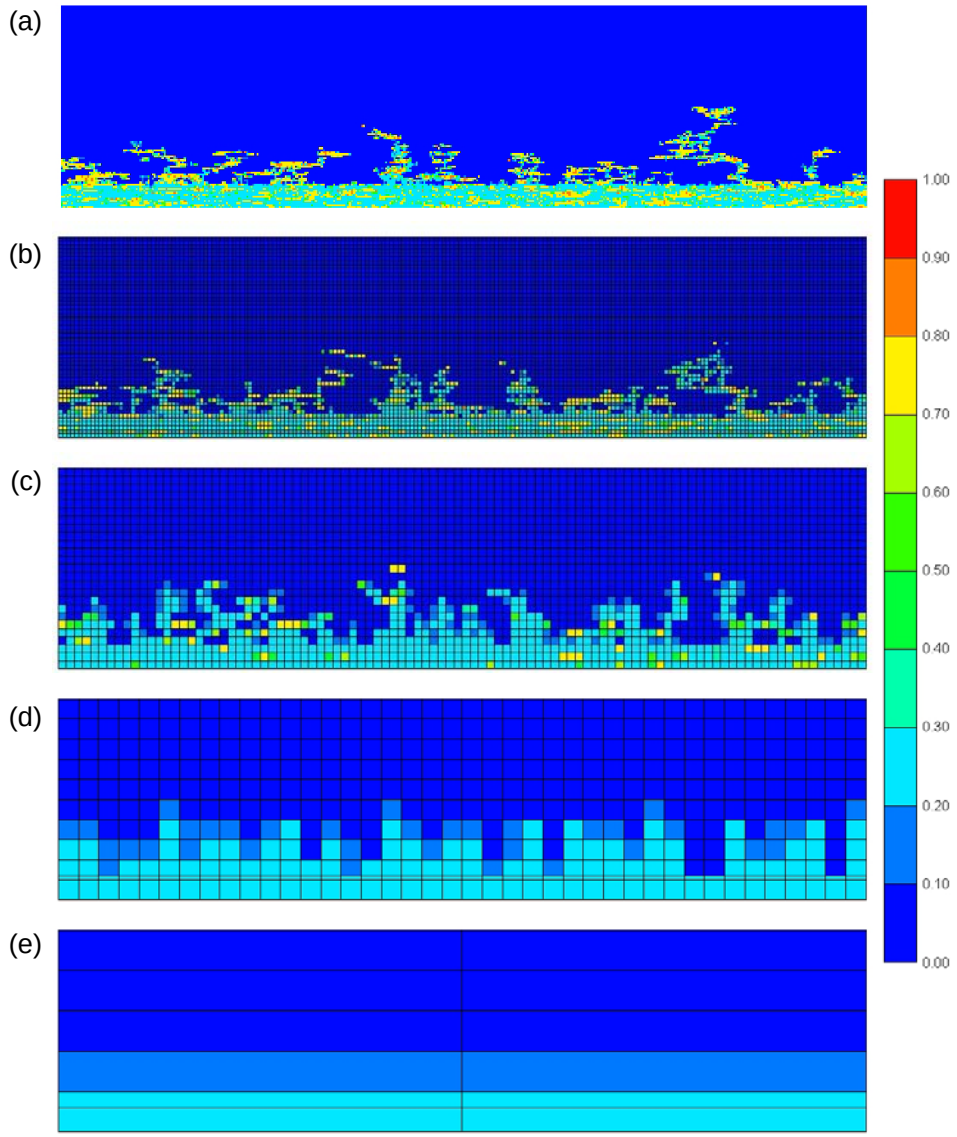

Figure 216: Gas saturation profile of base case in Figure 214 after 25 years (a) with 0.3×0.3 m fine grid system, and when grid and single phase flow properties are upscaled to blocks of (b) 0.6×0.6 m, (c) 1.2×1.2 m , (d) 3×3 m, and (e) 6×60 m.

Table 25 shows average gas saturation and also mass of CO_2 in both phases (aqueous and supercritical CO_2) in the storage formation above the initial emplacement zone, i.e., in the top 26.4 m of the storage aquifer in Figure 214, after 25 years of buoyant flow. The average gas saturation above the emplacement zone increases as degree of coarsening increases. The reason is that the extremes of permeability are eliminated by upscaling. The occurrence of regions of large capillary entry pressure is therefore reduced, which decreases the opportunity for local capillary trapping. Hence, less CO_2 is locally trapped in the storage formation after buoyant flow. The total mass of CO_2 in the same zone also increases as the grid is upscaled. Simultaneously, less CO_2 remains in the initial zone of emplacement (the lower 3.6 m of the aquifer) as the grid is coarsened. Since the size of grid blocks in (d) and (e) is well above the correlation length (more than twice), then the permeability domain acts as a homogeneous domain and hence, the average gas saturation and mass of CO_2 is almost the same in both cases. If we just consider square grid

blocks, a linear relationship can be observed between the mass of CO_2 above the initial emplacement zone and the logarithm of the block size. This relationship can be used to estimate the results for fine-scale grid from two coarse grid simulations.

Table 25: Average Gas Saturation and mass of CO_2 (in metric tonnes) in Storage Formation Above the Initial Emplacement Zone for Cases in Figure 216[*]

	Degree of Coarsening in x and z				
	1×1	2×2	4×4	10×10	20×200
Average gas saturation	3.86%	4.39%	4.93%	5.66%	5.86%
Mass of CO_2 (in aqueous phase)	1.44	1.90	2.62	3.38	2.86
Mass of CO_2 (in $scCO_2$ phase)	5.97	6.74	7.31	7.71	8.14
Mass of CO_2 (in both phases)	7.41	8.65	9.93	11.1	11.0
% of originally emplaced CO_2	41.8%	49.1%	56.9%	63.8%	63.2%

[*]All values are at 25 years.

Table 26 shows the same parameters in the same zone after 100 years of CO_2 upward movement. There is a very slight change compared to Table 25 which shows that steady state is reached in 25 years. Although there is a small increase in mass of risen CO_2, the average gas saturation is decreased after 75 more years of flow, because more CO_2 goes from $scCO_2$ phase into solution during time.

Table 26: Average Gas Saturation and Mass of CO_2 in Storage Formation Above the Initial Emplacement Zone for Cases in Figure 216[*]

	Degree of Coarsening in x and z				
	1×1	2×2	4×4	10×10	20×200
Average Gas Saturation	3.71%	4.25%	4.80%	5.60%	5.86%
Mass of CO_2 (% of Originally Emplaced CO_2)	42.2%	49.3%	56.9%	64.0%	63.2%

[*]All values are at 100 years

Effect of Upscaling on Gas Column Height

If sufficient CO_2 is initially emplaced, it can reach the top seal in its upward buoyant flow. Figure 217 shows gas saturation profile at 25 years while h_2=3 m of additional CO_2 initially present. In Figure 217(a) with original fine grid, the CO_2 has just found a path to the top seal at 25 years and gas column height is equal to the height of the storage formation. In other words, the initial volume of CO_2 is the threshold volume of injection that does not lead to accumulation of gas as bulk phase in any point under the top seal of the storage aquifer.

Figure 217(b) through Figure 217(e) show the results of the same case simulated using coarse grid blocks of 0.6×0.6 m, 1.2×1.2 m, 3×3 m and 6×60 m blocks, respectively which are upscaled from the original grid of Figure 217(a). Again in (b) and (c) CO_2 follows the same preferential flow paths as in (a), but only (b) shows that the CO_2 reaches the top of the aquifer. The arrival of CO_2 at the top of the domain introduces the possibility of accumulation beneath the top seal or migration along the top seal in a tilted aquifer. Both of these events increase the risk of undesired CO_2 movement, either leakage through an unanticipated leak in the seal, or migration beyond an authorized boundary. Thus, the simulation in (c), in which CO_2 stops rising more than 6 m below the top seal, would underestimate the risk associated with this amount of storage.

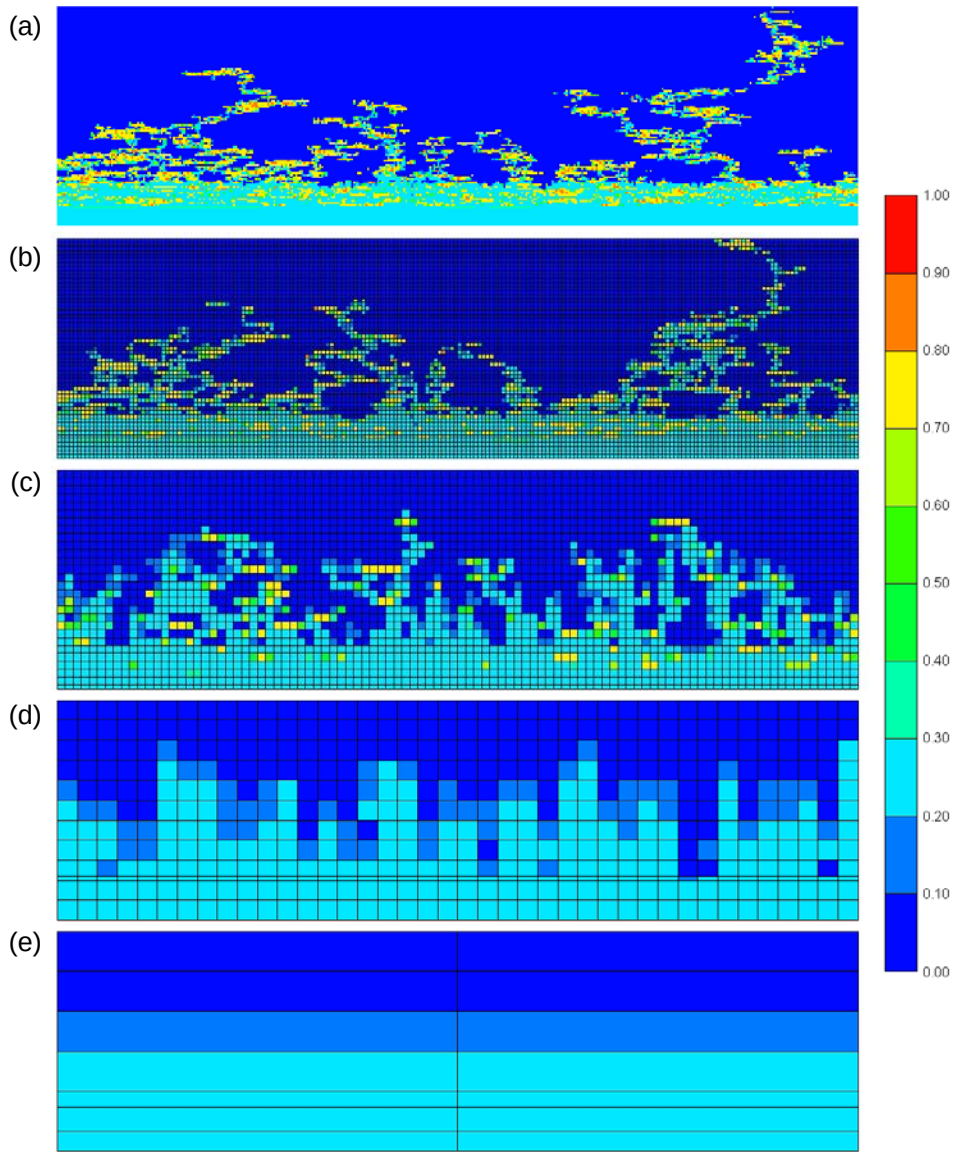

Figure 217: Gas saturation profile of base case with 10 extra feet of initially injected CO_2 after 25 years (a) with 0.3×0.3 m fine grid system, and when grid and single phase flow properties are upscaled to blocks of (b) 0.6×0.6 m, (c) 1.2×1.2 m , (d) 3×3 m, and (e) 6×60 m.

Careful comparison of Figure 217(a) and Figure 217(b) shows that a very narrow high permeable channel with low entry pressure at top right of the domain that delivers the CO_2 to top seal is lost as a result of upscaling. The CO_2 makes its way the last three meters or so in (b) through a different flow path than in (a). So, even if the scale of upscaling is smaller than correlation length, it might still disturb the results of simulation in showing the CO_2 column height.

In Figure 217(d) and Figure 217(e) capillary trapping no longer occurs, and the rising plume behaves differently. Figure 217(d) still shows the general tendency of the gas column to reach near the top and shows the same gas column height as in (c), but (e) acts like a completely homogeneous domain with a uniform front of gas which has barely passed the mid-way through

the top seal. The grid blocks are too coarse to be able to help in assessing whether CO_2 will reach the top, and hence, in assessing this aspect of the safe storage capacity of the aquifer.

Table 27 shows average gas saturation and also mass of CO_2 in the storage zone above the initial emplacement zone, i.e., top 26.4 m of the storage aquifer (cf. Figure 215) after 25 years of buoyant flow. The results are at steady state. Again due to effect of upscaling in reducing heterogeneity, coarser grid blocks enable more gas to rise into the storage zone of the aquifer. As degree of coarsening increases, we can see that mass of CO_2 in the storage zone is the same percentage of injected CO_2 as in previous case with 3.6 m of initial CO_2, i.e., Table 25. When using 3×3 m grid blocks, 63% of injected CO_2 will rise to the storage formation for either amount of initial emplacement. This shows that local capillary trapping has been suppressed in this level of upscaling. Considering size of square grid blocks, the linear relationship again exists between the mass of CO_2 in the storage zone and the logarithm of the block size.

Table 27: Average Gas Saturation and Mass of CO_2 (in metric tonnes) in Storage Formation Above the Initial Emplacement Zone for Cases in Figure 217[*]

	Degree of Coarsening in x and z				
	1×1	2×2	4×4	10×10	20×200
Average Gas Saturation	8.94%	9.26%	9.80%	10.68%	10.97%
Mass of CO_2 (in Aqueous Phase)	2.9	3.6	4.4	5.4	4.6
Mass of CO_2 (in $scCO_2$ Phase)	13.8	14.2	14.6	14.7	15.3
Mass of CO_2 (in Both Phases)	16.7	17.8	19.0	20.1	19.9
% of Originally Emplaced CO_2	50.9%	54.7%	59.0%	63.4%	62.9%

[*]All values are at 25 years.

Effect of Upscaling on Gas Leakage

Development of a leak in the top seal is simulated to study the risk involved in accumulation of CO_2 below the top seal. The CO_2 flows inside the aquifer for 25 years under the effect of buoyancy. The leak then appears at the top seal. Our studies show that different positions of leak in the top seal lead to a wide range of CO_2 leakage amount. We assume that a leak at x=33 m from the left boundary results in the maximum value of gas leakage. Figure 218 shows gas saturation profile at 25 years after development of the leak (i.e., 50 years after injection) while h_2=15 m of additional CO_2 is emplaced initially. Figure 218(a) uses the original fine grid, while Figure 218(b) through Figure 218(e) use upscaled versions of original grid in 0.6×0.6 m, 1.2×1.2 m, 3×3 m and 6×60 m block size. In all cases, the 0.3 m shale layer is refined to 0.3×0.3 m grid blocks and the 1.2 m wide leak is located at the exact same position in this layer. In the coarsest grid, the blocks at the top and bottom of the leak are refined to have the CO_2 flow through the leak. The general behavior is similar in all cases, as a relatively large portion of CO_2 has escaped through the leak and still a large volume of above-residual saturation CO_2 is trapped below the seal at the top right of the storage aquifer. But the volume of escaped CO_2 in (a) seems to be less than other cases.

To quantify the amount of CO_2 escaped through the leak we post process the results and calculate mass of escaped CO_2 as percent of originally emplaced CO_2. The results are shown in Table 28. Remarkably, the mass of escaped CO_2 is almost equal in all upscaled cases (around

15% of injected CO_2). Still more remarkably, mass of escaped CO_2 in original grid is substantially smaller than all the upscaled cases. We conjecture that the reason may be a key heterogeneity in original grid which is removed (averaged out) in the upscaling process. This shows that although a small degree of coarsening might preserve the dynamics of buoyant flow, still it can disturb the risk assessment calculations and estimations.

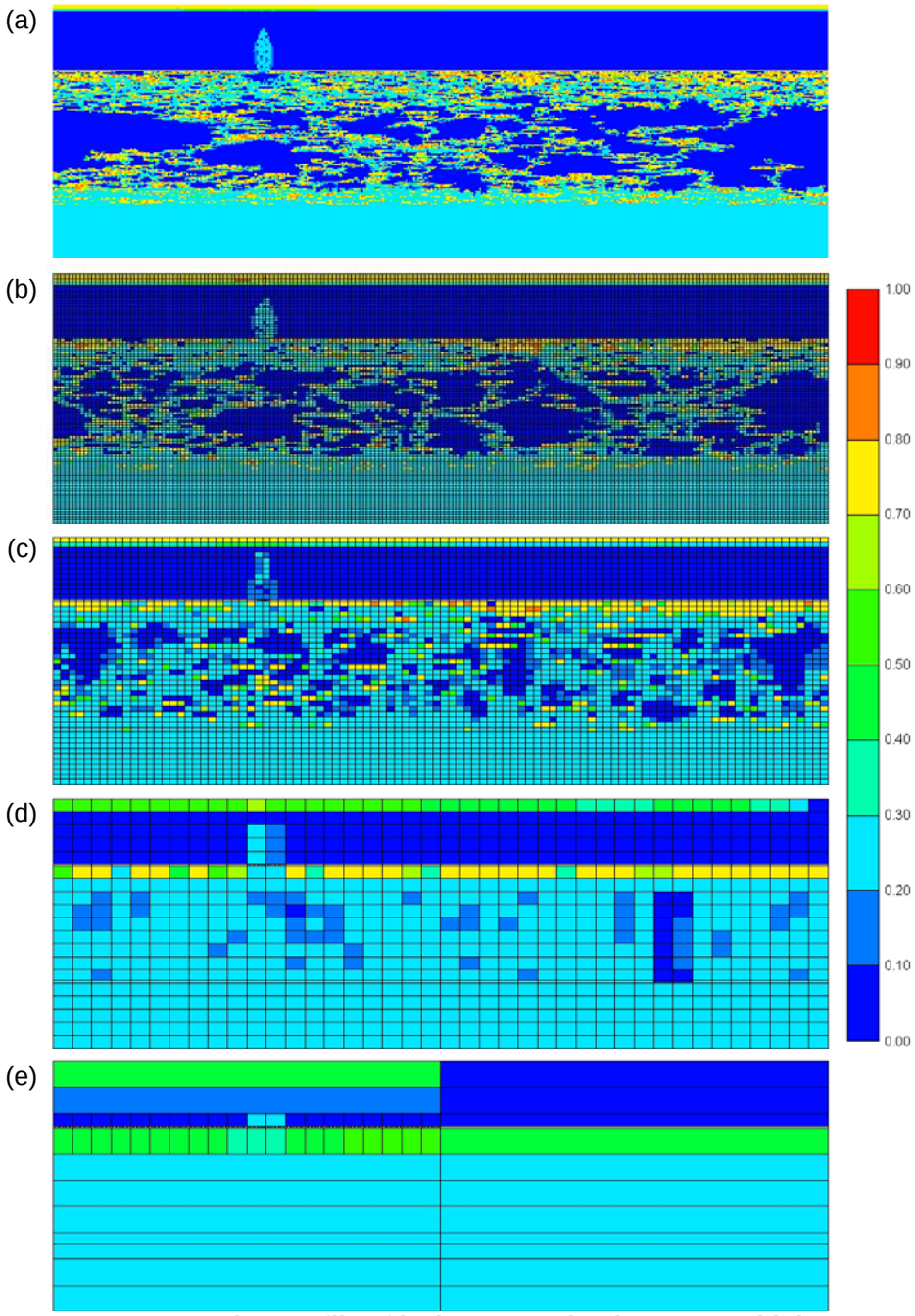

Figure 218: Gas saturation profile of leakage case in Figure 215 with h_2=15 m after 25 years of buoyant flow and then 25 years of leakage (a) with 0.3×0.3 m fine grid system, and when grid and single phase flow properties are upscaled to blocks of (b) 0.6×0.6 m, (c) 1.2×1.2 m , (d) 3×3 m, and (e) 6×60 m.

Table 28: Mass of Escaped CO_2 (in metric tonnes) at 25 Years After Leakage in Top Seal

	Degree of Coarsening in x and z				
	1×1	2×2	4×4	10×10	20×200
Mass of CO_2 (in Aqueous Phase)	2.95	2.70	3.13	3.44	2.68
Mass of CO_2 (in $scCO_2$ Phase)	6.08	11.9	9.55	9.83	11.1
Mass of CO_2 (in Both Phases)	9.03	14.6	12.7	13.3	13.8
% of Originally Emplaced CO_2	10.2%	16.4%	14.7%	14.9%	15.5%

Effective Residual Saturation

In the preceding simulations, we only upscaled porosity and permeability, keeping relative permeability the same throughout the domain and scaling drainage capillary pressure curves by the upscaled porosity and permeability. The results indicated that an appropriate upscaling method may be different for different applications. From point of view of risk assessment in a carbon sequestration project, an appropriate upscaling method can be defined as the one which enables the correct estimation of secure storage capacity and extent of escape due to a presumptive leakage. Here we want to see if we can change multiphase flow properties (along with porosity and permeability as before) in the upscaling process such that the coarse-scale grid give the same amount of leakage as original grid.

We first propose to find an effective residual gas saturation for the upscaled aquifer such that it gives the same value for escaped CO_2 as original fine-scale grid (10.2% in Table 28). The whole process of leakage simulation (buoyant flow for 25 years in the closed aquifer and then 25 years after leak development) is repeated by changing the maximum residual gas saturation in gas relative permeability curve. Table 29 and Table 30 show the results for 3×3 m and 6×60 m block size, respectively. The results show that mass of escaped CO_2 changes linearly with S_{gr}^{max} in the upscaled simulations, Figure 219. The reason is decrease of degree of heterogeneity and elimination of local capillary trapping due to upscaling. Hence, it is natural to consider increasing the upscaled or effective residual saturation to compensate for the loss of local capillary trapping. The effective residual saturation is 0.324 for 3×3 m grid blocks and 0.337 for 6×60 m grid blocks, because they give 10.16% escaped CO_2 as did the original fine grid with residual saturation of 0.286. Figure 220 plots these values of effective residual saturation versus standard deviation of permeability of their grid system. The linear relationship in this graph suggests that the Holtz (2002) correlation for maximum residual gas saturation might be modified in order to consider the effect of upscaling in leakage simulation. More studies are required to develop and verify the validity of such correlation. In particular, we anticipate a dependence on the correlation length in the original permeability field and a plateau value of effective residual saturation for coarsening beyond that correlation length. A plot of effective residual saturation versus grid block size/correlation length in Figure 221 shows this behavior.

Table 29: Mass of Escaped CO_2 (in metric tonnes) at 25 Years After Leakage in the Top Seal for Different Values of S_{gr}^{max} — Grid blocks are 3×3 m*

	S_{gr}^{max}				
	Base (0.286)	0.324	0.327	0.337	0.350
Mass of escaped CO_2	13.3	9.23	8.82	8.01	6.75
% of Originally Emplaced CO_2	14.9%	10.3%	9.9%	9.0%	7.6%

*True solution is 10.3% escape, obtained in fine grid (0.3 x 0.3 m grid) and S_g^{rmax} = 0.286.

Table 30: Mass of Escaped CO_2 (in metric tonnes) at 25 Years After Leakage in the Top Seal for Different Values of S_{gr}^{max} — Grid blocks are 6×60 m*

	S_{gr}^{max}				
	Base (0.286)	0.300	0.324	0.337	0.350
Mass of escaped CO_2	13.8	12.4	10.2	9.03	7.85
% of Originally Emplaced CO_2	15.5%	13.9%	11.5%	10.2%	8.8%

*True solution is 10.3% escape, obtained in fine grid (0.3 x 0.3 m grid) and S_{gr}^{max} = 0.286.

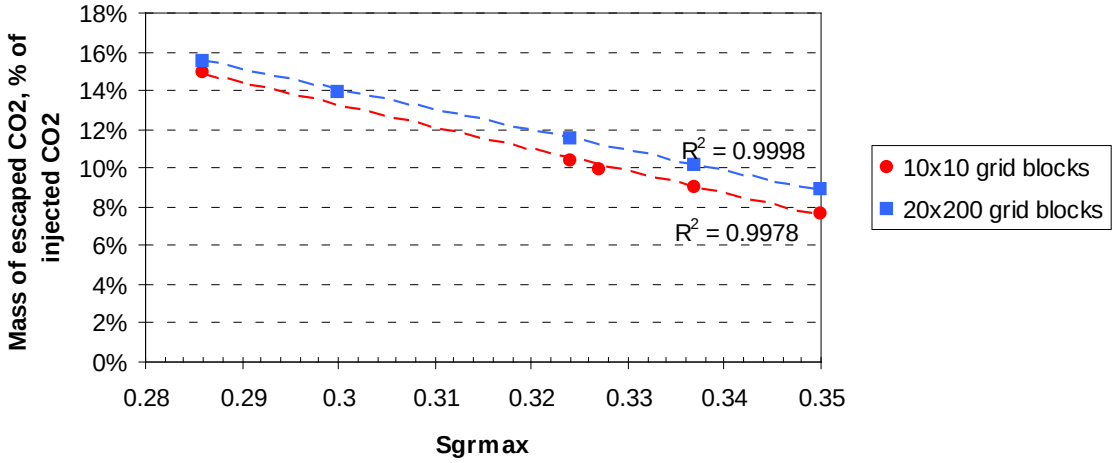

Figure 219: Mass of escaped CO_2 (as percent of injected CO_2) versus maximum residual gas saturation for upscaled grids with 3×3 m and 6×60 m block size. Permeability field has 1.5 m correlation length. [15]

[15] This plot and the succeeding two plots constitute part of Deliverable 8.0 A function in a form readily incorporated in existing data structures in reservoir simulators that accounts for the amount of local capillary trapping in terms of geologic and petrophysical and operating parameters.

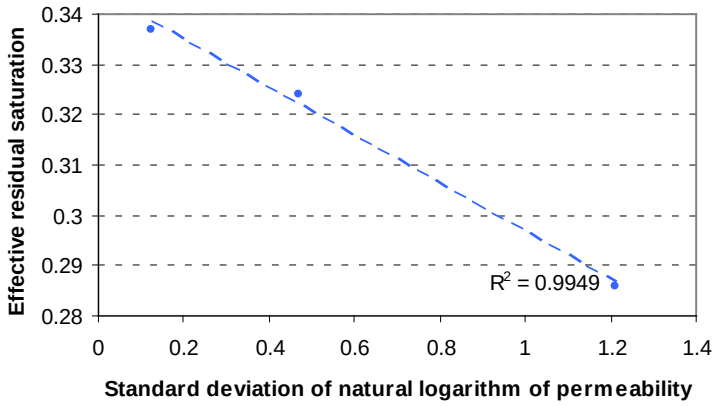

Figure 220: Effective residual gas saturation versus standard deviation of natural logarithm of permeability. Permeability field has 1.5 m correlation length.

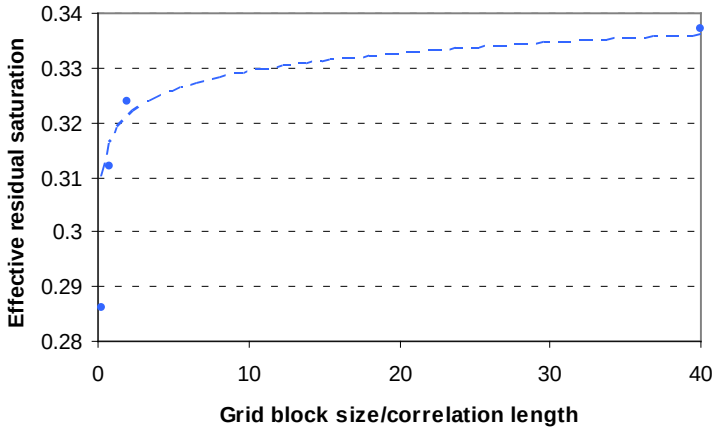

Figure 221: Effective residual gas saturation versus grid block size (as factor of correlation length). Permeability field has 1.5 m correlation length.

Permeability Field with 15 m Correlation Length

Effect of Upscaling on Local Capillary Trapping

6.6 m of CO_2-saturated layers are assumed to be present at the bottom of the 33 m high 2D aquifer at the beginning of post-injection relaxation period. The CO_2 then moves upward due to the buoyancy effect while competing with capillary forces. Figure 222 shows gas saturation profile after 50 years of buoyancy-driven flow in the original fine grid system as well as upscaled systems with different levels of coarsening. In all cases buoyant flow is almost at steady state.

In the original 0.3×0.3 m fine grid, Figure 222(a), large saturations (yellow and orange pixels) of gas have remained below local capillary barriers throughout the flow path. These accumulations constitute the local capillary trapping.

Figure 222(b) through Figure 222(e) show the saturation profile for upscaled system with coarse grid blocks of 0.6×0.6 m, 1.2×1.2 m, 3×3 m and 6×6 m, respectively. Even in Figure 222(b) with grid blocks of 0.6×0.6 m, the CO_2 does not follow the same preferential flow paths as in original grid. This shows that the conventional upscaling of a permeability field with large correlation length compared to the block size will substantially change a buoyancy-driven multiphase

displacement. This is because local capillary barriers are large and tend to induce horizontal flow. The existence of the barriers is due to local variation in permeability which is diminished by conventional upscaling. Thus, upscaling opens new vertical flow paths which the gas follows; hence, the saturation distribution substantially changes.

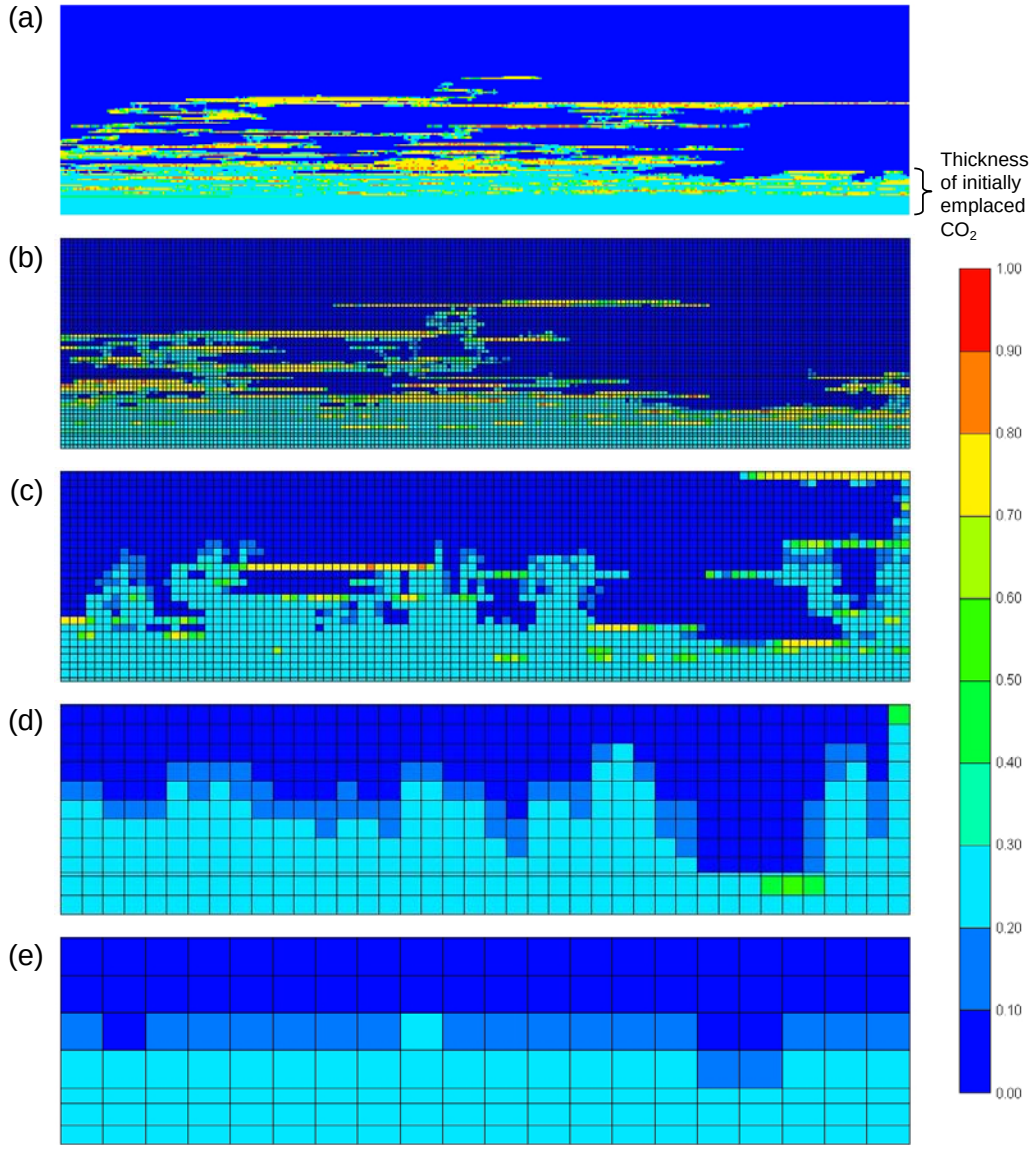

Figure 222: Gas saturation profile of the base case with 6.6 m of initially emplaced CO_2 after 50 years (a) with 0.3×0.3 m fine grid system with 15 m horizontal correlation length. The grid and single phase flow properties are upscaled to blocks of (b) 0.6×0.6 m, (c) 1.2×1.2 m, (d) 3×3 m, and (e) 6×6 m.

As can be seen in Figure 222(b) through Figure 222(e), as the degree of coarsening increases, the amount of local capillary trapping decreases. In Figure 222(c) some local capillary trapping can still be seen. In Figure 222(d) the gas displacement still shows the heterogeneity of the domain but no local capillary trapping; instead the behavior is almost identical to that when capillary pressure is homogeneous throughout a heterogeneous domain. Figure 222(e) shows little evidence of heterogeneity. Although this approaches the grid size needed for field-scale

simulations, the comparison with fine-scale simulations shows that the dynamics of the behavior have completely changed after upscaling.

Table 31 shows the average saturation and mass of CO_2 in the top 26.4 m of the storage aquifer, seen in Figure 222, after 50 years of buoyant flow. As discussed earlier, as the extremes of permeability are smeared by upscaling, the behavior becomes more homogeneous and less CO_2 is trapped in local capillary traps inside the emplacement zone, so the average gas saturation above the emplacement zone slightly increases. This is clearer when we see a similar trend for the total mass of CO_2 in the same zone. An equal amount of CO_2 in the storage zone for 10×10 and 20×20 grid blocks shows that local capillary trapping has been suppressed in this level of upscaling.

Table 31: Average gas saturation and mass of CO_2 (in metric tonnes) in the storage formation above the initial emplacement zone for cases seen in Figure 222, after 50 years of buoyant flow.

	Degree of Coarsening in x and z				
	1×1	2×2	4×4	10×10	20×20
Average Gas Saturation	9.9%	10.6%	10.2%	11.0%	10.9%
Mass of CO_2 (in Aqueous Phase)	2.7	2.7	4.6	5.6	5.3
Mass of CO_2 (in scCO_2 Phase)	15.2	16.2	15.3	15.1	14.9
Mass of CO_2 (in Both Phases)	17.9	18.9	19.9	20.7	20.2
% of Originally Emplaced CO_2	54.1%	57.3%	60.3%	62.7%	63.4%

Effect of Upscaling on Gas Column Height

In Figure 222(a) with the original fine grid, the CO_2 has risen to a height of 9 m below the seal at steady state. All of the emplaced CO_2 is trapped in the form of residual, dissolution, or local capillary trapping without any risk of leakage. Although in Figure 222(b) more CO_2 has made its way to the storage zone, it goes through some horizontal flow paths and the gas column height is still the same for both. This level of upscaling has maintained the model's ability to predict the gas column height.

In contrast, upscaling to coarser grid blocks has changed the prediction. Comparison with Figure 222(c) and Figure 222(d) shows that some local capillary barriers are lost as a result of upscaling; hence, the CO_2 has found a narrow high permeable channel with low entry pressure at the right side of the domain that acts as a connecting path to the top seal. This introduces the risk of undesired CO_2 movement, either migration beyond an authorized zone or leakage through an unexpected leak in the seal. Thus, the simulation in (c) and (d) would overestimate the risk associated with this amount of storage.

Effect of Upscaling on Gas Leakage

The results of leak simulation are shown in Figure 223. Initially, 18.6 m of CO_2-saturated layers are emplaced at the bottom of the 45 m high aquifer and arrive at steady state after 50 years of relaxation. Then a leak is developed at 33 m to the left of the domain. We assume that a leak at this position gives the maximum value of gas leakage from this formation. The gas saturation profile after 50 years of leak development (i.e., 100 years after injection) is shown in Figure 223 for the original and upscaled grid blocks. In all of the grids, the 0.3 m thick shale layer is

constructed by 0.3×0.3 m grid blocks and the 0.6 m wide leak is located at the exact same position in this layer. In 6×6 m grid, the blocks at the top and bottom of the leak are refined to have the CO_2 flow through the narrow leak.

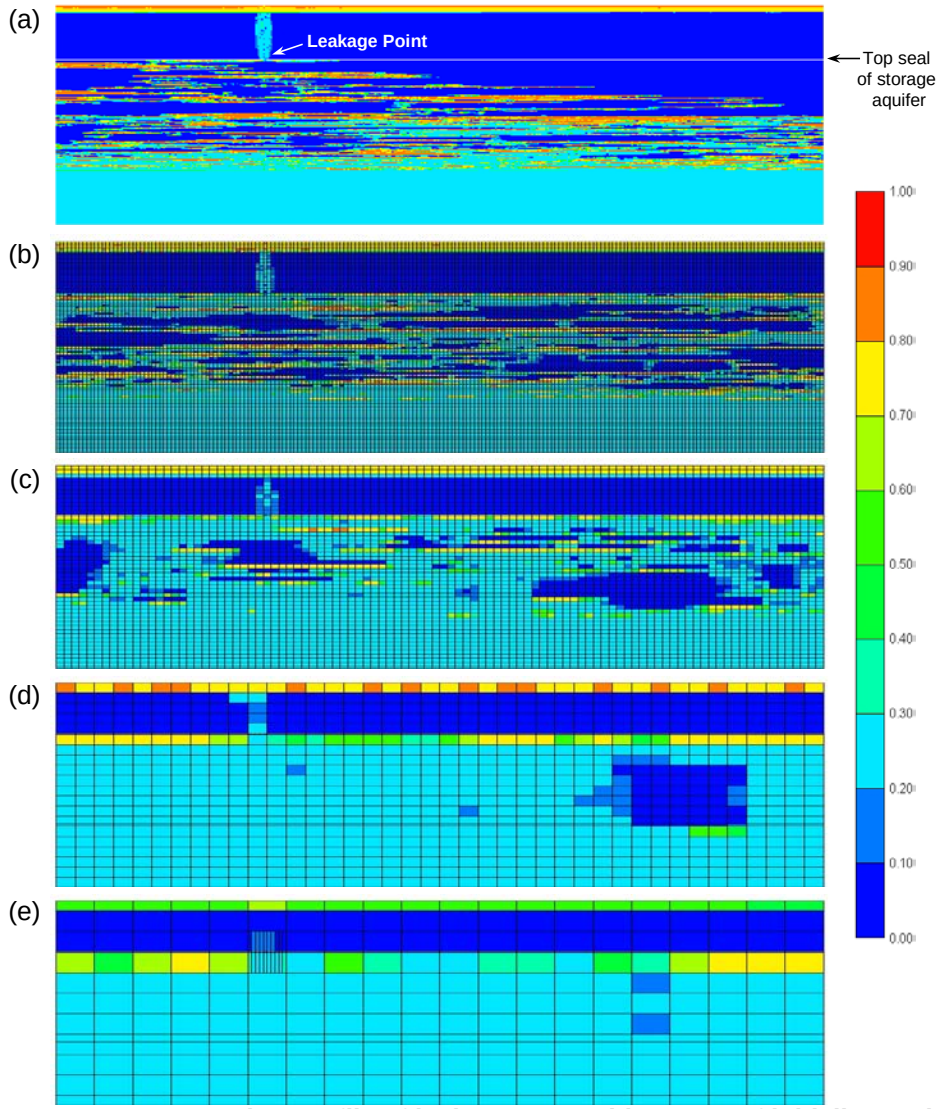

Figure 223: Gas saturation profile of leakage case with 18.6 m of initially emplaced CO_2 after 50 years of leakage (a) with 0.3×0.3 m fine grid system. The grid and single phase flow properties are upscaled to blocks of (b) 0.6×0.6 m, (c) 1.2×1.2 m , (d) 3×3 m, and (e) 6×6 m.

In Figure 223(a) with the original fine grid, while a lot of CO_2 is trapped below the wide horizontal local capillary barriers inside the storage formation, there is a path for CO_2 to reach the top seal at the left side of the domain and no CO_2 has reached the top right of the domain. In Figure 223(b), again the loss of these wide horizontal local capillary barriers has made it possible for CO_2 to invade the top right zone as well. The saturation profile and swept zone substantially changes with more upscaling, as can be seen in Figure 223(c) through Figure 223(e). Table 32 quantifies the amount of CO_2 escaped through the leak as mass percent of originally emplaced CO_2. Remarkably smaller masses of CO_2 escape in the original fine grid block compared to the

upscaled grids. Again, the loss of several major horizontal local capillary barriers in the upscaling process can be the reason. This shows that even a small degree of coarsening can disturb the risk assessment calculations and estimations, although it might still be helpful in predicting some flow behaviour like gas column height.

Table 32: Mass of Escaped CO_2 (in metric tonnes) for Cases Seen in Figure 223, at 50 Years After the Leakage, for Fine Grid and Four Coarsened Grids

	Degree of Coarsening in x and z				
	1×1	2×2	4×4	10×10	20×20
Mass of CO_2 (in Aqueous Phase)	3.19	3.50	3.79	3.98	3.04
Mass of CO_2 (in $scCO_2$ Phase)	9.82	13.8	14.0	14.7	9.48
Mass of CO_2 (in Both Phases)	13.0	17.3	17.8	18.7	12.5
% of Originally Emplaced CO_2	13.3%	17.6%	18.3%	19.7%	14.1%

Effective Residual Saturation

As we saw in preceding simulations, single phase upscaling cannot be used for CO_2 storage applications where there is a special interest in gas column height and amount of gas leakage. Some multiphase flow property should also be involved in upscaling process in order to use it for risk assessment purposes. Here we examine the potential of maximum residual gas saturation as a candidate. We try to find an effective residual gas saturation for the upscaled grid that leads to same amount of escaped gas due to presumptive leakage as in the original fine grid after 100 years (13.3% in Table 32). Table 33 and Table 34 show the results for 1.2×1.2 m and 3×3 m block size, respectively. A value of S_{gr}^{max} = 0.345 gives the best match to the true (fine grid) solution, i.e. 13.3% of the stored CO_2 escapes. As can be seen in Figure 224, mass of escaped CO_2 has a linear relationship with S_{gr}^{max} in the upscaled simulations.

Table 33: Mass of Escaped CO_2 (in metric tonnes) at 50 Years After Leakage in Top Seal for Different Values of S_{gr}^{max} — Grid Blocks are 1.2×1.2 m*

	S_{gr}^{max}			
	Base (0.286)	0.325	0.345	0.350
Mass of Escaped CO_2	18.7	13.8	12.6	11.0
% of Originally Emplaced CO_2	19.7%	14.6%	13.4%	11.7%

*Permeability field has 15 m correlation length.

Table 34: Mass of Escaped CO_2 (in metric tonnes) at 50 Years After Leakage in Top Seal for Different Values of S_{gr}^{max} — Grid Blocks are 3×3 m*

	S_{gr}^{max}			
	Base (0.286)	0.325	0.345	0.350
Mass of Escaped CO_2	17.8	14.7	13.1	12.5
% of Originally Emplaced CO_2	18.3%	15.1%	13.5%	12.9%

*Permeability field has 15 m correlation length.

The upscaling has two different effects on the dynamics of CO_2 flow. Decreasing the degree of heterogeneity causes the elimination of local capillary barriers which decreases the mass of local capillary trapping. On the other hand, it also increases the sweep efficiency, and hence, increases

the mass of residual trapping. In order to compensate for these effects, the maximum residual gas saturation needs to increase and decrease, respectively. Therefore, the net effect is not the same for different cases. Here for the large correlation length of 15 m, the S_{gr}^{max} should increase for coarser grid block to give the same value of escaped gas, which means the effect of local barrier elimination is dominant. In section *Effective Residual Saturation* we showed that in case of a 1.5 m correlation length, the S_{gr}^{max} should increase for coarser grid block to give the same value of escaped gas.

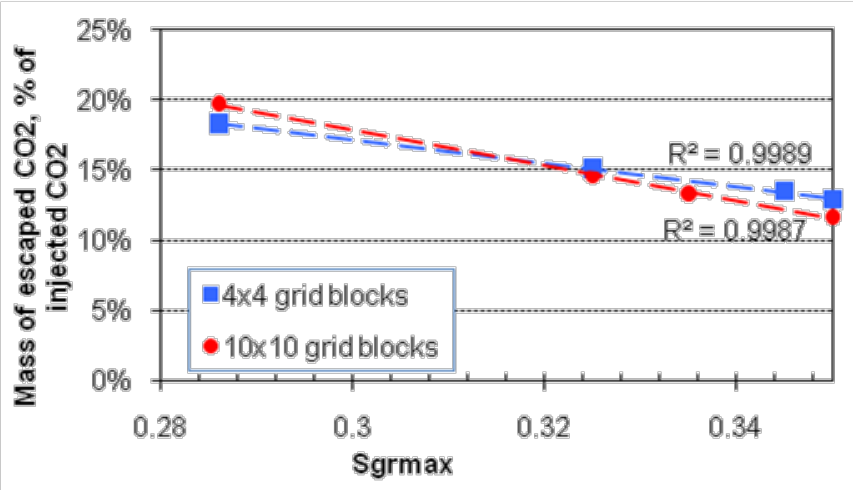

Figure 224: Mass of escaped CO_2 (as percent of injected CO_2) versus maximum residual gas saturation for upscaled grids with 4×4 and 10×10 block size. Permeability field has 15 m correlation length.[16]

Implications for Upscaling

In sufficiently heterogeneous formations, considering effect of heterogeneous capillary pressure gives rise to local capillary trapping as capillary barriers alter the flow paths of buoyant CO_2. Local capillary trapping is, hence, dependent on heterogeneity of the domain. Single phase upscaling methods for permeability and porosity that are practically verified and universally used in reservoir engineering reduce the local capillary trapping. This is because they smear the extremes of permeability and decrease the heterogeneity. The resulting domains show more homogeneous behavior as degree of coarsening increases. Upscaling below the limits of correlation length of heterogeneity can preserve the dynamics of buoyant flow while greatly improving the simulation speed. Still, even this upscaling can be deceptive in risk assessment of a carbon sequestration project.

A new method of upscaling which appropriately changes the multiphase flow properties needs to be done in order to estimate the storage capacity or amount of leakage in a CO_2 storage project. Residual gas saturation is a good candidate for this method of upscaling. A decrease of variance in the permeability field (as a result of upscaling) has opposing effects on value of effective residual saturation. On one hand, it causes a decrease in local capillary trapping; hence,

[16] This plot constitutes part of Deliverable 8.0 A function in a form readily incorporated in existing data structures in reservoir simulators that accounts for the amount of local capillary trapping in terms of geologic and petrophysical and operating parameters

promoting an increase in residual saturation to make up for this effect. On the other hand, the resulting domain is more homogeneous and a larger area of the domain is invaded by gas; therefore, a decrease in residual saturation is needed to adjust for this effect. The net result could be either a larger value of effective residual saturation (see results for a permeability field with 1.5 m correlation length in section *Permeability Field with 1.5 m Correlation Length*) or a smaller value as was the case in section *Permeability Field with 15 m Correlation Length*. The effective residual saturation can be used for more accurate risk assessment of a project with an economical coarse grid model.

4 CONCLUSIONS

Local capillary trapping (LCT) refers to the phenomenon in which CO_2 migrating under buoyancy within the storage reservoir encounters locally continuous regions of larger-than-average capillary entry pressure. The CO_2 accumulates beneath these local capillary barriers, establishing large saturations before continuing its migration beyond the spill points of the local barriers

Bench-scale (0.6 m by 0.6 m by 0.03 m) experiments examined the migration of a buoyant nonwetting phase accompanied by displacement of a denser nonwetting phase using surrogate fluids (brine/glycerol mixture and a decane/mineral oil mixture served as analogs to reservoir brine and supercritical CO_2, respectively). Importantly, these experiments provided the first empirical confirmation of two key concepts underlying LCT. One concept is that a buoyant nonwetting phase (CO_2 in the storage reservoir; hydrocarbon in these laboratory experiments) can accumulate beneath capillary barriers in a variety of structures. The second concept is that buoyant nonwetting phase accumulated in this fashion remains immobile as long as the capillary pressure gradient does not exceed the value prevailing when the accumulation was established. Conversely, when the boundary conditions were manipulated in the laboratory so as to increase the capillary pressure gradient, the accumulated nonwetting phase could be displaced. In this manner the research confirmed that capillarity is the essential physical mechanism that governs this mode of immobilization and that LCT does establish above-residual saturations. The latter point is a critical distinction between LCT and the more familiar "residual saturation trapping" mode of immobilization.

To predict the possible extent of LCT in a storage reservoir, an algorithm was developed to find all potential local traps assuming a geostatistical realization of the permeability in the reservoir is available. The Leverett *J*-function was used to compute the spatial arrangement of capillary entry pressure in the reservoir. The algorithm represents the driving force for CO_2 migration as a single value of "critical capillary entry pressure" $P_{c,entry}^{crit}$, such that regions with capillary entry pressure exceeding $P_{c,entry}^{crit}$ act as barriers to CO_2 migration, while regions with capillary entry pressure less than the $P_{c,entry}^{crit}$ can be invaded by migrating CO_2. The concept of a critical entry pressure introduces a percolation threshold which has significant influence on the extent of LCT. In essence, if $P_{c,entry}^{crit}$ is small compared to the median capillary entry pressure in the reservoir, then almost the entire reservoir acts as a barrier to CO_2 migration, with correspondingly few potential traps and little LCT expected. At the other extreme, if $P_{c,entry}^{crit}$ is large, then very few regions in the reservoir act as barriers, and consequently little LCT can occur.

Testing predictions of this simple algorithm against full-physics simulations of buoyancy-driven CO_2 migration show that the concept of critical capillary entry pressure is a reasonable approximation of the physical process by which traps are filled. For one limiting case storage scenario (emplacement of CO_2 in lower portion of non-dipping reservoir, so that CO_2 migrates vertically from an areally extensive plume), a single value of critical capillary entry pressure may not be sufficient to determine which traps actually get filled. In the opposite limiting case of CO_2 invading the entire thickness of the reservoir during high-rate injection, a single value of $P_{c,entry}^{crit}$ appears adequate to account for the filling of traps. However further research is needed to to determine that value from the physical and geologic conditions of the storage process.

Simulations of injection into high-resolution (cells 0.3 m on a side) 2D and 3D heterogeneous domains show two characteristic behaviors. At small gravity numbers (vertical flow velocity much less than horizontal flow velocity) the CO_2 invades the entire thickness of perforated interval in the storage reservoir, and thus fills local traps as well as regions that would act as local barriers if CO_2 were moving only due to buoyancy. When injection ceases, the CO_2 migrates vertically to establish large saturations within local traps and residual saturation elsewhere. At large gravity numbers, the CO_2 flow regime is "capillary channeling" in which the CO_2 movement is buoyancy dominated and thus invades a smaller portion of the perforated interval. Within this smaller swept zone the local barriers are not invaded at all, but local traps are filled to large saturation. The small gravity number behavior is expected in the region within 100 m of a vertical injection well at expected rates for commercial GCS (ca. 1000 ton CO_2/day per well). The large gravity number behavior becomes dominant at greater distances from the injection well. Thus injection of CO_2 is expected to yield more LCT than the opposite limiting case scenario of CO_2 rising vertically from an areally extensive plume at the bottom of a formation.

Simulations of leakage scenarios in which the overlying seal became highly permeable in one or two locations showed that LCT was persistent (large fraction of regions of locally large saturations remained intact). Because the steady state distribution of CO_2 saturation in local traps was practically independent of the rate at which CO_2 was injected, the persistence of LCT was also independent of injection rate. Although fewer traps are filled for the other limiting case of CO_2 migrating vertically from an areally extensive emplacement in the lower portion of a reservoir, the CO_2 in those traps remains largely intact in the same leakage scenario. We conclude that LCT is a robust means of immobilizing CO_2.

This research has two broad implications for GCS. The first is that neglecting heterogeneity of capillary entry pressures in storage reservoirs gives a worst-case estimate of long-term storage security. That is, LCT can retain a significant fraction of the CO_2 stored in a reservoir – above and beyond the residual saturation—if the overlying seal were to fail. Thus frameworks for risk assessment should be extended to account for LCT. The second implication is that CO_2 migration and trapping are qualitatively different in heterogeneous reservoirs when buoyancy is the dominant driving force for flow. This is often the case: in most of the storage reservoir far from vertical injection wells, in almost all the reservoir when horizontal injection wells are used, in the entire reservoir after injection ends. Thus simulations of GCS that neglect capillary heterogeneity will fail to capture important features of the CO_2 plume.

While existing commercial reservoir simulation software can account for fine scale capillary heterogeneity, it has not been designed to work efficiently with such domains, and no simulators can handle fine-scale resolution throughout the reservoir. To address this problem, the possibility of representing LCT in fine-scale grids as an "effective residual saturation" in coarse-scale grids was investigated. While the extent of overall immobilization can be correlated in this way, all coarser grids failed to capture the distance traveled by the migrating CO_2 in the capillary channeling flow regime (buoyancy dominated, large gravity number). Thus it remains unclear how best to account for LCT in the routine simulation work-flow that will be needed for large-scale GCS. Alternatives such as streamline methods, reduced-physics proxies (e.g. particle tracking), and biased invasion percolation algorithms, which are based on precisely the capillary heterogeneity essential for LCT, are suggested.

REFERENCES

Begg, S. H., R. R. Carter, and P. Dranfield. "Assigning Effective Values to Simulator Gridblock Parameters for Heterogeneous Reservoirs." *SPE Res Eng* 4, no. 4 (1989): 455-463.

Bennion, B., and S. Bachu. "The impact of interfacial tension and pore size distribution/capillary pressure character on CO_2 relative permeability at reservoir conditions in CO_2-brine systems." *SPE/DOE Symposium on Improved Oil Recovery*. Tulsa, Oklahoma: SPE, 2006.

Brooks, R. H., and A. T. Corey. "Properties of Porous Media Affecting Fluid Flow." *J. Irrig. Drain. Eng. Div.* (ASCE) 92 (1966): 61-88.

Bryant, S. L., Lakshminarasimhan, S., and Pope, G.A., "Buoyancy-Dominated Multiphase Flow and Its Effect on Geological Sequestration of CO_2," *Society of Petroleum Engineers Journal*, Volume 13, Number 4, pp. 447-454, December 2008.

Caers, J. *Petroleum Geostatistics*. Richardson, Texas: Society of Petroleum Engineers, 2005.

Chalbaud, C. A., Robin, M., & Egermann, P. "Interfacial Tension Data and Correlations of Brine-CO_2 Systems under Reservoir Conditions. Society of Petroleum Engineers." *SPE Annual Technical Conference and Exhibition*. San Antonio, TX: SPE 102918, 2006.

Cinar, Y., A. Riaz, and H. A. Tchelepi. "Experimental Study of CO_2 Injection into Saline Formations." *SPE Annual Technical Conference and Exhibition.* Anaheim, California: SPE 110628, 2007.

Deutsch, C. V. *Geostatistical Reservoir Modeling.* New York: Oxford University Press, 2002.

Harter, T. "Finite-size scaling analysis of percolation in three-dimensional correlated binary Markov chain random fields." *Physical Review E* 72 (2005): 026120.

Hernandez, A. "Observations of Buoyant Plumes in Countercurrent Displacement." Master's thesis, The University of Texas at Austin, 2011.

Holtz, H. M. "Residual Gas Saturation to Aquifer Influx: A Calculation Method for 3-D Computer Reservoir Model Construction." *SPE Gas Technology Symposium.* Calgary, Alberta, Canada: SPE 75502, 2002.

Jennings, J. W., S. C. Ruppel, and W. B. Ward. "Geostatistical analysis of permeability data and modeling of fluid-flow effects in carbonate outcrops." *SPE Reservoir Evaluation and Engineering* 3 (2000): 292-303.

Journel, A. G., C. Deutsch, and A. J. Desbarats. "Power Averaging for Block Effective Permeability." *SPE California Regional Meeting.* Oakland, California: SPE, 1986.

Keelan, D. K., and V. J. Pugh. "Trapped-Gas Saturations in Carbonate Formations." *SPE J.* 15, no. 2 (1975): 149-160.

Kumar, A. *A simulation study of carbon sequestration in deep saline aquifers.* M.S. thesis, Austin, Texas: The University of Texas at Austin, 2004.

Kumar, A., R.C. Ozah, M. Noh, G.A. Pope, S.L. Bryant, K. Sepehrnoori, L.W. Lake. "Reservoir Simulation of CO_2 Storage in Deep Saline Aquifers." *SPE J.* 10, no. 3 (2005): 336-348.

Leverett, M. C. "Capillary Behavior in Porous Solids." *Trans. AIME*, 1941

Li, D. *Scaling and Upscaling of Fluid Flow through Permeable Media.* PhD dissertation, Austin, Texas: The University of Texas at Austin, 1995.

Newman, M. E., and R. M. Ziff. "Efficient Monte Carlo algorithm and high-precision results for percolation." 85, no. 19 (2000): 4104-4107.

Pedersen, K. S., A. Fredenslund, P. L. Christensen, and P. Thomassen. "Viscosity of Crude Oils." *Chemical Engineering Science* 39, no. 6 (1984): 1011-1016.

Pini, R., S. C.M. Krevor, and S. M. Benson. "Capillary pressure and heterogeneity for the CO_2/water system in sandstone rocks at reservoir conditions." *Advances in Water Resources* 38 (2012): 48-59.

Plug, W. J., and J. Bruining. "Capillary pressure for the sand–CO_2–water system under various pressure conditions. Application to CO_2 sequestration." *Advances in Water Resources* 30 (2007): 2339–2353.

Qi, D., and T. Hesketh. “An Analysis of Upscaling Techniques for Reservoir Simulation.” *Petroleum Science and Technology* 23, no. 7 (2005): 827-842.

Saadatpoor, E., Bryant, S.L. and Sepehrnoori, K., “New Trapping Mechanism in Carbon Sequestration,” *Transport in Porous Media,* Volume 82, Issue 1, pp. 3-17, 2010a. DOI: 10.1007/s11242-009-9446-6

Saadatpoor, E., S. L. Bryant, and K. Sepehrnoori. “CO_2 Leakage from Heterogeneous Storage Formations.” *SPE Annual Technical Conference and Exhibition.* Florence, Italy, 2010b.

Saadatpoor, E. “Local Capillary Trapping in Geological Carbon Storage,” Ph.D. dissertation, The University of Texas at Austin, 2012.

Timur, A. “An investigation of permeability, porosity and residual water saturation relationships for sandstone reservoirs.” *The Log Analyst* (Society of Petrophysicists and Well-Log Analysts) IX, no. 4 (1968).

Warren, J. E., and H. S. Price. “Flow in Heterogeneous Porous Media.” *SPE J.* 1, no. 3 (1961): 153-169.

LIST OF ACRONYMS AND ABBREVIATIONS

BIC	binary interaction coefficient
BIN	GEM keyword for binary interaction coefficient
CMG	Computer Modeling Group, Ltd.
DEN	GEM keyword to indicate use of density as identifying characteristic of a phase
EOS	equation of state
FFT	Fast Fourier transform
GCS	geologic CO_2 storage
GEM	generalized equation of state model
LCT	local capillary trapping
PCGMAX	scale factor for capillary pressure curve (GEM keyword)
PEDERSEN	GEM keyword for the Pedersen viscosity correlation
PHASEID	GEM keyword for method of identifying a fluid phase
PREOS	Peng Robinson equation of state
VISCOEFF	GEM keyword for coefficient in viscosity correlation
VISCOR	GEM keyword for viscosity correlation
VOLMOD	volume modifier (GEM keyword that multiples nominal grid block volume; used to approximate constant pressure boundaries)
VSP	volume shift parameter
VSHIFT	GEM keyword for volume shift parameter